

Vat 3D printable materials and post-3D printing procedures for the development of engineered devices for the biomedical field

*Original*

Vat 3D printable materials and post-3D printing procedures for the development of engineered devices for the biomedical field / GONZALEZ FLORES, GUSTAVO ADOLFO. - (2021 Mar 30), pp. 1-244.

*Availability:*

This version is available at: 11583/2897002 since: 2021-04-26T10:23:22Z

*Publisher:*

Politecnico di Torino

*Published*

DOI:

*Terms of use:*

Altro tipo di accesso

This article is made available under terms and conditions as specified in the corresponding bibliographic description in the repository

*Publisher copyright*

(Article begins on next page)



# ScuDo

Scuola di Dottorato ~ Doctoral School  
WHAT YOU ARE, TAKES YOU FAR



Doctoral Dissertation  
Doctoral Program in Material Science and Technology (XXXIII Cycle)

## **Vat 3D printable materials and post-3D printing procedures for the development of engineered devices for the biomedical field**

Gustavo Adolfo González Flores

### **Supervisor:**

- Prof. Fabrizio C. Pirri – Department of Applied Science and Technology, Politecnico di Torino, Italy.

### **Co-supervisors:**

- Dr. Annalisa Chiappone - Department of Applied Science and Technology, Politecnico di Torino, Italy.
- Dr. Ignazio Roppolo - Department of Applied Science and Technology, Politecnico di Torino, Italy.

### **Referees:**

- Prof. Albert Folch - Bioengineering Department, University of Washington, United States.
- Prof. Victor Sans Sangorrin - Institute of Advanced Materials (INAM), Universitat Jaume I, Spain.

Politecnico di Torino

2020

# Declaration

I herein declare that this thesis dissertation's content and organization constitute my own original work. It does not in any way compromise the rights of third parties, including those related to the security of personal data.

Gustavo Adolfo González Flores  
Turin, 2020

# Acknowledgment

I would like to thank Professor Candido Fabrizio Pirri for tutoring my thesis and supporting me in these years of research activity. I would like to express my endless gratitude to Ph.D. Annalisa Chiappone and Ph.D. Ignazio Roppolo, for supporting me (and enduring me) during these years of research activities helping me in scientific and non-scientific topics, and football activities. Many thanks for their complete availability, wisdom, advice, and patience in these years. I would also like thanks to Prof. Paula Bosch for her guidance and precious pieces of advice that she gave me during my research period at Instituto de Ciencia y Tecnologia de Polimeros (ICTP) in Madrid. For all the people and colleagues that I had the opportunity to cooperate over these years, resulting in interesting work, good ideas, and collaborations.

My deepest gratitude to my mother, Lizbeth Josefina Flores, and my other parents: Haydee Marcano, and Omar Hernandez, for giving me always their unconditional support in my academic and personal life. To my brothers, Gerardo y Vicente González, we have always been a team despite the distance.

Finally, I would like to thank Daniela for supporting and believing in me during these years, helping me in the bad moments, and celebrating with me in the good ones. Thanks for being always there with me and smiling constantly. Thanks for being Daniela.



# Abstract

3D printing technology is changing how objects are designed and manufactured by gradually introducing novel production concepts. Indeed, 3D printing is considered as one of the fundamental pillars of the so-called Industry 4.0. It enables the fabrication, in a short time, of bespoke parts with *quasi* any geometry from a digital model and without requiring tooling or expensive equipment. Moreover, most digital models can be found online, simplifying sharing, and publishing designs between users. 3D printing techniques are based on the layer-by-layer spatial-controlled joining of materials, a concept that can be applied to metallic powders, ceramic slurries, polymers, and composites in different conditions, i.e., liquid, gel, powder, or solid filaments. Moreover, 3D printing allows the fast production of customized objects and, at the same time, a better way of using raw materials, generating economic savings.

In the biomedical field, 3D printing has found a particular ground for producing customized goods such as medical implants, biological models, and biomedical analytical systems. In this scenario, polymers' 3D printing is largely exploited for medical applications thanks to the relatively wide availability of printable polymers, offering a palette of different properties. Furthermore, they can also be processed by cost-affordable printer machines. All this has gradually led doctors, experts, and scientists to approach 3D printing for many particular biomedical purposes where personalized devices or implants are promptly required.

A clear example was observed during the recent pandemic outbreak related to COVID-19, where customized pieces were on-demand and rapidly

produced near hospitals, demonstrating how polymeric 3D printing can play a fundamental role in crisis moments. Nevertheless, to keep up with the rise of 3D printing in the biomedical field, new materials must be developed to satisfy basic biomedical properties, e.g., biocompatibility. The current market for printable polymers shows that only a few are considered biocompatible, and post-printing treatments play a crucial role in reducing the potential toxic agents.

The investigations presented in this dissertation focus on the development of custom-made photosensitive polymers or photopolymers for light-based 3D printing applications, also noted as vat polymerization, intending to produce bespoke objects with biomedical features. By combining appropriate materials during the printable polymer preparation and the freedom of design given by 3D printing, unique structures can be produced with interesting bioproperties; the following chapters will present different approaches to achieve such purposes. An overview of the 3D printing technology, its achievements, and challenges, focusing on the light-induced techniques, is first reported in Chapter 1 of this thesis. It follows in Chapter 2, a literature review on polymeric 3D printing applications in the biomedical field.

The first experimental part is based on preparing and testing commonly-used photopolymers for vat 3D printing to produce parts for biological studies (Chapter 3, Part I). Post-printing treatments will also be explored to eliminate the potentially toxic elements from the printed parts, thus enhancing cell lines' biocompatibility. Other polymeric systems based on acrylate-polydimethylsiloxane (PDMS) resins are also presented to print complex-shaped and three-dimensional structures with good printing resolution (Chapter 3, Part II). In this case, the specific idea is to fabricate 3D printed PDMS-based microfluidic chips with characteristics similar to the conventional PDMS material used for microchip fabrication. The final goal consists of obtaining parts with great optical features, high chemical stability, and good mechanical properties.

Chapter 4 reports the second experimental contribution based on the investigation of specific post-printing protocols to induce surface modification on the printed parts, intending to expand their bioproperties. The changes in the printed objects' properties will be assessed by taking advantage of some reactive functional groups exposed on their surface after 3D printing. These functional groups can be used to link additional molecules of biological interest. The surface functionalization can proceed during the necessary post-curing step via UV-induced grafting polymerization techniques, even in close microfluidic devices (Chapter 4, Part I: Functionalization of 3D printed microfluidic chips.), or via microwave radiation (Chapter 4, Part II: Surface modification by microwave radiation.).

The last experimental part focuses on exploiting an unique additive during the photopolymer preparation for increasing the printed parts' functionality (Chapter 5). A custom-made photopolymer is prepared by integrating a functional dye to obtain 3D printed structures with inner properties such as convenient optical characteristics, adequate light-guiding performances, and high sensitivity to different environments.

The research findings reported in this manuscript describe the efforts to shorten distances between the potential medical application of 3D printing and the available polymeric materials to produce more reliable and suitable biomedical parts. This doctoral dissertation's main idea is to enlarge the palette of the processable polymers with biological characteristics; each of the developed materials and methods reported here might be used as novel tools for biomedical purposes, particularly in point-of-a-care medicine.

Turin, Italy

Gustavo A. Gonzalez F.

# Table of content

<b>Acknowledgment</b> .....	<b>III</b>
<b>Abstract</b> .....	<b>IV</b>
<b>Chapter 1 3D Printing Overview: Basic concepts and principles</b> .....	<b>1</b>
1.1. 3D printing technology.....	1
1.1.1. Background and evolution.....	3
1.1.2. Fields of applications.....	5
1.1.3. Different 3D printing techniques.....	8
1.2. Vat polymerization (VP) 3D printing.....	9
1.2.1. Principle of photopolymerization.....	12
1.2.2. 3D printable formulations.....	15
Monomers and oligomers.....	15
Photoinitiators.....	18
Additives.....	21
1.2.3. Vat polymerization techniques.....	22
Stereolithography (SL) technique.....	22
Other light-based 3D printing techniques.....	24
1.2.4. 3D printing reliability.....	26
<b>Chapter 2 Biomedical vat 3D printing: Printable resins and main strategies</b> .....	<b>30</b>
2.1. Polymeric 3D printing for biomedical applications.....	30
2.2. Toward the 3D printing of microfluidic medical devices.....	34
2.2.1. Overview of microfluidic devices.....	34

2.2.2. 3D printed polymeric microfluidic devices. ....	40
Vat 3D printing for the production of microfluidic devices .....	46
2.2.3. Photopolymerizable biomaterials for microfluidic chip fabrication through vat 3D printing.....	56
<b>Chapter 3 3D printing fluidic devices: Design, fabrication, and testing protocols. ....</b>	<b>61</b>
3.1. Outline and motivation. ....	61
3.2. Part I: Biocompatibility of 3D printable conventional resins. ....	64
3.2.1. Experimental section. ....	65
Materials and chemicals .....	65
Preparation of the acrylate-based printable resin .....	65
Digital light processing DLP-3D printing.....	65
Washing and UV post-curing protocols .....	66
Sterilization protocols .....	67
Characterization methods .....	67
Cell culture .....	68
Cell viability and proliferation.....	69
3.2.2. Results and discussion. ....	70
3D printing and material characterization .....	70
Cytotoxic effect of 3D printed wells toward A549 cells. ....	74
Cell viability and proliferation on the 3D printed wells.....	77
3.2.3. Conclusion. ....	79
3.3. Part II: 3D printing of PDMS-based microfluidic devices. ....	80
3.3.1. Experimental section. ....	82
Materials.....	82
Preparation of the PDMS-based printable resin.....	82
Digital light processing DLP-3D printer .....	83
Characterization methods .....	84
3.3.2. Results and discussion. ....	86
Initial characterization and 3D printing step.....	86
Solvent stability of the 3D printed materials .....	92
Mechanical tests.....	95
3.3.3. Conclusion. ....	97
3.4. Conclusions of the chapter. ....	98

<b>Chapter 4</b>	<b>Post-printing treatments: Enhancing the surface properties.</b>	<b>100</b>
4.1.	Overview and motivation.	100
4.2.	Part I: Functionalization of 3D printed microfluidic chips.	103
4.2.1.	Experimental section.	104
	Materials.	104
	Preparation of the grafting solution	104
	Characterization methods	104
4.2.2.	Results and discussion.	104
	UV-induced surface modification	104
4.2.3.	Conclusion.	109
4.3.	Part II: Surface modification by microwave radiation.	110
4.3.1.	Experimental section.	112
	Materials.	112
	Preparation of the photopolymers and grafting solutions	113
	Digital light processing DLP-3D printer	113
	Surface functionalization procedure with microwave	114
	Characterization methods	115
	Bacterial seeding	115
	Bacteria viability and proliferation	116
4.3.2.	Results and discussion.	117
	Characterization and functionalization of the 3D printed samples	117
	Microwave-assisted surface modification	121
	Antibacterial tests	129
4.3.3.	Conclusion.	132
4.4.	Conclusions of the chapter.	133
<b>Chapter 5</b>	<b>Integrated functionalities: A functional dye for 3D printable resins.</b>	<b>135</b>
5.1.	Outline and motivation.	135
5.1.1.	Experimental section.	140
	Materials.	140
	Synthesis of NBD-MA dye	140
	Preparation of the photoluminescent photopolymers	141
	Digital light processing DLP-3D printer	141
	Characterization methods	142

5.1.2. Results and discussion.....	145
5.1.3. Conclusion.....	157
<b>Final considerations and Conclusions .....</b>	<b>158</b>
<b>References.....</b>	<b>162</b>
<b>Appendix A.....</b>	<b>209</b>
List of figures.....	209
List of tables.....	223
List of publications and conferences from the author .....	225
Peer-reviewed publications .....	225
Related to side research topics.....	225
Abroad research activities .....	226
Conferences and workshops attended.....	226
<b>Appendix B.....</b>	<b>227</b>
<b>Characterization techniques .....</b>	<b>227</b>
Spectroscopy techniques.....	227
Ultraviolet-Visible (UV-VIS) spectroscopy.....	227
Fourier transformed infrared (FTIR) spectroscopy.....	228
Microplate reader.....	228
Microscopy techniques.....	228
Fluorescence microscopy.....	228
Spinning disk confocal microscopy.....	229
Scanning Electron microscopy (SEM).....	229
Thermal analysis and thermo-mechanical techniques.....	229
Differential scanning calorimetry (DSC). .....	229
Dynamic mechanical analysis (DMA). .....	230
Tensile testing.....	230
Other characterization techniques .....	231
Rheology experiments.....	231
Contact angle methods.....	232







## Chapter 1

# 3D Printing Overview:

Basic concepts and principles.

### 1.1. 3D printing technology.

Additive manufacturing (AM), or more frequently called 3D printing, is one of the most thriving technologies nowadays, with the potential to transform the traditional supply chain of parts and items. Indeed, it is considered one of the fundamental technological pillars of the so-called Industry 4.0.<sup>1,2</sup> 3D printing (3DP) is changing how products are designed and manufactured. It enables the on-demand production of parts from different types of materials that can be used in numerous applications: from aerospace components to wearable and fashion products, from sports accessories to customized prosthetics, from building architectural structures to nanometric devices.<sup>3,4</sup> The basic principle behind 3D printing technology is creating objects from a three-dimensional Computer-Aided Design (3D CAD) in a single machine and without using complex production chains or process planning. The models are created by the selective and successive addition of material, one layer at a time, until the part completion; each layer is a thin cross-section of the original model. Before the printing process, the 3D CAD is converted into computer-readable formats (STL, OBJ, 3MF, or AMF files) that give the

necessary digital codes to the printing machine for creating the part. The main features of 3DP techniques are the capability to accurately produce customized objects in a few minutes or hours, without molds and cutting tools, and from different raw materials such as plastics or polymers, metal, ceramic, or even composites.<sup>5,6</sup> By the selective addition of materials, 3D printing offers fascinating advantages over traditional production methods, e.g., subtractive manufacturing, in which the material is removed from a bulk piece, or forming and casting manufacturing, in which the material is shaped through a mold or dies.<sup>7-9</sup> The main benefits of 3D printing are:

- The fabrication of innovative and complex-shaped structures of any shape in a matter of minutes or hours.
- The direct production of complex objects from a 3D digital model (CAD) without requiring tools, molds, or complicated and expensive equipment.
- The production on-demand of customized products from small batches according to consumer needs.
- The digital CAD models can be easily shared, facilitating the CAD model's distribution and adjustment.
- Compared to traditional subtractive and mass production methods, the layer-by-layer concept delivers savings in raw materials consumption, costs, and energy, which is a crucial contribution to environmental sustainability.
- The improvement of the interaction among local consumers, clients, and producers.

3D printing has introduced innovative industrial strategies to design and fabricate many products for different applications.<sup>10,11</sup> In its beginnings, 3DP technology was first noted as rapid prototyping (RP) since, at the time, it was used for the fast-physical representation of objects before the final commercialization, i.e., a prototype. However, as the years passed, this term was less and less used as it does not effectively represent the essential characteristic of all the additive manufacturing processes, which is to join materials until the object completion.<sup>12</sup> Additive manufacturing and 3D printing emerged as the preferred terms to describe this process. Although “additive manufacturing” and “3D printing” are often used as synonymous, this indistinct use of both terms is not entirely correct. The former more likely refers to techniques on an industrial scale that involve multiple and expensive steps of production and complex equipment.

On the other hand, “3D printing” is more associated with lower-cost techniques, with equipment and materials that can be used beyond the industrial fields, e.g., research centers, business stores, and homes. Hand in

hand with engineers, software developers, and 3D designers, different additive manufacturing technologies have been developed today. They can be grouped according to how the layers are created and bonded, the type of material used, and the process's overall cost. These features determine the viability to produce a single piece, the accuracy of the objects, and the final properties. In an entire 3D printing process, up to seven (7) steps are involved for the correct realization of the object; these steps are summarized in Figure 1-1.<sup>13</sup>

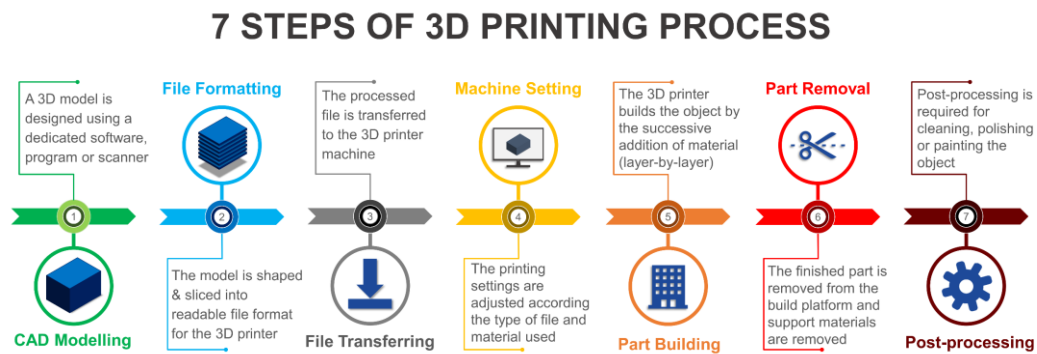


Figure 1-1. Illustration of the seven (7) steps involved in a typical 3D printing process.

### 1.1.1. Background and evolution.

Although only today, 3D printing technology is considered a serious candidate to create new production strategies in terms of sustainability and process optimization, its invention is not recent.<sup>8,9</sup> One of the earliest records was presented in 1980 by Hideo Kodama from Nagoya Municipal Industrial Research Institute.<sup>14</sup> He introduced an innovative manufacturing method that consisted of the selective hardening of polymeric layers upon UV light, depositing them one after the other. Although his idea was published in scientific journals, he could not patent his invention due to funding issues.<sup>15</sup> Later, in 1983, an engineer working on protecting furniture with acrylic coatings had a similar idea for fabricating three-dimensional objects by overlapping many polymeric layers just by manipulating UV light. This man was Charles "Chuck" Hull, a physical engineer from the University of Colorado and currently CEO of *3D Systems*. Hull translated his idea into the US patent issued on March 11, 1986, titled "Apparatus for Production of Three-Dimensional Objects by Stereolithography," or just as stereolithography.<sup>16</sup> He developed a system where a beam of light is focused into a vat containing an acrylic resin (a photopolymer) and traces the object's shape in the X-Y plane, creating multiple layers through polymerization. The subsequent layers are "printed" following the same procedure until the complete formation of the object. From that moment, Hull started the revolution in the manufacturing

business, merging materials science with electronic and software development. He sowed the seed for the growth of what is now known as additive manufacturing. 1988 was the golden year for 3D printing technology as we know it today, with the invention of two methods that contributed significantly to the extensive diffusion of additive manufacturing in different sectors. Carl Deckard and Joe Beaman developed an advanced additive method through the selective sintering of powders layers (which can be either polymer, metal, or ceramic) spread in a platform, known as Selective Laser Sintering (SLS). Their idea was issued from 1990 onwards in multiple US patents.<sup>17-19</sup> In the same year, it was developed one of the most diffused 3DP techniques used in companies, commercial businesses, and even in homes. Scott Crump, trying to create toys for his daughter with candle wax and plastics, observed that fascinating objects could be created in an entirely automated process coupling a hot glue gun with a robotic XYZ movable system originating thus the Fused Deposition Modelling (FDM). His idea was issued in 1989 under US patent n° 5121329.<sup>20</sup> Years later, he founded the Stratasys company. The subsequent rise of FDM technology arrived in 2009 when Crump's patent expired, and people started to use and fabricate their FDM printers without compensating *Stratasys*, decreasing the costs of equipment and materials. Stratasys still owns the FDM term; therefore, these methods have been renamed Fused Filament Fabrication (FFF).

In 2019, the investment in 3D printing was around 14 billion dollars, and it is expected to be almost \$ 64 billion by 2025, with the Asian Pacific region as the main protagonist.<sup>21</sup> The 3D printing market is currently a consolidated business shared by the top players in the industry, such as Proto-Labs Inc., 3D Systems Corporation, Arcam AB (GE Aviation), Stratasys Ltd., ExOne Co., Hewlett Packard Inc., among others. These companies have gained significant sizes of consumers, investing continually in research and development (R&D). For example, within its current technological expansion project, the company 3D systems opened its new advanced additive manufacturing center in Pinerolo, Italy, in 2019.<sup>22</sup> In the last years, 3D systems began a multi-million-dollar expansion to more than double manufacturing capacity to meet growing customer demand. According to Sculpteo's report, future trends of 3DP will be focused on four (4) categories: affordability, sustainability, technological evolution, and materials.<sup>23</sup> The main challenges of each of them are listed:

- **Affordability:** Lower costs for 3D printing machines and materials and the cost reduction of the post-printing processing. The sharing of designs and instruments.
- **Sustainability:** the development of biodegradable and bio-sourced printable materials. 3D printing in applications of renewable energy and energy efficiency. Local production of parts for reducing shipping and environmental costs.

- Technological evolution: more user-friendly software and printers. Improvement in printing speed and 3D scanning looking to mass production applications. Generative designs.
- Materials: New and affordable materials (metals and polymers) are required to satisfy the growing demand and the possibility to produce multi-material prints quickly. The consistency and the quality of the printed objects and the post-processing technologies will be improved.

### 1.1.2. Fields of applications.

As described previously, 3D printing offers valuable options for the fabrication of structures with *quasi* any shape and dimension, built with different types of raw materials, as is represented in Figure 1-2. These structures can be used in various categories of industrial, scientific applications, and socio-cultural purposes.<sup>3</sup> 3D printing offers remarkable benefits for the on-demand fabrication of customized and highly complex-shaped components. After optimizing the digital design and setting the proper 3D-fabrication parameters, lightweights and bespoke parts can be obtained, saving at the same time energy and resources.<sup>24</sup> Moreover, unlike conventional manufacturing processes, with 3D printing, these parts can be created without requiring expensive tools such as molds, dies, or longer production chains, making the whole process more convenient in terms of costs and time.<sup>25</sup>

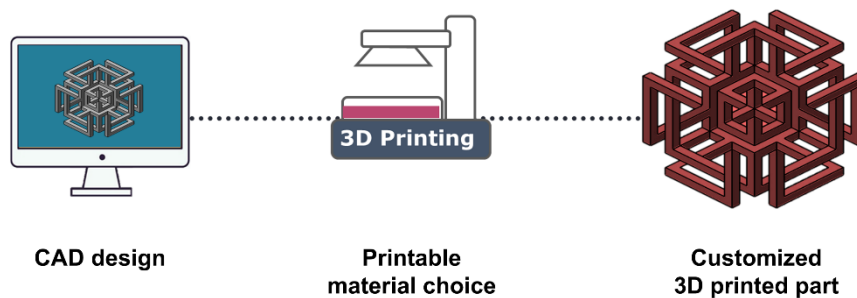


**Figure 1-2. Example of how 3D printing can be used to produce customized and complex-shaped structures difficult or laborious to create with other conventional manufacturing methods from a simple digital CAD model.**

The 3D printing capabilities have been recognized by a demanding sector, such as aerospace. The aerospace industry uses principally costly and advanced metallic materials, such as titanium, nickel-based, high-strength steel superalloys, or ultra-high temperature ceramics. With 3D printing methods, these materials can be more easily processable to produce advanced

components such as airplane components.<sup>26,27</sup> Besides, raw material wastes can be reduced considerably from 95 % to 10 %.<sup>28</sup> Indeed, Airbus, one of the most relevant aerospace companies, has already implemented 3D printing for manufacturing bracket connectors made of titanium alloy for the Airbus A350 XWB airplane (Figure 1-3.b).<sup>29</sup> As in this and other cases, one of the principal scopes is aiming to produce lightweight parts; in fact, Airbus's brake presented a 30% weight reduction with similar performances compared to standard parts. The weight reduction interest has led commercial additive manufacturing companies, such as *Materialize NV*, to propose lightweight services production for metallic components. For instance, using dedicated software programs, such as *Materialise 3-Matic*, it is possible to obtain weight reduction up to 63 % (Figure 1-3.a).<sup>30</sup>

Similarly, in the automotive world, 3D printing has been widely employed to develop lighter and more complex objects in shorter times. It has been of valuable interest in luxury and low volume vehicle production since customized parts can be on-demand produced from small batches.<sup>31</sup> For example, the German car manufacturer *Porsche* started to use 3D printing to produce spare parts for classic and luxury vehicles. In particular, *Porsche* 3D printed a release pedal for the clutch of a Porsche 959, a collection car. With 3D printing, *Porsche* stated that it could be a considerable cost saving as they will not need to store any physical part, only digitally, and print it when necessary.<sup>32</sup> 3D printing in the automotive industry might enable numerous improvements in the production stages for effective automotive part design, reducing at the same time raw material wasting, costs, and time, allowing testing new designs promptly.<sup>33</sup> In the medical field, 3D printing has found a particular place in manufacturing customized biomedical parts and diagnostic systems.<sup>34</sup> 3D printing's foray into the medical field starts in the early 2000s with dental implants and prosthetics production.<sup>35</sup> Nowadays, it is widely employed for research departments and industries in various healthcare settings, taking advantage of one of these technology's main features, customization. The versatility of the different 3D printing technologies can be utilized in bioimplants' on-demand production (Figure 1-3.c), organ models, biological entities, microfluidic devices, and tissue engineering scaffolds.<sup>36-38</sup>

3D printing has made possible the construction of houses and massive structures in less time than conventional building processes in a more economical and environmental approach in moving toward the building industry. It is foreseen that 3D printing could increase the building industry's sustainability, which consumes a high percentage of resources with relatively high environmental impact.<sup>48</sup> With 3D printing, these environmental drawbacks might be overcome, reducing the building times and increasing the buildings' customization. Although 3D printing is still making its first steps in the building industry, Apis Cor company recently made feasible the

construction of a 640 square meter building in Dubai, using only local resources, see Figure 1-3.d.<sup>45</sup> The building, used for administrative purposes, was on-site constructed in two weeks requiring only three workers.

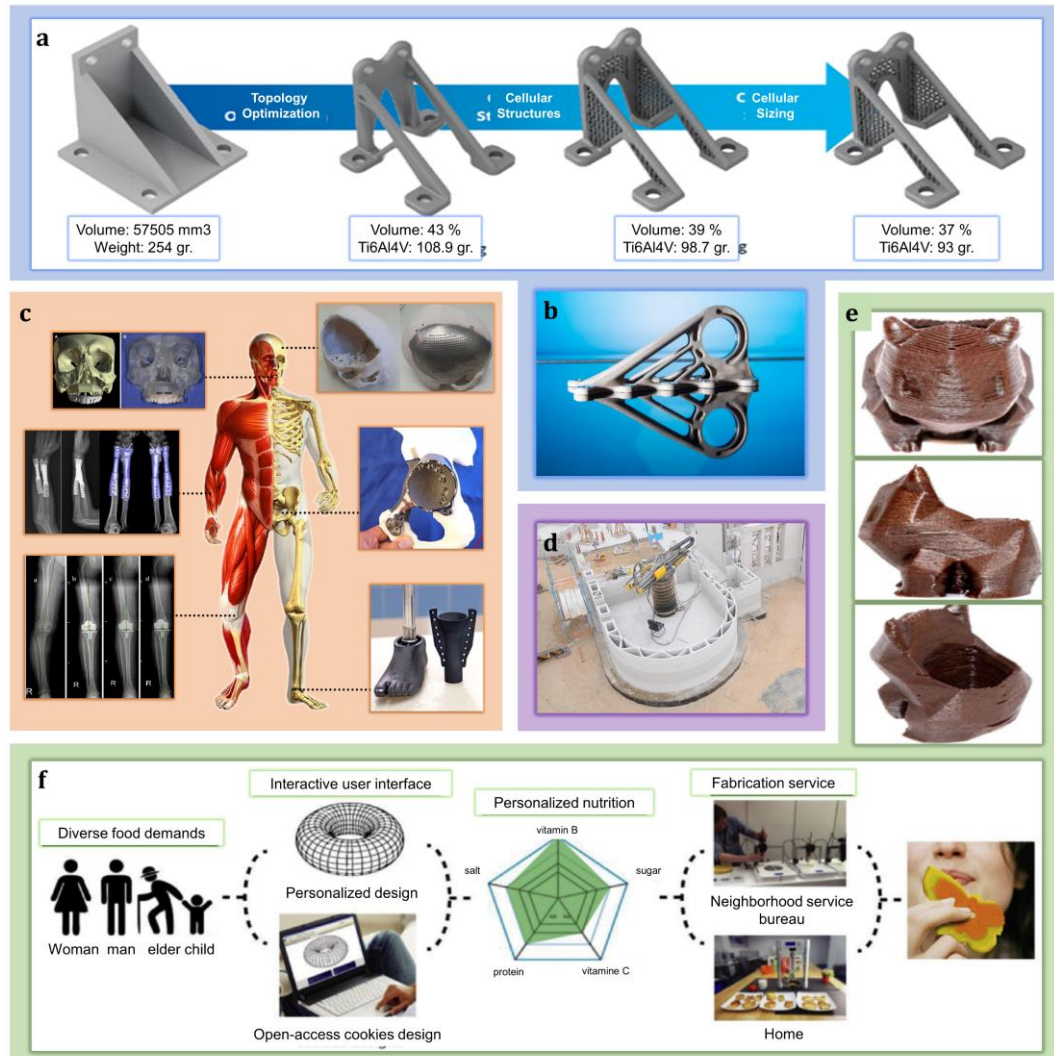


Figure 1-3. **Examples of 3D printing in the biomedical sector.** (a) Representation of the production flow of metallic parts optimized for weight reduction of up to 63%.<sup>30</sup> (b) 3D printed cabin bracket using a titanium alloy for the Airbus A350 XWB.<sup>29</sup> (c) bioimplants and prosthesis obtained through 3D printing.<sup>39-44</sup> (d) 640 m<sup>2</sup> building produced from *Apis Cor* company. <sup>45</sup> (e) 3D printed structure made of chocolate.<sup>46</sup> (f) flow plan for developing specific food items with the required nutrient features.<sup>47</sup>

3D printing technology can also be used for food processing, where the printable materials are based on edible ingredients such as sugar, chocolate, and gelatin.<sup>46</sup> Taking advantage of the freedom in geometry design that 3D printing delivers, spectacular food designs with personalized structures have been created by chefs and food designers, as reported in Figure 1-3.e.



Moreover, with 3D food printing methods, diet and nutrition experts could benefit from the production of individualized supplement pills for a particular person according to its physical and energy requirements (see Figure 1-3.f).<sup>47</sup> With 3D food printing, one of the main foreseen advantages is that it may shorten the supply chain of food and broaden the range of available eatables products using innovative plant and animal-based materials.<sup>49</sup> In this context, material properties such as viscosity, processing temperature, and tribological characteristics are of great importance, and indeed, they are widely studied to obtain food pieces with the desired characteristics and shape.<sup>50,51</sup> Powder food material (e.g., sugar) can be processed with sintering 3D printing, but also techniques such as hot air sintering or liquid bending can be used for such purpose.<sup>52</sup> Other materials used for extrusion-based methods need to present a suitable viscosity range for being adequately dispensed through the machine's nozzles without suffering from deformations during its process through extrusion-based methods.<sup>53,54</sup>

As seen, the significant and multiple versatilities in terms of customization, sustainability, and production times of 3D printing has been successfully used in different industrial and scientific disciplines. This tendency is increasing due to the tremendous technological advances in the field, which have led to the inclusion of these technologies in other sectors such as textiles and sports for protective clothing, baby diaper, shoe cleats applications, and the wearable electrical components industry.<sup>55-60</sup> The establishment of 3D printing in the different daily social applications can be focused on two fronts: the technological one regarding new automatized, faster, and more precise technologies and processes for 3D printing, and the materialistic one, where new materials are continuously required to produce functional parts for numerous types of applications.<sup>61,62</sup> In this perspective, the growing world demand for new production and manufacturing approaches made new materials more urgent. Materials with useful characteristics and properties can provide more valuable utility to the printed parts far beyond the classic prototyping and hobbyist use.

### **1.1.3. Different 3D printing techniques.**

From the invention of the initial systems in the '80s to the present day, many different 3D technologies have been developed. They can be classified in various ways, for example, by the type of basal technology employed to create the object (e.g., based on laser, extrusion, liquid bonding, or sheet lamination).<sup>3,5,13,63</sup> Pham and coworkers proposed one of the first methods to classify them.<sup>64</sup> They grouped 3D printing processes by the type and the condition of the raw materials: particles, laminated solid films, and

liquid/molten materials. After the publication of Pham's work in 1998, innovative 3DP techniques were developed; however, most of them fall within the same classification system since their operational principles are similar or derived from those created earlier. Another classification is based on the type of machine used and the transformation of the material during the process, as depicted in Figure 1-4: material extrusion, binder jetting, material jetting, powder bed fusion, directed energy deposition, sheet lamination, and vat polymerization.<sup>65</sup>

Each of the technologies offers unique characteristics, as briefly presented in Figure 1-4. They have been extensively evaluated in multiple literature reviews, where it is possible to find a summary of the materials used, application areas, benefits, and drawbacks of the principal 3D printing methods.<sup>3,6,56,64-68</sup> Considering the investigations conducted in this thesis, only the techniques based on the photopolymerization of liquid resins, specifically vat polymerization 3D printing techniques, will be described in detail in the following sections.

## **1.2. Vat polymerization (VP) 3D printing.**

Vat polymerization (VP) 3D printing involves using a vat containing a liquid photopolymer that is selectively polymerized or cured upon light irradiation through a chemical reaction called photopolymerization. It enables objects' production by the sequential overlapping of thin polymerized layers positioned on a movable platform, which moves (in the z-axis) according to the following layers' formation. This technique allows the fabrication of precise parts of complex geometry without specific supporting tools nor complicated machine configurations.<sup>69</sup> During the 3D printing process, the part (placed on the platform) repeatedly comes into contact with the liquid photopolymer or resin. Therefore, a crucial point in this process is that the polymerized piece in production is insoluble in the liquid photopolymer, i.e., the cured structure remains dimensionally and mechanically invariable when in contact with the liquid resin; such requirement is accomplished by using cross-linkable photopolymers and supplying the system with sufficient light energy to reach the material's gel point. The gel point is when the liquid system undergoes a sudden change in its fluidity due to the formation of a three-dimensional crosslinked matrix (the gel). Beyond this point, the system is no longer a liquid material, showing more solid-like mechanical properties, and becoming an insoluble polymeric material progressively, as better described in the following sections. Photopolymers can also be used in other 3D printing techniques such as Inkjet, Multijet, or some Binder Jetting methods. However, these methods cannot be considered among the VP techniques since they build the objects by the

selective addition and hardening of the liquid polymer and support material from jetted from tiny nozzles.

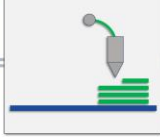
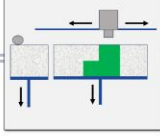
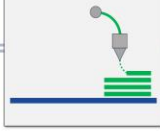
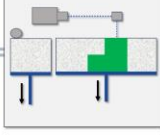
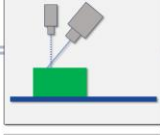
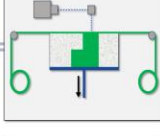
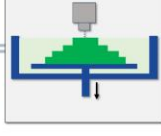
Technology	Scheme	Methods	Process	Advantages	Drawbacks
Material extrusion		Fused deposition modelling (FDM) Fused filament fabrication (FFF) Direct ink writing (DIW) Embedded 3D printing (EM3D)	A nozzle gun builds objects by layering wires of molten materials or pastes.	<ul style="list-style-type: none"> <li>- Functional objects from standard plastics.</li> <li>- Biocompatible materials</li> </ul>	<ul style="list-style-type: none"> <li>- Z-direction anisotropy.</li> <li>- High cost of systems.</li> <li>- Small build volume.</li> </ul>
Binder jetting		3D printing Binder jetting (BJ)	Selective dispense of binder for joining powder in a bed	<ul style="list-style-type: none"> <li>- Wide range of materials.</li> <li>- Produce multicolored parts.</li> <li>- Cost-affordable</li> </ul>	<ul style="list-style-type: none"> <li>- Limited mechanical properties.</li> </ul>
Material jetting		MultiJet (MJ) Drop-on-demand (DOD) Inkjet printing Polyjet printing Nanoparticle jetting (NPJ)	Material deposition and subsequent curing	<ul style="list-style-type: none"> <li>- Good accuracy and surface finish.</li> <li>- Multi-color materials can be used</li> </ul>	<ul style="list-style-type: none"> <li>- Only works with wax-like materials.</li> <li>- Materials are not durable in time.</li> </ul>
Powder Bed fusion		Selective laser sintering (SLS) Selective laser melting (SLM) Electron beam melting (EBM) MultiJet fusion (MJF)	Fusion of powder in a bed by melting the selected region	<ul style="list-style-type: none"> <li>- No support material is required.</li> <li>- Good mechanical properties.</li> </ul>	<ul style="list-style-type: none"> <li>- Limited surface finish.</li> <li>- Expensive equipment.</li> <li>- Produces large waste.</li> </ul>
Direct energy deposition		Laser engineered net shaping (LENS) Electron beam additive manufacture (EBAM) Direct metal tooling (DMT)	Direct and selective fusion of the material	<ul style="list-style-type: none"> <li>- Good granular metal structures</li> <li>- Uses powder or wire products</li> </ul>	<ul style="list-style-type: none"> <li>- Low dimensional accuracy</li> <li>- May require machining or polishing steps</li> </ul>
Sheet lamination		Laminated object manufacturing (LOM) Ultrasonic consolidation (UC)	Bonding of individual sheets of material	<ul style="list-style-type: none"> <li>- Large scale models</li> <li>- Fast and accurate</li> <li>- Good handling strength</li> </ul>	<ul style="list-style-type: none"> <li>- Requires many post-3D processing labor</li> </ul>
Vat polymerization		Stereolithography (SLA or SL) Digital light processing (DLP) Continuous direct light processing (CDLP)	Selective curing of photo-curable resin in a liquid container	<ul style="list-style-type: none"> <li>- High accuracy</li> <li>- Good surface finish</li> <li>- Flexibility on raw material development</li> </ul>	<ul style="list-style-type: none"> <li>- Some resins are not stable over time.</li> <li>- Limited mechanical features.</li> </ul>

Figure 1-4. The seven Additive Manufacturing classification and its main advantages and drawbacks.<sup>56,65</sup>

From a technological perspective, vat polymerization 3D printing can be classified into two main subgroups, depending on their optical arrangement, as will be described in the following sections. The first one to be developed is the technique known as stereolithography (SL), which is a point-by-point method that involves a movable laser beam focused on the photopolymer surface, activating the photopolymerization of the liquid substance selectively and printing solid films one on top of the other. The second method is known as digital light processing (DLP) 3D printing, which derives from the laser-based SL method, but instead of employing a movable laser beam, involves using a light source projector for irradiating an entire cross-section of the

object at once.<sup>70</sup> Although vat polymerization (VP) was introduced during the eighties, this technology is still of great scientific and industrial interest, and it grows year after year.<sup>71,72</sup> This statement is corroborated by the vast number of scientific articles (including only papers, proceedings, and preprints files) and patents issued over the last decades using vat polymerization or similar keywords, as represented in Figure 1-5.

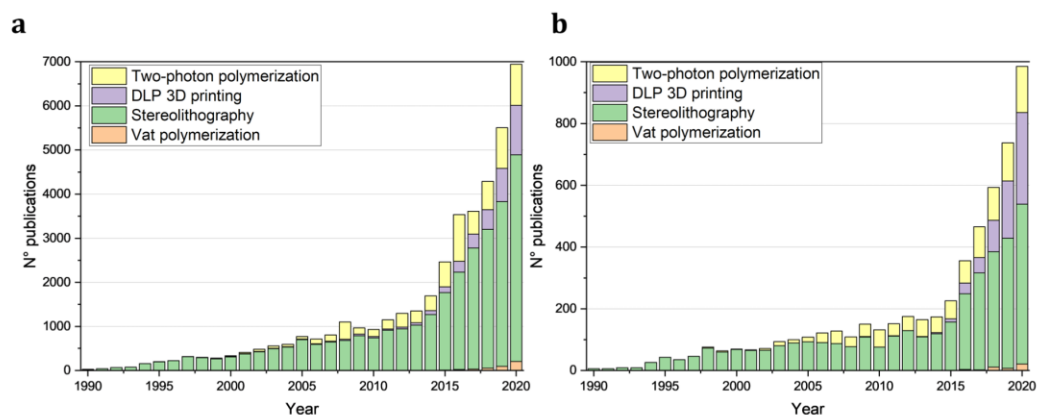


Figure 1-5. **Publications per year using vat polymerization or similar terms (as detailed in the legend inset) from 1990 to 2020.** (a) N° publications per year in which the keywords appear at least once during the article's full text. (b) N° of publications per year in which the keywords appear in the scientific article's title or the abstract. Data obtained from the dimensions.ai database.

One of the principal advantages of vat polymerization methods over other 3D printing techniques is the possibility of modifying the starting liquid material, the photopolymer, which is a combination of chemical compounds and reagents (both liquids and powders). The tailoring of the liquid photopolymers opens many possibilities to produce parts where the properties can be designed by integrating the right elements.<sup>70</sup> Commonly, the photopolymers for 3D printing are composed of three main components:

- **Monomers and oligomers:** liquid resins having reactive groups necessary to create the polymeric network. The backbone of these reagents defines the polymerized part's final physical and mechanical properties, also considering the appropriate adhesion between cured layers.
- **Photoinitiators:** compounds that absorb the incident light, generating reactive species or radicals through chemical transformations. These species interact with monomers and oligomers, enabling the photopolymerization mechanism.
- **Additives:** some additives can be added to change printable material features or add specific properties to the printed part. Few examples are reactive diluents, which are employed to adjust

the photopolymer's viscosity, or dyes/colorants, which are added to control the light's penetration during 3D printing (Z-axis) and to guarantee high resolution (XY plane).

Therefore, by fine-tuning these primary elements, functional 3D printed objects can be obtained with specific properties (e.g., mechanical, chemical, and optical, among others) depending on the designated application.<sup>38</sup> The following sections will detail the principle of photopolymerization, the most used materials for 3D printing, and the main differences between the main VP configurations.

### **1.2.1. Principle of photopolymerization.**

Photopolymers are a class of polymers whose synthesis process is induced by light irradiation. In this method, known as photopolymerization, polymers with different macromolecular structures can be synthesized depending on the type and the number of reactive groups in the monomers/oligomers involved, such as linear, branched, or crosslinked (Figure 1-6.a).<sup>73</sup> Over other methods such as thermal curing, light-induced polymerization offers remarkable advantages. It delivers rapid polymerization rates, room temperature treatments, the use of solvent-free formulations, low energy requirements, and high dimensional accuracy as the photopolymerization can be spatially controlled by managing the light settings during the process. The last one is also the reason why photopolymers are crucial for shaping complex structures in 3D printing. Besides, the photopolymer can be custom-prepared according to the envisaged application.<sup>74</sup>

The first synthetic photopolymer development was reported in 1952 by The Eastman Kodak industry under the US patent n° 2610120;<sup>75</sup> since then, photopolymers have been employed in various commercial applications: as decorative and protective coatings for metals, papers, and woods; as ink for producing integrated and printed circuits by photolithography, and for creating dental components.<sup>76</sup> The photopolymerization process occurs when liquid photosensitive resins, composed of monomer and photoinitiator, are polymerized or cured upon light irradiation. When the liquid system is subjected to light irradiation, the photoinitiator absorbs part of the incident light, undergoing chemical transformation and generating reactive species, either radicals (see Figure 1-6.b.) or ions.<sup>70</sup>

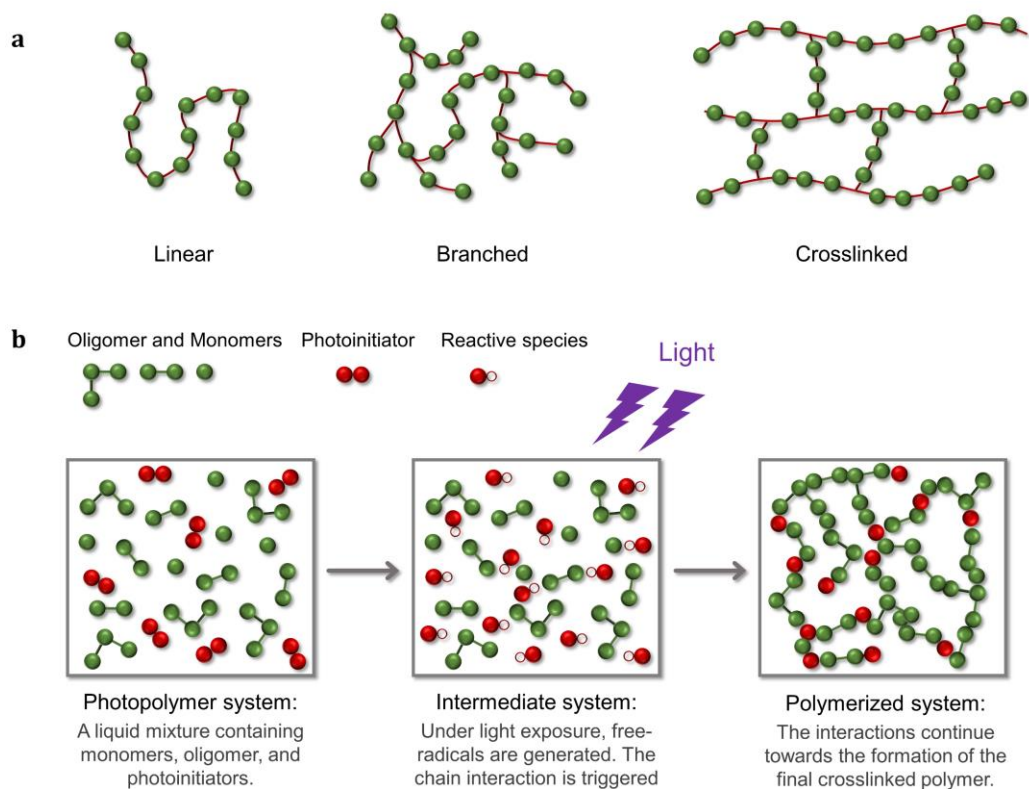


Figure 1-6. **Principle of polymer formation.** (a) Common macromolecular polymer structures. (b) Illustration of the free-radical-based photocuring process. The initial system is a mixture of monomers/oligomers and a photoinitiator, in which under light exposure, the photoinitiator is decomposed, generating reactive species. In the beginning, these reactive species promote the interaction between the prepolymer chains. At last, the interaction between chains continues until the formation of the final polymer is completed.

These species, interacting with the nearby monomers and oligomers' reactive groups, trigger a sequence of reactions in the photopolymer. In most cases, the reaction occurs through a chain-growing mechanism, which involves the sequential reaction of the unreacted molecules to form propagating polymeric chains.<sup>77</sup> As the reaction proceeds, the number of chains' interactions increases, resulting in high molecular weight polymeric chains. Depending on the number of active functional groups, linear chains or crosslinked networks (thermosets) can be formed using monofunctional and polyfunctional monomers.<sup>78,79</sup> In these processes, the light serves only as an initiating tool, and it does not interfere with the propagation and termination stages of the chain interaction. Radiation of different wavelengths (and thus energy) ranging from X-rays to the NIR range can activate the photopolymerization.<sup>80-82</sup> However, most of the photopolymerization processes are performed with UV or visible light.<sup>83-86</sup> Photopolymerization reactions can be divided into two classes, according to the mechanism of the initiation:

- 1) Free-radical polymerization systems. In these photopolymerization processes, the photoinitiator decomposes, generating radical species. Those activate the polymerization process through free-radical mechanisms by interacting with unsaturated carbon-carbon (C=C) double bonds; monomers/oligomers possess mainly (meth)acrylate ( $\text{H}_2\text{C}=\text{CH}-\text{C}(=\text{O})-\text{R}$ ) or vinyl ( $\text{H}_2\text{C}=\text{CH}-\text{R}$ ) functional groups.
- 2) Ionic polymerization systems. In this case, under light irradiation, the photoinitiator generates cations (or less commonly anions) that enable the polymerization mechanism with monomers and oligomers such as epoxy, caprolactones, vinyl ethers, oxetanes, and thioethers.<sup>87,88</sup>

Free-radical photopolymers were the first developed, and currently, most of the commercially available resins used in vat photopolymerization are based on these systems.<sup>89</sup> Although specific photopolymers can be prepared by combining both systems.<sup>90,91</sup> Free-radical and cationic systems proceed through chain-growth polymerization and can be schematized as depicted in Figure 1-7. Considering the radical polymerization, under light irradiation, reactive species or radicals ( $R^*$ ) is generated from the photoinitiator ( $PI$ ). The radical reacts with the reactive functional groups of the monomer ( $M$ ) to give the first macroradical ( $RM^*$ ) noted as the initiation step. The propagation of the reaction occurs through the subsequent addition of multiple monomer chains to the growing macroradical, forming longer polymer molecules. The final stage is the mono or bimolecular termination reactions that depend on the experimental conditions.<sup>92,93</sup> The bimolecular termination occurs through either the recombination of two polymer chains by joining two radicals and through disproportionation or “cancelation” of one radical by another without joining. Instead, the monomolecular termination, also known as occlusion, arises when the photopolymerizable resin becomes quite viscous or rigid that traps the radicals within the forming network, preventing those from reacting with other monomer molecules or polymers by the limited mobility. Consequently, the conversion of the system will be lower than 100%.<sup>94</sup> Therefore, the occluded reactive species remained still active and could eventually react with another reactive species able to reach them (such as oxygen) by diffusing through the polymeric network. This may be the cause of aging or other changes in the mechanical properties of the cured material. The system suffers from dramatic alterations observed by the photopolymer's physical-mechanic characteristic changes during the photopolymerization process. The initial system starts from a liquid soluble phase formed mainly by low molecular weight monomers. As the reaction proceeds, the chain growth begins, increasing the system's molecular weight, the degree of branching or crosslinking (in the case of polyfunctional monomers), still having a liquid-like behavior. The reaction continues, the degree of branching increases in the

polyfunctional system, and intermolecular connection leads to forming a polymer molecule of infinite size that percolates the system. This rapid and irreversible change is the so-called gelation and indicates the first appearance of the infinite network (the gel). Beyond this point, the system is no more fully liquid-like. It becomes gradually insoluble as the crosslinking advances until the final formation of a three-dimensional network. In this final stage, the insoluble polymer (or thermoset) changes dramatically, increasing the crosslinking density, glass transition temperature, and the final physical properties.<sup>95</sup>

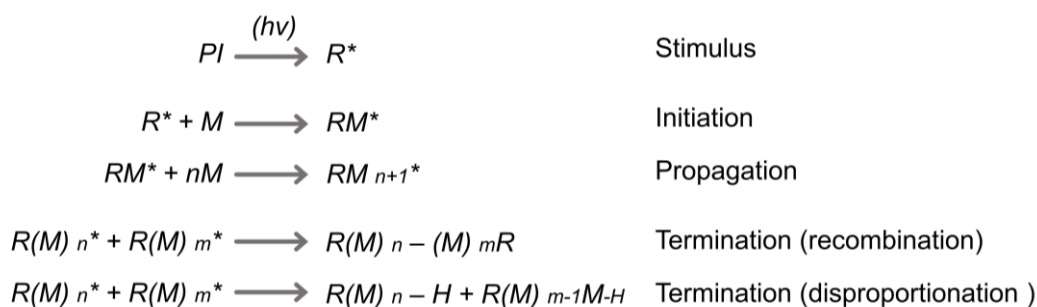


Figure 1-7. **Schematic representation of the different steps of the chain-growth polymerization reaction.**

### 1.2.2. 3D printable formulations.

As previously mentioned, most of the photopolymers for vat polymerization are composed of a mixture of monomers and oligomers, photoinitiators, and few additives such as reactive diluents, dye, or fillers. In the following paragraphs, those will be introduced.

#### *Monomers and oligomers*

Photopolymers for vat 3D printing are mainly based on free-radically polymerizable resins. These resins are characterized by unsaturated C=C double bonds, more frequently (meth)acrylate functionalities. Such reactive groups are employed since they present high reactivity upon light irradiation and well-established mechanisms of reactions. Furthermore, a wide range of (meth)acrylate-based substances compatible with vat polymerization techniques are commercially available.<sup>79</sup> Other functionalities can also be employed, such as unsaturated polyester, vinyl, vinyl ether, or thiol-ene/yne systems.<sup>96-98</sup> The selection of acrylate-based reagents for vat polymerization is based on the specific application and the processing technology to be used. The first criterion is the resin functionality, which is defined by the number of available acrylate double bonds leading to polymerization. Most of these chemicals are mixtures of monomers and oligomers mono-, di- or



polyfunctional. Few examples of acrylate-based monomers and oligomers are depicted in Figure 1-8.

Among them, 1,6-hexanediol diacrylate (HDDA), polyethylene glycol diacrylate (PEGDA), bisphenol A ethoxylate diacrylate (BEDA), trimethylolpropane triacrylate (TMPTA), polyethylene glycol methyl ether methacrylate (PEGMEMA), and butyl acrylates (BA) are some of the most used in light-based 3D printing. Other criteria for selecting suitable monomers or oligomers are viscosity, reaction kinetic, hydrophobicity/hydrophilicity, shrinkage, costs, shelf life, volatility, odor, toxicity, and, importantly, the final mechanical and functional characteristic of the polymerized product.<sup>99</sup>

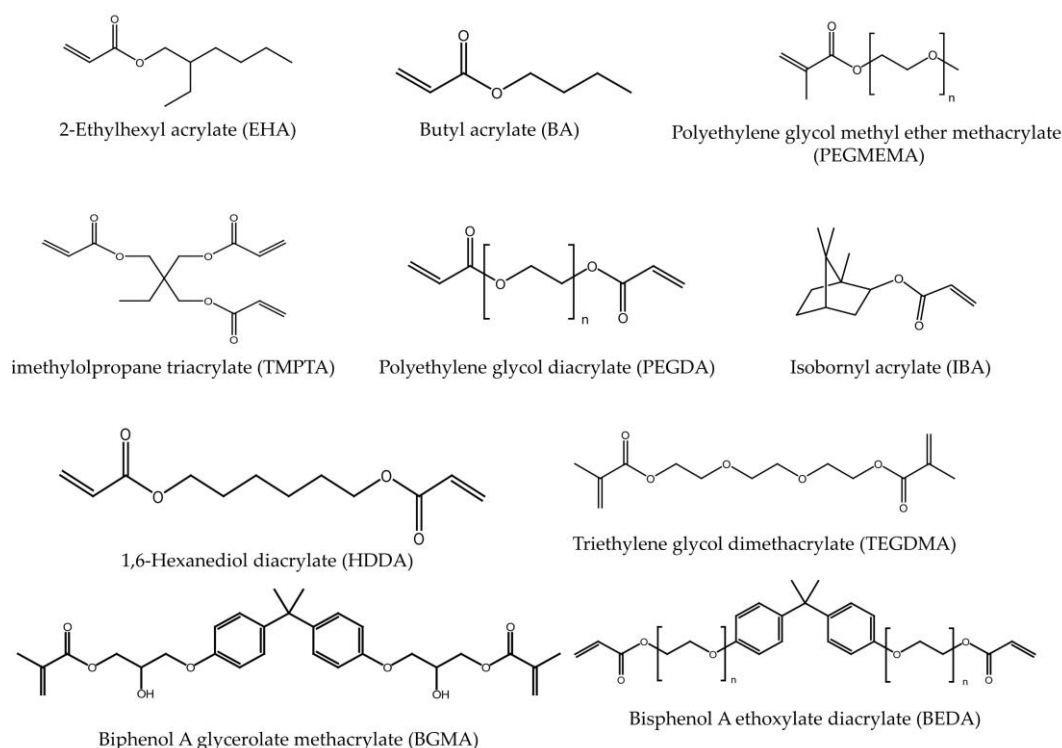


Figure 1-8. Examples of most common free-radical (meth)acrylate-based monomers and oligomers used for vat polymerization 3D printing.

The (meth)acrylate-based resins tend to be suffering from oxygen inhibition during the photopolymerization process. Since molecular oxygen is a di-radical, if oxygen molecules are present in the photopolymerizable system, the primary radicals (the radical formed from the interaction between free-radicals and the C=C bond groups) might react with them instead to continues reacting with nearby C=C double bonds. At this point, carbonyl groups and peroxide radicals are formed, which are not capable of reacting with more acrylates C=C double bonds.<sup>100</sup> The oxygen inhibition can be problematic in some photopolymerization applications, such as in acrylate-based coating, leading to an incomplete cure of the polymers. Multiple

strategies have been proposed to overcome such a drawback, e.g., using an inert nitrogen atmosphere, increasing the photoinitiator's concentration, increasing the duration and intensity of the light irradiation, and using reducing agent hydrogen donors.<sup>101,102</sup> However, in vat 3D printing, oxygen inhibition is an important part of the process. The oxygen molecules inhibit part of the free-radical on the just polymerized film, decelerating the double-bond consumption. Those unreacted C=C can react with the next polymerized film's double bonds leading to a stronger interface between layers.<sup>103</sup> Moreover, the oxygen inhibited-printed film can be more easily to be detached from the bottom of the vat during the printing process. Indeed, as will be better detailed in the following sections, 3D printing techniques, known as continuous liquid interface production or CLIP, are based on accurate control of oxygen inhibition during the photopolymerization.<sup>104,105</sup> By exploiting this principle, a thin layer of oxygen-inhibited resin is intentionally produced, avoiding adhesion between polymerized material and the vat's bottom.

A further drawback of meth(acrylate) resins is that they tend to suffer from shrinkage during free-radical polymerization.<sup>106</sup> Depending on the functionality of the (meth)acrylate substances involved, the resins can gel at low percentages of double bond (C=C) conversion, limiting the fluidity of the still uncured monomers inside the system. Such a phenomenon might lead to shrinkage stress during photopolymerization since the monomers' intermolecular distance in this 'gelled' phase is reduced than the distance in the liquid phase. The shrinkage phenomenon depends on the type and volumetric concentration of reactive groups and the polymeric network's ability to reach a spatial configuration that minimizes the system's free energy.<sup>107,108</sup> Various strategies can be used to overcome this problem of shrinkage. One method is to combine free-radical (meth)acrylate-based resins with radical step-growth polymerizable resins that can react either through thiol-ene (thiols react with carbon-carbon double bonds) or thiol-yne (thiols react with carbon-carbon triple bonds).<sup>109,110</sup> Moreover, thiols can act as a hydrogen donor during photopolymerization that can drive the formation of peroxides and thiyl radicals, reducing the oxygen inhibition problem. Another strategy to reduce the shrinkage inconvenient is by combining both (meth)acrylate and epoxide resins to form interpenetrating polymer networks (IPN).<sup>111</sup> While the former polymerizes through free-radical polymerization; epoxy resins can react through cationic polymerization using suitable photoinitiators such as aryl iodonium salts or sulfonium photoinitiators. These IPN systems are a class of polymers in which both acrylate and epoxy polymer networks are formed independently. However, in particular circumstances, both polymerized systems can be copolymerized, forming a bond between the two networks.<sup>112</sup> These hybrid systems combine the main advantages of both types of resins: epoxy resins provide low shrinkage (around 1-2%), while

acrylate resins provide high curing speed, low sensitivity to humidity, and good mechanical characteristics.

### *Photoinitiators*

Photoinitiators are chemical compounds that, upon light irradiation, absorb part of the incident light, generating active species capable of initiating the polymerization process through the reaction with acrylates or vinyl double bonds (if the species are free-radicals) or with epoxy moieties (if the species are ions).<sup>78,92</sup> Different chemical compounds can act as photoinitiators and can operate in different wavelengths of the electromagnetic spectrum, such as UV, visible, and NIR (Figure 1-9).<sup>113-118</sup> These chemical compounds have been widely explored in the literature, and most of them can be found commercially,<sup>87,119-126</sup> nonetheless, the development of more efficient photoinitiators are still of great scientific interest nowadays.<sup>127-133</sup> Among them, free-radical photoinitiators are the most common type of photoinitiators employed in light-based 3D printing. The selection of an appropriate photoinitiator for these technologies is crucial for the correct production of printed parts.<sup>70</sup> It determines the reaction efficiency and photopolymerization rates, which directly influence printing resolution and accuracy. Therefore, for an efficient photo-crosslinking process, the absorption spectrum of the photoinitiator selected must match the emission light from the printer's light source. There are two types of compounds for free-radical photopolymerization that differ from the mechanism to generate the reactive species: type I or unimolecular photoinitiators and type II or bimolecular photoinitiators. Table 1-1 shows the most typical type I and II photoinitiators.<sup>89</sup>

Type I photoinitiators are organic compounds that undergo homolytic bond cleavage when absorbing suitable photons. This photoinduced cleavage generates two free radicals from Norrish type I reactions, which can induce the polymerization process.<sup>84</sup> The cleavage process starts once the molecule reaches the excited singlet or triplet state. Depending on the photoinitiator's chemical structures, the light required for inducing an efficient cleavage of the molecule can vary in wavelength and intensity.<sup>134</sup> Most Type I photoinitiators are composed of aromatic carbonyl groups since they undergo rapid bond cleavage (at the  $\alpha$ -position) for the formation of a pair of radicals; Figure 1-10 shows an example of the homolytic  $\alpha$ -bond cleavage of the phenyl bis (2,4,6-trimethyl benzoyl)-phosphine oxide (BAPO) photoinitiator.<sup>135</sup>

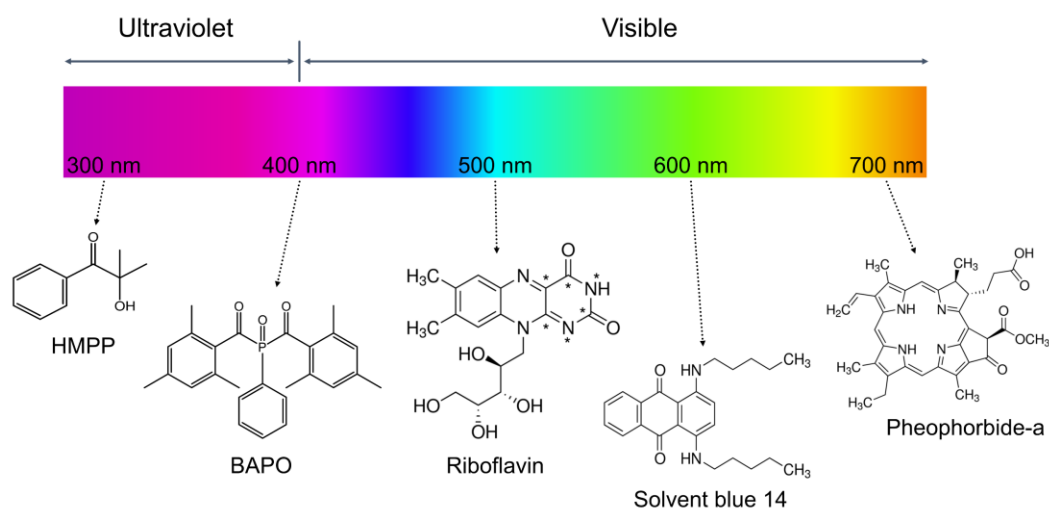


Figure 1-9. **Examples of some of the compounds used as photoinitiators in photopolymerization processes.** 2,2-dimethoxy-2-phenylacetophenone (HMMP), phenyl bis (2,4,6-trimethylbenzoyl)-phosphine oxide (BAPO), 7,8-Dimethyl-10-ribitylisoalloxazine (Riboflavin), 1,4-Bis(pentylamino)anthracene-9,10-dione (solvent blue 14), and (3S,4S, 21R)-9-ethenyl-14-ethyl-21-(methoxycarbonyl)-4,8,13,18-tetramethyl-20-oxo-3-phorbinepropanoic acid (Pheophorbide-a).

One of the first commercially available type I photoinitiators was based on the benzoin ethers family, such as benzoin ethyl ether. These compounds cleave into benzoyl radical and benzyl ether radical by photon absorption. Benzil ketals such as 2-hydroxy-2-methylpropiophenone (HMMP) or 2,2-dimethoxy-2-phenyl acetophenone (DMPA) absorbs more in the UV-light range since their relatively low energy  $n \rightarrow \pi^*$ , being one of the most efficient and stables photoinitiators for UV curable resins. Acyl phosphine oxides such as (2,4,6-trimethylbenzoyl) diphenylphosphine oxide or phenyl bis (2,4,6-trimethylbenzoyl)-phosphine oxide present lower energy level of the  $\pi^*$  state, therefore shifting the peak of the  $n \rightarrow \pi^*$  transition toward higher wavelengths, which is preferable for the visible-light curable resins. Moreover, they produce radicals that are much more reactive towards olefinic compounds than carbon-centered radicals.<sup>136</sup>

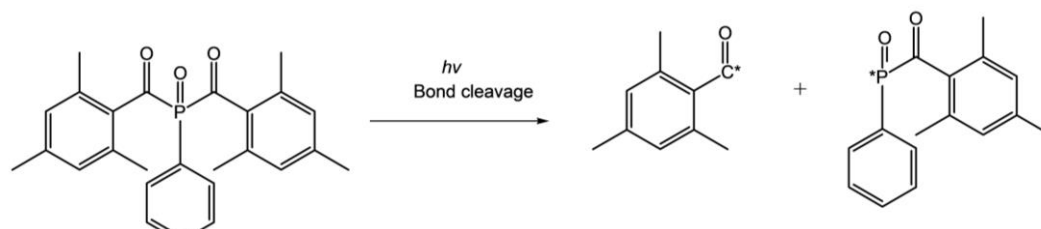
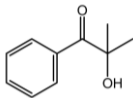
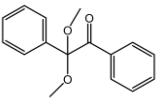
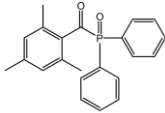
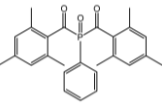
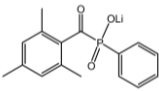
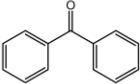
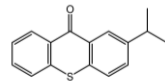
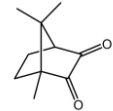


Figure 1-10. **Example of homolytic  $\alpha$ -bond cleavage of phenyl bis (2,4,6-trimethyl benzoyl)-phosphine oxide.**<sup>135</sup>

Table 1-1. Most common type I and type II free radical photoinitiators for vat polymerization 3D printing.

Compound name	Type	Structure	Range of absorption (nm)
2,2-dimethoxy-2-phenylacetophenone (HMMP)	I		[320-360] <sup>137</sup>
2,2-dimethoxy-2-phenylacetophenone (DMPA)	I		[310-370 nm] <sup>138</sup>
Diphenyl(2,4,6-trimethylbenzoyl)-phosphine oxide (TPO)	I		[350-410 nm] <sup>85,139</sup>
phenyl bis (2,4,6-trimethylbenzoyl)-phosphine oxide (BAPO)	I		[360-440 nm] <sup>85</sup>
lithium phenyl-2,4,6-trimethylbenzoyl phosphinate (LAP)	I		[340-400 nm] <sup>140</sup>
Benzophenone	II		[230-280 nm] <sup>141</sup>
2-Isopropylthioxanthone (ITX)	II		[320-400 nm] <sup>142</sup>
Camphorquinone (CQ)	II		[420-490 nm] <sup>143</sup>

Type II photoinitiators are uncleavable organic molecules that have a more complex initiating mechanism.<sup>144</sup> Type II compounds form relatively long-lived excited triplet states after absorbing a photon, capable of producing the free radicals by abstracting one hydrogen (forming H-donor radicals) or electron ( $e^-$ ) from a co-initiator molecule that is purposely added to the light-curable system. Camphorquinone (CQ), benzophenone, or thioxanthone derivatives are among the most used uncleavable bimolecular photoinitiators that can abstract hydrogen atoms from a hydrogen donor to produce excited-complexes for initiating the polymerization. One of these bimolecular

compounds' main advantages is that they can react with oxygen in the air, reducing the oxygen inhibition during photopolymerization.<sup>145</sup>

### *Additives*

During the photopolymer preparation, additives or specific components might also be used to tailor the resin properties.<sup>146</sup> These components deliver specific features to both the liquid formulation and the final cured material. For example, the initiating system can be composed of different photoinitiators, such as a combination of type I and II compounds or thermal and light-absorbing initiators.<sup>92</sup> Likewise, other strategies can combine photoinitiators with a photosensitizer to shift the absorption toward longer wavelengths or increase their absorption.<sup>147</sup> A common additive added during the preparation of the photopolymers is a reactive diluent. The reactive diluent is used mainly to adjust the resin's viscosity within an appropriate range for vat polymerization 3D printing and enhance the solubility of few printable resin components such as photoinitiators dyes.<sup>148,149</sup> Moreover, this substance can also participate in the polymerization process by using mono-, bi-, or polyfunctional monomers as a reactive diluent, which remained linked to the polymer backbone after the curing step.<sup>150,151</sup> The choice of a suitable reactive diluent is based on the characteristics searched, i.e., the affinity with the photopolymer components, the formulation's processability, and the final physical properties of the cured material, the volatility of the substance's, among others.<sup>149</sup>

Dyes might also be incorporated into a printable photopolymer to enhance the printing accuracy and obtain thus well-defined and reliable 3D printed structures. These compounds are commonly based on organic or organometallic molecules and, added in low concentrations, can help confine the light's penetration during the 3D printing step (*Z-axis*) and guarantee high resolution (*X-Y plane*) without affecting the printability of the object.<sup>152</sup> The dye selection is based typically on the light source of the 3D printer, while its concentration should be balanced considering the rest of the photopolymer's components. High concentrations of dye may lead to a photoinitiator efficiency loss; instead, low concentrations may lead to poor printing resolution.<sup>153</sup> Recently, the interest in these compounds in 3D printing has been boosted due to functional dyes' introduction.<sup>154</sup> Functional dyes, used correctly, can improve printing resolution and accuracy and confer specific characteristics to the printed object.<sup>148</sup> For example, by incorporating azo-type organic compounds, i.e., methyl red (MR) or dispersed red on methacrylate (DR1-MA), into a 3D printable formulation, the mechanical properties of the cured polymer matrix can be reversibly changed under the effect of laser radiation at 532 nm.<sup>152</sup> These compounds are characterized by R-N=N-R' chemical conformation, which can be adjusted by an external stimulus through the cis-

trans isomerism behavior of the azo-molecule.<sup>155,156</sup> Hence, the physical and mechanical features, i.e., Young's modulus, of the material can be locally changed by laser irradiation or temperature by benefiting of thus cis-trans switching within a polymeric network with a higher or lower crosslinking density. Likewise, recently, 3D printed devices have been reported using azo molecules with good gas permeability.<sup>157</sup> These devices were locally irradiated with an Nd: YAG laser at 532 nm, and due to the cis-trans switching behavior of dyes, the permeability of CO<sub>2</sub> and O<sub>2</sub> was selectively controlled.

In addition to these functional agents' advantages, an important characteristic was that one of the dyes (DR1-MA) could be polymerized with the polymer matrix during 3D printing. This dye bearing a methacrylic functionality could participate in the photopolymerization process. Another element frequently added to the resin formulations are (nano)fillers used to develop high-performance polymer composites. Composites are multiphase materials consisting of reinforcements dispersed in a continuous matrix. For the development of nanocomposites, one of the phases must be at a nanometric scale. These nanofillers, mostly composed of organic, inorganic, or metallic compounds, are used in polymeric 3D printing to produce structures with enhanced properties such as mechanical strength, thermal resistance, and electrical conductivity. The most frequently employed are carbon nanotubes, graphene, and nano clay.<sup>5,158-162</sup> Additionally, some precursor elements can be used to develop unique composites. For example, adding silver salts or tetraethyl orthosilicate (TEOS) as a functional precursor into a suitable photopolymer, advanced polymeric nanocomposite objects might be obtained in a dedicated post-printing process for in-situ generating nanofillers, such as silver and silica nanoparticles.<sup>163-169</sup> With this latter strategy of using nanofiller precursors, some problems related to the photopolymer stability may be solved.<sup>170</sup>

### **1.2.3. Vat polymerization techniques.**

#### *Stereolithography (SL) technique*

Stereolithography (SL) techniques rely on the selective polymerization of photopolymers by using a laser beam, which is focused on the liquid photopolymer contained in the vat, as represented in Figure 1-11.a. The polymer is formed by tracing the laser on the resin surface (*X-Y* plane), usually using a galvanometric head to control the laser patterning, creating the first layer of the sliced object. The layer remains on a building platform lowered in the *Z*-axis according to the layer slicing step. In this way, the printed object is consequently submerged in the uncured liquid resin, ready to be

photopolymerized. The subsequent layers are 'printed' following the same procedure, progressively overlapping each other until the object's complete formation. SL machines can be configured either in a top-down (the one in Figure 1-11.a) or a bottom-up approach or inverted configuration.<sup>171</sup> While in the top-down configuration, the platform is submerged in the liquid resin as the part is created, in the inverted one, the object remains attached to the platform, and it rises after each polymerized layer. In this case, the laser beam hits the resin from below the vat through a transparent bottom. The bottom-up approach is preferred over the top-down for many reasons. It is independent of the depth of the vat container, it requires less printable material (since it is not necessary to fill the entire vat to print), and most importantly, it avoids the direct contact of the resin with the ambient, which can reduce the oxygen inhibition. After the 3D printing step, the objects are frequently subjected to post-printing processes, including the removal of exceeding resins and post-curing treatment to reach higher conversions.<sup>38</sup> With SL-3D printing technology, high printing features can be achieved as low as 10  $\mu\text{m}$ .<sup>172</sup> A derivative SL technology has also been reported as a micro-stereolithography 3D printing (MSL or  $\mu\text{SL}$ ).

MLS-3D printing appeared in 1993 with the development of the Integrated Hardening approach.<sup>173</sup> In these methods, the scanning laser (5  $\mu\text{m}$  of spot) is focused underneath the resin through a transparent window to cure the material. Through these methods, captivating structures have been built, such as tubes, actuators, microfluidic chips, fluid channels on silicon. MSL-3D printing has been described to achieve sub-1  $\mu\text{m}$  as a minimum feature size.<sup>174</sup> DLP-based 3D printers are built by a deformable mirror device (DMD) such as the Digital Light Processing (DLP®) chips produced by Texas Instruments (see Figure 1-11.b).<sup>104,105</sup> In these configurations, each micromirror on the DMD represents one pixel in the digital image, which can drive to printing resolutions of 3 -5  $\mu\text{m}$  in the *X-Y* plane according to the optical setup.<sup>77</sup> The photopolymerization of an entire cross-section portion of the object with good precision reduces the printing times significantly compared to SL techniques.

Nevertheless, SL methods present the highest printing resolutions with the finest results in terms of surface finishing.<sup>70,175</sup> Through commercial DLP-based printers, the resolution can be as small as 40x40  $\mu\text{m}$ ,<sup>110</sup> although recently, using a customized DLP-based 3D printer, features of 18x20  $\mu\text{m}$  have been achieved.<sup>153</sup> An exciting variation of DLP-3D printing is the CLIP method that stands for continuous liquid interface production. Unlike the layer-by-layer strategy of DLP and SL approaches, CLIP-3D printing allows the continuous fabrication of objects by creating a thin interfacial of oxygen through an oxygen-permeable window. This thin oxygen layer (noted as a dead zone) inhibits the free-radical polymerization only in the interface between the polymer film and the transparent window. Therefore, the just-



built film does not adhere to the vat bottom, and the printing speed increased considerably up to hundreds of millimeters per hour. Besides, large-scale structures can be produced with the CLIP approach while the high resolution is maintained.<sup>176,177</sup> Other light-based 3D printing methods have been developed over the years and might not be diffused as stereolithography or DLP-3D printing. They can be used for gripping purposes. In the following paragraphs, some of these innovative techniques are briefly presented.<sup>77</sup>

#### *Other light-based 3D printing techniques*

Two-photon polymerization (2PP) processes are another light-based 3D printing technique similar to stereolithography (SL) as lasers scan a photopolymer. The main peculiarity of the 2PP process is that the photoinitiator molecule absorbs two photons simultaneously, starting then the free-radical polymerization.<sup>178</sup> In conventional photopolymerization, the photoinitiator reaches its lowest excited state after absorbing one photon, as long as the photon's energy is equal to the energy difference between the excited state and the ground state of the molecule.<sup>179</sup> Such an energy transition can also be reached if the molecule contemporaneously absorbs two identical photons, each with half of the single-photon energy in the one-photopolymerization process. However, the two photons can also be of different energy, in a process called non-degenerate.<sup>180</sup>

2PP method is a point-by-point approach that uses two femtosecond pulsed lasers to polymerize the resin in the focus spot (at nanometric scale) between the two laser beams, see Figure 1-11.c. Since the polymerization reaction remains confined in a small volume (a point), the printing resolution is higher than other light-based printing techniques with features of 0.2  $\mu\text{m}$  or smaller.<sup>181</sup> A further advantage is that the focal intersection point can be moved in *the x-y-z-directions* to cure the polymer inside the resin's volume and creating internal traces. With this 3-dimensional writing approach, it is possible to use high viscosity resins and create complex geometry without supporting structures.<sup>180</sup>

The first 2PP was developed in 1975 by Swanson and coworkers intended to fabricated *quasi* arbitrary 3D microstructures.<sup>183</sup> However, the interest in this technology started to grow in the mid-90s for microfabrication purposes.<sup>184,185</sup> The ability to penetrate the printable resin is given by the laser's light source, in the Near-infrared (NIR) range. NIR penetrates deeper into the photocurable resin, and it has lower scattering and photodamage than UV or visible light.<sup>186,187</sup> 2PP setup is typically composed of high-power femtosecond Ti: sapphire laser with a wavelength near 790 nm, pulse width between 50-150 fs, and laser powers between 10 and 700 mW (Figure 1-11.c).<sup>182</sup> The laser beam passes through a series of optical arrangements,

including an acousto-optical modulator (AOM) to disperse the laser beam, a sequence of scanning mirrors to adjust the laser beam, and a microscope objective to focus it into the resin vat.

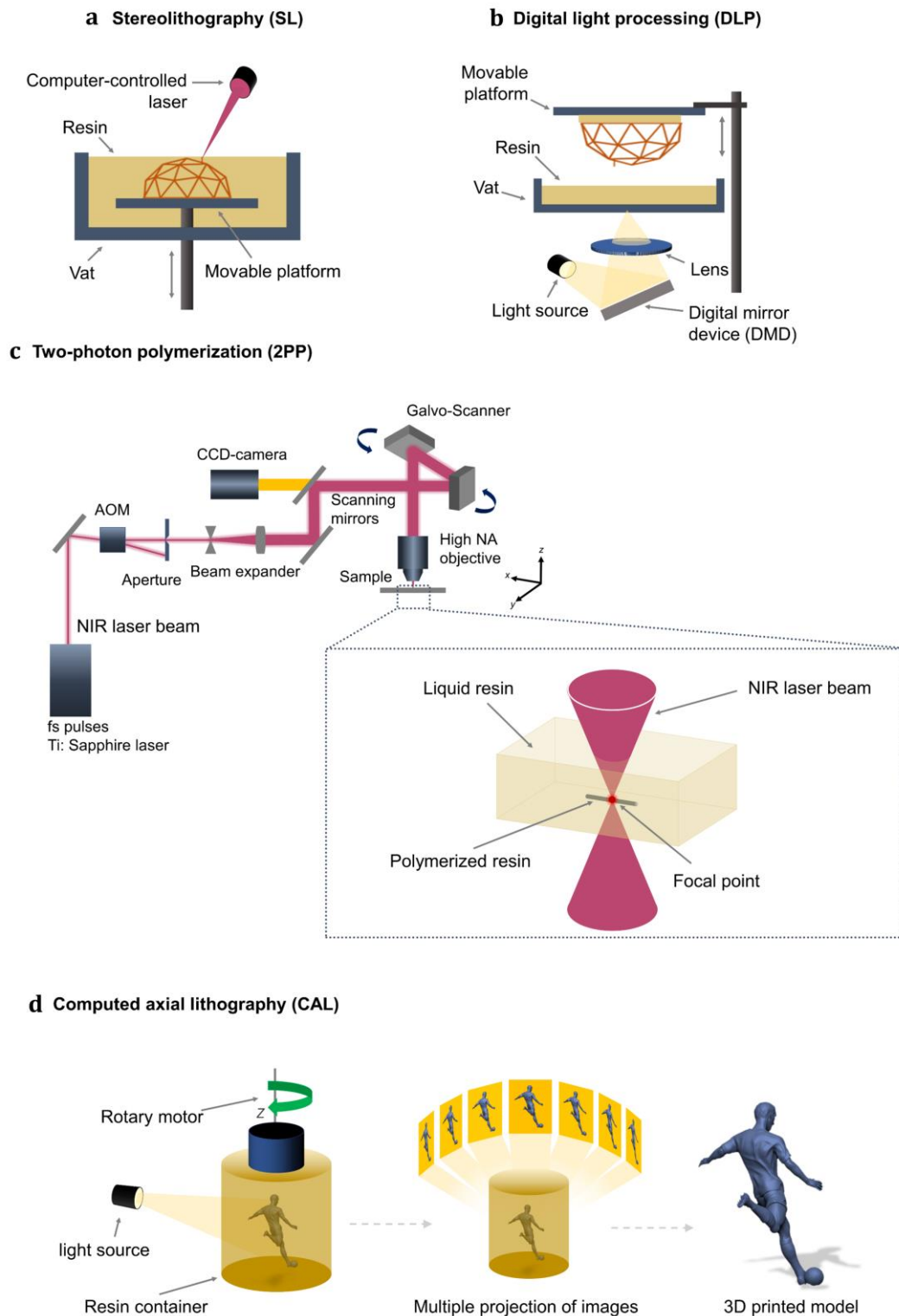


Figure 1-11. Representation of the most representative Vat 3D printing and 3D printing techniques by photopolymerization. (a) Stereolithography (SL). (b)

Digital light processing 3D printing (DLP). (c) Typical two-photon polymerization setup.<sup>182</sup> (d) Computed axial lithography (CAL).

After completing the micro-object, the unreacted resin is removed by washing/rising protocols in ethanol or isopropanol.<sup>188</sup> Although 2PP offers remarkable advantages, few drawbacks arise, such as the limited dimensions of the produced objects (no more than 1 mm height) and the low printing velocity, which is about 0.5-1 mm/s compared to some SL techniques (200-300 mm/s).<sup>189</sup> Moreover, these techniques require expensive equipment to generate the pulsed NIR laser beam and involve high energy to cure the material since the limited two-photon absorbing (TPA) cross-section ( $\delta_{\text{TPA}}$ ) of typical 2PP photoinitiators and their high fluorescence quantum yields ( $\Phi_{\text{F}}$ ).<sup>190</sup>

In another alternative to layer-by-layer 3D printing approaches, recently, a novel volumetric 3D printing system known as CAL (Computed Axial Lithography) has been developed.<sup>191</sup> Contrary to other light-based techniques, CAL methods are based on computed tomography (CT) scans techniques to generate a hologram within a controlled volume of the photopolymer, see Figure 1-11.d.<sup>192</sup> This hologram is created by the simultaneous projection of multiple 2D images while the vat container is rotating. The 2D images propagate through the liquid resin from different angles, resulting in a 3-dimensional hologram with enough energy to photocuring, at once, a volume of photopolymer in the desired geometry.<sup>193</sup> A fundamental parameter of CAL techniques is the rotation velocity that might directly influence the printing features when the rotary system is not in sync with the projected images. The photopolymers' viscosity is another crucial point during the CAL-3D printing since it has to be high enough to avoid the relative shift between the 3D printed model and the rest of the liquid resin. With this method, some 3D printing drawbacks related to the poor surface definition and slow fabrication printing speeds can be surpassed. In addition to CAL techniques' advantages in terms of production speed and surface definition, this technique can polymerize high viscosity resins (up to approximately 90 000 cP) that are difficult to achieve with other techniques such as DLP or SL.<sup>194</sup>

#### **1.2.4. 3D printing reliability.**

Several factors must be considered during the printing step to obtain reliable 3D printed structures with the desired properties. One of the fundamental aspects is the composition of the photopolymer. Components such as monomers, oligomers, photoinitiators, and additives or fillers must be well-balanced in the photosensitive resin so that each one of them performs its function adequately. As previously discussed, these elements' choice is based on the reagents' functionality, the type and the light source of the 3D

printer, the looked-for dimensional resolution, and the envisaged final properties.<sup>77</sup>

A typical problem that arises when a photocurable formulation is prepared is the low affinity of the components used, directly impacting the printable formulation's homogeneity when they are not well integrated.<sup>195</sup> For example, most of the resins are non-polar reagents, while other elements, such as dyes, might be of different polarity.<sup>196,197</sup> The direct mixing of those components might result in an inhomogeneous photopolymer due to the dye's aggregation that, according to the application, could have adverse consequences.<sup>198</sup> For example, the dye clusters might lead to light scattering or reflection during the 3D printing step, causing inaccurate printed objects. One alternative to increase the dye solubility into the monomer could be using reactive diluents as an intermediate reagent. A proper reactive diluent might disperse the dye and be compatible with the photopolymer. For example, Wang et al. studied the use of different reactive diluents for increasing the miscibility of commercial dyes, such as Rhodamine B, Solvent Yellow 98, and BBOT, into acrylate-based monomers.<sup>148</sup> They developed various photopolymers for 3D printing applications with photoluminescent properties in which, by adding the proper reactive diluent, the homogeneity of the formulation increases notably. The reactive diluent helped increase the dye's solubility and, having (meth)acrylate functionalities, they participated in the photopolymerization process. The reactive diluents' selection was based on the chemical structure similarity with the dye employed.

A similar stability problem could be found when additives such as (nano)fillers are added to the photopolymers. As previously discussed, these additives are typically employed to enhance specific characteristics of the parts obtained by 3D printing, e.g., mechanical strength or thermal and electrical conductivity.<sup>199</sup> However, some photopolymer features can negatively change when fillers are used, such as the formulation's transparency or light dispersion (X-Y plane), affecting the parts' final resolution after 3D printing.<sup>200,201</sup> The photopolymerizable resins become significantly opaque already at lower amounts of such as nanofillers, using carbon nanotubes (CNTs), for example. The added fillers might also absorb part of the incident light during the photopolymerization process, competing with photoinitiator conversion.<sup>202</sup> These opaque or darker formulations require higher light doses (e.g., longer exposure times or higher light power) to balance light absorption from the nanofiller and perform the correct polymerization process. As with CNTs, the resins' optical features can change using other nanofillers additives such as graphene oxide (GO), silver or gold nanoparticles, and nanopowder made of hydroxyapatite, silicate, or glass.<sup>203-2055</sup> Multiple works have been developed using these additives; in all of them, the photopolymer's optical features changed significantly and their

printability. Therefore, there will be a compromise between the nanofillers amount and the photopolymer printability to obtain 3D printed objects with the desired shape and properties.<sup>206,207</sup>

Another drawback when using nanofillers is the rise in the formulation viscosity, which increases *quasi* exponentially by increasing nanocomponents' content due to their large response of surface areas per unit of volume.<sup>208</sup> Usually, for vat polymerization printing, it is desired a high or considerable amount of nanofillers in the photopolymers looking to obtain 3D printed parts with the most significant improvement in their properties, electrical or thermal, as possible.<sup>158</sup> Nevertheless, the photopolymer's low flowability might cause problems during the printing step, leading to processing defects, reducing accuracy, and poor mechanical properties.<sup>209</sup> Herein the difficulty of finding a compromise between the amount of loaded nanofiller in the resin, the photopolymer's printability, and the properties looked-for. In this context, different alternatives have been followed to 3D printing highly viscous nanocomposite photopolymers by functionalizing the fillers in order to increase the compatibility with the printable formulations. For example, by modifying graphene oxide (GO) nanosheets with (meth)acrylate functionalities, such as 2-hydroxyethyl methacrylate or acryloyl chloride, the interfacial compatibility with acrylate-based resins can be enhanced, obtaining photopolymers with adequate viscosity range for vat 3D printing.<sup>210,211</sup> Following similar strategies, it can be possible to functionalize other types of nanofillers, such as ZrO<sub>2</sub> or SiO<sub>2</sub> ceramic nanoparticles with acrylate functionalities or carbon nanotubes (CNTs) with amines groups, to obtain 3D printed parts loaded with the highest content of fillers as possible from photopolymers with good rheological properties.<sup>208,158</sup> Focusing on the technological boundaries, highly viscous photopolymers can be processed through specific vat 3D printing methods such as hot-lithography printing or lithography-based ceramic (LCM). The former uses heating systems to reach temperatures up to 140 °C and process the printable viscous resin more easily by reducing its viscosity.<sup>212-214</sup> Moreover, with hot-lithography, printing times can be reduced while resulting in higher conversion and better mechanical properties. The LCM techniques instead, developed by Lithoz in 2006, has a recoating blade used to continuously mix, homogenize the material, and generate a thin layer of photopolymer, allowing the production of complex-shaped 3D printed parts with micrometric precision of around 100 μm, with this technology part with 99% of ceramic particles content has been successfully 3D printed.<sup>215,216</sup>

Even if the printable photosensitive material presents the desired characteristics in terms of chemical composition and component stability, each element, especially photoinitiators and additives, has a crucial role in the vat 3D printing step. As discussed, both components can absorb part of the

incident light, affecting the light penetration across the photopolymer and the depth of cured material. Understanding the cure depth for an established photopolymer is of unique importance, intending to produce objects as faithful as possible to the CAD model.<sup>217,218</sup> The cure depth ( $C_d$ ) can be expressed following a mathematical expression as broadly reported in the literature:<sup>148,219-223</sup>

$$C_d = \frac{1}{(\alpha_i c_i + \alpha_a c_a)} \ln\left[\frac{t}{t_o}\right] \quad (\text{equation 1})$$

Where  $\alpha_i$  and  $c_i$  are the absorption coefficient and concentration of the photoinitiator, respectively,  $\alpha_a$  and  $c_a$  are the absorption coefficient and concentration of the dye, respectively,  $t_o$  is the critical time, the time required to start the photopolymerization, and  $t$  is the light exposure time. Unlike other similar mathematical expressions, *equation 1* represents the relationship between photoinitiator and dye (or light absorber) content. However, through other mathematical approaches, the cure depth can be directly expressed against the incident light dosage, and the energy ( $\text{mJ}/\text{cm}^2$ ) required to start the polymerization.<sup>224</sup> Identifying these variables for a specific photopolymer, the printing settings such as light intensity, slice printing thickness, and exposure time can be optimized to achieve the desired axial and lateral printing resolution.<sup>77</sup> For example, the material can polymerize in the z-axis (axial resolution) and the x-y plane (lateral resolution) far beyond the desired thickness and shapes upon excessive light irradiation. Herein, the importance of finding an equilibrium between additives such as dyes or light absorbers and the photoinitiators to confine the light in the desired region vat 3D printing. Well-balancing the suitable components can be enhanced the photopolymer's absorption coefficient, and thus axial resolution (z-axis) is improved.<sup>201</sup>

## Chapter 2

# Biomedical vat 3D printing: Printable resins and main strategies.

### 2.1. Polymeric 3D printing for biomedical applications.

Ever since the arrival of 3D printing, many scientific and industrial areas have shown great interest in this manufacturing method. Significantly, the areas related to medicine and biology have witnessed how 3D printing might introduce brand-new procedures for the on-demand manufacturing of biomedical parts.<sup>37,38,58,77</sup> Compared to conventional methods of production of medical devices, 3D printing allows the development of personalized and precise structures of any geometry due to its spatial-temporal control methods of manufacturing.<sup>225-227</sup> Indeed, today, 3D printing is being extensively employed to develop customized biomedical components covering areas in prosthesis fabrication, biomodelling studies, *in vitro*, and *in vivo* analyses.<sup>36</sup> These customized parts can be used in different applications and can be fabricated using different printable materials with biomedical properties, summarized in Table 2-1.

Although the field of application may be broad, the use of 3D printing beyond specific cases remains still vague due to some technical and economic factors that have not been overcome yet.<sup>225</sup> Despite this, the biomedical

interest in these technologies is gradually increasing, particularly in the methods based on polymeric material processing.<sup>242</sup> The 3D printing of polymeric materials is the most versatile and robust method for producing customized biomedical components. Polymeric 3D printing offers cost-affordable equipment and supplies, a broad palette of processable polymeric materials, high printing precision, and fast production speed, enabling extraordinary advances in the medical and healthcare disciplines.<sup>70,243</sup> Polymeric 3D printing technologies are being employed in numerous biomedical branches, e.g., prototyping organ models, producing *in-vitro* platforms for cell culturing or scaffold structures for tissue engineering, on-demand fabrication of medical implants and prostheses, and multiple situations where it is required a fast production of customized parts.<sup>242-247</sup> Indeed, during the recent pandemic crisis, polymeric 3D printing took a step forward and demonstrated that it could be a valuable instrument in hospitals and ambulatories to help with critical cases of respiratory diseases. It allowed the fast production of plastic valves and connector devices for mitigating the shortage of respiratory tools during the coronavirus disease (COVID-19) caused by the novel coronavirus (Sars-CoV-2).<sup>248,249</sup> During these last months, polymeric 3D printing was revealed as a strategic partner in emergency times, especially when the procurement of disposable materials and the supply of small series of ad-hoc devices is complicated.<sup>250,251</sup>

The medical applications of polymeric 3D printing appear to be vast and will continue to grow, which may lead to outstanding advances in specific clinical cases where the production of customized and patient-specific structures is required.<sup>252-254</sup> For example, patient-specific incisor teeth with adequate mechanical properties have been successfully produced through FFF-3D printing technology using biopolymers such as polylactic acid and polyamide 11 (Figure 2-1.a).<sup>255</sup> These 3D-printed teeth models were created by first scanning the patient mouth affected zone and then producing the incisor teeth implants after optimizing the process parameters. FFF-3D printing method allowed the rapid and cost-affordable creation of bespoke objects in simple steps. Polymeric 3D printing can also be used in more subtle applications, such as the production of precise anatomical patient-specific implants (PSI) for orbital bone reconstruction.<sup>256</sup> Through stereolithography (SL), these parts can be accurately produced from a digital model generated first scanning the patient's affected area and producing the customized pieces, as shown in see Figure 2-1.b. Geven et al. produced 3D printed implants using a photo-crosslinkable photopolymer based on poly(trimethylene carbonate) (PTMC) and loaded with nanohydroxyapatite (nHAp).<sup>241</sup> Polymeric 3D printing can also assist doctors and nurses in subtle clinical situations by producing precise patient-specific models.<sup>257-259</sup> These models can be used for preoperative simulation purposes to provide a tactile and visible appreciation of the medical situation, enhancing surgical planning (see Figure 2-1.c).



Table 2-1. Some of the most used materials in 3D printing for biomedical applications.

Material	Technique	Biomaterial	Application	Ref.
Metal	Selective laser melting (SLM)	Ti-6Al-4V	Crown, bridges, screw, abutment, or other dentures components. Knee joint, hip joint, spinal implants, and bone fixation.	228-233
	Electron beam melting (EBM)	Ti-5Al-2.5Fe		
	Selective laser sintering (SLS)	Co-Ni-Cr-Mo		
		Stainless steel		
Ceramic	PolyJet Vat polymerization (VP)	Tricalcium phosphate (TCP)	For dental and porous implants, bone regeneration, orthopedic parts.	234-239
	Selective laser sintering (SLS)	Hydroxyapatite (HAp)		
Polymers	Fused filament fabrication (FFF)	SiO <sub>2</sub> -CaO-Na <sub>2</sub> O-P <sub>2</sub> O <sub>5</sub>	Dental implants, cartilages, scaffolds, in-vitro platforms, cell culture studies, microfluidic devices, hip joint, knee joint	70,170,171,224,240,241
	Multijet Vat polymerization (VP)	Zirconia		
	Selective laser sintering (SLS)	Al <sub>2</sub> O <sub>3</sub>		
	Direct ink writing (DIW)	Polymethyl methacrylate (PMMA)		
		Acrylonitrile butadiene styrene (ABS)		
		Polyether ether ketone (PEEK)		
	Polyethylene glycol (PEG)-based hydrogels			
	Bio inks			

Other advanced 3D printing methods have been reported in which cells, bioactive molecules, or biomaterials are used for developing structures with inherent bioproperties. These methods are commonly known as bioprinting and enable the production of precise, complex, and functional structures made from biological elements that can be used, for instance, in tissue engineering studies and cell-regenerative medicine.<sup>260</sup> The bioprintable materials or bioinks employed in these techniques are generally based on polymer and elastomer materials, either synthetic or natural, loaded with living cells encapsulated adequately. In particular, water-soluble polymers, or hydrogels, are preferred since their chemical configurations and ability to hold large amounts of water might create suitable cell growth conditions.

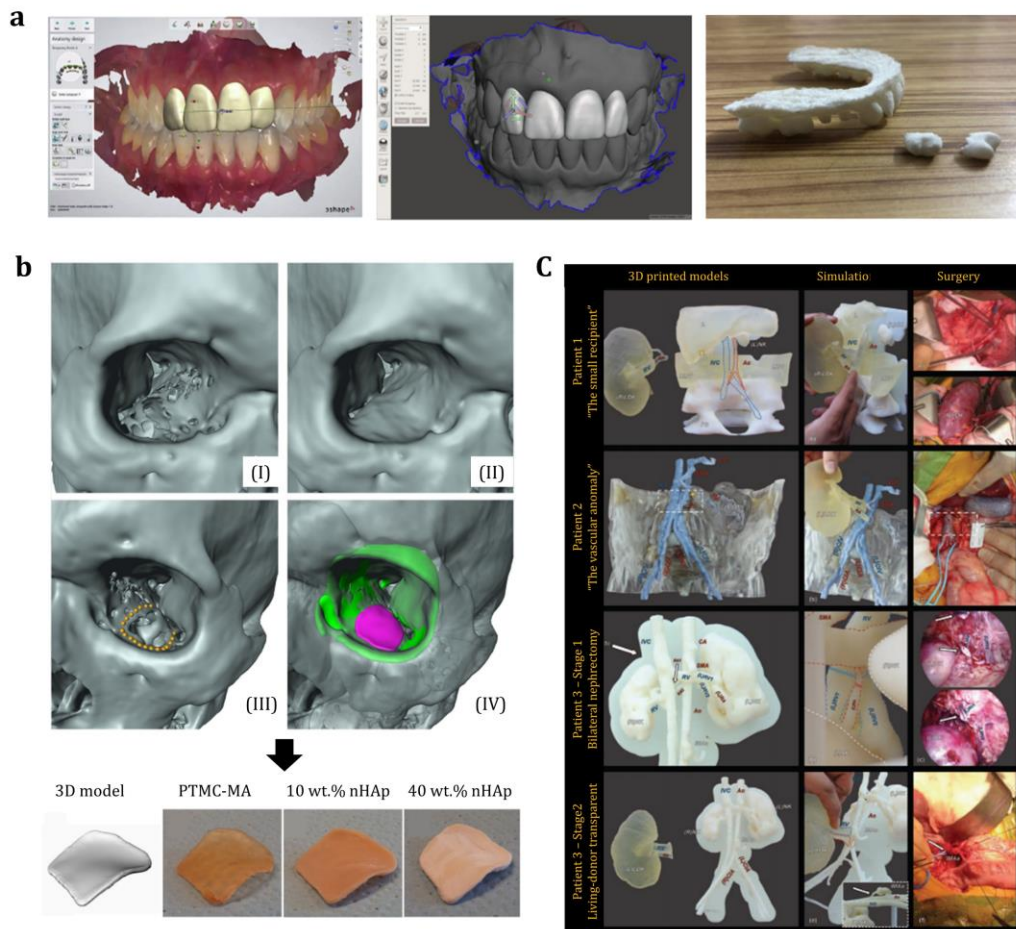


Figure 2-1. **Examples of medical applications of polymeric 3D printing.** (a) Alignment of the patient-specific teeth followed by the incisor teeth' processing in a mesh mixer software for obtaining the biocompatible PLA 3D printed incisor teeth.<sup>255</sup> (b) Above: the 3D digital model of a patient orbit, showing the procedure followed: I) analysis and II) elimination/ patterning of the pseudo-hole, III) locating the fracture zone, IV) the implant position is colored in magenta; below is shown the 3D printed pieces obtained from the CAD model. The parts were produced from polytrimethylene carbonate (PTMC) methacrylate with various nanohydroxyapatite (nHAp) amounts into the resin.<sup>241</sup> (c) Interaction with the 3D printed models providing an immediate appreciation of the patients' anatomical situation, informing planning and subsequent surgery.<sup>259</sup>

Hydrogels can be classified according to the material used to obtain them, that can be natural: collagen, silk, chitosan, fibrin, hyaluronic acid, gelatin, alginate; synthetic: polyethylene glycol (PEG)-, polycaprolactone (PCL)-, or acrylamide-based polymers; or a combination of them.<sup>261-264</sup> Different 3D printing techniques can be employed for bioprinting purposes, such as inkjet, vat polymerization, and extrusion-based techniques.<sup>134,260</sup> In the last method, also referred to as direct ink writing (DIW), the material is deposited by electric-mechanical force (driven by screws or pistons) or pneumatically (driven by gas or pressurized air). When the extrusion material

contains cells or other biological entities, these techniques are frequently known as bioplotting. This bioprinting method is of great interest for advanced medical applications related to tissue engineering, regenerative medicine, and biostructures fabrication since it allows the processing of living matter and biocompatible materials.<sup>265-267</sup> As a part of the direct writing methods, the operational principle of the bioplotting technique is based on the line-by-line material deposition approach. While other common extrusion-based methods, such as FFF-3D printing, mainly uses a heated nozzle to extrude the thermoplastic material onto a build platform, the bioplotting involves using bioinks with adequate viscoelastic features to allow the extrusion of the material by either electromechanical or pneumatic forces.<sup>268-270</sup> The whole bioink deposition is carried out in particular and controlled environment conditions to preserve the living cells and generate well-defined biomedical compositions for tissue and organ transplantation. Bioplotting potential applications are boundless with a particular interest in human-scale entities development such as skin, cartilage, aortic valves, tracheal splints, kidneys, among others.<sup>170,244,271-273</sup>

## **2.2. Toward the 3D printing of microfluidic medical devices.**

One of the medical fields in which 3D printing of polymers has become of great interest is in the fabrication of milli/microfluidic platforms. Polymeric 3D printing techniques may offer multiples benefits in this framework, such as fast printing times, cost-affordable materials and equipment, and high printing resolution.<sup>246</sup> Over the last years, several studies have been reported associated with these systems' microfabrication using different polymeric printing methods for various *in-vitro* studies, such as bioreactors for real-time biological analysis or analytical systems.<sup>153,274-277</sup> Techniques such as PolyJet, Fused Filament Fabrication (FFF), and vat polymerization 3D printing are among the most used techniques for fabricating microfluidic medical chips. The last one is considered the most suitable candidate for the microfluidic chip fabrication for multiple reasons, i.e., higher printing resolution and faster printing times, as will be reviewed in detail in the following sections.

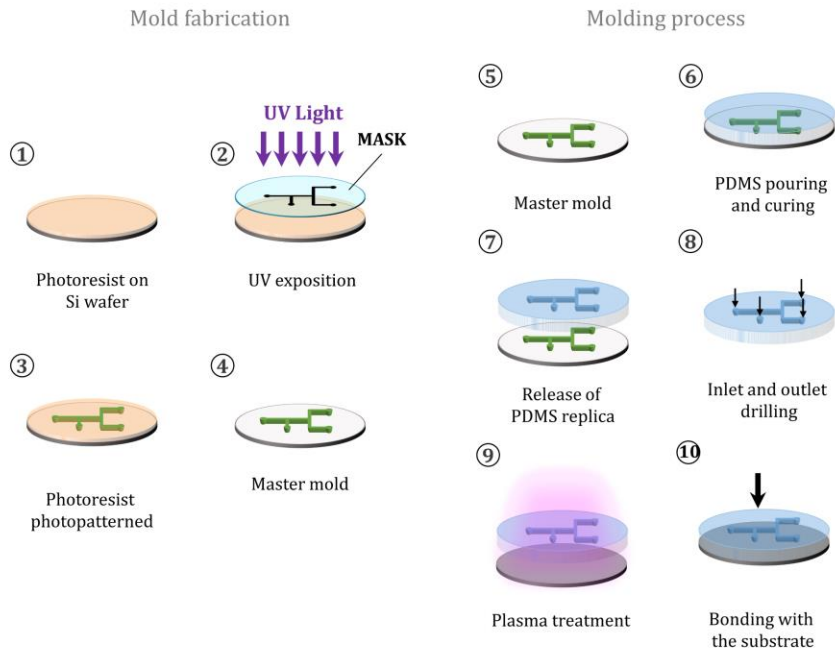
### **2.2.1. Overview of microfluidic devices.**

In general, the interest in microfluidic platforms lies mainly in performing precise chemical and biological analyses on a much smaller scale than conventional laboratory procedures; this allows savings in sample consumption and reduces the overall costs and instrumentation sizes

compared to conventional laboratory procedures to actual research methods.<sup>278-281</sup> These devices are generally produced with a series of micro-scale channels etched or molded, specifically created to achieve the desired features, e.g., mix, pump, or sort.<sup>282</sup> The first microfluidic devices' creation dates to the 50s and 60s, fueled by the upsurge of miniaturization processes during the aerospace race between world power countries.<sup>283</sup> In the 80s, the development of novel miniaturization methods such as lithography allowed the integration of many transistors on semiconductor wafers for the microelectronic industry.<sup>284</sup> The novel micro-systems were called MEMS or Micro Electromechanical Systems. Later, in the 90s, the world witnessed the beginning of what is known today as a microfluidic device or lab-on-a-chip when these MEMS were used for biological, chemical, and biomedical applications intending to control and monitor the behavior of analytical solutions in microchannels. Indeed, microfluidic platforms have been used for different medical and chemical applications such as rapid DNA sequencing, electrophoretic separation, and disease diagnosis in point-of-care settings with a high level of precision.<sup>285-288</sup> A crucial point in developing a microfluidic platform is selecting the material for its fabrication.<sup>289</sup> The material's final choice is based on the required microfluidic platform's desired function and properties, e.g., compatibility with biological units (biocompatibility), chemical stability toward common reagents, and good optical transparency that might allow the correct imaging/observing of analytes in biomedical analysis.<sup>290</sup> Initially, most of these microdevices were fabricated with silicon, metals, and glass through expensive and intricate equipment.<sup>291</sup> The spreading of microfluidic systems in laboratories and industries was marked by the introduction of polymers, such as poly(methyl methacrylate) (PMMA), polycarbonate, polystyrene, polyethylene terephthalate (PET), and especially polydimethylsiloxane (PDMS). Today, PDMS elastomer is the most used material for molding microfluidic chips since it is an inexpensive, biocompatible, transparent, and deformable material easy to mold.<sup>292</sup> These features make PDMS the ideal material to produce biomedical microfluidic chips compared to other polymeric materials.<sup>293-295</sup>

PDMS-based microfluidic chips are often fabricated through Soft Lithography methods. This conventional production process involves multiple and complex steps and requires high expertise and controlled conditions.<sup>296</sup> The process starts from a computer-aided design of the microchannel that is transferred on a photomask made of either chrome coated glass plates or, most commonly, plastic film templates. The transfer step is performed in a cleanroom by etching chromium (if the substrate is glass) or UV opaque inks (if the substrate is plastic film). This photomask is then used to produce a replica of the microchannels with polymer (see Figure 2-2.a).

## a - Soft Lithography



## b - Vat polymerization 3D printing

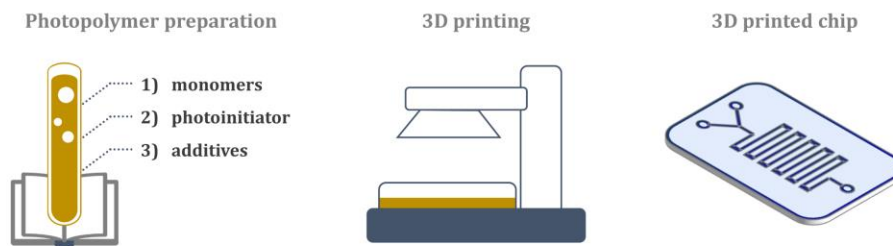


Figure 2-2. Representation of the (a) soft lithography procedure compared to (b) vat polymerization 3D printing for producing microfluidic devices.

In this step, a UV curable resin (or photoresist) is spread on a silicon wafer (1) with the desired thickness that determines the microchannels' height. The resin is illuminated through the photomask, inducing a hardening of the exposed areas (2). Then, the obtained system (3) is developed in a solvent that eliminates the uncured resin, and a master mold is obtained (4,5). The process continues with the molding step. A mixture of thermal curable liquid PDMS and crosslinker is poured into the master mold (6) and heated according to the PDMS's curing temperature, usually over 80 °. Once the PDMS is cured, the part is taken out from the mold, thus obtaining replicas of the microdevice in a PDMS bulk (7). The chip is then punched to create the inputs and output to inject the fluids during the experiments (8). Finally, the system

is subjected to plasma treatment (9) to guarantee the adhesion between the PDMS bulk with microchannels and the glass slide (10).

Even though PDMS elastomer is widely used for microfluidic fabrication, this material presents some drawbacks, such as nonspecific adsorption of biological and chemical analytes and high hydrophobicity. This latter could be problematic when the microfluidic chips are applied for biological assays using aqueous solutions.<sup>297</sup> In this context, numerous modifications have been developed to tailor the channels' surfaces in PDMS-based microfluidic chips, e.g., adsorption of surfactants, chemical vapor deposition, coatings with proteins and lipid agents using oxidative solutions, microwave radiation, oxygen plasma, and photo-mediated grafting polymerization.<sup>298-306</sup> Oxygen plasma and surfactant coating strategies have been successfully employed for hydrophilizing the surface of the PDMS microchips with great results. Nevertheless, these methods frequently suffer from a lack of long-term stability and might be ineffective if surface patterning is required.<sup>308</sup> Other surface modification methods based on the surface-attached polymerization provide more stable surfaces since the covalent attachments of polymer chains onto the substrate.<sup>309</sup> These methods can be applied either to liquid phase systems or vapor phase systems and can be promoted by different procedures such as plasma discharge, microwave radiation, and oxidation by ozone and light irradiation. Since the first three methods typically start the polymerization on all available points on the surface, they are not the most suitable for patterning surfaces.<sup>310</sup> Instead, the light-mediated strategy, or photo-grafting polymerization, has been described as one of the easiest and versatile methods for various reasons: it allows an easy and selective chemical introduction of polymeric chains of different nature on the substrate with high surface density and precision, and long stability of the grafted chains.<sup>311</sup> The photo-grafting polymerization of surfaces can be achieved by either the "grafting-to" or the "grafting-from" approaches. The former techniques are accomplished by coupling end-functionalized polymer molecules with complementary functional groups exposed on the substrate's surface, tethering polymeric chains. While the "grafting-from" techniques proceed by first covalently attaching functional groups (anchors) and using them to initiate the polymerization from the substrate's surface, i.e., the polymeric chains start to grow from the surface.<sup>312-314</sup> Both approaches can be catalyzed for photoinitiators' presence. In "grafting-to" approaches, photoinitiators (such as phosphine oxide derivative compounds) can promote the chemical reaction between the surface-bonds functionalities and the polymer-end groups by generating free-radicals upon light irradiation. In "grafting-from" approaches, the photoinitiator might be anchored on the substrate surface, and after light exposure, it generates radicals that start the polymerization.<sup>315,316</sup>

In general, both strategies (*grafting-to* and *grafting-from*) can produce stable modifications due to the chemical interaction between surface and polymer chains.<sup>317</sup> Exploiting the photo-mediated “grafting from” polymerization, Ebara et al. functionalized PDMS microfluidic chips with different polymers, including N-poly(N-isopropyl acrylamide) (pNIPAAm), polyethylene glycol diacrylate (PEGDA), and a pH-responsive copolymer of pNIPAAm and acrylic acid (AA).<sup>318</sup> After optimizing the treatment protocol, the objects' wettability was adjusted upon external stimuli, e.g., temperature or pH (Figure 2-3.a). They induced reversible changes in hydrophobic PDMS chips (from 105 ° to 35 °) by first flushing for 1 minute a solution made of the benzophenone (BP) photoinitiator diluted in acetone (at different concentrations from 5 to 20 wt. %), in this stage, the BP penetrates within the channel surface regions. Secondly, the channels (washed extensively with water) are loaded with the grafting solution containing the polymer. The grafting polymerization was achieved upon UV irradiation. This grafting process's base was the radicals generated within the PDMS channel's surface regions under the light exposure. As demonstrated in numerous studies, upon light irradiation, benzophenone molecules can abstract hydrogen from the substrate remaining linked to the surface and forming benzyhydrols molecules.<sup>319-321</sup> Upon prolonged light irradiation, these surface molecules can form benzopinacol radicals (BP-OH\*) that are not so reactive as benzophenone but can still participate during the photopolymerization process.<sup>322</sup> Similar approaches have been followed for selectively functionalizing PDMS-based microchannels using photomasks. In these cases, the “grafting-from” method allowed to spatially control the grafting of monomers such as acrylic acid (AA), poly(ethylene glycol) methyl ether acrylate (PEGMEMA), or poly(ethylene glycol) diacrylate (PEGDA).<sup>323,324</sup> Even though great surface modifications were achieved in these works, these methods are mainly based on multi-steps and time-consuming methodology involving: first the BP pre-adsorption, extensive washing steps (otherwise, the eventual BP leaking might polymerize beyond the channel walls leading to clogging), and reloading the channels with the grafting solution.

Through “grafting-to” instead, the surface modification can be achieved in fewer steps. This approach was followed by Carlborg and coworkers using vinyl- or thiol-terminated PDMS oligomers to functionalize PDMS-based microfluidic chips under UV light.<sup>325</sup> Taking advantage of the well-studied chemistry of thiol-ene systems, they prepared off-stoichiometry (OSTE) UV-curable formulations for producing a series of microfluidic devices with functional groups exposed (either thiol or vinyl) on the surface of the channels. The functional groups were then used to link functional molecules in a UV-mediated step and selectively manipulate the devices' surface wettability, see Figure 2-3.b. Carlborg and colleagues achieved microfluidic chips with photo-patterned surfaces and different surface features.<sup>326</sup> PDMS-based microfluidic



chips can be fabricated with high-precision and remarkable surface properties. However, the further diffusion of these platforms beyond research departments is conditioned by the multiple steps required for their fabrications, such as soft-lithography, which involves a considerable level of expertise, human labor, and expensive equipment.<sup>284</sup> Therefore, new manufacturing methods might boost the microfluidic chips' fabrication, maintaining good precision. With 3D printing, these technological drawbacks could be overcome, as well as it could simplify the production of microfluidic chips assembled with inner three-dimensional channels compared to conventional micro-manufacturing methods.<sup>327–331</sup>

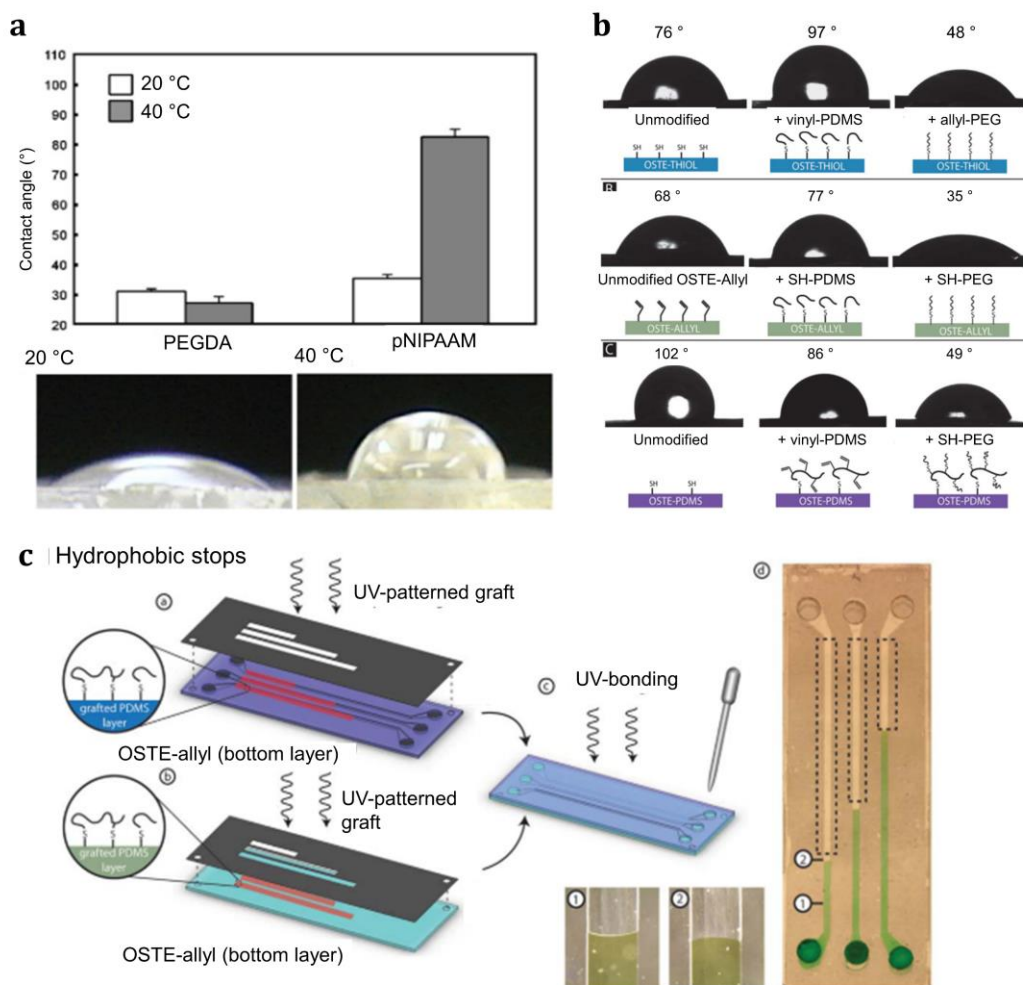


Figure 2-3. **Photo-mediated surface modifications of polydimethylsiloxane chips.** (a) Contact angle measurements on PEGDA-grafted and pNIPAAm-grafted PDMS surface at 20 °C and 40 °C, the photograph below shows the changes in wettability of the pNIPAAm-grafted PDMS at both temperatures.<sup>318</sup> (b) Contact angle measurements of the different OSTE PDMS material with different surface wettability after UV-mediated polymerization. (c) UV patterning of the microfluidic chips exploiting the allyl and thiol groups of the microchannel's surface, which is appreciated by the difference in the meniscus behavior when a green-colored liquid is led flow.<sup>325</sup>



### 2.2.2. 3D printed polymeric microfluidic devices.

Recently, polymeric 3D printing has been proposed as an alternative for the manufacturing of bespoke microdevices for bioengineering applications, such as nonplanar lab-on-a-chip (LOC), bioreactors for real-time analysis, and analytical systems with antibacterial properties for studying cell responses.<sup>332-335</sup> Many studies demonstrated how microfluidic devices could be successfully fabricated through different polymeric 3D printing techniques, involving mainly Fused Filament Fabrication (FFF), photopolymer inkjet printing (PolyJet), and vat polymerization (VP) 3D printing.<sup>336</sup> Each of them offers different characteristics that can be beneficial according to the microfluidic system and its application.<sup>337</sup> Table 2-2 summarizes the main characteristics of these three technologies for microfluidic chip fabrications.

FFF methods are the cheapest in equipment and materials; besides, there is a wide range of commercial thermoplastic materials, including polylactic acid (PLA), polymethylmethacrylate (PMMA), acrylonitrile butadiene styrene (ABS), poly- $\epsilon$ -caprolactone (PCL), and cyclic olefin copolymer (COC), few of them with biocompatible properties.<sup>338-340</sup> With FDM, many fascinating procedures for microfluidic chip fabrication have been reported. For example, Kotz and coworkers produced transparent chips using commercially available polymethylmethacrylate (PMMA) filament, one of the most used materials for microfluidic chip fabrication on a scientific scale.<sup>341</sup> With PMMA filaments (from *Material4print*), they created chips with a minimum channel width of  $\sim 300 \mu\text{m}$ . The chips' bottom transparency (the region of interest for proteins patterning) was significantly improved by directly printing onto PMMA films. These chips were used for mixing dyed water; the chip's surface was then selectively photopatterned with fluorescently labeled biotin (F5B), showing the easy biofunctionalization of 3D printed closed PMMA chips (Figure 2-4.a).

Likewise, transparent microfluidic chips were also obtained from Nelson et al. using a commercial thermoplastic polyurethane filament (SainSmart Clear flexible TPU).<sup>342</sup> They developed microfluidic chips with the desired characteristics, including optical transparency (up to 85 % of transmission), chemical solvent stability, high-pressure resistance, and flexibility (see Figure 2-4.b). The printed chips' biocompatibility was demonstrated by culturing mouse inner medullary collecting duct cells (mIMCD3). Moreover, they demonstrated how low-cost FFF techniques could be a viable technique for developing microfluidic chips, printing channel features as small as  $50 \mu\text{m}$  in less than 25 minutes. Bressan et al. developed 3D printed microfluidic chips based on polylactic acid (PLA), with channels as small as  $260 \times 260 \mu\text{m}$  for the synthesis of silver and gold nanoparticles.<sup>346,347</sup> By optimizing the printing parameter, the chips were fabricated to well-control the fluid flow behavior for obtaining the desired particle features. These particles were then used for

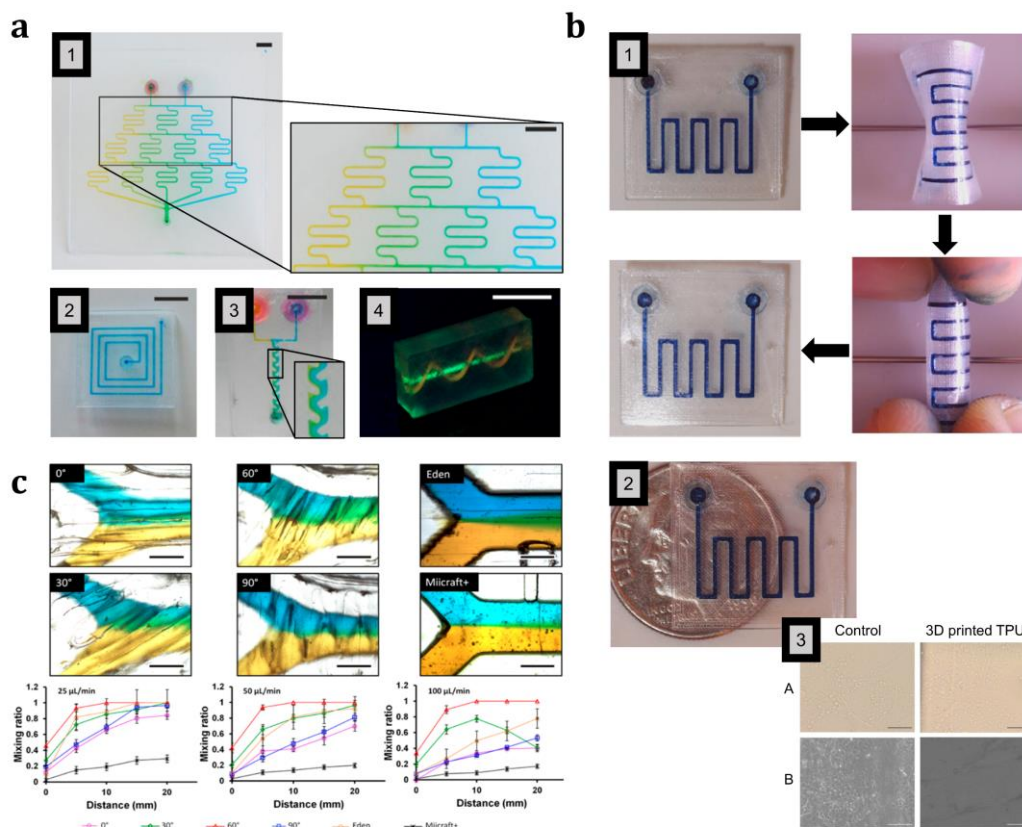
biological applications such as crystal violet (CV) through SERS analysis or to improve the electrocatalytic capability of carbon paste electrode (CPE) for the electrochemical determination of gallic acid (GA) and thiocyanate ions.

Table 2-2. Comparison between the three most used polymeric 3D printing technologies (FDM, PolyJet, and Vat polymerization) for the manufacture of microfluidic chips in terms of materials used, energy source required for joining material, benefits, and drawbacks of each technology, small features reached and application in the biomedical field.

	<b>Fused filament fabrication (FFF)</b>	<b>Photopolymer 3D printing (PolyJet)</b>	<b>Vat polymerization (VP)</b>
Material	Thermoplastics, e.g., Polylactic acid (PLA), Acrylonitrile butadiene styrene (ABS), Polycaprolactone (PCL), Polymethylmethacrylate (PMMA) Polyurethane (PU)	Photocurable resins/photopolymers. (meth)acrylate-based.	Photocurable resins/photopolymers. (meth)acrylate-based.
Energy Source	Thermal	UV-Visible light/Laser	UV-Visible light/Laser.
Benefits	Cost-affordable material.	Fast printing times, multi-material objects.	High printing resolution, fast printing times, good surface finishing.
Drawbacks	Limited printing precision, reduce transparent materials, low printing times.	Laborious material remotion from the microchannels.	Post-treatment to remove unreacted material from channels, post-curing to remove support structures.
Smallest features	50 $\mu\text{m}$ <sup>342</sup>	50 $\mu\text{m}$ <sup>343</sup>	0.6 - 30 $\mu\text{m}$ <sup>344,345</sup>

Other researchers developed transparent and sealed microfluidic chips with PLA as an alternative to conventional polydimethylsiloxane material (PDMS), which might act as an electronic tongue (e-tongue). These flexible and interdigitated microfluidic chips were capable of distinguishing tastes below the human threshold. The chips were built within less than one hour, using a home-made 3D printer.<sup>348</sup> In addition to PLA, other types of cost-affordable materials can also be used. As reported in 2018 by Romanov and coworkers, 3D printed microfluidic chips with a channel dimension of about 400  $\mu\text{m}$  were produced with either polylactic acid (PLA) or polyethylene terephthalate glycol (PETg) through two different types of commercially available low-cost

FDM-3D printers: Prusa i3 (\$ 600) and LulzBot (\$ 2500).<sup>349</sup> Such devices presented high-pressure, heat resistance, and glass-like layer characteristics; those features were useful for DNA melting analysis and facilitated the optical visualization of fluids in droplet generation and tracking and identifying DNA.



**Figure 2-4. 3D printed milli- and microfluidic chips fabricated by Fused Filament Fabrication (FFF)-3D printing methods.** (a) 3D printed chips in PMMA. 1) Microchip cascade for mixing of yellow/blue-dyed water. 2) 3D printed chip with a square channel of 600x600 μm. 3) improved mixer structure of 600x600 μm channel. 4) 3D printed channel produced around a straight channel, using an aqueous fluorescent dye. For the four images, the scale bar is 10 mm.<sup>341</sup> (b) Transparent 3D printed microfluidic chips made of polyurethane (TPU) images showing a) the flexibility, 2) the transparency of the chip, and 3) mIMCD3 cells behavior where a characteristic cobblestone appearance was observed in both control wells, and 3D printed TPU (scale bars = 100 μm).<sup>342</sup> (c) Microscopic photographs of the laminar fluid flow inside 500x500 μm channel toward a 750 μm x 500 μm channel, where yellow/blue dyed water is passed at 25 μL/min through microfluidic chips fabricated with FDM at 0°, 30°, 60°, and 90° of filament orientation, Eden (Polyjet), and Miicraft+ (DLP-SLA), respectively. Plots of distance vs. mixing ratio demonstrated the diffusion through the laminar flow channel at 25, 50, and 100 μL/min.<sup>350</sup>

Focusing on the surface finishing, Li et al. demonstrated how the extruded filament orientation could enhance fluidic behavior control.<sup>350</sup> They developed different microfluidic chips (channels of 500x500 μm) with

different printing orientation of the filament (0°, 30°, 60°, and 90°) respecting the fluid flow direction in order to examine the fluid mixing performance (Figure 2-4.c). The Li and coworkers' work evidenced that in microfluidic chips where the extruded filament was oriented at 60° to the flow direction, the mixing of fluids in laminar flow was achieved without any complex channel geometry, specific surface patterning, or other passive mixers. The chips' mixing performance can be adjusted by changing the filament orientation at 0° and 90°. The importance of controlling fluid flow was proven by performing analytical analysis such as Isotachopheresis (ITP) electrophoresis separation of fluorescein, where the mixing behavior is undesired. Furthermore, they performed simple colorimetric assays for measuring the iron content in environmental water samples, where instead, the mixing property is desired. These chips were produced with good optical transparency using a commercial filament, Crystal Clear acrylonitrile-butadiene-styrene (ABS) from *3D Systems*.

Although interesting microfluidic chips have been developed through FFF techniques, the chips' surface finishing is one of these methods' main setbacks. Surface finishing might be beneficial in specific cases depending on the application; however, in the biomedical field, precision and high homogeneity of the microfluidic chips' channels are frequently requested to avoid alterations in the flow of fluids in high precision laboratory analyses. Moreover, the relatively small number of materials available for FFF further limits microfluidic systems development in advanced bioengineering applications where the surface features must be excellent or at least to do not disturb the studied fluidic medium.<sup>337</sup> Using another polymeric 3D printing technique, PolyJet, the printed microchips' surface features and definition could be significantly enhanced. PolyJet 3D printing is a method that employs photocurable photopolymers deposited selectively on a substrate drop-by-drop.<sup>351</sup> Once the photopolymer drops are deposited, they are rapidly photocured with a UV light source present in the jetting material chamber. PolyJet also employs support materials, which are similarly deposited and UV-cured, according to the design, that can be easily removed in post-printing procedures. When the first layer is created, the stage is lowered, and the next film is built. With the PolyJet technique, the printing time speed and the microfluidic chips' accuracy are superior in all axes than the FFF technique by setting the proper printing parameters.<sup>352</sup> As reported by Lee et al. work, microfluidic chips made from PolyJet can be produced with a nominal *X-Y* plane and *z* dimensions of 500  $\mu\text{m}$  and 100  $\mu\text{m}$ , respectively, with an average deviation (between the printed part and the CAD design) of 25.2  $\mu\text{m}$  and with smoother features (surface roughness of 0.47  $\mu\text{m}$ ) compared to 67.8  $\mu\text{m}$  of average deviation and 42.97  $\mu\text{m}$  of surface roughness of FFF-3D printed parts (Figure 2-5.a).<sup>353</sup> These precise and accurate microfluidic chips, made from commercial material (FullCure, *Stratasys*), also presented high cell viability

toward C2C12 cells as a function of an appropriate post-printing sterilization step. Highly transparent chips with intricate microchannels can also be produced using PolyJet technology with excellent precision and accuracy to enable efficient fluid mixing and optical analysis. The fluid profile in most of the microfluidic systems is in a laminar flow; therefore, the ability to mix different fluids efficiently and rapidly in this regime is a fundamental aspect of microfluidic chips for biological and chemical applications.<sup>261,282,354</sup> Enders et al. produced different micro-passive mixers through PolyJet methods with great optical features and sophisticated channel paths to study and compare the mixing performances between each mixing configuration (Figure 2-5.b).<sup>355</sup> The designs of the most diffused mixers (Caterpillar mixer, enhanced Caterpillar mixer, Tesla-like mixer, and HC mixer) were used to produce those chips employing an acrylate-based material (VisiJet M2R-CL, 3D System). After a series of experimental and simulation comparison tests, they observed that Tesla-like and especially HC chips were the most suitable for the rapid and efficient mixing of biological fluids such as CHO-K1 (Chinese hamster ovary) cells.

Despite the higher resolution of the PolyJet compared to the FFF method, it is still challenging to obtain sub-100  $\mu\text{m}$  channels since this technique requires using a support material to avoid filling the built microchannel during printing. The removal of the support material after printing implies complex post-printing treatments.<sup>277,356,357</sup> This setback could become even trickier when the microfluidic channel configuration increases in complexity, e.g., serpentine or spiral-shaped channels. Castiaux and collaborators proposed a different strategy: instead of using conventional support material, the researchers stopped at a certain point the printing step to incorporate either a thin polycarbonate membrane or a liquid (composed of glycerol/isopropanol 65:35 v:v) as a physical barrier that can support the additional covering layers.<sup>343</sup> Both techniques demonstrated to be useful for creating complex-shaped microfluidic chips with channels dimensions as small as  $15 \times 250 \mu\text{m}$  that are challenging dimensions to be achieved by conventional PolyJet methods using support material. However, the results obtained appear not-so-reliable since the  $15 \times 250 \mu\text{m}$  channel was intended to be  $54 \times 124 \mu\text{m}$  in the CAD design. Besides, it must be considered that stopping the printing procedure for placing extra material manually inevitably introduces additional labor in the process. One of the PolyJet technique's main advantages is that it is a multi-material technique; i.e., it can print various materials during the same printing process.<sup>56,358</sup> Taking advantage of this characteristic, S. Keating et al. reported the 3D printing of multi-material valves using both rigid (VeroWhitePlus, RGD835, Stratasys) and flexible (TangoPlus, FLX930, Stratasys) materials. They compared the multi-material valves with single material valves observing that the former ones present a more robust capability to deformation, enabling better and precise control of fluids, leading

to automated production of microfluidic devices (Figure 2-5.c).<sup>359</sup> The researchers reported that such types of multipurpose fluidic chips with channels  $800 \times 800 \mu\text{m}$  and with programmable valves might be used for various advanced biological applications such as DNA assembly and analysis, continuous sampling sensing and soft robotics.

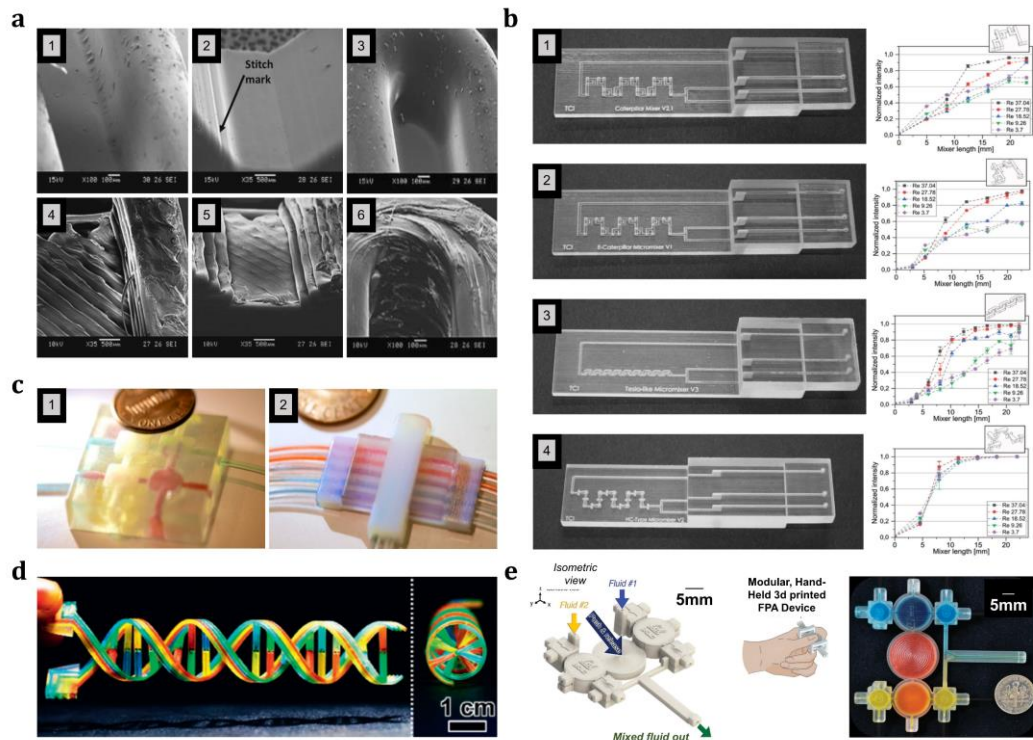


**Figure 2-5. 3D printed milli- and microfluidic chips fabricated by PolyJet-3D printing methods.** a) Scanning electron microscope (SEM) images of the 3D printed channels through 1-3) PolyJet printing and 4-6) FDM 3D printing where is depicted the surface roughness features between both techniques.<sup>353</sup> b) Photographs of the 3D printed microfluidic mixers: 1) Caterpillar mixer, 2) enhanced Caterpillar mixer, 3) Tesla-like mixer, and 4) HC mixer. Next to each image is shown the calculated mixing performances (from simulation tests) as a mixer length function.<sup>355</sup> c) 3D printed microfluidic multichannel valves made of 1) a single material and 2) a multi-material.<sup>359</sup> d) 3D printed DNA-inspired fluidic devices that comprise eight fluidic channels ( $750 \mu\text{m}$  in diameter) filled with distinct dye-colored solution.<sup>360</sup> e) Working principle of a finger-powered two-fluid FPA prototype for fluid mixing two distinct dyed-colored solutions.<sup>362</sup>

Sochol et al. developed advanced components, as shown in Figure 2-5.d, used as fluidic capacitors, diodes, and transistors to construct integrated fluidic circuits (IFC).<sup>360</sup> The components were fabricated with a commercial material, Visijet M3 Crystal (3D Systems), which presents limited biocompatibility. Indeed, the investigators evidenced that further works are required using biocompatible material for PolyJet printing, such as MED610, or performing the appropriate post-processing steps to provide higher biocompatibility to the chips. Nevertheless, they produced reliable and

sophisticated chips in which their functionalities can be customized by modifying the geometric parameters. In Sweet and coworkers' work, a series of finger-powered actuator (FPA) prototypes were produced using Visijet material through PolyJet 3D printing.<sup>361</sup> The pulsatile fluid motion capability of the produced devices was used as modular models for microfluidic actuation and mixing purposes in an integrated fluidic platform; see Figure 2-5.e. A further advantage of PolyJet printing is that it allows the fabrication of multiple microfluidic chips contemporaneously with precise and small channels. Walczak et al. presented the fabrication of a series of microfluidic chips (up to 170 chips) during a single 3D printing process. The chips with diameter dimensions of 400  $\mu\text{m}$  and with semi-transparent features were used for capillarity gel electrophoresis. After optimizing the printing parameters in terms of printing orientation, the fluorescence detection of DNA was possible.<sup>362</sup> Although the remarkable works reported for microfluidic chip fabrication using PolyJet 3D printing, this technique requires a considerable level of post-printing process focused mainly on the proper cleaning of the microchannels). Besides, it presents high initial costs in equipment and consumables compared to other polymeric 3D printing, and only specific and limited commercial materials can be used, few of them with truly biocompatibility properties.<sup>363</sup>

#### *Vat 3D printing for the production of microfluidic devices*

Vat polymerization (VP) 3D printing techniques have been proposed as a robust alternative for microfluidic device fabrication. VP 3D printing offers great spatial resolutions and printing accuracy as well as cost-affordable instruments and supplies.<sup>171,337,364,365</sup> Indeed, the easiness and speed of fabrication of these techniques led scientists to employ VP-3D printing to create on-demand integrated microfluidic devices by combining the printed parts with other materials and techniques. For instance, VP-3D printing could be used to fabricate molds for PDMS molding, aiding the production of precise microfluidic chips with a higher level of geometrical complexity in fewer steps than conventional lithography procedures and micro-etching methods.<sup>366,367</sup> The 3D printing-mold strategy has been in the biological field to manufacture PDMS-based microfluidic chips for in-vitro cell culture that can roughly mimic the vessel architectures. Both healthy and stenotic arteries were reproduced by combining computed tomography angiography (CTA) with SL-3D printing.<sup>368</sup> Alternatively, PDMS-based microfluidic chips with connected crossed-channels and a suspended physiological bilayer composed of physiological lipids were also produced by this strategy.<sup>369</sup> Nonetheless, the interest of the microfluidic field on vat 3D printing lies mainly in the possibility of producing microfluidic devices and components in a single or few steps of fabrication.<sup>370</sup> A further advantage given by vat 3D printing is the possibility

of preparing or tailoring the printable material (the photopolymer) by combining the appropriate components into the photocurable resin, which might allow obtaining printed structures with the desired properties.<sup>371</sup> These features make vat 3D printing (VP) one of the most promising technologies for the fast and precise fabrication of customized milli- and microfluidic platforms (see Figure 2-2.b). The printed parts obtained by VP-3D printing can be produced with specific surface/bulk features of biomedical interest, including optical transparency, water and gas permeability, chemical resistance, and biocompatibility.<sup>99</sup> However, the development of reliable polymeric 3D printed fluidic systems with all these properties is a challenging task that has led researchers to study several types of printable photopolymers through the last years, ranging from commercially available photopolymers to custom-made formulations and even carrying out dedicated post-printing protocols on the 3D printed parts.<sup>336</sup>

The interest in producing microfluidic chips by VP-3D printing methods started at the beginning of the 2000s, with Kang et al. paper.<sup>372</sup> though greater attention (at least at the publishing level) was paid around a decade ago.<sup>373-375</sup> One of the first attempts in exploring the VP-3D printed fluidic field was reported by Au et al. in 2014.<sup>374</sup> The researchers presented the building of microfluidic devices by using commercial products: a 3D systems Viper SL 3D printer (in high-resolution mode,  $100\ \mu\text{m}$  XY resolution and  $50\ \mu\text{m}$  Z-steps) and the Somos® WaterShed XC 11122 resin, which is marketed as a suitable resin for obtaining biocompatible, transparent, and hard thermosets objects. The researchers reported the precise microfluidic chip fabrication with the smallest channel dimension down to  $400\ \mu\text{m}$ . Also, in Au's work, a technological scan is presented based on how far the society is from adopting VP-3D printing to produce truly end-user microfluidic devices discussing and analyzing digital design, file sharing, fabrication procedures, and aspects, and possible applications. Another try to reproduce microfluidic chips by VP-3D printing was presented by Shalan and lead by Prof. Breadmore, also in 2014.<sup>375</sup> The team explored the possibility of using a commercial VP-3D printer and commercial colorless acrylate-based resin (from the printer owner) for the direct fabrication of enclosed fluidic devices ranging from milli to micro dimensions. In this case, the printer used was the DLP-based Miicraft (Hsinchu, Taiwan) with averaging \$2000 back then, cheaper than the \$5000 of 3D systems SL printers at that time. The Miicraft is a bottom-up machine with a plane resolution of  $56\ \mu\text{m} \times 56\ \mu\text{m}$ , and a Z-resolution around  $50$  and  $100\ \mu\text{m}$  that allowed researchers to produce visible transparent microchips within few minutes, with channel dimensions small as  $250\ \mu\text{m}$  and averaging \$1 per chip. As described by the authors, VP-3D printing could greatly benefit from producing analytical microfluidic elements in some research centers with limited budgets aid by the printer's low cost and the simplicity of producing complex-shaped chips. Despite the technological limitations in terms of



printer's hardware, equipment, and resin chemistry that researchers faced in 2014, they probably provided the real starting signal for the effective production of microfluidic devices through VP-3D printing, highlighting the multiple possibilities that this technology could offer in the field.

Indeed, in 2015, the Lee et al. work, Led by Prof. Folch, employed the 3D systems Viper SL 3D printer and the Somos® WaterShed XC 11122 resin to produce complex-shaped 3D print microfluidic devices for the detection of pathogenic bacteria, see Figure 2-6.a.<sup>376</sup> Their method was based on using magnetic nanoparticle clusters (MNCs). First, the printed microchips were manufactured hosting a spiral microchannel with a trapezoidal cross-section (inner and outer heights of 250  $\mu\text{m}$  and 500  $\mu\text{m}$ , respectively). Then Ferro-nanoparticles functionalized with antibody were used for capturing *E. coli* bacteria in milk. Using a permanent magnet, the pristine magnetic nanoparticle clusters (MNCs) and those MNCs with *E. coli* over them were separated from the milk. Both types of MCNs (with and without linked bacteria) were first dispersed in a buffer solution, and then the solution was flushed through the helical microchannel chip with or without a sheath flow. By controlling the fluidic properties and exploiting the fluid inertial, magnetic nanoparticles (with and without linked bacteria) were successfully separated. This was an example of how the three-dimensional structures' design can take a crucial role according to the applications.

Other investigators were more concerned about taking advantage of the VP-3D printing versatilities for producing hybrid fluidic systems with satisfactory biocompatibility features instead of focusing on achieving the smallest channel dimension. That was the case for the report presented by Takenaga et al. in 2015.<sup>379</sup> The researcher group employed a commercial printer (PicoPlus 27) from Asiga and one of the commercial resin from the same company (PlasCLEAR) to print fluidic systems. In such as work, the researchers presented an innovative microfluidic assembly method in which the 3D printed fluidic chip is arranged on a light-addressable potentiometric sensor (LAPS) chip made from the same photopolymer. They used these types of assembled devices for Chinese hamster ovary (CHO)-cell growth yielding comparable results to standard cell-culture flasks and giving the possibility to monitor cells' reaction in the channels in real-time. Also, in 2015, a mathematical model and experimental optical characterization carried out on a customized photopolymer were presented for Gong et al.<sup>380</sup> The work was focused on developing microfluidic systems with the smallest possible channel dimension. In this case, the researchers developed their photopolymer based on a low-molecular PEGDA (Mn 250 g/mol) monomer with 1 wt.% of phenyl bis(2,4,6-trimethylbenzoyl) phosphine photoinitiator or BAPO (one of the most diffused photoinitiators) and varying the concentration of Solvent Yellow 14 dye. Slight amounts of the dye were used to increase the printing resolution

by limiting transversally light diffusion ( $X$ - $Y$  plane) and controlling the light penetration ( $Z$ -axes) during the printing process. By setting the appropriate printing parameters and experimental conditions (e.g., light dose, build layer thickness, and resin composition), channel sizes as small as  $60\ \mu\text{m} \times 108\ \mu\text{m}$  were successfully achieved by the researchers.

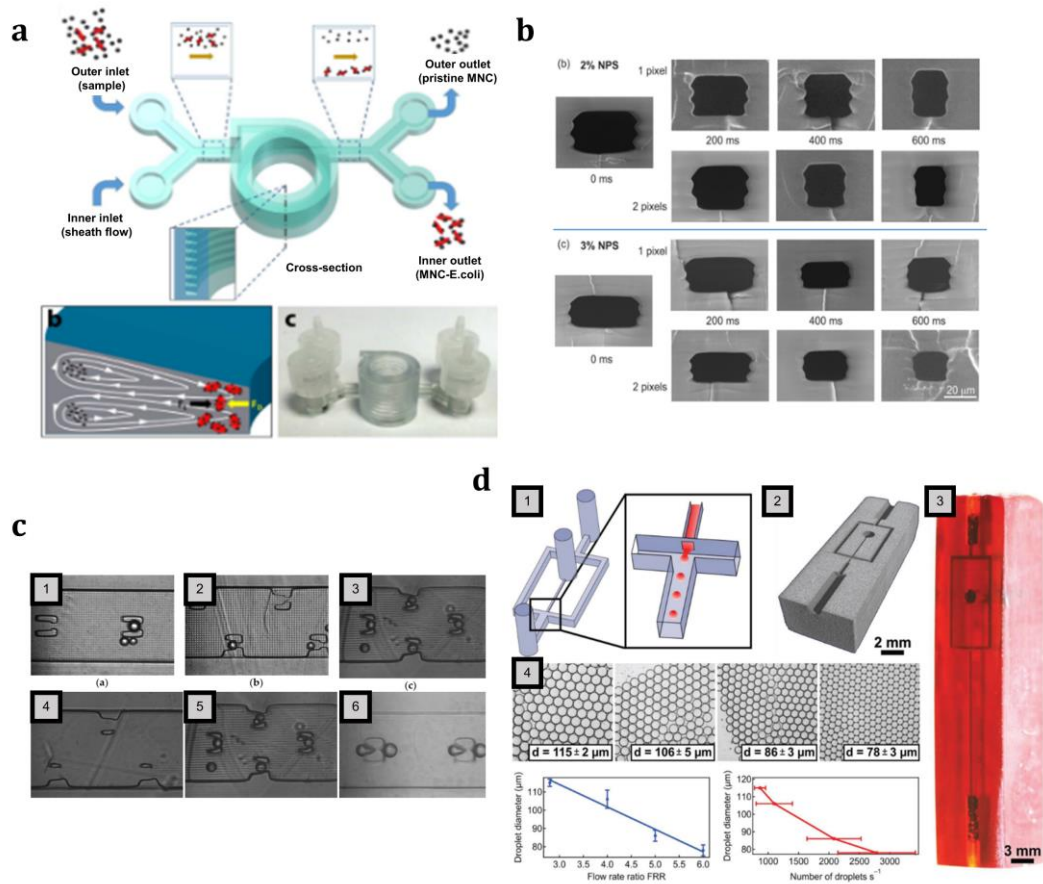
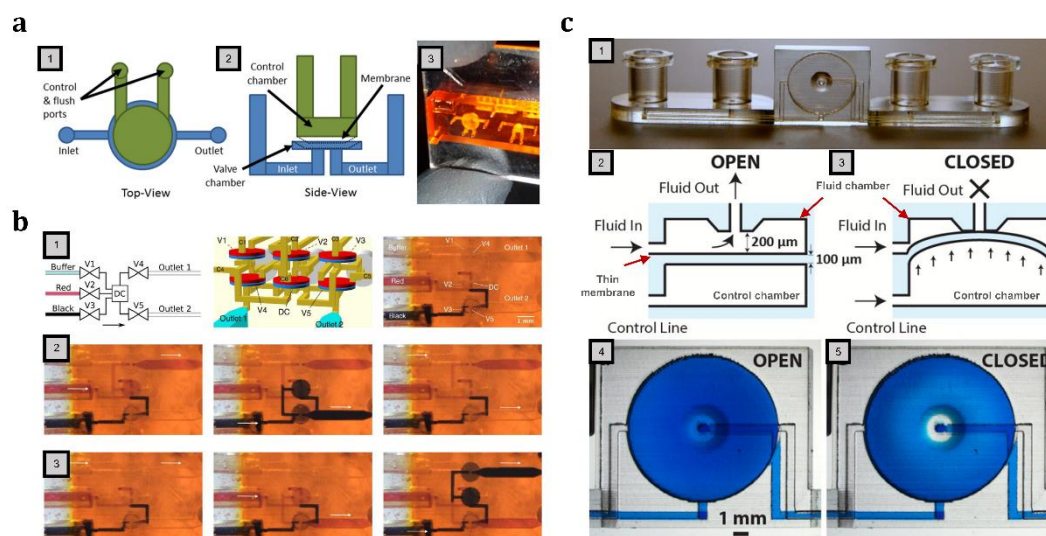


Figure 2-6. **3D printed milli- and microfluidic chips fabricated by vat polymerization-3D printing methods.** (a) 3D printed microfluidic with helical microchannel used for separating pathogenic *E. coli* bacteria (linked to magnetic nanoparticles clusters) taking advantage of the Dean forces within the channel's trapezoidal cross-section.<sup>376</sup> (b) photograph of the microchannel obtained (height of about  $18\ \mu\text{m}$ ) from the three (3) wt. % NPS into PEGDA-based resin.<sup>153</sup> (c) photograph showing the effect of the 3D printed particles trappers positioned at different zones of the microchannel: traps positioned 1) in the center of the channels, 2) staggered along the sides of the channel, 3) staggered along the sides, and in the middle of the channel, 4) traps partially formed after 500 ms of light exposure with no bead capture, 5) particle captured in well-formed traps after 750 ms of exposure, 6) overexposed traps after 1000 ms.<sup>377</sup> (d) nonplanar 3D printed flow-focusing device: 1) representation of the microfluidic flow cell chip, 2) CAD image of the flow cell model; 3) photograph of the printed chip using R11 resin, and 4) diameter of the droplet generated depending on the flow rate ratio (FRR) of dispersed and continuous water-oil phases.<sup>378</sup>

Later, in 2017, the same researcher group, led by Nordin G.P. and Woolley A.T, continued their studies and surpassed themselves, achieving flow channels as small as  $18 \mu\text{m} \times 20 \mu\text{m}$  aided by previous investigations and analysis.<sup>277</sup> In this case, the researchers employed a customized UV-3D printer (emitting at 385 nm) and used a customized PEGDA-based photopolymer with 2-nitrophenyl phenyl sulfide (NPS) as a dye, as shown in (Figure 2-6.b).<sup>153</sup> The results obtained from these 'preliminary' works led the team to produce microfluidic chips for various applications, for entrapping microparticles ( $25 \mu\text{m}$ ) inside a microfluidic channel built with pillars and ridged of  $\sim 30 \mu\text{m}$  for instance, as shown in Figure 2-6.c;<sup>377</sup> or in a more advanced application, for the extraction and separation preterm birth (PTB) biomarkers (ferritin).<sup>381</sup> In this last work, Parker et al. produced porous polymeric monoliths based on glycidyl methacrylate (GMA) and ethylene glycol dimethacrylate (EGDMA) inside microfluidic channels ( $45 \mu\text{m} \times 50 \mu\text{m}$ ), obtaining an immunoaffinity stable physical barrier. In the same line, they recently developed microfluidic devices with cross-section channel dimensions of  $\sim 50 \mu\text{m}$  for microchip electrophoresis ( $\mu\text{CE}$ ) separation of various fluorescently labeled amino acids and biomarkers that related to risk preterm birth (PTB).<sup>382</sup> By optimizing the conditions of separations such as devices layout, running buffer, and the voltages applied to the systems, the yield of separation of the printed devices was comparable or slightly reduced compared to conventional material for microchip electrophoresis analysis with a limit of detection in the high picomolar (pM) to low nanomolar (nM) range. Although more studies are required for evaluating different classes of biomarkers, it was successfully demonstrated that light-based 3D printing methods could be used to produce microfluidic devices for the analysis of significant medical biomarkers.

Other fundamental components of microfluidic chips, such as microvalves, micropumps, and any other actuator, can also be produced by VP-3D printing. These components can program the fluid, create mixtures and liquid gradients during the analysis, and spare the human labor during the tests. In this context, Gong, Woolley, and Nording demonstrated the potentiality of VP-3D printing as a great method for producing microfluidic chips with functional components. In 2015 the researchers reported the production of 3D printed valves.<sup>383</sup> These printed actuators were driven pneumatically by wilfully making deflect a thin membrane with compressed air and blocking the fluid flow; see Figure 2-7.a. These actuators were produced using a commercial 3D printer (the B9 Creator printer v1.1) and a lab-made resin based on a low-molecular PEGDA ( $M_n$  250 g/mol) monomer with 1 wt.% of phenyl bis(2,4,6-trimethylbenzoyl) phosphine photoinitiator or BAPO and 0.2 wt.% of Sudan I dye. The same researcher team improved the stability over time of the valves and pumps by adding a thermal initiator, the azobisisobutyronitrile (0.01 wt.%), into the same PEGDA-based resin (using, however, 0.4 wt.% of Sudan I) and subjecting the printed parts to a 30 min

thermal-post-curing step, which allowed the pumps to have a performance of up to 1 million of actuation.<sup>384</sup> Additionally, the valve's volume was reduced considerably (to a tenth of the original design), allowing the production of multiplexers with high-density valves integrated into microfluidic devices, see Figure 2-7.b.



**Figure 2-7. Examples of 3D printed microfluidic valves and pumps fabricated by vat polymerization-3D printing methods.** (a) Schematic view of the 3D design. 1) Top view and 2) side illustration view of the valve design. The control chamber (in green color) and fluidic chamber (blue color) are voids in the 3D printed device. The control chamber has 2 access ports to enable it to be drained after printing. Pressure can be applied through both ports to actuate the valve, or one channel can be sealed, and pressure applied through the other to actuate the valve. Pressurized membrane (black dotted line) shows valve closure.<sup>383</sup> (b) 3D printed multiplexer devices. 1) schematic view of the multiplexer working principles and CAD design. Next to the design images is displayed the multiplexer's bottom view fabricated according to the CAD design. From 2) to 3) is shown the arbitrary 3-to-2 multiplexing.<sup>384</sup> (c) Design of the printed valve. 1) photograph of the single-valve device. Schematics of a valve unit when it is open (2) and closed (3). Micrographs of the valve unit when it is open (4) and closed (5).<sup>386</sup>

An analogous work was reported by Au and coworkers presenting a fully 3D printed valve that could be integrated into microfluidic systems, which enabled the correct distribution and mixing of fluids, see Figure 2-7.c. The model was fabricated using the WaterShed XC 11122 photopolymer (a colorless resin promoted as a suitable resin for obtaining biocompatible, transparent, and hard thermosets objects) and the 3D systems Viper SL 3D printer machine set in high-resolution mode. The printed valve consisted of two chambers separated by a thin film or membrane: a control chamber and a fluid chamber. By flushing compressed air in the control chamber, the thin membrane deflects and remains stable, blocking the liquids off with no leaking. As a proof of concept, the research team coupled four printed valves for

routing four different liquids into a 3D-printed cell culture chamber, and in this way, CHO-K1 cells were stimulated with ATP solutions, with the possibility to track their  $\text{Ca}^{2+}$ -answer using a fluorescent dye (Fluo-4). The same group presented an article issued by Lee, Bhattacharjee, and Folch, where transparent and biocompatible microfluidic chips arranged with a series of large arrays of valves were produced cost-effectively. The devices were produced using a customized photopolymer based on low-molecular-weight (MW=258) poly(ethylene diacrylate) monomers and using a commercial DLP-SL 3D printer from Asiga (Pico2-HD, X-Y resolution of 27  $\mu\text{m}$  and Z-axis resolution of 10  $\mu\text{m}$ ) that had an emitting wavelength at 385 nm.<sup>385</sup> These previous work focused on microfluidic actuators boosted the viability of adopting VP-3D printing for fluidic chip fabrication by providing them with connectors, pumps, and valves, increasing the microsystems' functionalities for more automated analysis.

Over the next years, multiple and interesting works were published presenting how VP-3D printing can be used in microfluidic device production for diversified and assorted applications. For instance, Wang et al. presented in 2017 multilayered 3D microfluidic devices for flow-focusing water/oil droplet generation employing a liquid crystal display (LCD)-based SLA 3D printer.<sup>387</sup> The chips were obtained from a commercial acrylate-based photopolymer, the Spot-LV from Spot-A materials; however, intending to increase the light-absorbing effect, and thus the printing resolution, the researchers opted for adding up to 2 wt.% of a green dye into the commercial photopolymer. Various characterization analyses were performed (e.g., curing times and printing resolution in each direction) to create microfluidic chips with dimensional microchannel features down to 400  $\mu\text{m}$  in the X-Y plane and 800  $\mu\text{m}$  in the Z-axis for vertical and interconnection features, leading to obtaining 3D printed flow-focusing droplet generators that generated droplets with sizes between 50 and 185  $\mu\text{m}^2$ . A similar work developed by Männel and colleagues in 2019 presented the production of nonplanar microfluidic flow cell devices for emulsion and polymeric hydrophilic/hydrophobic micro-particle formation.<sup>378</sup> The printed chips were produced through a commercial micro-stereolithography ( $\mu\text{SL}$ ) machine (Perfactory P4 mini) and using a commercial photopolymer (R11), both from *Envisiontec*. Printing settings such as object-resin vat separation distance, Z-axis building distance, and X-Y plane-light compensation at the edge's stages were adjusted to print precise microfluidic with closed channel sizes down to 75  $\mu\text{m}$  in a single-fabrication step (Figure 2-6.d). The 3D printed microfluidic chips presented a similar drop-making yield compared to multi-step PDMS-based flow cell models fabricated by photo- and soft-lithography.



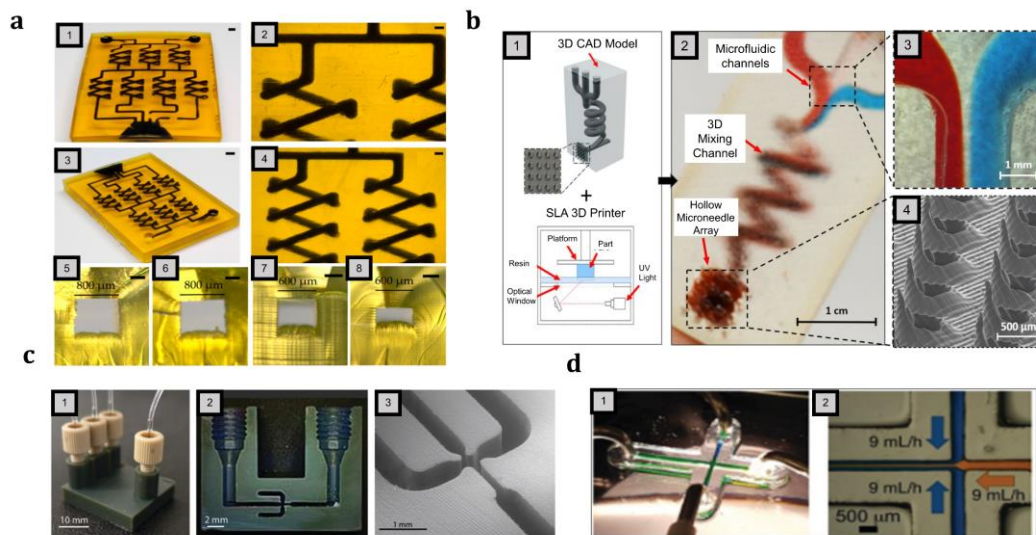


**Figure 2-8. Examples of 3D printed milli- and microfluidic chips fabricated by vat polymerization-3D printing methods.** (a) 3D printed perfluoropolyether (PFPE) microfluidic chip: 1) front view of the gradient mixing chip (scale bar: 2 mm) with channel 2)  $800\ \mu\text{m} \times 800\ \mu\text{m}$  filled with black ink (scale bar:  $500\ \mu\text{m}$ ), 3) isometric view of the gradient mixing chip (scale bar: 2 mm) with channel 4)  $600\ \mu\text{m} \times 600\ \mu\text{m}$  filled with black ink (scale bar:  $500\ \mu\text{m}$ ), 5) lateral view of the  $800\ \mu\text{m}$  channel width at the inlet and 6) in the middle (scale bar:  $250\ \mu\text{m}$ ), 7) lateral view of the  $600\ \mu\text{m}$  channel width at the inlet and 8) in the middle (scale bar:  $250\ \mu\text{m}$ ).<sup>388</sup> (b) 3D printed microfluidic-enabled hollow microneedle devices: 1) CAD model and representation of the SL-3D printing method, 2) the printed device composed with 3) three microfluidic inlets converging into a 3D spiral mixing chamber and a 4) hollow microneedle array outlet.<sup>389</sup> (c) 3D printed microfluidic: (1) the device with integrated connectors, (2) cross-sectional image of the chips showing the internal microchannel structure, and (3) micrograph image (scale bar 1 mm) of the device with details of the asymmetric focusing channels.<sup>390</sup> (d) Microfluidic devices obtained using a methacrylate-polydimethylsiloxane oligomer. 1) photograph of a PDMS-based microfluidic device with  $500\ \mu\text{m}$  wide channels printed with a commercial 385 nm SL machine. 2) a central stream of yellow dye ( $9\ \text{mL/h}$ ) flanked by two streams of blue dye ( $9\ \text{mL/h}$  each) produces a heterogeneous laminar flow ( $9\ \text{mL h}^{-1}$ ) in the 3D printed PDMS-based microfluidic chip.<sup>391</sup>

Kotz and coworkers presented a simple method in 2018 to 3D print microfluidic devices using a commercial stereolithography printer (Asiga Pico 2) from a custom-made photopolymer based on highly fluorinated (PFPE) methacrylate resin.<sup>388</sup> The authors selected the PFPE photocurable resin due to the high optical transparency and the polymerized parts' high chemical resistance. They evaluated the addition in the PFPE methacrylate resin of adequate components necessary to achieve the looked-for features. Two photoinitiators: Diphenyl(2,4,6-trimethylbenzoyl) phosphine oxide (TPO) and phenyl bis(2,4,6-trimethylbenzoyl) phosphine photoinitiator (BAPO), and various types of light absorbers: Sudan Orange G (SOG), Tinuvin 326 (T326), and Tinuvin 384-2 (T384-2) were tested. The researchers observed that the photopolymer stability was better using a SOG absorber, which also exhibits

an intense absorption in the printer's light-emitting source (about 385 nm), leading to the 3D printing of embedded microfluidic chips (Figure 2-8.a). As a result of the fine selection of materials, the 3D printed chips were produced with a channel width of 800  $\mu\text{m}$  and a height of 600  $\mu\text{m}$  as well as with high optical transparency. The printed chip presented excellent resistance toward organic solvents such as dichloromethane (DCM), N, N-dimethylformamide (DMF), tetrahydrofuran (THF), toluene, acetone, and n-heptane.

In a curious work, Yeung et al. produced complex-shaped microfluidic chips composed of an array of hollow microneedles positioned at the devices' outlet end (Figure 2-8.b).<sup>389</sup> A commercial SL-3D printer (Form2) and a biocompatible commercial material (Dental LT clear), both from FormLab, were used for the precise and reliable fabrication of the microfluidic-enabled hollow microneedle devices. The devices were designed and printed with three separate inlet microfluidic channels that converge in one 3D spiral chamber. The incoming fluids are hydrodynamically mixed in this last chamber, emerging well-homogenized at the outlet where the microneedles (width between 800  $\mu\text{m}$  and 600  $\mu\text{m}$ , height below 1 mm.) are positioned. Through the channels (2 mm roughly), three-fluorochrome model-drug solutions were injected, and it was observed by *ex-vivo* confocal microscopy analysis that the developed devices were able to achieve the transdermal drug delivery to porcine skin. The authors reported that such systems might be applied in preclinical drug therapy situations, allowing the in-situ mixing and tuning of multiple drugs. Many works have also been reported utilizing custom-made photopolymers as alternatives to commercial printable materials. Chen et al. developed precise microfluidic flow-focusing chips with high-aspect-ratio using a commercial DLP-SL 3D printer (Perfactory 4, *Envisiontec*) machine and a commercial resin (HTM140) from the same company.<sup>390</sup> After optimizing the design and process parameters, the chips were successfully fabricated with a critical channel dimension of 200  $\mu\text{m}$  (Figure 2-8.c) that allowed the high-throughput synthesis of biocompatibility liposome nanoparticles (convenient for drug delivery applications), with tunable dimensions below 100 nm. The researchers asserted that higher-resolution printers could enable next-generation flow-focusing devices with smaller channels to synthesize even tinier lipid vesicles. Kuo et al. developed transparent and biocompatible microfluidic chips from a photocurable resin based on low-molecular-weight polyethylene glycol diacrylate (PEGDA, Mw 250), with 0.4 wt.% of phenyl bis(2,4,6-trimethylbenzoyl) phosphine photoinitiator (BAPO) photoinitiator and a photosensitizer, the isopropyl thioxanthone (ITX).<sup>147</sup> The ITX compound is a Type II photoinitiator that could start the polymerization process in the presence of a co-initiator, as explained in Chapter 1. However, in Kuo et al.'s work, no co-initiators were added in the custom-made resin, and the ITX was used as a UV absorber due to the high molar absorption at 385 nm, the printer's light-emitting source. The addition

of this compound neither affected the printed transparency of the microfluidic chips nor introduced unwanted coloration. The transparent chips were printed with the smallest microchannel width of 500  $\mu\text{m}$  and having surface pillars in the order of a single-pixel (27  $\mu\text{m}$ ) and sub-pixel (around 10  $\mu\text{m}$ ). The printed chips' biocompatibility was tested after a post-printing process to remove toxic and leachable components, investigating the cell viability and proliferation of Chinese hamster ovary (CHO-K1) with promising results.

Other interesting works have been reported using polydimethylsiloxane (PDMS)-based resins to produce 3D printed microfluidic devices through vat polymerization 3D printing with features similar to the conventional PDMS elastomers user conventionally for microfluidic chips fabrication: the Sylgard 184<sup>®</sup>. For instance, Bhattacharjee and coworkers developed an alternative approach for the conventional PDMS molding fabrication.<sup>391</sup> They created optically transparent PDMS-based microfluidic devices from a custom-made methacrylate-polydimethylsiloxane oligomer using a commercial desktop-SL 3D printer, see Figure 2-8.d. The printed PDMS-based devices presented similar characteristics to the standard Sylgard 184 PDMS elastomer used for microfluidic chip fabrication, and with channel dimensions down to 500  $\mu\text{m}$ . The researchers also performed a series of post-3D printing treatments to remove the unreacted products and improve the printed chips' biocompatibility. Indeed, these devices presented a promising cytocompatibility toward mammalian cell lines. More recently, Zips et al. presented silicone-hydrogel hybrid resins' preparation to produce flexible microfluidic devices with integrated valves, mixers, and chambers through a commercial stereolithography 3D printer.<sup>392</sup> The obtained microfluidic structures with internal channels with a minimum cross-section area of 450x500  $\mu\text{m}^2$ , reaching smaller channel dimensions when the printed chip is bonded (top and down) to a glass slide. As a proof of concept, the researchers used their 3D printed silicone-based microfluidic device to cultivate cardiac cells (cardiomyocyte-like HL-1) in a specifically-designed chamber inside the printed chip, showing that the cardiac cells retained their electrophysiological activity inside the silicone-based chamber. Although the different work presented in the last year related to VP-3D printed microfluidic devices, the range of application of such systems can be enhanced by adding functional groups into the printable photopolymer to exploit the chips' surface features. For example, by adding acrylic acid into an acrylate-based photopolymer, 3D printed fluidic devices can be produced with functional molecules on the channel surfaces.<sup>334</sup> BAPO photoinitiator (1 wt.%) and reactive orange dye as a light absorber (0.08 wt. %) were added into three different acrylate monomers: bisphenol A ethoxylate diacrylate (BEDA, Mn 512 g/mol), 1,6 hexanediol diacrylate (HDDA), poly(ethylene glycol) diacrylate (PEGDA, Mn 575 g/mol). By varying the acrylic acid concentration into the printable formulation, the authors were able to control the number of functional



carboxyl groups (COOH-) on the surfaces of the microchannels. The exposed carboxyl groups were then used to immobilize aminated bio-receptors inside the fluidic device chemically. The devices' usefulness was demonstrated by performing the enzyme-linked immunosorbent assays (ELISA) to detect protein biomarkers, angiogenesis-2. This biomarker plays a fundamental role in the onset of cancer and the progressive metastatic behaviors of tumors; therefore, such 3D printed devices may be used in the early diagnosis of cancer pathology in a less invasive therapy for the patient.

### **2.2.3. Photopolymerizable biomaterials for microfluidic chip fabrication through vat 3D printing.**

Although vat 3D printing is considered a robust candidate for microfluidic chip fabrication, there are still important aspects to investigate for correctly implement these printed microdevices in the biomedical field. Currently, most of these studies are addressed in developing more biocompatible photopolymers.<sup>134,393,394</sup> Considering the nature of printable photopolymers (either commercial or lab-made compounds), the obtained structures frequently contain unreacted chemical products (monomers, photoinitiators, and additives) after the printing step that are prominently toxic toward biological entities, hindering the full potential application in the biomedical field.<sup>395,396</sup> Looking to solve this, many researchers have reported the preparation of photosensitive formulations for VP-3D printing to obtain hydrogel-based structures.<sup>170,178,224,397,398</sup> Hydrogel's main characteristic is their great compatibility with biological units owing to their nature. These materials are prepared with biocompatible components and internally structured to uptake high water content (> 90 wt.%).<sup>399</sup> These characteristics make hydrogels one of the most attractive polymeric materials in recent times, especially in the biomedical field.<sup>400,401</sup> Although these materials might present fascinating bio-properties, their implementation for microfluidic devices' production has not been completely adopted since, due to their watery nature, these materials could interact undesirably with the fluids flushing through the microchannels made of hydrogels; in some cases, hydrogels might absorb part of the fluid, leading to structural changes of the chips.<sup>224</sup> Such a situation is highly noteworthy, suggesting on that the printed microfluidic devices need to operate with delicate aqueous-based analytes in cell culture or tissue engineering applications,<sup>402</sup> which could be solved by using hydrogel with partially hydrophobic characteristics.<sup>392</sup>

On the other hand, using fluidic platforms made with more dimensionally stable and water-free polymers could allow a better performance of such printed devices. From a materialistic perspective, these materials (either

thermoplastic or thermoset) have been widely studied for microfluidic device production through 3D printing, as presented in previous sections. However, more and more attention is being paid to improving the biocompatibility of such water-free structures.<sup>403,402</sup> Moreover, other factors to consider for the correct implementation of a printed microfluidic chip are mechanical properties, structural and chemical stability, and practical optical features, according to the application.<sup>77</sup> In this frame, diverse commercial photopolymers marketed as a biocompatible have been reported,<sup>404</sup> e.g., BioMed Clear and Dental LT Clear resins from Formlabs, AccuraClear Vue and Accura SL Y-C 9300 resins from 3D Systems, and E-Guard and E-Dent resins from Envisiontec,<sup>378,405</sup> however, only a few studies have been carried out related to the material-biological unit interactions. For instance, a detailed characterization of four commercially available photopolymers: Clear, High Temp, Dental SH, and Dental LT clear photopolymer (all from Formlab company) were carried out by Piironen et al. for studying the compatibility toward cell lines.<sup>406</sup> They concluded that even if a commercial resin is ISO-certified as biocompatible, it does not imply an adequate cell interaction of the printed parts. They concluded that more critical is performing a post-printing procedure on the printed parts to guarantee a normal cell proliferation and reduced cell death. The researchers sterilized the parts by autoclaving (where the material must present good thermal stability), enhancing even the cell-biocompatibility of the polymeric obtained from a resin that is not considered biocompatible: The High Temp resin. Dental SG was found to be the most suitable for long-term 3T3 cells and hepatocytes and hiPSCs cultivation.

Macdonald and coworkers tested and compared two of the most diffused commercial photopolymers for vat 3D printing: the Watershed 11122XC and Fototec SLA 7150 Clear resins, with two commercial resins marketed as biocompatible: the VisiJet Crystal EX200 used in PolyJet methods and ABSplus P430 filament used in FFF printing methods.<sup>407</sup> In their work, published in 2016, they evaluated each of the polymeric 3D printed parts' cytotoxicity as a function of post-treatment procedures toward zebrafish embryos. The researchers determined that all the just 3D printed parts (with any post-treatment) resulted in cytotoxic. After performing a suitable post-printing protocol (washing in different high-grade ethanol), only the parts obtained from Fototec SLA 7150 (not distributed as biocompatible) resulted in higher compatibility with biological entities. The results obtained in the Macdonald et al. works were noteworthy since they showed that polymers certified as biocompatible (USP Class VI) such as VisiJet and Watershed are unsafe for biological units (zebrafish embryos). The biocompatibility of them might be somehow improved only after a post-printing treatment. Kreß and coworkers reached a similar conclusion in a more recent paper issued in 2020.<sup>408</sup> They tested the cytotoxicity toward Human mesenchymal stem cells (MSCs) of six (6) commercial resins distributed for Formlabs: High Temp, Clear, Dental SG,

Dental LT, Black, and Flexible resins, determining that none of them should be considered as noncytotoxic, even if materials, such as dental resins is marketed as a biocompatible. In their work, the researchers opted to cover the pieces with Parylene to protect the MSCs from toxic components and enhance the printed parts' biocompatibility. While Rimington et al. demonstrated, in 2018, that the Clear-FL resin from Formlabs could partially support the proliferation of skeletal muscle (C<sub>2</sub>C<sub>12</sub>) cell line but, at the same time, resulted in being toxic to neuronal (SH-SY5Y) and hepatic (HepG2).<sup>409</sup> They suggest that more attention must be paid to the post-printing procedures for reducing the leaching of toxic compounds from the printed parts. Thus, the printed parts need to be subjected to specific procedures for enhancing their biocompatibility to a satisfactory level, as reported in other studies.<sup>410,411</sup> Nevertheless, even if a suitable post-printing procedure is followed, the lack of detailed information about the chemical composition of the commercial photopolymers from the supplier further complicates the possibility of predicting the performance of the printed parts toward biological entities. Herein, the growing interest in developing custom-made photopolymers for vat polymerization 3D printing with biocompatibility features.<sup>105,412</sup> Starting from a lab-scale study, knowing the photopolymer's real composition could be more intuitive to anticipate the performance and the interaction of the printed parts towards specific biological entities. It is possible to formulate photopolymers to obtain 3D printed parts with adequate biocompatibility and reduced cytotoxicity, which could be foreseen as biocompatible materials for advanced applications after standard treatment validations.<sup>38,403</sup>

In this frame, some researchers have studied the biocompatibility of polymeric 3D printed parts obtained from custom-made photopolymers. For example, in 2020, Warr et al., from Nordin's research group, demonstrated printed parts from a resin based on low-molecular-weight polyethylene glycol diacrylate (PEGDA, MW 258) resin containing 1 wt.% of BAPO and 0.38% wt.% of avobenzone UV absorber was noncytotoxic toward endothelial cells (EA.hy926). The researchers observed good biocompatible results even from printed parts without any post-printing treatment. In contrast, a PEGDA258-based photopolymer containing 2 wt.% of nitrophenyl phenyl sulfide (NPS) UV absorber can be made noncytotoxic after 12 hours of washing in ethanol for removing the excess of the toxic NPS.<sup>403</sup> The noncytotoxic effect of the PEGDA resin with avobenzone was illustrated by forming spheroids (from different cell lines: A549, EA.hy926, and lung fibroblast) in a non-adherent printed well, where a spheroid adhesion was observed only on the surfaces after short plasma treatment. Urrios and coworker performed an analogous test in 2016, using a PEGDA-based resin for the long-term culture of adherent mammalian cells.<sup>413</sup> The parts' biocompatibility toward the cell line was enhanced after performing UV-post curing of the printed parts submerged in a water bath for removing the unreacted agents. The biocompatibility of other

(meth)acrylate resins was evaluated by Männel et al. for producing polymeric 3D printed parts using a  $\mu$ SL-3D printer.<sup>402</sup> They tested resins such as poly(ethylene glycol) methyl ether methacrylate (PEGMEMA, Mn 500 g/mol), tri(propylene glycol) diacrylate (TPGDA, Mn 300.55 g/mol), 2-phenoxy ethyl acrylate (POEA, Mw 192.21 g/mol) and PEGDA (Mn 575 g/mol). The TPO photoinitiator and Sudan 1 dye were used, also 1,3,5-Triallyl-1,3,5-triazine-2,4,6(1H,3H,5H)-trione (TATAO) as a crosslinker in the case of monofunctional monomers. The cytotoxicity of the printed parts was evaluated toward human umbilical vein endothelial cells (HUVECs). By implementing appropriate post-processing steps, unpolymerized products were removed, but the cell viability was hindered for the release of Sudan 1. They noticed that a combination of PEGDA and PEGMEMA was the most suitable composition observing a cell proliferation after five (5) days of culture.

As explored by different researchers, by performing appropriate post-printing procedures, the biocompatibility of the polymeric printed parts could be considerably increased by removing or reducing the unreacted and potential cytotoxic products. This strategy has been followed in multiple studies and will still be pursued to sterilize the printed parts, becoming another aspect to consider for improving the photopolymer's bio-characteristics (commercial or custom-made).<sup>71,414</sup> Though the printed objects' bio-functionality can also be enhanced by performing particular post-3D printing protocols to modify their surface properties. Instead of "passivating" the parts' surface, carried out to avoid undesirable biological effects by eliminating the potentially cytotoxic elements from the printed object, the parts can be "activated" by coupling functional groups on their surfaces. These functional groups might be active biological molecules such as antibodies, peptides, nucleic acids, or biocompatible compounds to promote biological interactions such as carboxylic acid groups or thiols. As proposed by Männel and coworkers in their work, the bioproperties 3D printed parts might be significantly enhanced if RGD tripeptides (composed of arginine, glycine, and aspartate) are incorporated in the photosensitive resin rather than performing post-printing procedures.<sup>402</sup> By adding Br-containing vinyl-terminated initiator into a commercial UV curable resin, 3D printed objects with modifiable surfaces can be obtained.<sup>415</sup> This promotes polymer brushes' growth via surface-initiated atom transfer radical polymerization (SI-ATRP) that can be potentially used in the biomedical field. Other researchers developed 3D printed microcantilevers (MCs) for mass-biosensing by adjusting active carboxylic groups' content on the 3D cantilevers. The devices were produced varying concentrations of acrylic acid added in a monomer in the photopolymer. The obtained structures were successfully employed for an easy enzymatic functionalization.<sup>416</sup>



## Chapter 3

# 3D printing fluidic devices:

Design, fabrication, and testing protocols.

### 3.1. Outline and motivation.

In recent times, one of the biomedical branches having a high development growth is related to microfluidic platforms' development to perform accurate chemical and biological analyses, e.g., drug screening.<sup>337</sup> These devices are produced with a series of channels (on the milli- or microscale) designed to transport biological or chemical fluids on a much smaller range than current laboratory protocols; this allows savings in sample consumption, instrument size, and general costs.<sup>280,281,283</sup> Nevertheless, the spreading of these microfluidic devices is somehow limited by their current manufacturing process, including subtle and laborious methods such as etching of silicon and glass, SU-8 photolithography, and soft lithography of polydimethylsiloxane (PDMS), injection molding, and hot embossing.<sup>406</sup> For these reasons, their production is now constrained to specialized research laboratories with dedicated facilities, such as clean rooms.

The 3D printing of polymeric materials has recently emerged as an alternative for manufacturing precise fluidic devices in a cost-affordable and easier way.<sup>147,417</sup> Polymeric 3D printing might change microfluidic devices' fabrication procedure by decreasing costs and time of production and allowing

the manufacturing of complex-shaped and three-dimensional microdevices. Among the 3D printing methods for polymers, vat polymerization (VP) techniques, such as stereolithographic (SL) and digital light processing (DLP), offer higher spatial resolutions, faster printing times, and greater accuracy compared to other polymeric printing techniques such as FFF, SLM, or inkjet printing.<sup>171,364</sup> Furthermore, VP techniques allow the production of functional structures by combining and tailoring the appropriate components (monomers/oligomers, photoinitiators, and dyes), which might offer multiple possibilities in the bioengineering area.<sup>99</sup> By customizing the printable material, 3D printed microfluidic structures can be obtained with specific surface or bulk features with biomedical interest, comprising other interesting features such as transparency, water and gas permeability, flexibility, and biocompatibility. Though, developing fluidic systems through VP-3D printing having these properties is a challenging task, which has led researchers to study several types of printable photopolymers, ranging from commercially available resins to lab-made formulations acting on various post-printing protocols as well. Therefore, in this chapter, the development of tailor-made photocurable resins will be presented to obtain structures with specific bio-properties through vat polymerization 3D printing methods. Such features of biomedical interest could be further enhanced by performing adequate post-printing treatments.<sup>105,245,418</sup>

Part I of chapter 3 explores the cytocompatibility of 3D printed parts made from custom-made photocurable formulations. The main objective is to study the biocompatibility of transparent structures obtained through a commercial DLP-3D printer from acrylate-based printable formulations. These objects' biocompatibility will be investigated toward cell lines by adjusting the resins' composition and performing a series of post-printing procedures for removing unreacted and potentially toxic products. The printable photopolymers are prepared using commercially available acrylate-based resins, widely employed in vat polymerization 3D printing. Here, it will be aimed to enhance the cytocompatibility of these 3D printed structures. Part II of chapter 3 reports the photopolymer's preparation based on acrylate-polydimethylsiloxane (PDMS) resin to fabricate complex-shaped microfluidic chips composed with three-dimensional channels through digital light processing 3D printing. By adequately preparing the acrylate-PDMS-based photopolymer, microfluidic chips with good optical characteristics, high chemical strength, and suitable mechanical features might be obtained. Different photopolymers will be developed and studied through the two parts of the chapter intending to produce bespoke 3D printed parts that can deliver different characteristics according to the formulation's composition. Each photopolymer offers distinct features that could be employed, for example, to 3D print multi-material fluidic systems, as depicted in Figure 3-1, where specific regions of the devices might display different surface properties. The

correct integration of these resins could contribute to developing fluidic platforms for automated study in chemistry or biology.<sup>404</sup>

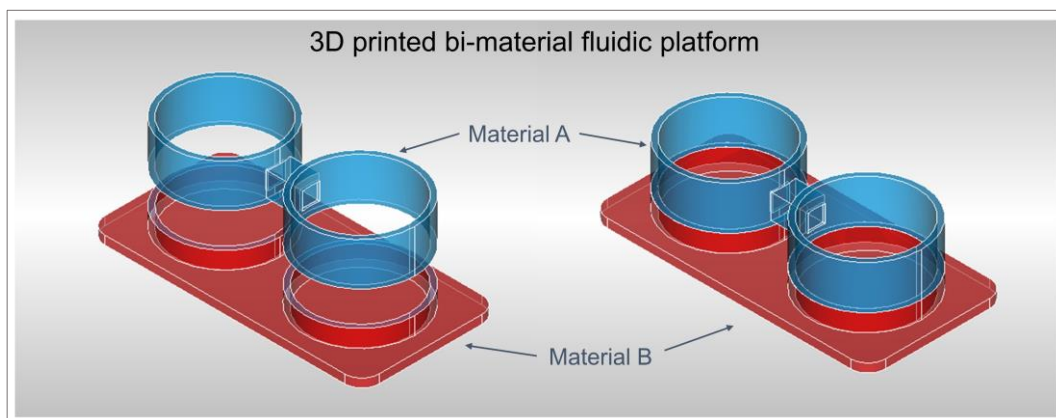


Figure 3-1. **CAD design representation of a multi-material fluidic chip.** The device consists of two wells connected with a millifluidic channel (1 mm diameter).



### 3.2. Part I: Biocompatibility of 3D printable conventional resins.

Part I of Chapter 3 is based on the original research article titled "*Materials testing for the development of biocompatible devices through vat-polymerization 3D printing.*" The paper was published in the scientific journal *Nanomaterials* in the special issue "3D Printing and Nanotechnology in Biology and Medical Applications" from Multidisciplinary Digital Publishing Institute (MDPI), **ISSN: 20794991**.<sup>419</sup>

This part of the chapter will introduce a procedure to 3D print biocompatible parts using some of the most diffused materials (monomers and a photoinitiator). These materials are selected since they have been widely used for light-based 3D printing with outstanding results;<sup>148,150-153,275,420-422</sup> though, the work presented here focuses more on improving the biocompatibility of such 3D printed parts. Different photopolymers will be prepared using acrylate monomers: bisphenol A ethoxylate diacrylate (BEDA), polyethylene glycol diacrylate (PEGDA250), and 1,6-hexanediol diacrylate (HDDA). As a photoinitiator, a phosphine oxide-based (BAPO) compound was selected, which adequately absorbs within the 3D printer's emission wavelength at 405 nm (see Figure 3-10.a). BAPO is not considered a biocompatible substance, such as Lithium phenyl-2,4,6-trimethyl benzoyl phosphinate (LAP),<sup>128,423</sup> though, it demonstrated BAPO might show low toxicity effects on cells when added in adequate concentrations.<sup>413,424,425</sup> Moreover, the components selected for this work have been previously used to prepare commercial photopolymers for VP-3D printing, such as E-Dent 100 (Envisiontec) or MED620 (Stratasys). These commercial mixtures have been certified by the European Union (ISO 13485) and authorized by the FDA (Food and Drugs Association) from the United States of America.<sup>217,426,427</sup> For carrying out the investigations, polymeric parts with geometry similar to multiwell plates (96 and 24 well-like dimensions) will be fabricated through VP 3D printing from each acrylate-based photopolymer. The biocompatibility of the printed wells will be investigated toward A549 cell lines as a function of the photopolymer composition and the type of post-3D printing protocols, including washing steps in common solvents and UV post-curing treatments.<sup>105,245,418</sup> The selection of suitable materials and the development of an adequate post-printing protocol might be fundamental for producing biocompatible devices.

### 3.2.1. Experimental section.

#### *Materials and chemicals*

The reactive monomers used are broadly used for VP 3D printing applications: bisphenol A ethoxylate diacrylate (**BEDA**,  $M_n \sim 512$  g/mol, EO/phenol 2), polyethylene glycol diacrylate (**PEGDA250**,  $M_n = 250$  g/mol), and 1,6-hexanediol diacrylate (**HDDA**,  $M_w = 226.3$  g/mol) were used. The phenyl bis(2,4,6-trimethylbenzoyl)phosphine oxide photoinitiator (**BAPO**, 97 %) was used since it adequately absorbs the 3D printer emission wavelength at 405 nm. Acetone ( $\geq 99.5\%$ ) and ethanol (EtOH, 99.8 %) solvents were also used for the different washing/sonication steps. All reagents and substances were purchased from Merck Company (Darmstadt, Germany) and used as received. The chemical structures of the components used for the photopolymers' preparation are shown in Figure 3-2.

#### *Preparation of the acrylate-based printable resin*

The printable formulations were prepared by adding a certain BAPO photoinitiator concentration to each acrylic monomer. Then, each mixture was sonicated for 30 minutes. In total, six formulations were prepared, and the composition and nomenclature of each of them are shown in Table 3-1.

#### *Digital light processing DLP-3D printing*

An Asiga PICO 2 DLP-3D printer was used for processing the photopolymers. The light source of the printer is based on LEDs that emit at 405 nm. The 3D printer characteristics are minimum nominal XY pixel resolution of 50  $\mu\text{m}$ , Z-axis control of 1  $\mu\text{m}$ , light intensity up to 3  $\text{mW}/\text{cm}^2$ . For the experiments, the slice thickness was set at 50  $\mu\text{m}$ , and the light intensity at 20  $\text{mW}/\text{cm}^2$ . The irradiation times used to 3D print each formulation are shown in Table 3-1. All CAD designs were produced with the FreeCAD program and exported in STL format. After the printing step, different post-3D printing protocols were tested, as detailed below.

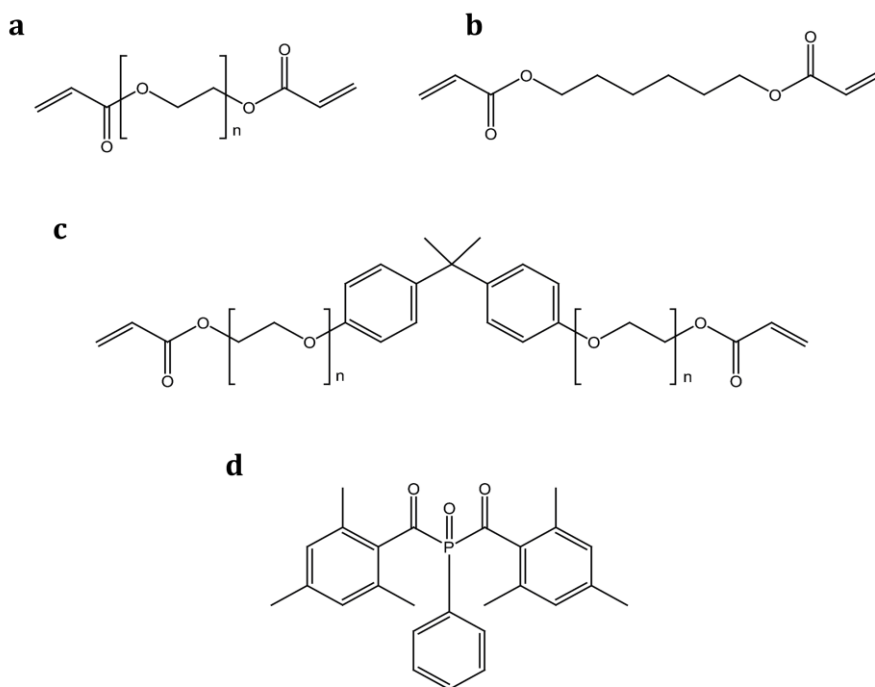


Figure 3-2. **Chemical structures of the chemical reagents used.** (a) polyethylene glycol diacrylate (PEGDA250), (b) 1,6-hexanediol diacrylate (HDDA), (c) bisphenol A ethoxylate diacrylate (BEDA), and (d) phenyl bis(2,4,6-trimethylbenzoyl)phosphine oxide (BAPO).

### *Washing and UV post-curing protocols*

The 3D printed structures obtained from each acrylate-based formulation were subjected to washing procedures in either ethanol or acetone. In this way, the unreacted products can be removed from the parts, potentially improving their cytocompatibility. Four different washing protocols were established, identifiable into two main categories, detailed as follows:

1. *Sonication procedures:* each sample was sonicated for five (5) minutes in either ethanol or acetone, followed by five 5 minutes of UV post-curing on the part's inner side and five (5) more minutes on the outer side. After the UV post-curing, the samples were kept overnight (o/n) in the same solvent used for sonication.
2. *Incubation procedures:* each sample was incubated for 2 hours in either ethanol or acetone, followed by five 5 minutes of UV post-curing on both sides of the samples.

### *Sterilization protocols*

Three different sterilization methods were performed on each of the printed samples, intending to select the most suitable method for the investigation purpose. The sterilization procedures were:

1. The samples are exposed to UV light for 30 minutes inside a biosafety cabinet.
2. The samples are immersed for 10 minutes in ethanol (70% v/v).
3. The samples are autoclaved for 20 minutes at 121 °C, following an air-drying at room temperature.

### *Characterization methods*

The Viscosity measurements were performed in parallel-plate mode using an Anton Paar rheometer (Physica MCR 302) at a constant temperature of 25 °C. The space between the two parallel plates was established at 50  $\mu\text{m}$ , and the shear rate range was from 1 to 100  $\text{s}^{-1}$ . The plates were of aluminum with a diameter of 20 mm.

Real-time photo-rheological tests were performed to measure the changes in the viscoelastic material properties during polymerization. The experiments were carried out using an Anton Paar rheometer (Physica MCR 302) configured in parallel mode with the lower plate consisting of 20 mm quartz and the upper parallel plate consisting of 20 mm aluminum. A Hamamatsu LC8 lamp was used to study the photopolymerization process. It is equipped with a visible bulb and a cutoff filter below 400 nm, and an 8 mm light guide. During the tests, the light irradiation was initiated after 60 seconds to stabilize the system before the photopolymerization process (light intensity set at 20  $\text{mW}/\text{cm}^2$ ). The gap between the two parallel plates was set at 50  $\mu\text{m}$ . The measurements were performed at a constant temperature (25 °C), at a constant strain amplitude of 1%, and a constant shear frequency of 1  $\text{rad}/\text{s}$ . The viscoelastic moduli variations of the resin upon light irradiation were measured against exposure time.

UV-vis spectroscopy measurements were conducted using a Synergy™ HTX Multi-Mode Microplate Reader instrument (BioTek, Winooski, Vermont, USA) set in spectrum mode range between 300–700 nm and at a scan step of 10 nm. The experiments on solid films were performed on 3D printed disks (thickness 50  $\mu\text{m}$ , diameter 20 mm) and introduced in a 6-well plate, and as a control, empty wells without polymeric material were used. Moreover, the UV-vis spectrometer was used to analyze the extracting chloroform solutions used for evaluating the insoluble fraction; in this case, pure chloroform was used as a blank solvent.

The insoluble (or crosslinked) fractions of the samples were obtained following the standard ASTM D2765–84 test procedure.<sup>428</sup> The samples were kept in a metal mesh, precisely weighed, and later submitted to extraction with chloroform (CHCl<sub>3</sub>) for 24 hours at room temperature to remove the unbounded components. Then, the samples were dried overnight at 80 °C, and the insoluble fraction percentage was determined as the weight difference before and after solvent extraction (relative error = ±1%).

An FT-IR spectrometer (Nicolet iS50, Thermo Scientific, Milano, IT) was used to calculate the acrylate double bond conversion on both liquid photopolymers and polymerized objects. The spectra were collected on an attenuated total reflectance (ATR) system (Smart iTX). The formulations were irradiated using a visible portable lamp (Hamamatsu LC8 lamp) at a 20 mW/cm<sup>2</sup> of light intensity. Spectra of 3D printed samples as printed and after different UV post-curing treatments were also collected. For the FTIR experiments, the spectra were recorded with a resolution of 4 cm<sup>-1</sup>, averaging 32 scans for each spectrum, wavenumbers range 650 – 4000 cm<sup>-1</sup>. The acrylate double bond (C=C) conversion was monitored by following the peak at 1409 cm<sup>-1</sup>, corresponding to the scissoring acrylate vibration. The acrylate signals were normalized using the constant signal at 1725 cm<sup>-1</sup>, corresponding to the carbonyl (C=O) peak.

A microscope (Eclipse Ti2 Nikon) equipped with a Crest X-Light spinning disk confocal microscope and a Lumencor SPECTRA X light engine was used for the collection of bright-field and fluorescence images. All images were displayed using the same scaling and were collected using a Plan Apo 20×0.75 NA (Nikon).

FEI Quanta 3D FEG Dual Beam Microscope was used to collect the Environmental Scanning Electron Microscopy (ESEM) images. This instrument allows operating in environmental conditions, which avoids thus the metallization of the sample. In detail, samples were observed at 5 kV and a chamber pressure of 60 millibars of H<sub>2</sub>O vapor. The cells were seeded into the 3D printed wells (inner diameter = 16.5 mm, cell number = 100 000), and after 48 hours, the samples (with cells) were prepared for SEM microscopy. The samples were washed twice with PBS, and then they were incubated with 2% glutaraldehyde in PBS for 1 hour at room temperature. After this incubation, the samples were dehydrated using increasing ethanol content: water (50%, 70%, 85%, and 100%) for 15 minutes each. At last, the samples were air-dried.

### *Cell culture*

Cancer cells (A549 lung epithelial cells) were used for cell culture tests. A549 cells are human alveolar basal cells that have been selected for this work since they are usually used for lung tumor studies in the development of drugs

against carcinomas entities.<sup>429,430</sup> The cells were maintained in RPMI 1640 medium, supplemented with 10% fetal bovine serum, 1% penicillin/streptomycin (all from Sigma Aldrich), and two mM glutamine (from Biowest). The cells were kindly provided by Valentina Monica, from the Department of Oncology, University of Torino, AOU San Luigi Gonzaga. The cell culture assays were performed in the biomedical engineering laboratories (Polito<sup>BiO</sup> Med Lab) by Désirée Baruffaldi (Ph.D. candidate) and Cinzia Martinengo (Postdoctoral research fellow), both from Polytechnic of Turin. Cell morphologies were evaluated, when necessary, with a phase-contrast microscope (DMi1, Leica Microsystems GmbH).

### *Cell viability and proliferation*

All samples were incubated overnight (o/n) before the cells seeding in deionized water at room temperature and then sterilized for 30 minutes under a biological hood's UV light. Live/dead fluorescence assays (Sigma Aldrich) were performed to evaluate the number of viable cells in culture. For live/dead staining tests,  $1 \times 10^5$  A549 cells were sowed into each of the 3D-printed wells, and the cell viability was assessed after 72 hours. The cells were washed three (3) times with PBS, and then they were dyed with  $1,5 \mu\text{M}$  Propidium Iodide (PI) and  $1 \mu\text{M}$  Calcein-AM for 15 minutes at room temperature. As a control, A549 cells were also seeded and analyzed into a conventional PS. The fluorescence images were obtained from a spinning disk confocal microscopy system.

Moreover, for the MTT assay, A549 cells ( $1.5 \times 10^4$ ) were seeded into each wells-type at  $37^\circ\text{C}$  of incubation in a complete medium. The medium was removed after 24 hours and 48 hours of incubation, and  $125 \mu\text{l}$  of fresh medium and  $125 \mu\text{l}$  of  $1 \text{ mg/ml}$  MTT (dissolved in PBS) were both added in each well and incubated for two more hours at  $37^\circ\text{C}$ . After incubation,  $250 \mu\text{l}$  of MTT solvent (10% SDS, 0.01 M HCl in H<sub>2</sub>O) was added to solubilize the formazan crystals, and the plate was incubated for two hours at  $37^\circ\text{C}$ . Synergy™ HTX Multi-Mode Microplate Reader (BioTek, Winooski, Vermont, USA) was used to read the optical density (OD) at a wavelength of 570 and 650 nm. As a control, blank media without polymeric material were used. The colorimetric signal in absorbance is proportional to the proliferating number of cells. Error bars show mean SD.

### 3.2.2. Results and discussion.

#### *3D printing and material characterization*

The reagents used in this work have been reported for vat polymerization 3D printing photopolymers with great results, presenting inherent biocompatible features, some of them.<sup>217,426,427</sup> Nonetheless, this study intends to study the 3D printed parts' biocompatibility after performing different post-printing protocols to remove the possibly toxic unreacted products. To establish the appropriate 3D printing settings and thus obtain a properly manufactured 3D printed object, it is essential to perform a series of preliminary tests. These include viscosity, reactivity, and degree of conversion, among others. The viscosity of the resin is the first characteristic to evaluate. As demonstrated in previous work, high viscosity resins could hinder the objects' fabrication process in the printing step.<sup>38,79</sup> Accordingly, photosensitive photopolymers with relatively low viscosity values are preferred for the accurate and fast production of solid three-dimensional pieces. PEGDA250, HDDA, and BEDA monomers have been widely used for light-based 3D printing; however, here, all formulations' viscosity was briefly evaluated, data reported in Table 3-1. The viscosity for PEGDA250 and HDDA monomers (at both 0.2 and 1 wt.% of BAPO concentration) were similar and lower than the BEDA monomer. Those values are suitable for vat polymerization techniques since they were lower than usually used commercial SL or DLP printers' viscosity values.<sup>148,380,416</sup> The following step was to evaluate the photopolymer's reactivity through real-time photorheology methods, in which the changes in viscoelastic properties, the storage modulus ( $G'$ ), are measured against irradiation times. Figure 3-3.a, the  $G'$  curves relative to the PEGDA250, HDDA, and BEDA monomers with either 0.2 wt.% and 1 wt.% of BAPO photoinitiator are reported. Once the visible lamp was switched on, all formulations presented high reactivity with a sudden increase of  $G'$  in the first 2 seconds. The formulations with lower photoinitiator amounts presented a slight delay of the reaction onset, as anticipated, which is better appreciated in Figure 3-3.b. Consequently, P-0.2, H-0.2, and B-0.2 formulations (those with lower BAPO concentration) will need prolonged light irradiation times during the printing stage to cure a layer of the same thickness than formulations with higher BAPO amount, P-1, H-1, and B-1.

Table 3-1. Composition and nomenclature of the home-made acrylate resins, average viscosity values at 25 ° C, 3D printing settings used for each formulation with a slicing thickness of 50  $\mu$ m, insoluble gel fraction (%), and acrylate conversion of the 3D printed objects.

Composition	Nomenclature	Viscosity	Exposure time	Initial exposure time	Acrylate conversion	Insoluble fraction
		(Pa.s) <sup>a)</sup>	(s/layer)	(s/layer) <sub>b)</sub>	(%)	(%) <sup>c)</sup>
PEGDA250 + 0.2 wt.% BAPO	P-0.2	0.018	1.5	3	88	98
HDDA + 0.2 wt.% BAPO	H-0.2	0.019	1.5	3	85	99
BEDA + 0.2 wt.% BAPO	B-0.2	0.071	2	3	72	95
PEGDA250 + 1 wt.% BAPO	P-1	0.018	1	2	89	99
HDDA + 1 wt.% BAPO	H-1	0.020	1	3	89	99
BEDA + 1 wt.% BAPO	B-1	0.073	1.5	2	78	96

<sup>a)</sup> average viscosity calculated between 1 and 100 s<sup>-1</sup> of shear rate.

<sup>b)</sup> irradiation times for the first three layers to guarantee an adequate adhesion of the parts.

<sup>d)</sup> insoluble gel fraction of 3D printed parts calculated after 24 h of extraction in chloroform.

The data obtained from these preliminary experiments was used to correctly 3D print the desired objects. 96- and 24-wells-like structures were printed (using the printing parameter reported in Table 3-1) with dimensions of inner diameters of 16.5 mm and 5.6 mm respectively, and 300 μm thickness bottom both (Figure 3-4.a). Figure 3-4.b shows only the photograph of 24-well-like 3D printed parts, and in Figure 3-4.c,d, they are compared to a conventional 24-multiwell plate. Noteworthy the more yellow color of samples with 1 wt.% of BAPO compared to samples with 0.2 wt.% of BAPO, which is caused by the higher concentration of photoinitiator. Even though samples at both BAPO concentrations displayed good optical characteristics (with the possibility of reading through the bottom of the well in Figure 3-4.b), the slight yellow coloration that samples with 1 wt. % of BAPO might hinder the correct cell's reading in the subsequent optical studies. Besides, the excess BAPO in the sample could have toxic effects on cells, as reported in the literature.<sup>424,425</sup>



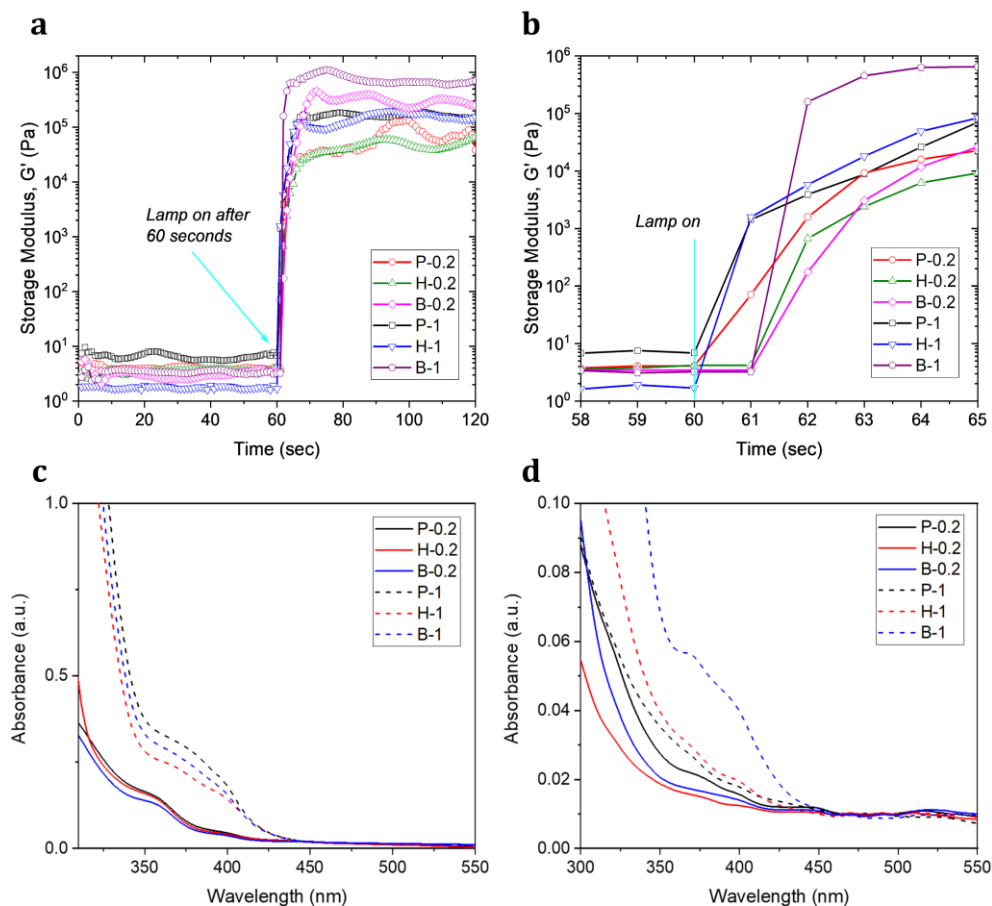


Figure 3-3. **Characterization of the six different acrylate resins.** (a) Storage modulus ( $G'$ ) versus irradiation time, where is observed the similarities between reaction times of PEGDA250, BEDA, and HDDA resins with 0.2 or 1 wt.% of BAPO. (b) Zoomed  $G'$  curve once the visible lamp is on. (c) UV-vis spectra collected on 100  $\mu\text{m}$  thick printed disks made of PEGDA250, BEDA, and HDDA resin with 0.2 wt.% (continue lines) and 1 wt.% (dashed line) of BAPO. The curves show a greater shoulder (related to the BAPO photoinitiator) between 350 and 420 nm for samples with the higher (1 wt.%) content of the photoinitiator, indicating more leaching out of the unreacted BAPO. (d) recorded UV-Vis spectrum from the extracting solvent used to calculate the insoluble gel fraction of the 3D printed parts, showing a higher released BAPO photoinitiator.

The 3D printed wells' transparency at both BAPO concentrations was further evaluated by using a microplate reader set up in the UV-vis scanning mode, results shown in Figure 3-3.c. As expected, the samples with higher BAPO amount, P-1, H-1, and B-1, revealed a broader absorption band from nearly 350 to 430 nm, which is associated with the BAPO compound.

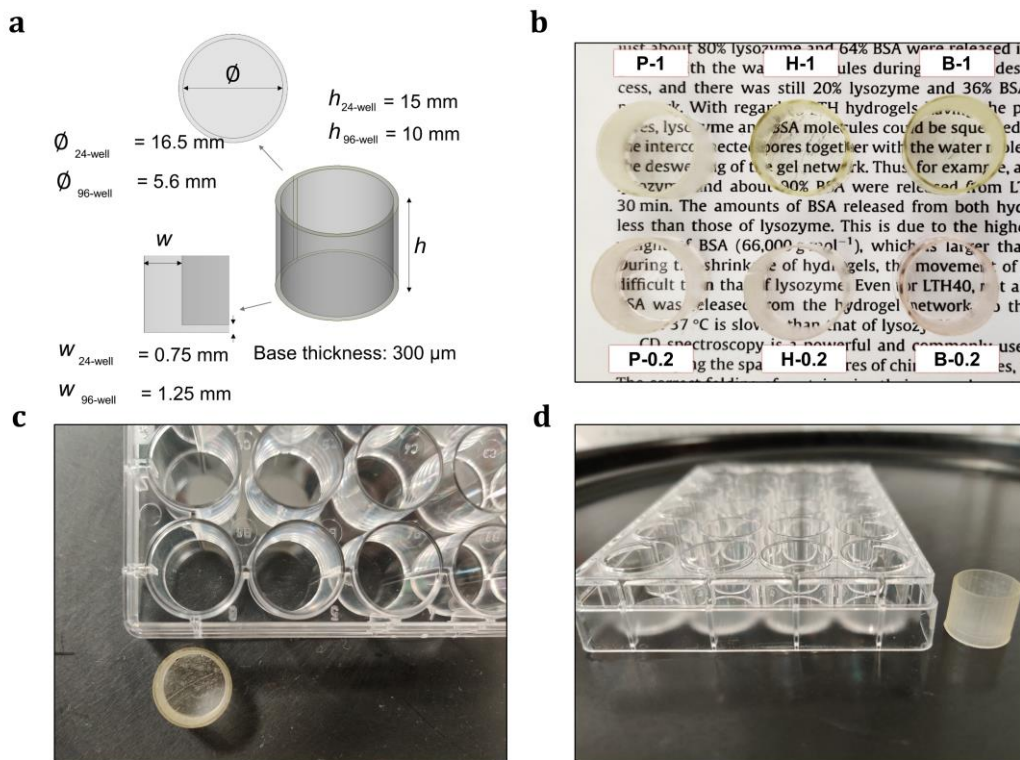


Figure 3-4. **CAD model and photographs of the printed wells.** (a) Isometric view of the CAD model showing the dimensions of 24- and 96-well-like designs. (b) Photograph of the 3D printed 24-well-like objects from each prepared acrylate-based photopolymer, showing the good transparency of the bottom of the well. (c) Top-view and (d) frontal-view of a 3D printed 24-well-like object (P-0.2) compared to a 24-multiwell plate.

The insoluble fraction of 3D printed samples was evaluated by following the standard test method ASTM D2765–84.<sup>428</sup> The test consists of subjecting the samples to chloroform extraction for 24 hours. The results are reported in Table 3-1. Despite the disparities in acrylate conversion, the insoluble fraction of the printed samples resulted in similar and relatively high for all of them, with only a slightly lower value for samples with 0.2 wt.% of BAPO. It is worth emphasizing that the extracted weight can be composed of both unbounded monomer and the photoinitiator. However, both elements may result in cytotoxic, so it would be preferable to eliminate this component. This point will be investigated more in detail by examining the post-processing step. The chloroform used for the insoluble fraction tests was later examined by UV-visible spectroscopy to evaluate the presence of any unreacted products released from the 3D printed parts. The results are plotted in Figure 3-3.d. As observed, an absorption shoulder appeared at around 350-430 nm for samples with the highest BAPO concentration. The latter might result in a higher content of unbounded general products (monomers and photoinitiators) after the printing step, particularly for B-1 samples.

### *Cytotoxic effect of 3D printed wells toward A549 cells.*

The MTT assay was performed to investigate the cell proliferation on 3D printed samples. The test was performed based on the prepared photopolymers composition and the different pots-printing processes. The A549 cells were also seeded in PS wells and considered as a positive control. The 3D printed wells were washed and sterilized following the specific protocols described in the Experimental section, then  $1.5 \times 10^4$  A549 were seeded on each sample and cultured for a maximum of 48 hours (Figure 3-5.a-c). All samples showed no significant differences in A549 cell proliferation after 48 hours, independently by the BAPO concentration. It could probably be associated with the washing steps' effectiveness, which allowed the removal of the unreacted products. Nevertheless, the samples with 0.2 wt.% of the BAPO photoinitiator were selected for the next experiments intending to use less reagent and minimize possible BAPO toxicity, as reported by previous works.<sup>424</sup>

For formulations with 0.2 wt.% of BAPO, the cell viability diverges considerably depending on the starting acrylic resin used. The cell viability after 24 hours was relatively low for B-0.2 despite the washing protocols used. Better results were obtained for H-0.2 and P-0.2 samples. In particular, samples subjected to the washing protocols defined as sonication (i.e., 5 minutes sonication into a solvent, 10 minutes UV post-curing (5 minutes by part's side), and overnight in the same solvent) showed a more pronounced cell proliferation after 24 and 48 hours compared to incubation method. This tendency indicates that cell proliferation was viable, and the 3D-printed substrates resulted in being in non-cytotoxic. Nonetheless, although the MTT assay indicated that sonicated H-0.2 samples resulted in being the most suitable materials, they presented low resistance to the solvents during washing protocols (see Figure 3-5.d), making an incline selecting the P-0.2 for the following analysis. Comparing the P-0.2 samples sonicated either in ethanol or acetone, the samples from ethanol were preferred since excellent optical transparency was obtained after the washing step, which is a crucial characteristic for optical monitoring.

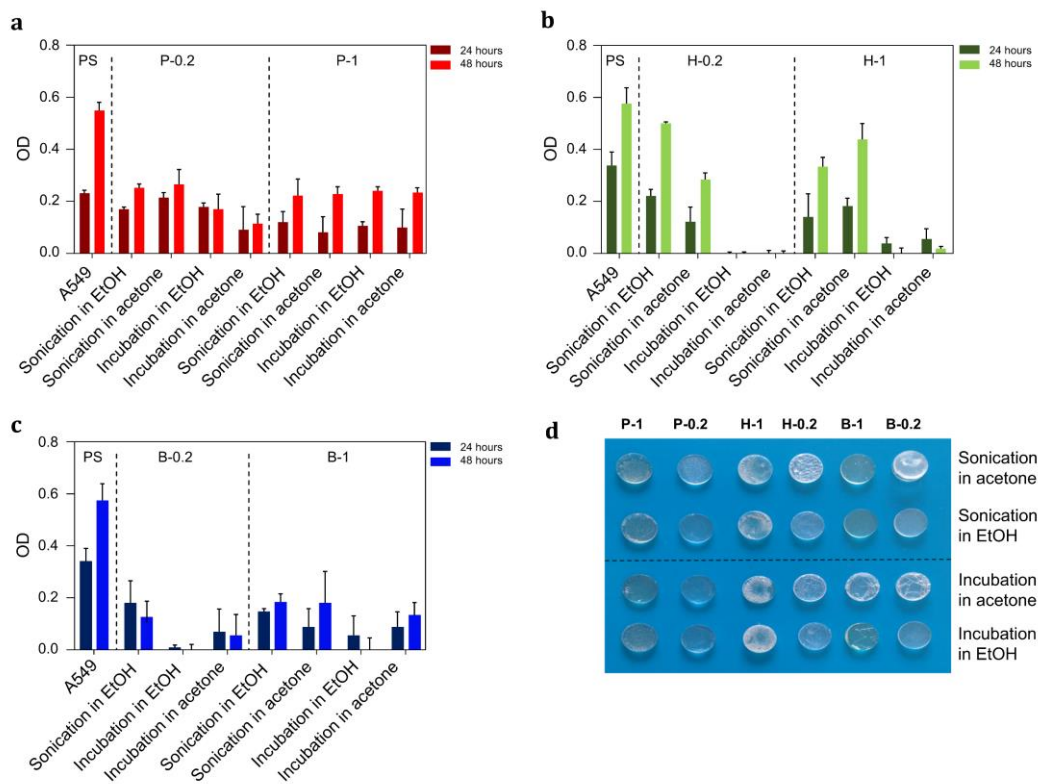


**Figure 3-5. MTT assay results showing the seeded A549 cells onto the three types of printed samples.** The graphs show the optical density (OD) of the cells grown on the printed wells after each of the four different washing protocols: sonication in ethanol, sonication in acetone, incubation in ethanol, and incubation in acetone for samples made from (a) PEGDA250, (b) HDDA, and (c) BEDA photopolymers (containing either 0.2 wt.% and 1 wt.% of the BAPO photoinitiator). The cell viability is measured after 24 and 48 hours. The results were compared to conventional cell culture on PS plate. Error bars mean standard deviation (c) Photograph of the washed samples where optical and mechanical characteristics of the 3D printed disks made from the six photopolymers and after the four washing protocols are displayed. The photograph shows that PEGDA samples better resisted the washing treatments.

Additionally, A549 cell morphology on the 3D printed wells (PEGDA250, HDDA, and BEDA monomers with 0.2 BAPO) was examined by Environmental Scanning Electron Microscopy (ESEM). Figure 3-6 displays the different biocompatibility of the three acrylate-based samples. In detail, the B-0.2 wells showed cells with significant morphology changes regarding the typical epithelial-like form of A549 cells; most of the cells appeared rounded and spongy. The cells morphology on the other two types of 3D printed wells (H-0.2 and P-0.2) were relatively analogous; both 3D printed structure presented cells with epithelial appearance, which suggest well-attached cells on the samples and with no apparent signs of cell apoptosis, even if for P-0.2 this aspect seemed to be more evident.

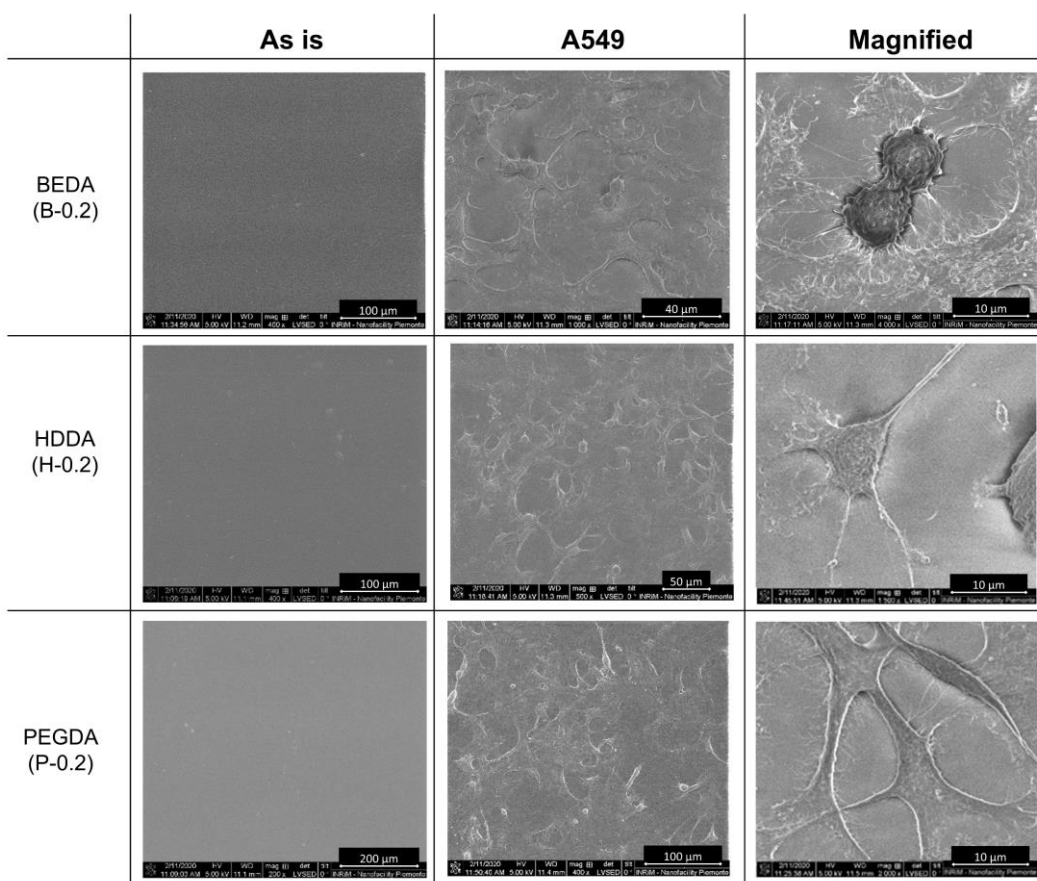


Figure 3-6. **Environmental Scanning Electron Microscope (ESEM) images collected from the 3D printed samples with 0.2 wt.% of BAPO.** The images show the difference between the cultured A549 cells on the different samples: on the BEDA (B-0.2) samples, the cells presented a rounded apotheosis aspect. The cells presented epithelial appearances on the HDDA (H-0.2) and the PEGDA250 (P-0.2) samples. Three different images were recorded for each sample type: samples without cells (as is) and with A549 cells at different degrees of magnification as reported in the images.

To further check the selected washing procedure's effectiveness on the best performing sample (P-0.2), the weight losses after both the sonication and the overnight washing in ethanol steps were evaluated. The results are compared to the weight variations observed by following the same procedure but using the chloroform as a solvent (the solvent used for the insoluble gel fraction tests). The data obtained for ethanol showed similar results to those obtained for chloroform, suggesting the excellent efficiency of ethanol as a washing solvent, as observed in the inset table in Figure 3-7, displaying the UV-Vis spectrum of the ethanol after the overnight washing step. In the absorbance spectrum in Figure 3-7, the presence of a released photoinitiator was no observed. Therefore, it can be assumed that the eventually unreacted and potentially toxic compound was removed entirely during the first sonication step or consumed during the post-curing treatment, with no further

release after prolonged washing protocol. Such observation confirms thus the effectiveness of the selected post-printing procedure to remove the unbounded products.

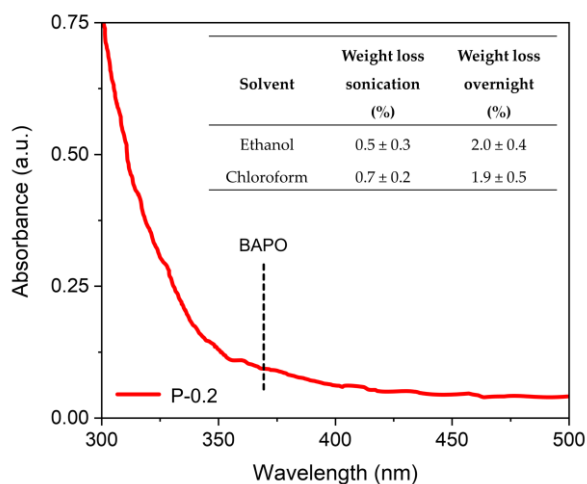


Figure 3-7. **UV-Vis spectrum collected from the ethanol used for the overnight washing step of PEGDA250 with 0.2 wt.% of BAPO.** The curve shows no BAPO-related shoulder (the region between 350 and 420 nm) appeared in the analysis. The inset table shows the weight losses of P-0.2 samples after different washing protocols in ethanol and chloroform.

### *Cell viability and proliferation on the 3D printed wells*

Once selected the most suitable sample composition (P-0.2) and the most suitable washing protocol (sonication in ethanol), the next step was to investigate the influence of different sterilization methods on the biocompatibility of the 3D-printed well. For this purpose, three different sterilization methods were evaluated: UV light for 30 minutes inside a biosafety cabinet, immersion in 70% ethanol for 10 minutes, and autoclave oven for 20 minutes at 121 °C. Before the sterilization procedures, half of the samples were incubated overnight in deionized water at room temperature.<sup>413</sup> The cells were seeded on both the 24-well-like parts made from P-0.2 formulation and the PS conventional wells used as a control. After 72 hours, the live/dead assay was performed to check cell viability, images shown in Figure 3-8. As observed, the samples previously subjected to an overnight water treatment presented living cells, compared to those with no previous water treatment, presenting only dead cells.

Additionally, the autoclave's printed wells lost their shape, see Figure 3-8.a; therefore, the autoclave cannot be considered a suitable solution for or purpose. The ethanol and the UV light sterilization methods instead did not damage the 3D printed wells: the live/dead assay showed cells growing in both types of samples. Some of the samples immersed in ethanol presented small



defects (especially on the sample's borders) compared to the UV treated ones. In general terms, both sample types (ethanol- and UV sterilized) presented good optical features) that can benefit cells' visualization at the phase-contrast microscope. As shown in Figure 3-8.b-c, those samples previously treated with water and UV sterilized presented the best results in terms of cell proliferation with no (or low) damage on the sample structure, resulting in the suitable strategy for further enhancing the biocompatibility of the printed parts.

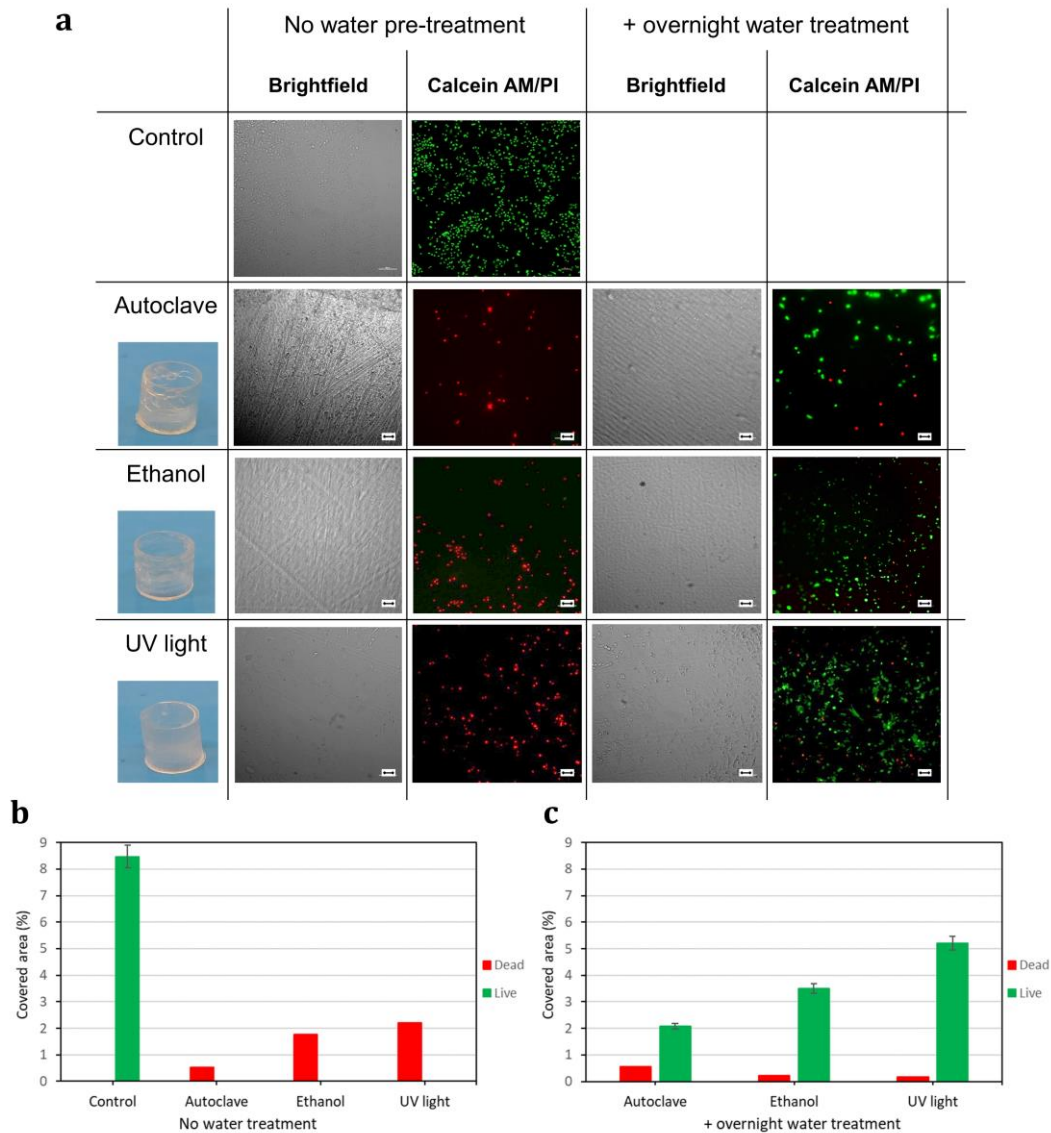


Figure 3-8. **Cell viability and proliferation on the 3D printed wells made from PEGDA 250 with 0.2 wt.% of BAPO.** (a) Phase-contrast and live/dead staining images from the cultured A549 cells on the 3D printed wells after different sterilization methods: autoclave, ethanol, and UV light either with or without water pre-treatment. The scale bar denotes 100  $\mu\text{m}$  for all images. Covered area (%) by the living and dead cells onto the 3D printed wells after the different sterilization types, and either (b) without or with (c) water pre-treatment. The histograms show a better cell proliferation on samples previously treated with water (overnight) and UV-sterilized.

### 3.2.3. Conclusion.

In the present study, acrylate-based photopolymers were prepared to produce bespoke parts through DLP-3D printing techniques using commercially available products such as polyethylene glycol diacrylate (PEGDA250), 1,6-hexanediol diacrylate (HDDA), bisphenol A ethoxylate diacrylate (BEDA) monomers, and the phenyl bis(2,4,6-trimethylbenzoyl)phosphine oxide (BAPO) photoinitiator. Although these components have been widely used for vat 3D printing applications with excellent results,<sup>148,150-153,275,420-422</sup> herein, the investigations were conducted to examine the biocompatibility of the printed objects. 3D printed 96- and 24-wells and disk were made from PEGDA250, HDDA, and BEDA monomers and adding different amounts of BAPO photoinitiator (0.2 and 1 wt.%). The 3D printed wells were tested following conventional cell culture assays for common PS multiwell; the advantages and drawbacks were evaluated for every object used for the cell culture experiments. In particular, using suitable materials and implementing a series of post-processing steps, objects made of PEGDA250 with 0.2 wt.% of BAPO (P-0.2) resulted in being the most suitable samples for this work., evidencing the importance of post-3D printing processing.

The adequate post-processing procedure resulted in a washing/sonication protocol in ethanol, followed by a sterilization method upon UV light irradiation. The cytotoxicity and growth viability of A549 cells on 3D printed wells were investigated. The results showed no harm in cells, confirming that the BAPO photoinitiator and the eventually unpolymerized acrylate monomer can be effectively rinsed out. After two (2) days of cultivation, the cells proliferated significantly, demonstrating a non-cytotoxicity behavior of the printed part. Compared to the positive control (cell seed into PS wells), the PEGDA250 samples achieved viability of around 50% after two (2) days of culture, a result that can be further enhanced, for example, by adding cell anchoring points. This work evidenced that the obtained structures fabricated with a commercial vat 3D printer, and using some of the most used reagents, might be suitable for the biomedical field even if they are not specially designed for bio-applications. What resulted in the most important aspect is establishing a suitable post-processing method for removing the unbounded products from the printed structures



### 3.3. Part II: 3D printing of PDMS-based microfluidic devices.

Part II of Chapter 3 is based on the original research article titled "*Fabrication and Functionalization of 3D Printed Polydimethylsiloxane-Based Microfluidic Devices Obtained through Digital Light Processing.*" The paper was published in the *Advanced Materials Technologies* scientific journal from Willey-Blackwell, ISSN: 2365709X.<sup>431</sup>

This part of the chapter will introduce the 3D printing of complex-shaped polydimethylsiloxane-based microfluidic chips fabricated through vat polymerization 3D printing methods. The purposes of this work are mainly two: 1) To create PDMS-based fluidic systems, hosting three-dimensional channels through a commercial SLA-DLP 3D printer. 2) To modify the printed PDMS-based chips' surface channel upon UV light irradiation by exploiting the unreacted surface functional groups after the printing step (Part I, chapter 4). Polydimethylsiloxane elastomer (PDMS) is one of the most used materials for microfluidic systems production since it offers valuable properties, especially for biological applications, such as biocompatibility, transparency, water and gas permeability, mechanical resistance, besides being an inexpensive polymer.<sup>294,432,433</sup> Most of the PDMS-based microfluidic devices are usually fabricated through the soft lithography method. A technique that allows obtaining high-precision microsystems that, however, requires expensive clean-room facilities and high-skilled personnel, making the diffusion of these devices beyond research laboratories hard.<sup>284</sup> Hence, new manufacturing methods such as 3D printing might boost the microfluidic chips' fabrication while maintaining good fabrication precision. Intending to take a step forward in the fabrication of microfluidic devices with PDMS-like features, the preparation and the 3D printing of a custom-made photopolymer based on acrylate-polydimethylsiloxane (PDMS) resins will be presented in this part of Chapter 3.

The scientific interest in printing objects with the PDMS bio-like characteristics has been evidenced in numerous works for diverse purposes. For instance, the work reported by Abdollahi et al., in which they utilized a direct ink writing technique, the freeform reversible embedding (FRE) 3D printing, for producing precise PDMS structures.<sup>434</sup> Those PDMS structures were then combined with flexible electronic devices and sensors to develop a series of patient-specific wearable pulse oximeters that yielded good results. Similarly, Hinton et al. presented a series of more structured PDMS-based parts, also fabricated through the freeform reversible embedding (FRE) method. Using a hydrophilic support bath made of Carbopol, they could obtain complex-shaped production of PDMS structures.<sup>435</sup> While Ozbolat and coworkers developed and studied PDMS-based inks for producing 3D printed organ models (e.g., human hand, noes, blood vessel) through a commercial bio-

plotter with improved mechanical (due to decreased porosity and bubbles entrapped in the material) and better cell adhesion properties (due to the uneven features of the parts) compared to the casted PDMS parts.<sup>436</sup>

For the fabrication of PDMS-based microfluidic devices, interesting works have also been reported, as discussed in Chapter 2. For instance, Bhattacharjee et al. developed an acrylate terminated-PDMS resin employed to produce optically transparent microfluidic devices using a commercial desktop-stereolithography 3D printer.<sup>391</sup> While in a more recent investigation, Zips et al. prepared and processed through a stereolithography 3D printer a silicone-hydrogel hybrid resin for producing flexible microfluidic devices with integrated valve, mixers, and chamber that they used for cell culture.<sup>392</sup> Beyond these works, the field of PDMS-based microfluidic devices is still limited, despite the advantages that vat polymerization 3D printing techniques might offer in printing resolution and material preparation versatility compared to other polymeric 3D printing methods.<sup>404</sup> Therefore, Part II, Chapter 3, aims to use vat 3D printing as an alternative to conventional soft lithography methods to produce complex-shaped and precise microfluidic chips with PDMS-like features able to host three-dimensional channels. By selecting and combining the suitable materials during the resins' preparation and with the freedom of design of 3D printing methods, microfluidic PDMS-like chips might be obtained with great optical features, high chemical stability, and good mechanical properties; such features are fundamental features for potential biological applications.<sup>77</sup> A series of evaluations were first carried out to optimize the printable formulation preparation, followed by chemical and mechanical characterizations of the obtained parts. The 3D printing of PDMS-like chips could transform the conventional manufacture of PDMS-based microfluidic devices by decreasing fabrication costs and time, allowing producing different geometry microdevices.

### 3.3.1. Experimental section.

#### *Materials*

As a reactive oligomer, a silicone-based resin (TEGO®Rad 2800, TRAD) was used to prepare the photopolymer. The TRAD is an acrylate polydimethylsiloxane copolymer kindly supplied by Evonik Industries AG (Essen, Germany) without further information on the resin's composition beyond that found on the Evonik company's website. The photoinitiator's selection was based on two fundamental aspects for the achievement of this investigation: it has to be soluble in the silicone-based resin, and it has to absorb in the wavelength of the light emitted by the printer, at 405 nm. Therefore, the photoinitiator selected was a liquid and silicone-soluble photoinitiator developed by Cunningham and coworkers.<sup>437</sup> This photoinitiator, which we will name BAPO-si for simplicity, is a derivate of phenyl bis(2,4,6-trimethylbenzoyl) phosphine oxide photoinitiator (BAPO), both with similar absorption spectra (see Figure 3-10.a) that match with the emission wavelength of the 3D printed at 405 nm. As indicated in the Cunningham et al. work, the BAPO-Si photoinitiator is a blend of a BAPO-methyl ester, a BAPO-isooctyl ester, and isooctanol, which synthesized in an industrially feasible procedure by BASF and ETH Zurich for commercial purposes (structures are shown in Figure 3-9.c). Disperse red one methacrylate (**DR1-MA**, 95 %) dye was also used for the resin preparation. This dye absorbs the wavelength of the light emitted from the printer (450 nm), Figure 3-10.b; therefore, it might block part of the incident radiation, constraining the visible light's penetration during the printing step, increasing thus the printed part's accuracy. Methyl methacrylate (**MMA**, 99 %) was used to solvate the dye. Isopropanol (**IPA**, ≥ 99.5%), acetone (≥ 99.5%), ethanol (**EtOH**, 99.8 %), distilled water, hydrogen peroxide (**H<sub>2</sub>O<sub>2</sub>**, 30 %v/v in H<sub>2</sub>O), acetonitrile (**ACN**, ≥ 99.8%), N,N-dimethylformamide (**DMF**, 99.8%), dimethyl sulfoxide (**DMSO**, ≥ 99.9 %), cyclohexane (99.5 %), tetrahydrofuran (**THF**, ≥ 99.9 %), dichloromethane (**DCM**, ≥ 99.8%), and toluene (99.8 %) chemicals were purchased from Merck Company (Darmstadt, Germany) and used as received. The chemical structures of the components used for the photopolymer preparation are shown in Figure 3-9.

#### *Preparation of the PDMS-based printable resin*

The photocurable formulation was prepared first by adding 0.6 wt.% of the BAPO-Si photoinitiator into the TRAD oligomer. The formulation was stirred at room temperature for six hours until the formulation became visibly homogeneous. DR1-MA dye was dissolved in methyl methacrylate (MMA) at a concentration of 100 mg mL<sup>-1</sup>, then some drops of this mixture were added to

the TRAD resins to obtain a concentration of 0.1 wt.% of DR1-MA. Finally, the formulation was kept under vacuum for 10 minutes at room temperature to degas.

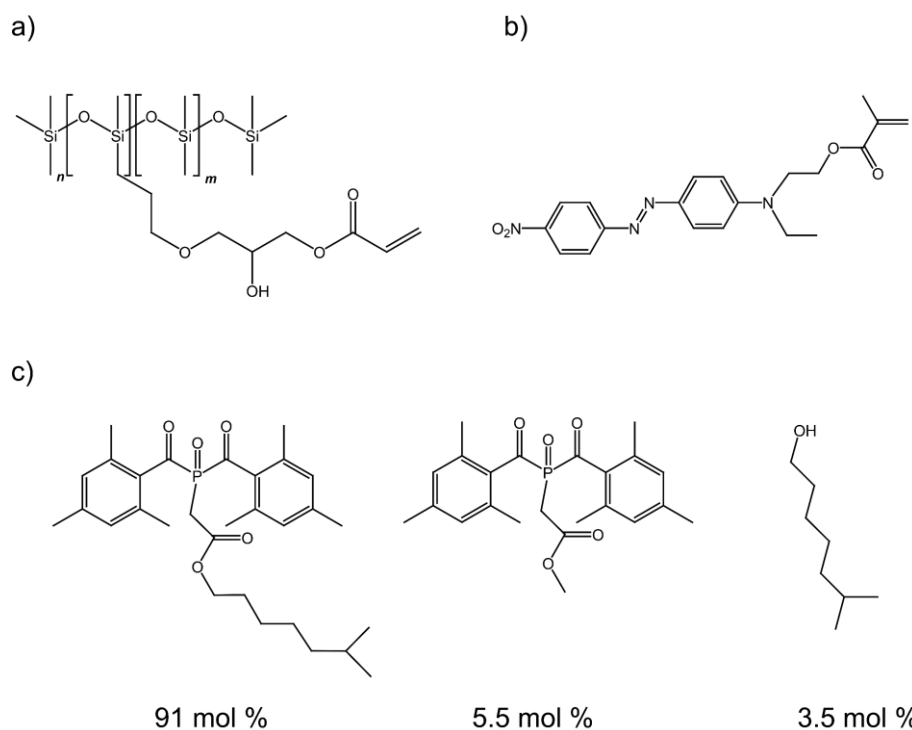


Figure 3-9. Chemical structures of the reagents used. (a) TegoRAD 2800® (TRAD), (b) dispersed red one methacrylate (DR1-MA), and (c) the BAPO derivate photoinitiator (BAPO-Si).

### *Digital light processing DLP-3D printer*

The 3D printing of the silicone-based photopolymer was performed using a PICO 2 DLP-3D printer (Asiga, Australia) equipped with a LED light-emitting source at 405 nm. The 3D printer characteristics are minimum nominal XY pixel resolution of 50  $\mu\text{m}$ , Z-axis control of 1  $\mu\text{m}$ , light intensity up to 30  $\text{mW}/\text{cm}^2$ . The printing parameters were set to layer thickness 50  $\mu\text{m}$ , light intensity 20  $\text{mW}/\text{cm}^2$ , exposure time of 10 seconds per layer. All CAD designs were produced with the FreeCAD program and exported in STL format. After the printing step, the printed objects were cleaned up with compressed air and soaked in ethanol for 15 min at room temperature to remove the unreacted resin. Finally, UV post-curing processes were performed on the printed samples using a mercury arc lamp Dymax ECE device in the air (5 minutes treatment at 10  $\text{mW}/\text{cm}^2$  of light intensity).

### *Characterization methods*

Real-time photo-rheological tests were performed to measure the changes in the viscoelastic material properties during polymerization. The experiments were carried out using an Anton Paar rheometer (Physica MCR 302) configured in parallel mode with the lower plate consisting of 20 mm quartz and the upper parallel plate consisting of 20 mm aluminum. A Hamamatsu LC8 lamp was used to study the photopolymerization process. It is equipped with a visible bulb and a cutoff filter below 400 nm, and an 8 mm light guide. During the tests, the light irradiation was initiated after 60 seconds to stabilize the system before the photopolymerization process (light intensity set at 20 mW/cm<sup>2</sup>). The gap between the two parallel plates was set at 100 μm. The measurements were performed at a constant temperature of 25 °C, at a constant strain amplitude of 0.1%, and a constant shear frequency of 10 Hz. The viscoelastic moduli variations of the resin upon light irradiation were measured against exposure time.

A Nicolet iS50 FT-IR spectrometer (from Thermo Scientific, Milano, IT) was used to evaluate the acrylate double bond conversion on both liquid photopolymers, and the polymerized parts. For the experiments, an attenuated total reflectance (ATR) accessory (Smart iTX) was used. The spectra were first collected on the liquid TRAD formulation and then on the polymerized formulation after direct irradiation on the ATR accessory with both visible and UV light. The formulation was irradiated using a visible portable lamp (Hamamatsu LC8 lamp, see description above) with a light intensity of 20 mW/cm<sup>2</sup>. The UV post-curing treatment was simulated using a UV portable lamp (Hamamatsu medium-pressure mercury lamp, a light intensity of 10 mW/cm<sup>2</sup>). Spectra of 3D printed samples as printed and after different UV post-curing treatments were also collected. The FTIR spectra were collected with a resolution of 2 cm<sup>-1</sup>, averaging 32 scans for each spectrum, in the range between 600 – 3800 cm<sup>-1</sup>. The acrylate double bond (C=C) conversion was monitored by following the reduction of the area of the peak of the single carbon-oxygen bond of acrylates moieties at 1196 cm<sup>-1</sup>, in which its vibration is modified by the opening of acrylate double bonds after photopolymerization.<sup>84</sup> The acrylate peak area was normalized by a constant signal in the spectra centered at 1257 cm<sup>-1</sup>, corresponding to methyl siloxane stretching vibrations.<sup>438</sup>

The dissolution extent of the 3D printed TRAD samples (5mm x 5mm x 2mm,  $lwh$  = length x width x height ) was evaluated toward common solvents. The samples were immersed in a specific solvent (~2 mL) for 24 hours at room temperature using a metal net. At last, they were extracted from the vial and left drying overnight at 120 °C. The percentage of extraction (wt.%) was

determined by the sample's mass difference before and after solvent extraction. The test was repeated three times for each solvent.

The swelling percentage (wt.%) in different solvents was determined by measuring the weight difference between the swelled polymer and the initial one. The samples (5mm x 5mm x 2mm, *lwh*) were immersed in the considered solvent (~2 mL) for different timeslots (5, 10, 15, 30, 60 minutes, and 24 hours) at 25 °C. The experiment was repeated up to three times for each solvent.

UV-vis measures were carried out using a double-beam Lambda 40 instrument (PerkinElmer Italia, Milano, Italy). The samples were examined in the range between 200 and 600 nm at a scan rate of 480 nm/min. The UV-vis spectrometer was also used to investigate the solvents used for the extraction tests. For these experiments, the sample was immersed in a vial containing the solvent selected; then, after a certain time, the sample was removed from it, and UV-Vis spectra were recorded on the solvent used. The UV-Vis method was replicated using a fresh solvent after each immersion test until no absorbance peak is observed in the recorded spectra.

Tensile tests were performed using the Instron 3360 dynamometer, which is equipped with a load cell of 500 N. For each type of sample, five (5) specimens with a gauge length of 20 mm were produced and tested. The crossheading speed was established at 5 mm/min.

### 3.3.2. Results and discussion.

#### *Initial characterization and 3D printing step*

Some preliminary studies were initially performed to adequately prepare the silicone-based photopolymer targeting to obtain complex-shaped microfluidic chips that can host three-dimensional channels through VP-3D printing. With this as an objective, one of the most challenging aspects of working with silicone oligomers is that they are highly hydrophobic, complicating the photoinitiator's correct dissolution and the dye inside them.<sup>439-441</sup> This might be problematic since they are indispensable components for preparing suitable 3D printable formulations. Here, the silicone oligomer (TRAD) has low compatibility with many chemicals and becomes hazy almost instantaneously when mixed with other compounds. Thus, special efforts were made to correctly prepare the TRAD-based photopolymer to obtain a printable material with good optical properties. The first criterion was to select a suitable photoinitiator, which has to be soluble in the TRAD oligomer and absorbs in the wavelength of the DLP-3D printer (405 nm). In these conditions, the most commonly used photoinitiators for vat 3D printing purposes are phosphine oxide-based compounds (TPO and BAPO).<sup>148,151,332</sup> These photoinitiators have been reported in the literature for silicone-based formulations.<sup>90,391,442</sup> However, these compounds were not mixable in the TRAD oligomer. Therefore, a phosphine-oxide derivate photoinitiator, BAPO-Si, synthesized by Cunningham and coworkers, was selected.<sup>437</sup> This photoinitiator is a yellowish liquid type I compound with an absorption spectrum (see Figure 3-10.a) and a photoactivity similar to the commercially available phenyl bis(2,4,6-trimethylbenzoyl)phosphine oxide (BAPO). Although, when more than 0.6 wt.% of BAPO-si is added into the TRAD oligomer, the formulation lost its transparency. Moreover, as will be presented in the following paragraphs, higher amounts of BAPO-si would not considerably increase the formulation's reactivity. Therefore, downstream experiments were prepared by fixing 0.6 wt.% of BAPO-Si as maximum photoinitiator concentration. The next criterion was to select a suitable visible light absorber for the resin preparation. In vat 3D printing applications, light absorbers or dyes are frequently added at low concentration into the printable mixture to control the spatial parameters (resolution) during printing and obtain thus well-defined 3D printed objects.<sup>152</sup> This element might limit the photopolymerization reaction's propagation on the Z-direction and the X-Y plane. The dye selected here was a disperse red 1-based molecule bearing a methacrylate group (DR1-MA), see Figure 3-9.c. DR1-MA dye is a commercial compound that absorbs properly in the printer's wavelength (at 405 nm) used for this work; see Figure 3-10.b. Furthermore, DR1-MA dye, having a methacrylate functionality, could copolymerize with the polymeric material

during the 3D printing step. By chemically integrating the dye in the polymer backbone, the uncontrolled and long-term dye releasing might be avoided during the microfluidic device usages. The latter might solve one of the 3D printed microfluidic devices' main problems: the contamination of the fluids passing through the microfluidic channels.<sup>335</sup> However, since DR1-MA is not directly mixable in the acrylate-polydimethylsiloxane, a small amount of methyl methacrylate (MMA) was used to solvate the dye into the TRAD oligomer.<sup>148</sup>

Real-time photo-rheological tests were carried out to evaluate the TRAD resin reactivity upon light irradiation. In Figure 3-10.c, the curves related to the storage ( $G'$ ) and loss ( $G''$ ) moduli of the TRAD formulation at different BAPO-si concentrations (0.1, 0.2, 0.4, 0.6, 0.8, and 1 wt. %) as a function of visible light irradiation time are plotted. For all the BAPO-si concentrations, the storage modulus ( $G'$ ) was lower than the loss modulus ( $G''$ ) under direct illumination, suggesting a viscous liquid-like behavior of the pre-polymer. After 60 seconds, the lamp was turned on, starting the polymerization. As observed, during this phase,  $G'$  curve crosses the  $G''$  curve at different points for all types of TRAD formulations. When the  $G'$  curve became predominant (crossing the  $G''$  curve), the material reflects an elastic response indicating a solid-like behavior. The point where both curves intersect ( $G'=G''$ ) is the formulation's gelation point, which varied according to BAPO-si concentration. Figure 3-10.d shows how by incrementing BAPO-si concentration, the time to reach the gelation point decreases following a negative exponential curve. Beyond 0.6 wt.% of BAPO-si concentration, the TRAD formulation did not considerably increase its reactivity, reaching a sort of "plateau" at around 9 seconds of irradiation (Figure 3-10.d).



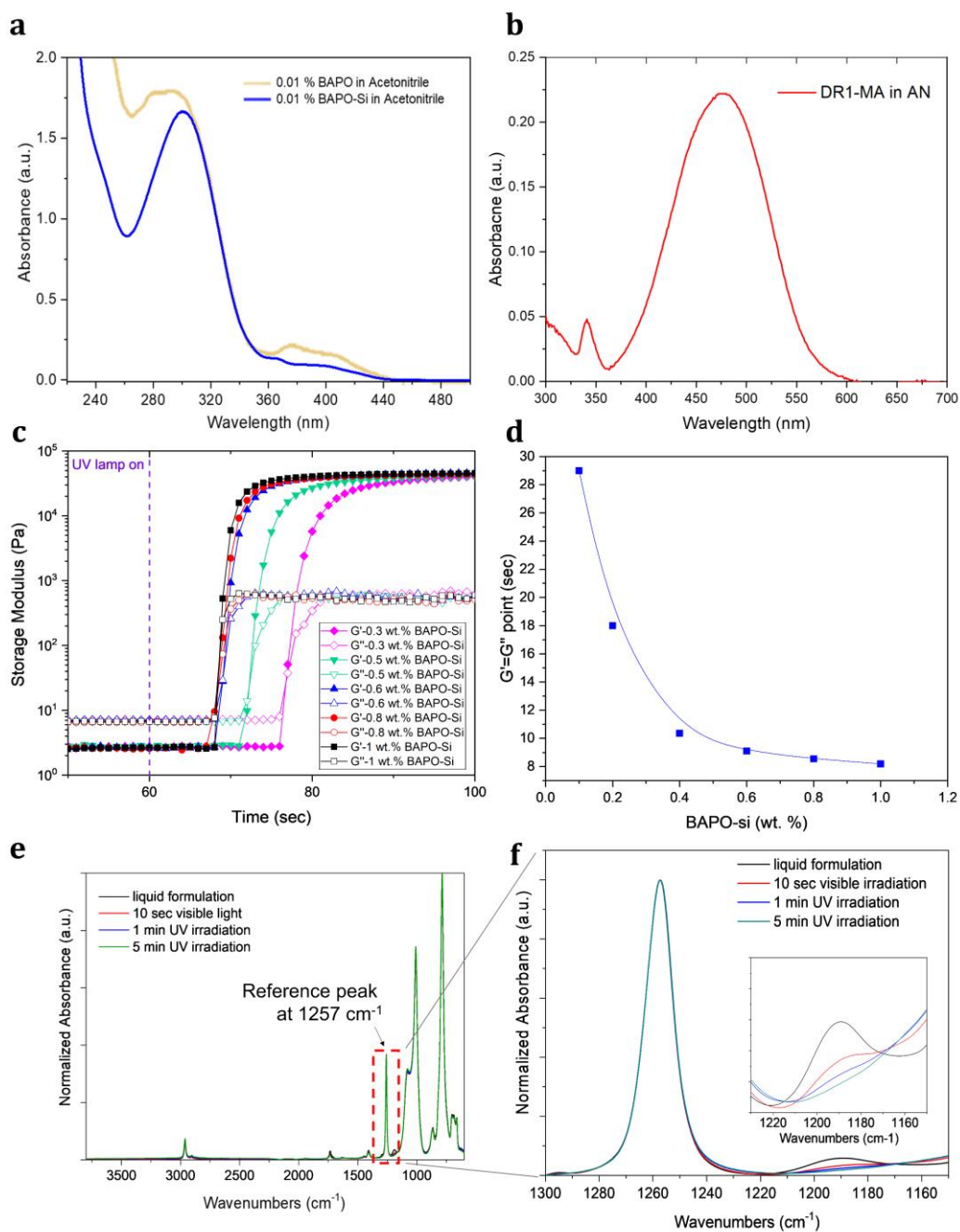


Figure 3-10. **Characterization of TRAD formulation components.** (a) Absorbance spectrum similarities between the BAPO-Si photoinitiator and the BAPO 819 photoinitiator. (b) absorbance spectrum of the DR1-MA showing a great absorption in the region of 405 nm, the printer's light emission. (c) storage ( $G'$ ) and loss ( $G''$ ) moduli curves against visible light times of TRAD resin varying the BAPO-si concentration and (d) moduli crossover ( $G'=G''$ ) of the TRAD resin at different concentrations of BAPO-si. These curves show that 0.6 wt.% of BAPO-si were enough to prepare a TRAD formulation with good reactivity as possible without changing the formulation optical features. (e) normalized ATR-FTIR spectra of the TRAD formulation at different conditions, with (f) the area of interest zoomed in the region between 1300-1150  $\text{cm}^{-1}$  where is shown the acrylate double bond decrease in the range 1220-1170  $\text{cm}^{-1}$  after visible and UV light irradiation.

The silicone-based resin's reactivity was also evaluated with the ATR-FTIR technique. The spectra were recorded on both liquid formulations and solid samples at different irradiation stages by following the decrease of the 1196  $\text{cm}^{-1}$  peak after different irradiation times, associated with the single carbon-oxygen bond acrylate moieties, which vibrations are altered by the reaction of acrylate bonds after polymerization.<sup>84</sup> The areas underneath the peaks were normalized using the signal centered at 1257  $\text{cm}^{-1}$  as a reference, which corresponds to methyl siloxane stretching vibrations.<sup>438</sup> The results at different stages of irradiation tests are reported in Figure 3-10.e-f and summarized in Table 3-2.

Table 3-2. Acrylate conversion (%) for TRAD formulation after visible light irradiation (10 seconds), 3D printing with similar irradiation conditions followed by 5 minutes of UV post-curing irradiation, and some mechanical properties of the 3D printed TRAD samples compared to those values for classical PDMS Sylgard 184 taken from literature. TRAD formulation contained 0.6 wt.% of BAPO-Si and 0.1 wt.% of DR1-MA.

Sample condition	Acrylate conversion (%)		Young's modulus (MPa)	Ultimate tensile stress (MPa)	Elongation at break (%)
	Real-time irradiation	3D printed			
Photopolymerized <sup>a)</sup>	74	78	1.4 ± 0,1	0.66 ± 0.13	63 ± 20
5 min UV post-curing <sup>b)</sup>	98	94	1.5 ± 0.1	0.70 ± 0.11	62 ± 15
PDMS Sylgard 184 (10:1) at 25 °C <sup>295</sup>	-	-	1.32 ± 0.07	5.13 ± 0.55	93.1

<sup>a)</sup> measured through ATR-FTIR after direct irradiation of visible (10 sec).

<sup>b)</sup> evolution of acrylate conversions versus UV irradiation times are shown in Figure 3-12.a-c.

Following 10 seconds of visible light exposure, the formulation reached 74 % of acrylate conversion. This conversion is acceptable considering that the test was performed under a standard environmental atmosphere, where oxygen-induced inhibition prevents complete conversion due to the well-known phenomenon of radical scavenging.<sup>443</sup> Although 74 % is not exceptionally high, it is still adequate to build the piece during 3D printing since the object reaches the gelation point, as shown previously during the photorheology experiments in similar light intensity conditions. The acrylate conversion further increases after 1 and 5 minutes of post-curing UV irradiation, to 97 % and 98 %, respectively. Such acrylate conversions are analogous to other reactive photopolymers used for VP 3D printing, bisphenol A ethoxylate (2 EO/phenol) diacrylate (Mw 572), and Poly(ethylene glycol) diacrylate (PEGDA, Mw 575), with 98 % and 97 % acrylate conversion.<sup>157,421</sup>

Once the photopolymer preparation was optimized, the following step was to print different 3D objects to demonstrate the silicone-based resin's suitability for producing complex structures and microfluidic chips. Figure 3-11.a shows the photographs of microfluidic chips with an S-shaped channel of 800  $\mu\text{m}$  in diameter, filled with a green-colored water solution.

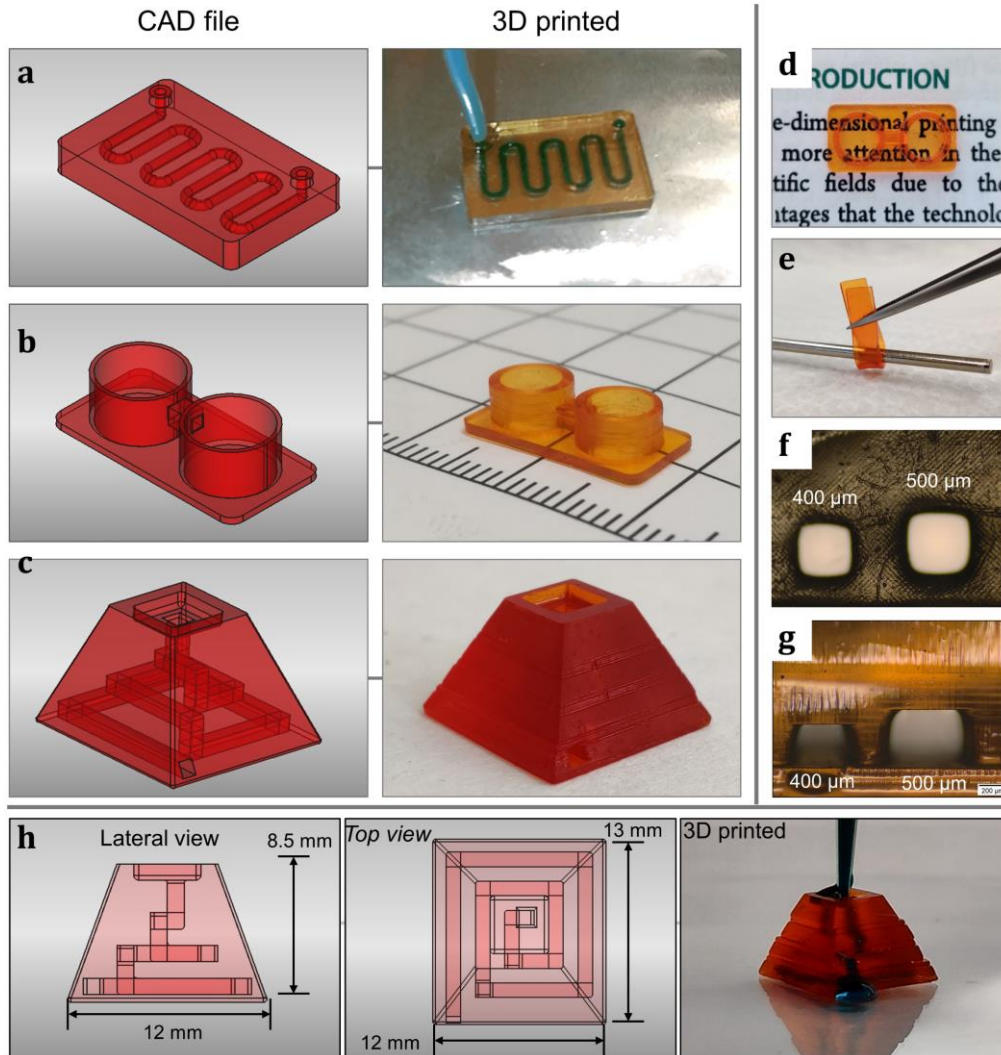


Figure 3-11. **CAD design illustration and photographs of different 3D printed fluidic chips and samples.** (a) 3D printed microfluidic chip with an s-shaped channel of 800  $\mu\text{m}$  in diameter, where the channel is filled with green colored water. (b) Two 3D printed wells connected by a  $1 \times 1 \text{ mm}^2$  square section channel. (c) trapezoidal 3D printed microfluidic chip with a  $1 \times 1 \text{ mm}^2$  channel square section. (d) photograph of the two-3D printed 96-wells showing the bottom's transparency with 500  $\mu\text{m}$  thickness, (e) a 3D printed strip ( $20 \times 5 \times 1 \text{ mm}^3$ ), showing the material's excellent stretchability when wrapped around a 3 mm diameter cylinder. Photograph (10x) of the smallest microchannel achieved in (f) XY-plane and (g) Z-axe. (h) CAD design (lateral and top views), and a photograph of the 3D printed trapezoidal microfluidic device with a dye liquid passing through its channel ( $1 \times 1 \text{ mm}^2$ ).

Figure 3-11.b shows a 3D printed chip consisting of two wells (with dimensions analogous to a single well of 96-multiwell plate used for cell culture) connected by a 1x1 mm<sup>2</sup> microfluidic channel with a transparent bottom of 500 μm (see Figure 3-11.d). More complex-shaped 3D printed structures were also obtained, as shown in Figure 3-11.c (see Figure 3-11.h for more details in its dimensions), which reports a trapezoidal chip in which inside it hosts a three-dimensional channel with a square section of 1x1 mm<sup>2</sup>. A green-colored liquid was flushed through the channel of the trapezoidal chips, see Figure 3-11.h. The printed elastomer exhibited excellent stretchability, as shown in Figure 3-11.e for a 3DP strip wrapped in a cylinder of 3 mm in diameter. The 3D printed structures were scrubbed with compressed air to remove the exceeding resin from the channels before the post-curing step; they were then rinsed in ethanol for 15 min and dried at room temperature overnight. The just-printed parts presented an adequate acrylate conversion of 78 %, as observed in Table 3-2, and after 5 minutes of UV post-curing, the maximum acrylate conversion was measured to be 94 % (Figure 3-12.c-d).

The printed samples were post cured, exposing only their upper side to UV light to better represent the curing reaction's evolution during the UV post-curing treatment. The ATR spectra were then collected on the lower side that was not directly exposed to UV light. As observed, 5 minutes of UV post-curing was enough to reach the possible maximum acrylic double bond conversion (all curing experiments were performed in the air). The smallest channel achieved with the prepared silicone-based resin was 400x400 μm<sup>2</sup> both in the X-Y plane and in the Z-axis, as shown in Figure 3-11.f-g, respectively. Smaller features (< 400 μm) were not obtained, mainly due to the problematic removal of uncured resin, which remained trapped in the channel, causing clogging.<sup>375</sup> Also, it could also be attributed to the TRAD oligomer's slow reactivity. Indeed, the TRAD formulation with 0.6 wt.% of BAPO-si takes around 9 seconds to reach the gel point (even at the higher concentration of BAPO-si), see in Figure 3-10. Those times are considerably longer compared to other more reactive resins, e.g., bisphenol A ethoxylate diacrylate (BEDA) or polyethylene glycol diacrylate (PEGDA250), that react within one (1) second upon visible light exposure at the same illumination conditions, see Figure 3-3, in Part I, Chapter 3. Hence, intending to balance TRAD formulation's slow reactivity, higher irradiation times are required, increasing the penetration of light during the printing process and polymerizing beyond the desired zones (the z-axis) by the effect also of greater diffusion of radicals.<sup>444</sup> This phenomenon might be solved, somehow, by enhancing the reactivity of the silicone-based resin. However, these results are aligned with the results presented in other works and slightly improving the smallest microchannel dimensions for 3D printed PDMS-like materials (500x500 μm<sup>2</sup>).<sup>391</sup> Furthermore, a genuinely 3D microchannel architecture was obtained that can be exploited in different

applications, such as the manufacturing of complex and passive microfluidic mixer with various 3D configurations,<sup>445</sup> or the fabrication of a three-dimensional lab-on-a-chip for cell culture and biological analysis.<sup>446</sup>

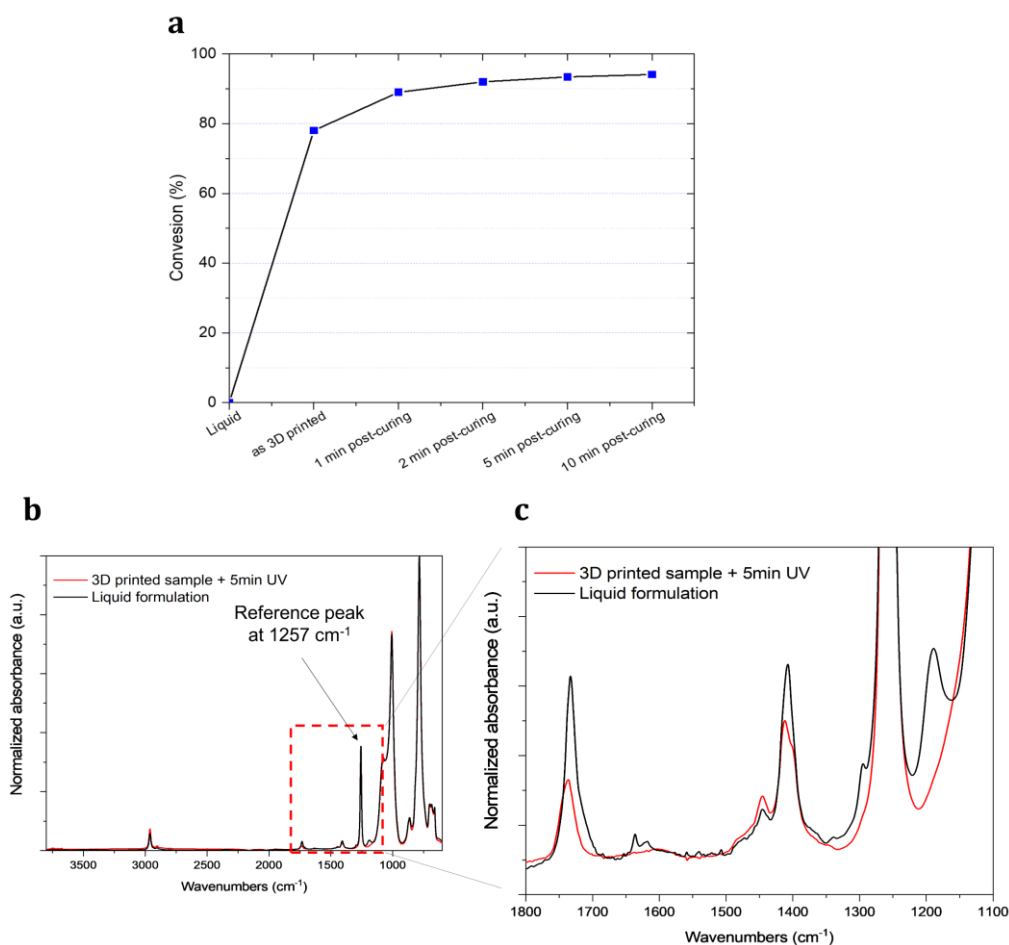


Figure 3-12. **Characterization of the 3D printed TRAD-based samples by the FTIR technique.** (a) Acrylate double-bond conversion (%) of the 3D printed samples and after different UV post-curing times (in the air), obtained by following the decrease of the peak at 1196 cm<sup>-1</sup> after the different radiation conditions. (b) Full normalized ATR-FTIR spectra of 3D printed TRAD samples followed by 5 min of UV post-curing treatment compared to the liquid formulation, where the acrylate-related band decreased after the UV post-curing step. (c) Shows the region between 1800-1100 cm<sup>-1</sup>.

### *Solvent stability of the 3D printed materials*

After the 3D printing step and the post-curing process, not all the substances of the photopolymer (oligomer, monomers, photoinitiators, and light absorber) end up in the photo crosslinked. These residual elements might be detrimental since, in microfluidic devices, the unreacted materials could diffuse through the liquid passing into the chip's channels during operations,

potentially contaminating the fluids. Therefore, it is important to develop a more thorough cleaning protocol to remove or extract all uncured residual elements from 3D printed parts. For this purpose, dissolution extension of the 3DP TRAD samples towards different solvents was measured by determining the swelling weight percent (wt.%) following a 24-hour immersion in various solvents and the extracted weight percent (wt.%) of uncured resin from dried samples. Results are summarized in Table 3-3 and plotted in Figure 3-3.c. 3DP TRAD samples swelled significantly more in non-polar and in some polar-aprotic solvents, such as DCM (229.7 %), THF (204.4 %), cyclohexane (184.5 %) and toluene (169.2 %), followed by acetone (27.1 %) and isopropanol (17.9 %). Regarding the extraction of uncured resins, the higher the solvent's capacity to penetrate the matrix, the higher the efficiency of extraction; this occurred for DCM, THF, cyclohexane, toluene, and acetone. After 24-hours of immersion, the samples were extracted from the respective solvent, observing that almost all of them were damaged, except those from acetone. This observation was attributed to the polymer's inability to sustain the stresses generated on the surface during the uneven evaporation of these highly swelling solvents, producing irreversible defects.

Table 3-3. Swelling percentage (wt.%) of 3D printed TRAD samples after immersion for 24 hours and 1 hour and extracted resin percentage (wt.%) of samples after 24 hours of immersion in different solvents at 25°C.

Chemical	Swelling	Extracted resin weight (wt.%)	Swelling
	(wt.%) <i>after 24-h immersion</i>		(wt.%) <i>after 60-min immersion</i>
Isopropanol	17.9	7.0	14.4
Acetone	27.1	7.5	25.8
Ethanol	5.1	5.0	4.5
Distilled Water	1.4	1.8	1.3
Hydrogen Peroxide	1.7	2.6	1.6
Acetonitrile	6.4	0.7	6.3
Dimethylformamide (DMF)	8.7	2.6	7.7
Dimethyl sulfoxide (DMSO)	9.8	2.6	5.2
Cyclohexane	184.5	9.2	161.8
Tetrahydrofuran (THF)	204.4	10.8	180.2
Dichloromethane (DCM)	229.7	12.5	192.5
Toluene	169.2	8.7	168.4

Another critical point is that most microfluidic devices usually operate during relatively short times in their usage (i.e., when a fluid is passing through the microchannel). Therefore, it is essential to know the 3D printed TRAD object's stability (post-cured, washed, and dried samples) towards different

solvents for brief periods. The dimensional stability of 3DP samples was determined by performing swelling tests for short intervals of 5, 10, 15, 30, and 60 minutes; the results are plotted in Figure 3-3.a-b and summarized in Table 3-3 (only for 60 minutes of immersion). As discussed, 3DP TRAD samples present different swelling percentage behaviors according to the solvent used.<sup>447</sup> After 60 minutes of immersion, the lowest values obtained were in distilled water (1.3%), while the highest values were reached using DCM (plateau reached at 30 min) and THF. This information is useful when envisaging how to employ these devices in different microfluidic applications.

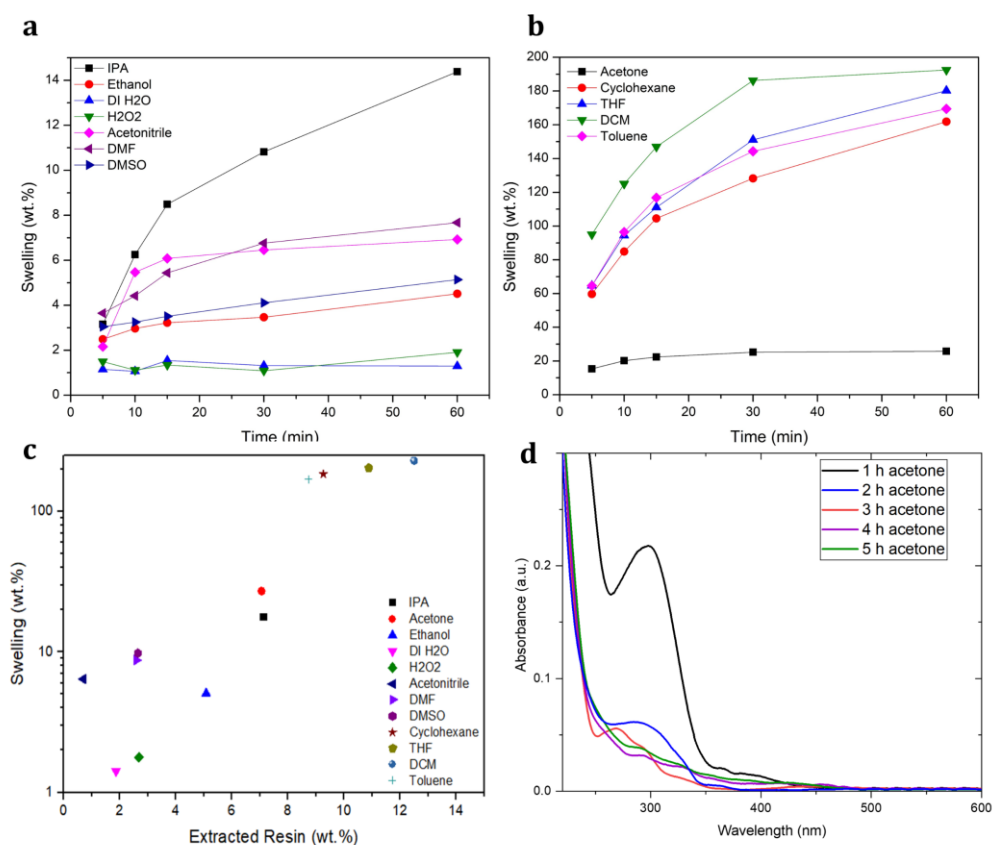


Figure 3-13. **Solvent compatibility of the 3D printed based samples toward common organic compounds.** (a,b) Swelling percentage (wt.%) versus time (min) curves for 3D printed TRAD samples after immersion in different solvents. (c) Scatter plot of the swelling percentage (wt.%) versus extracted resin percentage (wt.%) for 3D-printed TRAD samples after 24-hours of immersion in different solvents. (d) UV- VIS spectra of the acetone used to extract unreacted material from 3DP TRAD samples, in which after 5 hours of washing in acetone, the analyzed solution did not show any trace of unreacted substance (either photoinitiator or dye).

The next step was to select the appropriate solvent for a washing protocol that completely removes all unreacted elements within the samples

without deteriorating or damaging the 3D structures. Based on previous results, acetone was selected as the washing solvent since it offers the best compromise between the efficient extraction of residual material and no significant deterioration of the samples. Therefore, a series of washing procedures were performed using acetone, and ultraviolet-visible spectra of the washing solvent were collected (see Figure 3-13.d). With short washing times, all the other curves showed a shoulder around 300 nm corresponding to the absorbance of unreacted BAPO-Si photoinitiator (as detailed in Figure 3-10), while after 5 hours of washing treatment, the analyzed solvent did not present any trace of residual substances. Equally important, there was no release of the DR1-MA dye at each washing time, thus confirming the dye's copolymerization into the polymer backbone during the photopolymerization process.<sup>448</sup>

### *Mechanical tests*

The mechanical properties of the 3DP TRAD samples were also determined and compared to conventional PDMS polymer properties. Tensile test specimens were 3D printed (dog bone with a gauge length of 20 mm), and each sample was exposed to a post-curing treatment under UV irradiation for 5 minutes on each side. The specimens were then washed and dried following the protocol developed here for the TRAD microfluidic devices: immersion in acetone for 6 hours (using fresh solvent every hour) and overnight drying treatment at 120 °C. Besides, only 3D printed samples with no UV post-curing treatment were also tested for comparison reasons. The samples were mechanically tested to obtain ultimate tensile stress, fracture stress, and elongation at break (see Figure 3-14.c). Tensile results are summarized in Table 3-2 and plotted in Figure 3-14.a-b for UV post-cured and just 3D printed samples, both containing 0.6 wt.% of BAPO-Si photoinitiator and 0.1 wt.% of DR1-MA dye.

The values of ultimate tensile stress (UTS) and Young's modulus were somewhat higher for UV post-cured samples than 3D printed samples with no UV treatment. The values of elongation at break were similar for both types of samples. Significant differences were observed when the 3DP TRAD samples' tensile results are compared with those for conventional 10:1 PDMS (Sylgard 184). While Young's Modulus was similar, UTS values were considerably lower for 3D printed samples. Moreover, even elongation at break was lower in 3D printed samples. This behavior could be attributed to the fact that layer defects are randomly generated during the 3D printing process. They might act as a point of nucleation for cracks initiation and decrease the material's strength.



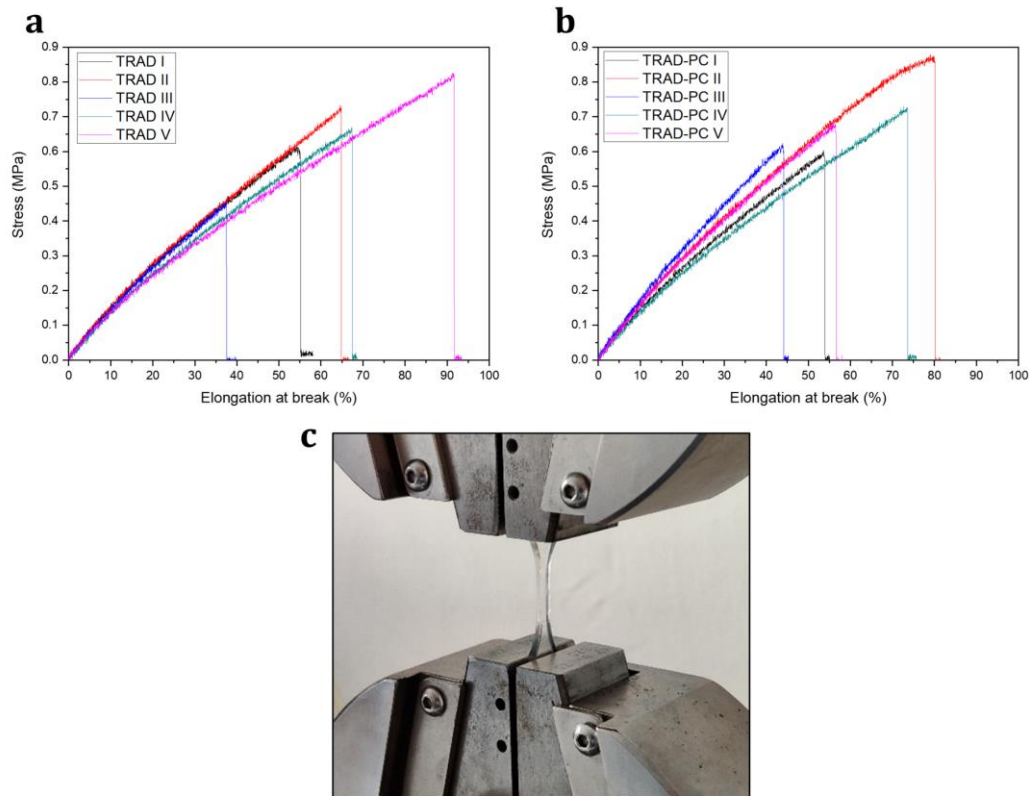


Figure 3-14. **Mechanical characterization of the 3D printed TRAD samples.** Stress (MPa) versus elongation at break (%) curves for (a) only 3D printed TRAD samples and (b) TRAD samples after 5 min of UV post-curing treatment. (c) photograph of one of the 3D printed TRAD samples used for the mechanical test (dog-bone with a gauge length of 20 mm). The UTS and young modulus values were higher for UV post-cured samples than just 3D printed samples, while elongation values at break were quite similar.

### 3.3.3. Conclusion.

In this part of the chapter, 3D printed acrylate-polydimethylsiloxane (PDMS) resins were processed through a commercial 3D-DLP printer to obtain complex-shaped 3D printed microfluidic devices giving thus, robust alternatives to conventional PDMS technologies. A study on the photocurable formulation was first performed by adequately selecting a compatible photoinitiator and a suitable dye with the silicone resin. Then, ATR-FTIR and photorheology analyses were performed to study the photopolymerization progress and conversion and obtain preliminary indications for the parameter optimization for the 3D printing step. Once the 3D printing settings were optimized, complex-shaped 3D printed structures with undeniably three-dimensional channels were fabricated. The 3D printed PDMS-based samples presented high chemical stability towards different solvents and good mechanical properties, comparable to the conventional PDMS elastomer used to fabricate microfluidic devices, Sylgard 184.

As a consequence of a correct selection of the components for the photopolymer's preparation, the printed pieces presented the characteristics sought, such as high optical transparency, stretchability, and flexibility. These features are fundamental to produce microfluidic chips, demonstrating thus the compatibility of this application with DLP-based 3D printing. The 3D printing of PDMS-based photopolymers could change the conventional routes of microfluidics fabrication by reducing the manufacturing costs and time, enabling the manufacturing of truly three-dimensional and complex-shaped microdevices.

The future activities on the developed silicone-based photopolymers will be focused on evaluating the cytotoxicity and biocompatibility of the obtained PDMS-like 3D printed structures and each of the formulation's components, following a series of investigations similar to those presented in Part I of this chapter. In this way, the potential application of such PDMS-based devices in the biomedical field could be genuinely evaluated, for instance, by using them for cell culture assays or drug screening experiments.

### 3.4. Conclusions of the chapter.

In this chapter, vat DLP 3D printing was used to 3D print objects with desired properties by fine-tuning the printable materials. Each of the elements used for the formulations' preparation was added to fulfill biomedical requirements (e.g., required optical transparency, good mechanical properties, suitable chemical resistance or stability, tunable surface characteristics, among others). Moreover, it was demonstrated that the structures' biocompatibility could be enhanced by performing a correct post-printing treatment. The different strategies showed in this chapter, in terms of materials used, post-printing treatments, and 3D printed freedom of design, could help develop practical microfluidic devices. Indeed, this thesis aims to combine different strategies and materials to produce biofunctional multi-material microfluidic platforms through 3D printing. As a proof of concept, a 3D printed bi-material fluidic chip was obtained in a single 3D printing step from two different photopolymers, as is shown in Figure 3-15.a,b. The printed object consisted of two-3D printed 96-well-like connected by a 1x1 mm channel. The transparent bottom of the chip (Figure 3-15.c) was made of the PEGDA250 formulation presented in Part I of Chapter 3 (with 0.2 wt.% of BAPO photoinitiator). The rest of the chip was made of the TRAD formulation presented in Part II of Chapter 3. Both materials remained well-attached after the printing process, allowing the creation of a bi-material object during the same 3D printing step by changing the photopolymer at a certain point in the process.

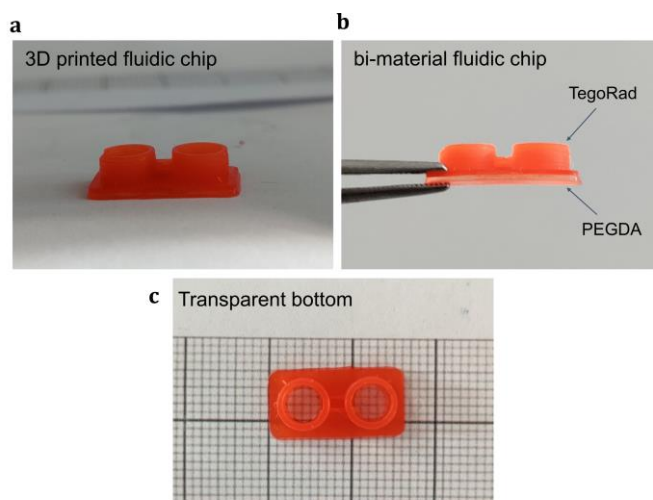


Figure 3-15. **3D printed bi-material fluidic chip.** (a) The devices were fabricated from a PEGDA250 formulation containing + 1 wt. % BAPO (the bottom of the chips) and the TRAD formulation with + 0.6 wt. % BAPO-Si + 0.01 wt. % DR1-MA dye (the rest of the chip). (b) Frontal view of the bi-material chip where is observed the distinction between both materials used. (c) top view of the chip showing the good transparency of the bottom of it. The bottom of the chip is 500  $\mu\text{m}$  thick. The device consists of two wells connected by a millifluidic channel of 1x1  $\text{mm}^2$  section.



## Chapter 4

# Post-printing treatments:

Enhancing the surface properties.

### 4.1. Overview and motivation.

As previously mentioned, vat 3D printing might enable the production of parts with controlled characteristics by operating on the formulation's elements and performing post-printing procedures. The latter was demonstrated as the utmost importance strategy to adjust the final features of the 3D parts, i.e., by removing the undesired elements from the components that can increase the biocompatibility (see Chapter 3, part I). An alternative approach could consist of surface functionalizing the printed parts by a dedicated post-3D printing treatment to induce additional features to the structures and achieve the highest potential for biomedical applications.<sup>414,415</sup> Such a procedure might be performed by coupling willfully functional groups on the 3D printed objects in a surface activation approach (unlike the post-printing protocol presented in Chapter 3, where the intention was to eliminate the cytotoxic elements from the printed parts through a surface passivation strategy). The functional groups can be either active biological molecules such as antibodies, peptides, nucleic acids, or biocompatible compounds that can stimulate specific bio-interactions.<sup>151,449</sup>

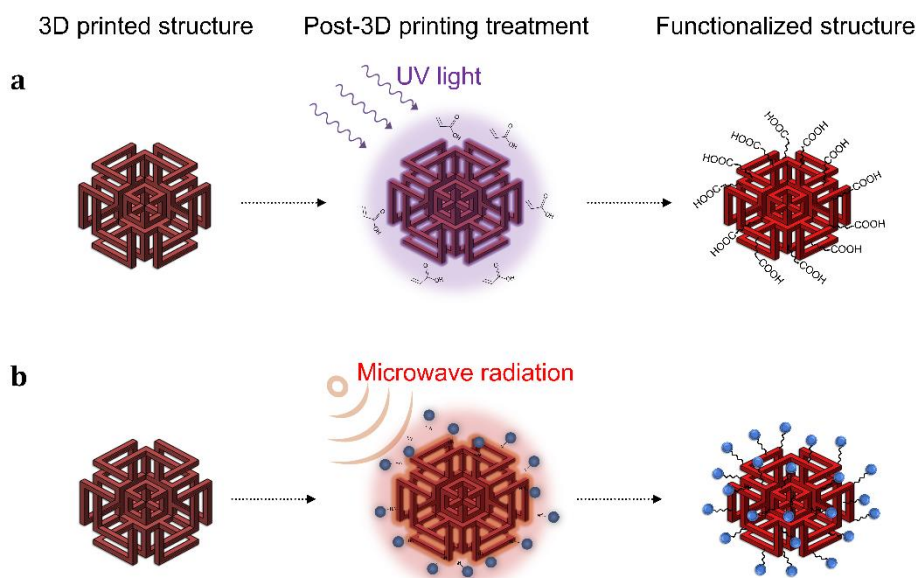


Figure 4-1. **Representation of the two functionalization strategies presented in Chapter 4.** Each strategy is based on chemically linking active molecules to the printed structures through a dedicated post-3D printing treatment following: (a) UV-induced approach or (b) microwave-induced approach.

Therefore, in this chapter, two post-3D printing protocols will be explored to activate the 3D printed parts surfaces, as represented in Figure 4-1. Part I will introduce a method to selectively surface functionalize PDMS-based structures (see Chapter 3, Part II) through UV-based post-3D printing strategy by exploiting the unreacted acrylate groups after the printing step, see Figure 4-1.a. These functional groups can be used to attach secondary molecules through UV-induced "grafting to" polymerization techniques during the required UV post-curing step.<sup>325</sup> The second functionalization strategy is presented in Part II, where a method based on the microwave-induced functionalization of polymeric 3D printed objects (containing both acrylate and epoxy functionalities) is proposed (see Figure 4-1.b). The epoxy moieties might remain pendent on the samples' surfaces since they do not react during the 3D printing step. Therefore, the epoxy groups' reactivity can be exploited in a dedicated post-printing procedure to induced surface modification on the hybrid 3D printed parts. The reaction involves using aliphatic polyamines of different molecular weights that could be attached through microwave irradiation. This process might allow the chemical linking of primary and secondary amines to the objects' surface due to the nucleophilic attack of the N atom's electron pair to both acrylate and glycidyl groups. Finally, taking advantage of amines' antimicrobial activity,<sup>450</sup> the antibacterial behavior of the microwave functionalized object will be briefly tested against *Staphylococcus aureus*.



## 4.2. Part I: Functionalization of 3D printed microfluidic chips.

Part II of Chapter 3 is based on the original research article titled "*Fabrication and Functionalization of 3D Printed Polydimethylsiloxane-Based Microfluidic Devices Obtained through Digital Light Processing.*" The paper was published in *Advanced Materials Technologies* scientific journal from Willey-Blackwell, **ISSN: 2365709X**.<sup>431</sup>

As demonstrated in Part II of Chapter 3, precise and complex-shaped microfluidic chips can be produced through DLP-3D printing techniques from a tailor-made photopolymer based on acrylate-polydimethylsiloxane (PDMS) resin. The printed chips presented the desired properties, e.g., such as chemical stability, flexibility, stretchability, and high optical transparency, due to the appropriate selection of materials during the printer resin preparation. Nevertheless, intending to increase these devices' versatility towards both well-established and new biomedical applications, these PDMS-based microfluidic chips' surface functionalization might be a crucial point. The literature has reported numerous methods for surface functionalizing PDMS-based microfluidic channels, including photo-mediated graft polymerization of monomers such as PEGDMA pNIPAAm acrylic acid onto PDMS.<sup>318,323,451</sup> Furthermore, more elaborate methods have also been reported based on "click" chemistry for the grafting of alkyne-PEG<sup>452</sup> or thiol groups.<sup>309</sup> Although these methods showed outstanding surface modification capabilities, they required multiple-step procedures to achieve the samples' functionalization.

Considering the characteristic of the 3D printed PDMS-based chips presented in Chapter 3, it will introduce a simple and selective surface functionalization method. After the printing step, all the 3D printed acrylate-based materials still present unreacted functional groups, including the acrylate-PDMS chips presented in Chapter 3. For this reason, a post-UV-curing treatment is usually performed on the samples to reach higher acrylic conversion, leading to an enhancement of the mechanical properties of the part, for example.<sup>145</sup> The unreacted acrylic double-bonds in the 3D printed TRAD parts can be exploited to attach other functional molecules through UV-induced "grafting to" polymerization techniques.<sup>325</sup> Thus, the required UV post-curing treatment could be used to achieve the highest possible acrylate conversion and, at the same time, functionalize the polymer surface. Therefore, these investigations aim to explore UV-induced modification strategies for chemically linking carboxylic functional groups to the sample's surfaces. The versatility of the 3D printed PDMS-based microfluidic chips could be increased by exploiting the required post-curing step, in this way, the surface properties of the printed microfluidic parts might be modified by following a suitable post-3D printing treatment.



#### 4.2.1. Experimental section.

##### *Materials*

Acrylic acid (**AA**, 99 %), acetonitrile (**ACN**,  $\geq 99.8\%$ ), and phenyl bis(2,4,6-trimethyl benzoyl)phosphine oxide (**BAPO**, 97 %) were used for preparing the grafting solution. All reagents were purchased from Merck Company (Darmstadt, Germany) and used as received.

##### *Preparation of the grafting solution*

The grafting solution used to functionalize the samples' surface was prepared by adding acrylic acid (AA) into acetonitrile (100 mg/mL); then two (2) wt.% (respect to the AA amount) of the BAPO photoinitiator was added for activating the polymerization. The solution was stirred mechanically for 5 minutes.

##### *Characterization methods*

Contact angle measurements were determined using an FTA 1000C goniometer, equipped with a video camera and an image analyzer. The tests were performed at room temperature using the sessile drop technique. A 3  $\mu\text{L}$  droplet of deionized water ( $72.1 \text{ mN}\cdot\text{m}^{-1}$ ) was placed onto the sample surface, and the static angle was measured. The test was repeated five times for each tested sample.

A Nicolet iS50 FT-IR spectrometer (Thermo Scientific, Milano, IT) equipped with attenuated total reflectance (ATR) accessory (Smart iTX) was used to investigate the presence of acrylate acid after the UV-induced surface functionalization step. The spectra were collected using an ATR accessory, collecting first the spectrum of untreated samples and after the different treatment conditions. For the FTIR experiments, the spectra were collected with a resolution of  $2 \text{ cm}^{-1}$ , averaging 32 scans for each spectrum, wavenumbers range  $600\text{--}3800 \text{ cm}^{-1}$ . The spectra were normalized using the  $790 \text{ cm}^{-1}$  peak corresponding to the Si-C asymmetrical bending or rocking vibration.<sup>453</sup>

#### 4.2.2. Results and discussion.

##### *UV-induced surface modification*

For the initial experiments, PDMS-based flat samples (10x15x1.5 mm) were 3D printed following the parameters presented in Chapter 3 for the

photopolymer based on the TegoRAD® oligomer. The procedure for the UV-induced surface modification is outlined in Figure 4-2. A few drops of the acrylic acid-based grafting solution were spread on the sample's surface and irradiated with UV light for different times (1, 5, and 10 min) using a high-pressure mercury arc lamp (Dymax ECE) set at  $10 \text{ mW}\cdot\text{cm}^{-2}$  of light intensity. Afterward, the samples were rinsed with ethanol for 10 min and washed extensively with deionized water for 30 minutes to remove unlinked polyacrylic acid.

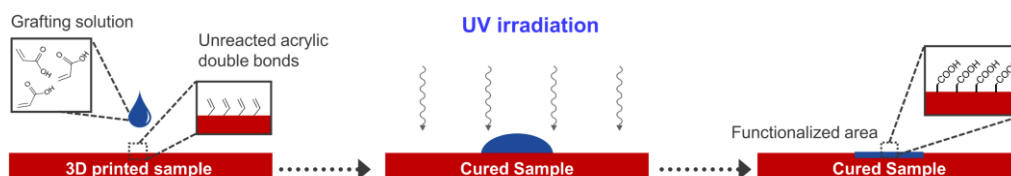
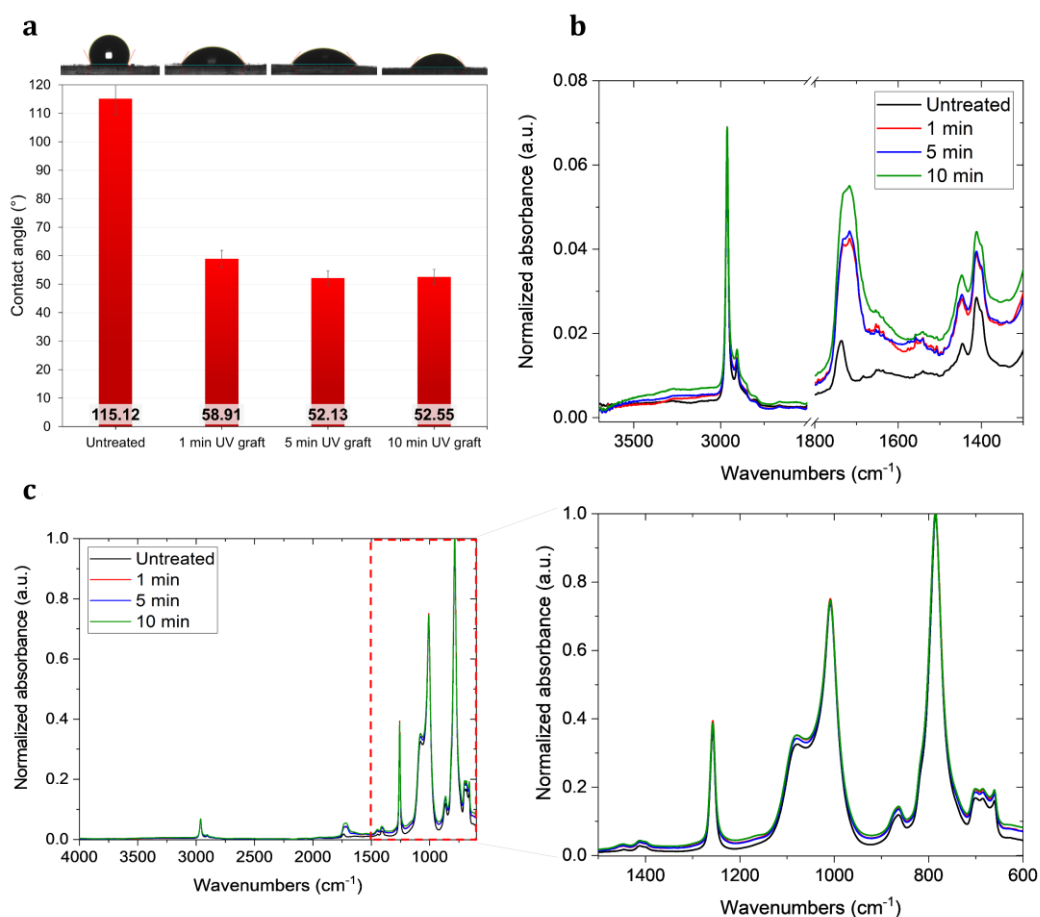


Figure 4-2. **Representation of the surface modification by UV light.** A few drops of the acrylic-based grafting solution are deposited over the sample surface; then, the system is UV irradiated for a certain time. The sample surface remained chemically modified after the UV-induced treatment.

The water contact angle changes were measured five times for treated and untreated samples (see Figure 4-3.a). The wettability of the samples was changed according to the UV-induced surface modification treatment: untreated TRAD samples presented a contact angle of  $115.1^\circ \pm 0.5^\circ$ , which drastically decreased to  $58.9^\circ \pm 2.7^\circ$  after 1 min of irradiation and did not further decrease for longer irradiation time. ATR-FTIR spectra were recorded on treated and untreated samples to confirm the presence of poly (acrylic acid), and the results are shown in Figure 4-3.b. The spectra were normalized using the  $790 \text{ cm}^{-1}$  peak corresponding to the Si-C asymmetrical bending or rocking vibration, see Figure 4-3.c.<sup>453</sup> The spectra revealed the presence of carboxylic acid groups with wide-ranging absorption bands of the O-H stretch around  $3500\text{-}2500 \text{ cm}^{-1}$ ,<sup>324</sup> and a sharp carbonyl peak (C=O) in the  $1760\text{-}1690 \text{ cm}^{-1}$  region.<sup>454</sup> These results confirmed the poly (acrylic acid) grafting onto silicone samples' surface due to UV-induced grafting.



**Figure 4-3. Surface properties changes of the TRAD samples after the UV-induced grafting surface modification.** (a) Contact angle measurements from untreated and UV-treated samples (at different irradiation times) showing a decrease of the contact angle after the UV-grafting surface modification. (b) ATR-FTIR spectra of untreated and UV-treated samples (at different irradiation times) where the presence of linked carboxylic acid groups over the samples can be observed by analyzing the increase in spectra regions of 3500-2500  $\text{cm}^{-1}$  (associated to O-H stretch) and 1760-1690  $\text{cm}^{-1}$  associated to the carbonyl group, confirming the surface modification. (c) Normalized spectra from the TRAD samples after the different UV-induced grafting treatments showing the peak used for normalizing the spectra centered at 790  $\text{cm}^{-1}$  peak that corresponds to the Si-C asymmetrical bending or rocking vibration.

ATR-FTIR spectra were recorded on treated and untreated samples to confirm the presence of poly (acrylic acid), and the results are shown in Figure 4-3.b. The spectra were normalized using the 790  $\text{cm}^{-1}$  peak corresponding to the Si-C asymmetrical bending or rocking vibration, see Figure 4-3.c.<sup>453</sup> The spectra revealed the presence of carboxylic acid groups with wide-ranging absorption bands of the O-H stretch around 3500-2500  $\text{cm}^{-1}$ ,<sup>324</sup> and a sharp carbonyl peak (C=O) in the 1760-1690  $\text{cm}^{-1}$  region.<sup>454</sup> These results confirmed the poly (acrylic acid) grafting onto silicone samples' surface due to UV-induced grafting. The next step investigated was to induce surface

modification inside the cavity of a 3D printed structure. For this purpose, chips with an inner chamber were designed and 3D printed as represented in Figure 4-4.a (see Figure 4-4.b for more details).

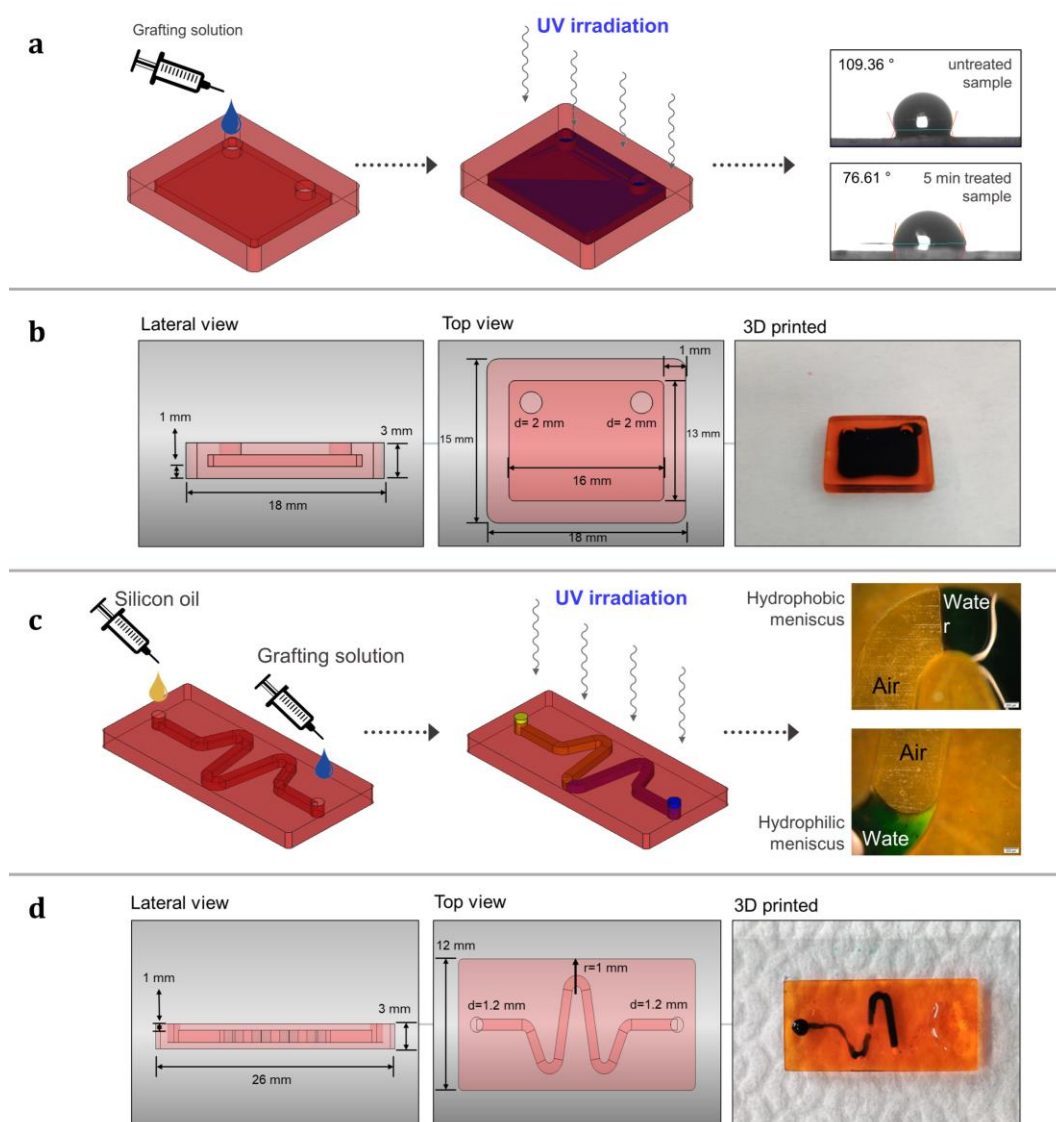


Figure 4-4. **Representation of the UV-induced surface modification of 3D printed TRAD samples.** (a) Representation of the surface modification carried out inside the inner chamber of a 3D printed TRAD samples, where on the right side of the image displays the contact angle decrease after functionalizing step compared to the untreated sample can be observed. (b) CAD designs and a photograph of a 3D printed chip with an internal chamber filled with green colored water is shown. (c) Representation of the UV-induced surface modifications in an S-shaped millifluidic chip. The test showed the channel's selective functionalization by observing, in the same channel, the hydrophobic behavior (part of the channel with no treatment) and the hydrophilic behavior of the treated part of the channel. (d) CAD designs and a photograph of the S-shaped 3D printed chip filled half with green colored water and a half with silicon oil.

The internal chamber ( $16 \times 13 \times 1 \text{ mm}^3$ ) was closed with a 1 mm thick cap-layer. A few drops of the AA-based grafting solution were introduced in the

chamber, and then the samples were subjected to UV irradiation for 5 minutes. After the rising/washing protocol in ethanol and water, respectively, the top of the samples was cut lengthwise, and changes in the wettability of the internal surfaces of the samples were determined. As shown in Figure 4-4.a, the water contact angle decreased from  $109.36^\circ$  to  $76.61^\circ$  for untreated and treated samples, respectively. This result validates that the UV-induced surface modification can be performed even in a closed 3D printed object, which confirms the high light transparency at these wavelengths achieved by this technology for microfluidic device preparation. A similar procedure was repeated on a 3D printed millifluidic chip fabricated with one S-shaped channel with a cross-section of  $1 \times 1 \text{ mm}^2$ . In this case, to selectively functionalize the channels (see Figure 4-4.d for more details), half of the microfluidic chip was filled with silicon oil and the other half with the grafting solution (Figure 4-4.c). After 5 minutes of UV irradiation followed by the washing protocol, the inner surface wettability was analyzed by loading the channels with green colored deionized water and observing the stationary meniscus changes through optical microscopy in Figure 4-4.c. As expected, a clear difference was observed between the two halves of the channel, passing from a hydrophobic meniscus in the unfunctionalized part of the channel to a hydrophilic meniscus in the UV-grafted side.

### 4.2.3. Conclusion.

This part of the present chapter demonstrated that 3D printed samples' surface properties can be modified through the correct post-printing protocol by exploiting the still reactive functional groups on the sample's surface. These groups were used to link other functional molecules during the required UV post-curing step through UV-induced grafting polymerization techniques. Following this strategy, 3D printed PDMS-based chips' surface properties were easily and selectively modified even in a closed 3D printed chip.

As proven, it was feasible to perform an easy surface functionalization taking advantage of the unreacted acrylate double bond remaining after the 3D printing step. This methodology gives an added value in terms of surface properties to the printed devices by engineering their surface properties comparing to traditional functionalization methods. For example, by employing this UV-grafting approach, the functionalities of a multi-material microfluidic device can be improved. The configuration of channels within this device could have different characteristics given by the various materials used and a post-3D printing practice that can introduce additional functional molecules, such as carboxyl groups (-COOH), in this case. These exposed groups can be used in biosensing applications as anchoring sites for the immobilization of amino-functionalized proteins.<sup>334,455-457</sup>

### 4.3. Part II: Surface modification by microwave radiation.

The investigations presented in Part II of Chapter 4 were performed at both the Institute of Polymer Science and Technology (ICTP) laboratories in Madrid, a division from the Spanish National Research Council (CSIC); and the Institute for Biofunctional Studies of the Universidad Complutense de Madrid.

In part I of this chapter, a UV-mediated approach was presented to functionalize the printed objects' surface by taking advantage of unreacted functional groups after the 3D printing step. Another strategy might include functional groups into the printable resin that can be exploited in a dedicated post-printing step to induce surface modification. In this context, here, it will be introduced a functionalization strategy based on exploiting pendant epoxy groups on the sample's surface for coupling other molecules through microwave radiation. The epoxy moieties were introduced in the 3D printed acrylate network through the use of glycidyl methacrylate. Since epoxy moieties do not cure nor react in the radical photopolymerization processes, those can be used for the subsequent functionalization step. The reaction proposed here proceeds through the nucleophilic ring-opening reaction of the epoxide groups, allowing the chemical link of aliphatic amines onto the reactive objects. The reaction between epoxy and amines functionalities is usually activated thermally and can even proceed at room temperature in the appropriate conditions.<sup>458</sup> Instead, here, this reaction will be induced using microwave irradiation. In this way, the reaction times could be considerably shortened by providing the right microwave energy to the system.<sup>459-461</sup> The extent of surface functionalization was evaluated by varying experimental parameters, such as the acrylate/epoxy ratio and irradiation conditions. The samples' functionalization will proceed under microwave radiation, a type of energy associated with electromagnetic radiation with wavelength ranging from 300 MHz (1 m) to 300 GHz (1 mm). The microwaves can easily penetrate the material and heat simultaneously the system by the vibration and rotation effects of the dielectric substance, decreasing the heat transfer problems.<sup>462</sup> Therefore, over conventional thermal methods, the microwave technique might offer novel possibilities in reaction performances by mainly shortening the reaction times, maintaining (or increasing) the yield of products. Besides, it is an inexpensive and facile technique that also minimized the by-product formation.<sup>463</sup> Due to MW-radiation methods' benefits, they have been used for performing various organic and inorganic chemical transformations, e.g., cycloaddition and aza-Michael reaction.<sup>464</sup> Indeed, they can be used to induce surface properties on materials such as polypropylene (PP) or metallocene polyethylene (mPE) films and thus obtain materials with improved wettability biocompatibility by partially oxidizing their surfaces.<sup>465,466</sup> Likewise, MW radiation can promote specific chemical reactions between functional groups,

e.g., the covalent functionalization of carbon nanotubes (CNTs) by coupling amine molecules to carboxyl groups; or the ring-opening polymerization of epoxy with amine-terminated compounds.<sup>459,467</sup> Therefore, by controlling the microwave radiation conditions (e.g., the energy delivered to the system and the time of MW exposure), interesting chemical reactions can efficiently be achieved.

A series of experimental analyses will be performed for optimizing the microwave-assisted functionalization procedure to find a compromise between the desired surface properties and the sample's condition. Once optimized the functionalization process for each sample obtained, the antibacterial behavior will be tested against *Staphylococcus aureus*, considering the antimicrobial activity of amines.<sup>450</sup> This model was chosen due to its clinical importance, being responsible for many diseases such as skin infections, pneumonia, septicemia, ocular infections, abscesses, central nervous system infections, and, in some cases, food poisoning.<sup>468-470</sup> Therefore, developing new antibiotic methods and materials against this bacterial model could be of great interest in the medical sector.



### 4.3.1. Experimental section.

#### Materials

As reactive monomers, poly(ethylene) glycol diacrylate (**PEGDA250250**,  $M_n = 250$  g/mol) and glycidyl methacrylate (**GMA**,  $M_n = 142.15$  g/mol) were used. As a photoinitiator, phenyl bis(2,4,6-trimethylbenzoyl)phosphine oxide (**BAPO**, 97 %) was used. To increase the printing resolutions, disperse red one methacrylate (**DR1-MA**, 95 %) was used as a visible light absorber. As amine-based reagents, diethylenetriamine (**DETA**,  $M_w = 103.17$  g/mol), and two types of hyperbranched polyethyleneimine (**PEI600**,  $M_n \sim 600$  g/mol) and 10kDa (**PEI10k**,  $M_n \sim 10000$  g/mol) were used. Ethanol (99.8 %) and acetonitrile ( $\geq 99.8\%$ ) were also used to prepare microwave solutions. All reagents were purchased from Merck Company (Darmstadt, Germany) and used as received. The chemical structures of the reagents used in this works are represented in Figure 4-5. The ratio of primary/secondary/tertiary amine groups in DETA, PIE600 and PEI10k are 1:0.5:0, 1:0.82:0.53, and 1:1.2:0.76.<sup>145,471</sup>

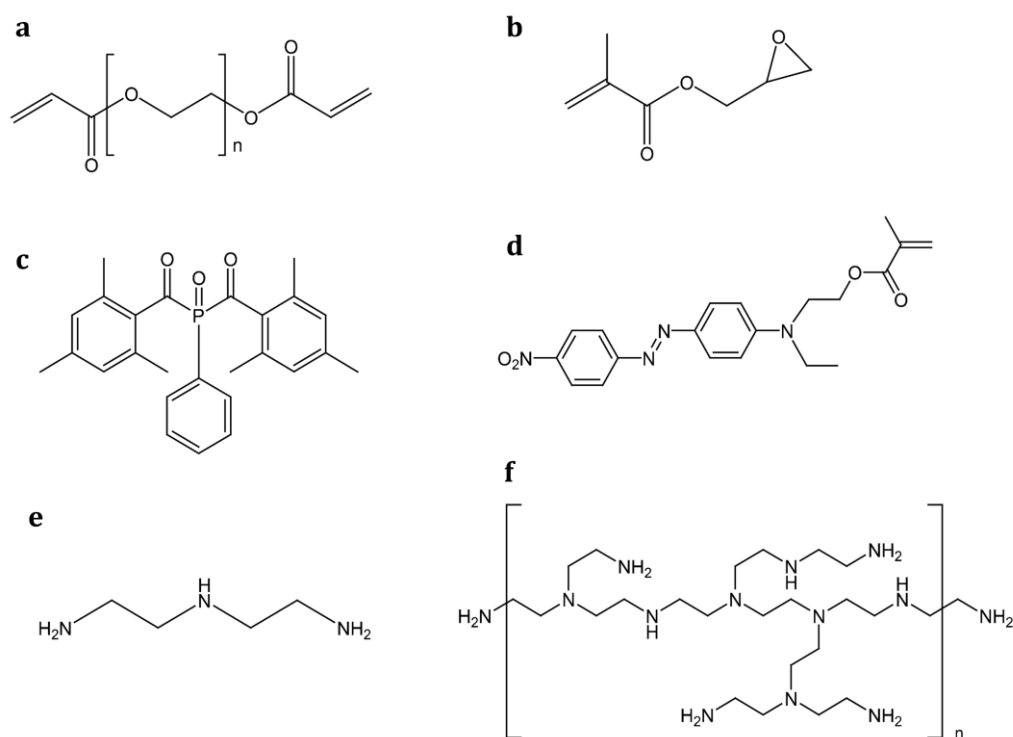


Figure 4-5. **Chemical structures of the chemical reagents used.** (a) polyethylene glycol diacrylate (**PEGDA250**). (b) glycidyl methacrylate (**GMA**). (c) phenyl bis(2,4,6-trimethylbenzoyl) phosphine oxide (**BAPO**). (d) disperse red one methacrylate (**DR1-MA**). (e) diethylenetriamine (**DETA**). (f) hyperbranched polyethyleneimine (**PEI**).

### *Preparation of the photopolymers and grafting solutions*

Four photocurable formulations were prepared with different weight ratios between monomers: 5:5, 7:3, 9:1, and 10:0 PEGDA250/GMA. The molar ratio between PEGDA250250 and GMA is reported in Table 4-1. Each formulation was prepared by adding 1 wt.% of BAPO and 0.01 wt.% of DR1-MA dye; then, they were stirred mechanically at room temperature until a complete homogeneous solution was obtained. For the microwave-assisted surface functionalization, three amines-based solutions were prepared:

- (i) DETA solution, composed of diethylenetriamine in acetonitrile (200 mg/6mL)
- (ii) PEI600 solution, composed of poly(ethylenimine) 600Da in acetonitrile (200 mg/6mL)
- (iii) PEI10k solution, composed of polyethyleneimine 10kDa in a 12:1 mixture of acetonitrile and ethanol (87 mg/6.5mL). Higher led to substance precipitation; ethanol was added to improve the miscibility of PEI10k.

### *Digital light processing DLP-3D printer*

As 3D printing equipment, a Pico 2 HD DLP-3D printer (Asiga, Australia). This 3D printer has a LED light source (405 nm), nominal XY pixel resolution of 50  $\mu\text{m}$ , and minimum Z-axis control of 1  $\mu\text{m}$ . The structures were produced by fixing a printing slicing of 50  $\mu\text{m}$  and a light intensity of 20 mW/cm<sup>2</sup>. The light exposure time was set according to the formulation used, as shown in Table 4-1. All CAD designs were produced with the FreeCAD program and exported in STL format.

Table 4-1. Weight percent (%), molar acrylate/epoxy ratio for each PEGDA250 and GMA formulation, and the 3D printing settings used for each formulation with 50  $\mu\text{m}$  of slicing thickness.

<b>Formulation</b>	<b>PEGDA250 (wt.%)</b>	<b>GMA (wt.%)</b>	<b>Acrylate/epoxy molar ratio</b>	<b>Exposure time (s/layer)</b>	<b>Initial exposure time (s/layer)<sup>a)</sup></b>
PEGDA250	100	-	-	1.2	3
9:1 PEGDA250/GMA	90	10	10.23:1	1.5	3
7:3 PEGDA250/GMA	70	30	2.65:1	5	9
5:5 PEGAD250/GMA	50	50	1.14:1	10	14

<sup>a)</sup> Irradiation time for the first three layers to guarantee an adequate adhesion of the parts.

### *Surface functionalization procedure with microwave*

An Anton Paar Monowave 300 microwave reactor provided with an infrared sensor (IR pyrometer) was used for the surface modifications. The reaction was performed under magnetic stirring inside a pressure-resistant 10 mL glass tube (0.9 cm diameter) sealed with silicon septum. For the microwave-assisted surface modification procedure, in a glass tube (vial of 10 mL), the samples were submerged into 5 mL of the desired amine solution; the vial was then introduced in the microwave reactor under the following conditions, as represented in Figure 4-6:

1. First, the sample is heated from room temperature to 150°.
2. According to the treatment process, the system is then subjected to an isothermal step of MW radiation for a specific time (t).
3. Finally, the sample is cooled down from 150 ° to 55 ° C.

The reactor delivers the energy (W) necessary to reach the input parameters (i.e., temperature and reaction time). After MW treatment, all samples were rapidly transferred to a vial filled with milli-Q water, in which they were kept for one hour under slow magnetic stirring to remove the excess of unreacted amines from the surface. At last, samples were placed under vacuum (-70 cmHg, 25°C) for 12 hours before surface characterization.

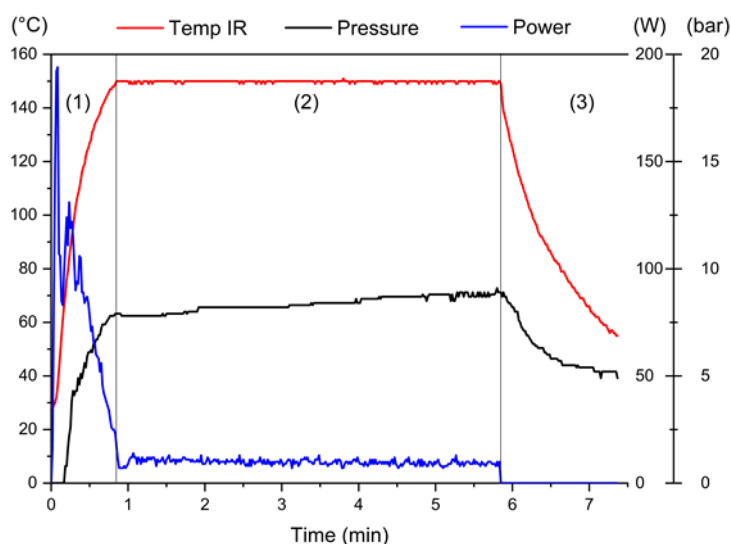


Figure 4-6. **Representative chart example of a microwave treatment performed on one of the samples used in this work.** The graph shows the different parameters during the microwave treatment, such as the power (W) and pressure (bar) given from the reactor to the system to reach the desired temperature (°C) during a specific time (t).

### Characterization methods

An FT-IR spectrometer (Nicolet iS50, Thermo Scientific, Milano, IT) was used to calculate the conversion of epoxy and acrylate double-bonds on the samples at different experimental conditions. The spectra were collected on an attenuated total reflectance (ATR) system (Smart iTX). Epoxy conversions were calculated by analyzing the peak at  $905\text{ cm}^{-1}$  related to the oxirane group's C-O deformation, while the acrylate double-bonds conversions were calculated by monitoring the peak at  $810\text{ cm}^{-1}$ , which corresponds to the C=C bonds' twisting.<sup>472,473461</sup> The spectra were collected with a resolution of  $4\text{ cm}^{-1}$  averaging 32 scans for each spectrum in the wavenumber range of  $650\text{--}4000\text{ cm}^{-1}$ . Furthermore, the surface properties of the microwave treated samples were evaluated following the region associated with N-H bond stretching of primary ( $3600\text{--}3400\text{ cm}^{-1}$ ) and secondary amines ( $3400\text{--}3200\text{ cm}^{-1}$ ), and the region associated with C-H bonds ( $3000\text{--}2800\text{ cm}^{-1}$ ). All IR spectra were normalized using carbonyl peak at  $1720\text{ cm}^{-1}$ .

Static contact angle measurements were performed on 3D printed flat samples after different microwave treatment conditions and untreated samples using a KSV instrument LTD with CAM 200 analyzer program (Helsinki, Finland) equipped with a Basler A602f-2 camera. The tests were performed at room temperature with the sessile drop technique. A  $3\text{ }\mu\text{L}$  droplet of deionized water ( $72.1\text{ mN}\cdot\text{m}^{-1}$ ) was placed onto the sample, and the static angle was measured immediately after drop deposition. The measurement was repeated five times for each condition.

### Bacterial seeding

The antibacterial activity was studied against the *Staphylococcus aureus* colony. To promote bacterial culture transition into the exponential growth phase, a single *S. aureus* colony was overnight cultured at  $37\text{ }^{\circ}\text{C}$  in a flask containing nutrient broth (NB) media ( $13\text{ g/L}$  distilled water) under constant shaking of  $120\text{ rpm}$ . The bacteria concentration was diluted in fresh NB media to obtain an optical density (OD) value of  $0.69$ . The PEGDA250/GMA samples (disks of  $150\text{ }\mu\text{m}$  thick and  $9\text{ mm}$  diameter) with and without MW-induced surface modification were collocated in a 24-well plate (three replicates). Then  $500\text{ }\mu\text{L}$  of the bacterial suspension was incubated in each well for one (1) hour. After the incubation, the samples were washed three times using PBS (Phosphate Saline Buffer,  $150\text{ mM NaCl}$ ,  $50\text{ mM phosphate pH }7.4$ ), and the bacteria culture was allowed to grow for  $48\text{ h}$ .

### *Bacteria viability and proliferation*

The bacterial viability was measured using live/dead BacLight Bacterial Viability Kit (Thermo Fischer Scientific, Massachusetts, USA) by following the manufacturer's instructions. This essay examines the cells' membrane integrity, staining green (SYTO® 9) when they are intact or red (propidium iodide) when the membrane is compromised. The fluorescent green bacteria were photographed using a FITC filter, and red fluorescent-labeled cells were observed with a TRICT filter ( $\lambda_{ex}/\lambda_{em} = 550/600$  nm).

The bacteria quantification on each sample was carried out by calculating the number of bacteria per unit area on the images obtained using the fluorescence microscope. The images were corrected in terms of brightness and contrast. Each photograph was divided into four quadrants for subsequent analysis and quantification of bacteria using the ImageJ software. Three (3) steps were carried out for the bacteria quantification: transforming the images to 8 bits, applying a manual threshold, and obtaining a coverage value in terms of percentage of the surface of live and dead bacteria for each sample.

### 4.3.2. Results and discussion.

#### *Characterization and functionalization of the 3D printed samples*

Photocurable acrylate/epoxy formulations were developed, aiming to produce polymeric components with surface-available epoxy groups that can be used to link aliphatic polyamines (DETA, PEI600, and PEI10k) upon microwave irradiation, as represented in Figure 4-7.a. By providing the system with the right microwave energy, the time of reactions might be considerably shortened compared to conventional approaches performed at standard pressure and temperature conditions.<sup>458</sup> For this purpose, formulations with different weight ratios between PEGDA250 and GMA monomers (5:5, 7:3, 9:1, and pristine PEGDA250) were prepared and processed using a desktop 3D-DLP printer. Low-molecular-weight polyethylene glycol diacrylate (PEGDA250) is a highly reactive photocurable monomer commonly used for light-based 3D printing.<sup>150,380,402</sup> Glycidyl methacrylate (GMA) monomer was selected for incorporating epoxy groups to the polymeric structures by copolymerization with PEGDA250 during the 3D printing step.<sup>112</sup>

All types of formulations were prepared with 1 wt.% of BAPO photoinitiator and 0.01 wt.% of DR1-MA dye. As shown in Figure 4-7.b-c, basic and complex-shaped structures were easily 3D printed from PEGDA250/GMA formulations following the printing settings reported in Table 4-1. Once the 3D printing step was finished, the surface features of the samples were evaluated through ATR-FTIR techniques, see Figure 4-8. The spectra showed epoxy groups' presence on the samples containing glycidyl monomer (5:5, 7:3, and 9:1 PEGDA250/GMA) by examining the 905  $\text{cm}^{-1}$  epoxy band.<sup>461,473</sup> These epoxy groups remained invariable after the 3D printing step, which indicates that the epoxy rings do not react during the 3D printing step, as expected. The signal of epoxy rings in the poly(PEGDA250-co-GMA) systems is more evident, increasing GMA monomer's amount in the formulation.

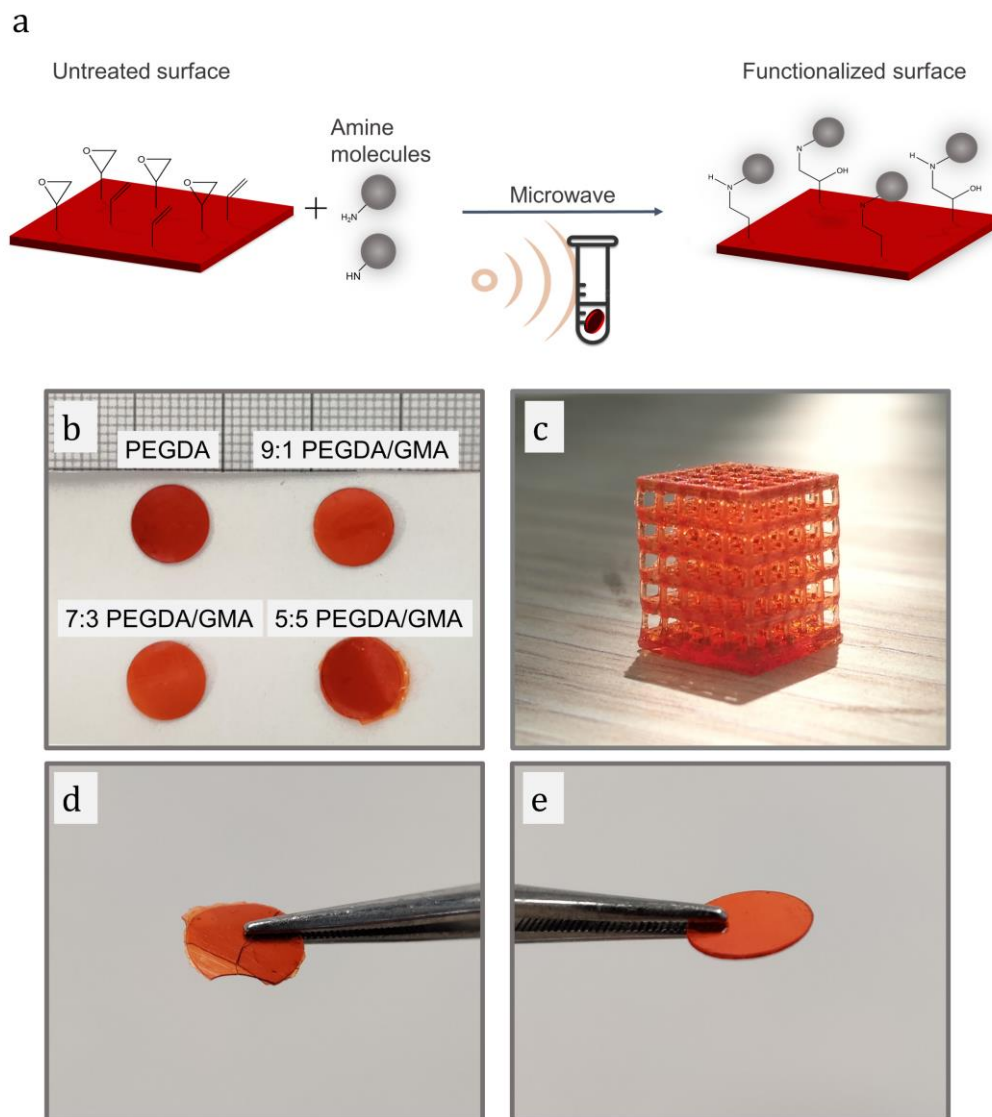


**Figure 4-7. Images of the microwave-induced surface modification of the 3D printed structures made from PEGDA250/GMA resins.** (a) An image that outlines the surface functionalization procedure with microwaves of 3D printed PEGDA250/GMA structures using amine-based solutions. (b) Photo of 3D printed disks (150  $\mu\text{m}$  thick and 9 mm in diameter) obtained from 5:5, 7:3, 9:1, and 10:0 PEGDA250/GMA formulations. (c) A complex-shaped 3D printed structure (10x10x10  $\text{mm}^3$ ) obtained from 7:3 PEGDA250/GMA formulation displaying the good resolution achieved. (d) MW-treated 3D printed samples with the PEI600 solution for 5 minutes where the sample's damage after the treatment is shown. (e) MW-treated samples in the PEI600 solution for 30 seconds showing the sample suffered no damage. All the formulations contained 1 wt.% of BAPO and 0.01 wt.% of DR1-MA dye

The difference in acrylate peak reduction between the systems is correlated to the GMA's lower functionality ( $f = 2$ ), which acts as a reactive diluent and tends to delay the gelation, leading to a more loosely network when comparing to the matrix formed by the homopolymerization of

PEGDA250 ( $f = 4$ ). Therefore, the poly(PEGDA250-co-GMA) structure had a better capacity to reach higher double bond conversion due to the component's diffusion effects in a less dense network, promoting a more significant reaction propagation.<sup>474,475</sup>

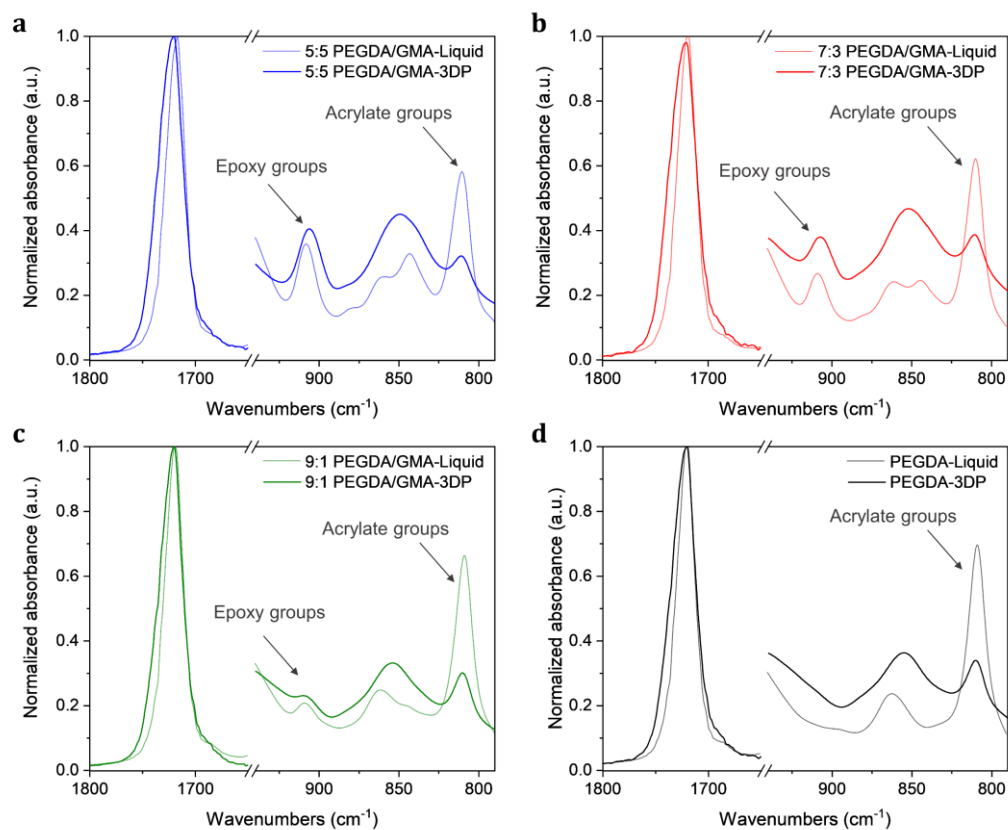


**Figure 4-8. Characterization of the 3D printed samples by the FTIR spectroscopy technique for determining the available functional groups.** In the graph, the acrylate and epoxy functional groups can be observed at  $810\text{ cm}^{-1}$  and  $905\text{ cm}^{-1}$ , respectively. The available functionalities might potentially be used for linking additional molecules (e.g., amines). Normalize FTIR spectra of liquid formulations, and 3D printed samples made of (a) 5:5 PEGDA250/GMA, (b) 7:3 PEGDA250/GMA, (c) 9:1 PEGDA250/GMA, and (d) pristine PEGDA250 mixtures with 1 wt.% of BAPO. The spectra were normalized using the carbonyl (C=O) signal centered at  $1720\text{ cm}^{-1}$ .

As shown in Figure 4-8, after the 3D printing step, both the epoxy and acrylate functionalities remained present in the objects. These reactive functionalities might be used to chemically link primary and secondary amines to the sample's surface (as represented in Figure 4-7.a). These reactions have been widely reported in the literature, and they proceed through the nucleophilic attack of the electron pair of the N atom to both acrylate and glycidyl groups.<sup>145,476–479</sup> Therefore, to assess the possibility of functionalizing the 3D printed samples with amines, a series of experiments were carried out to explore the samples' successful functionalization by either microwave



radiation or conventional stirring methods. These preliminary experiments were analyzed through the FTIR spectroscopy technique and measuring the changes in the treated samples' surface energy compared to the untreated ones. The correct incorporation of amino functionalities on the samples could introduce antibacterial properties over the printed structures, given the amines' known antimicrobial characteristic.<sup>450</sup> Indeed, the antimicrobial activity of the amine-treated samples will also be tested against *Staphylococcus aureus*. This bacteria model is known to be responsible for many infections-related diseases.<sup>468-470</sup>

The first set of experiments were addressed to functionalize the printed structures by submerging them in different amine-based grafting solutions. The system was then subjected to mechanical stirring and room temperature ( $T = 25^{\circ} \text{C}$ ). The grafting solutions were prepared as reported in the experimental section using three aliphatic polyamines of different molecular weights: linear diethylenetriamine (DETA) and two hyperbranched polyethyleneimine types (PEI600 and PEI10k). These amines were selected since they have been previously used in reactions with epoxy and acrylates with good results.<sup>480-483</sup> Besides, they present interesting antibacterial properties, which could be of great interest for our purposes.<sup>458,484-487</sup> For the treatment, 3D printed disks (disks of  $150 \mu\text{m}$  thick and  $9 \text{mm}$  diameter) were made from 5:5 PEGDA250/GMA (samples with higher glycidyl content) and immersed into a grafting solution composed of one of the aliphatic polyamines diluted in acetonitrile. The grafting solution could also be prepared using ethanol; however, all the samples broke after few minutes submerged in the solution; hence acetonitrile was preferred. After the modification treatment, the samples were washed in distilled water for 1 hour and vacuum dried for 12 hours for removing unbounded amines. The changes in the samples' surface properties of the treated samples were evaluated through the ATR-FTIR technique, see Figure 4-9. After 24 hours under mechanical stirring, only the samples treated with the DETA solution showed a considerable reduction of the epoxy-related band at  $905 \text{cm}^{-1}$ , see Figure 4-9.a-c, and longer stirring times in the DETA solution did not promote a higher epoxy reaction. Instead, the samples treated with the PEI600 and PEI10k solutions did not react even after 96 hours of continuous stirring at  $25^{\circ} \text{C}$ . The differences in epoxy conversion between the samples and the amine solution might be attributed to the amine molecules' steric hindrance and reactivity, being the DETA molecule more reactive than hyperbranched amine molecules with a bulkier molecule configuration.<sup>488</sup> Nevertheless, if the system is provided with thermal energy, the reaction could take place. As seen in Figure 4-9.d, there was a total disappearance of the epoxy-related band after 48 hours of mechanical stirring of the 5:5 PEGDA250/GMA samples using the PEI10k solution when the temperature was set at  $60^{\circ} \text{C}$ . Another observation is that acrylate-related bands at  $810 \text{cm}^{-1}$  decrease notably, having a greater

reduction than the epoxy band, for all the samples already after 24 hours. This behavior is attributed to the reaction between the vinyl double-bonds with primary/secondary amines.

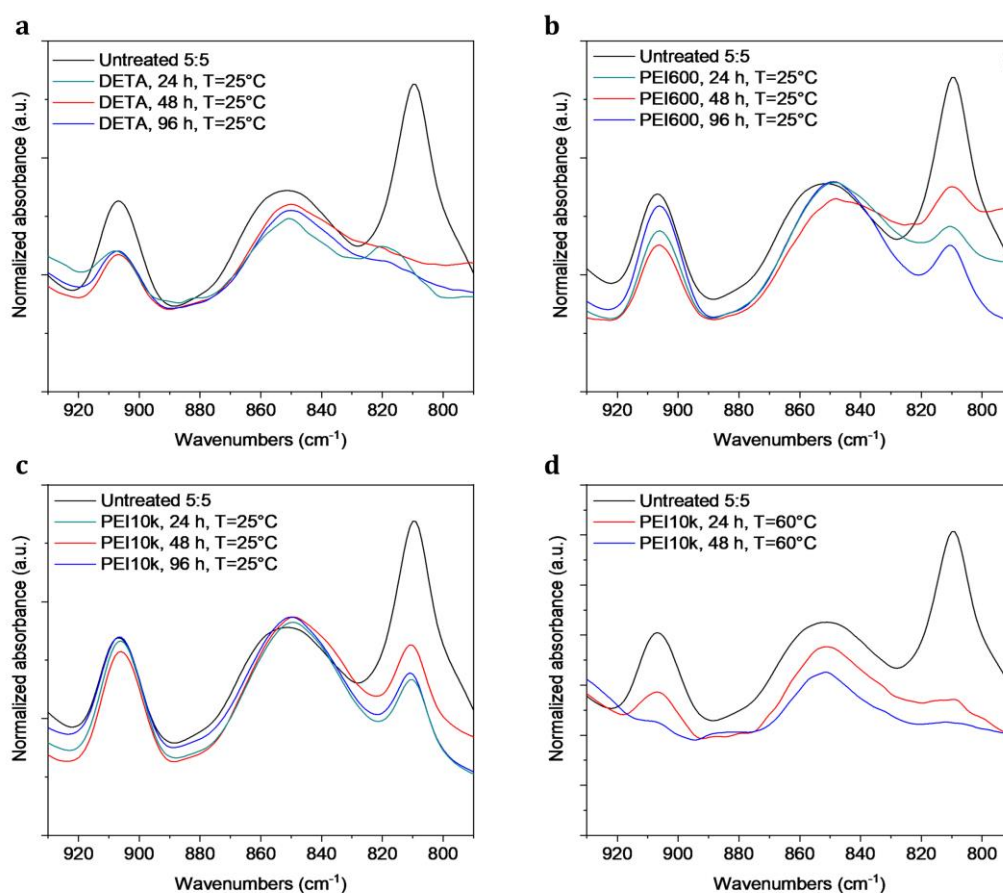


Figure 4-9. **Characterization of the 3D printed samples (by the FTIR spectroscopy technique) after functionalization under mechanical stirring and certain temperature conditions.** The FTIR spectra curves show the decreasing of the acrylate and epoxy-related bands at  $905\text{ cm}^{-1}$  and  $810\text{ cm}^{-1}$ , respectively, for the treated samples. The tests were performed on 5:5 PEGDA250/GMA samples using (a) DETA solution, (b) PEI600 solution, and (c) PEI10k solution; the tests were run at 24, 48, and 96 hours at room temperature ( $T = 25^\circ\text{C}$ ) under continuous mechanical stirring. Even though the reaction took place in this condition, the reaction times can be lengthy. (d) FTIR results from 5:5 PEGDA250/GMA treated with the PEI10k solution at  $60^\circ\text{C}$  under continuous mechanical stirring for 24 and 48 hours, where it can be observed that the conversion of the functional groups might be boosted by increasing the system temperature.

#### *Microwave-assisted surface modification*

The following tests were led to induce the same type of surface modification of the PEGDA250/GMA samples, this time, using microwave radiation to promote a more efficient reaction. The cationic reaction between amines and acrylate/epoxy groups might proceed faster through microwave

irradiation and might yield higher conversions. Over conventional reaction methods, microwave irradiation offers unique advantages, e.g., the reaction times and the generation of by-side products can be significantly reduced, and using inert atmospheres or toxic solvents during the process can be avoided.<sup>464,489-491</sup> The initial investigations were performed using the PEI600 solution, with an intermediate reactivity character and volume configuration than DETA and PEI10k molecules. Besides, PEI600 have been reported as efficient components to react with GMA.<sup>471,492</sup> These first trials were performed upon microwave irradiation for 5 minutes to guarantee sufficient time to achieve the functionalization. After the MW-treatment, the samples were washed in distilled water (1 hour) and vacuum dried (12 hours). The samples' surface properties were observed through the ATR-FTIR technique, see Figure 4-10. The spectra show a complete disappearance of the band related to epoxy rings at  $905\text{ cm}^{-1}$  for samples with glycidyl monomer after 5 minutes of MW-treatments, indicating that the epoxy ring-opening reaction with amines took place much faster than the previously reported conventional method under mechanical stirring. Likewise, in Figure 4-10, the acrylate double-bond band at  $810\text{ cm}^{-1}$  decreases considerably after the MW treatment. This behavior could be attributed to the reaction between the vinyl double-bonds with primary/secondary amines and the thermal contribution caused by the microwave radiation (as it will be evaluated later).

The surface functionalization of amine-treated samples (through covalent N-C bond) was demonstrated by the appearance of a new strong band in the  $3600\text{-}3200\text{ cm}^{-1}$  region, corresponding to N-H bond stretching. Besides, an increase in the band's intensity in the  $3000\text{-}2800\text{ cm}^{-1}$  region (C-H bonds) is observed. Hence, primary and secondary amines were ostensibly linked to the sample's surface, as reported in the literature.<sup>493</sup> Although the surface functionalization might be achieved in these conditions, some samples, in particular, 5:5 PEGDA250/GMA samples, presented evident surface deterioration after 5 minutes of MW treatment (Figure 4-7.d). Therefore, the following step was to find the minimum MW irradiation time necessary to functionalize the samples' surface with amines.

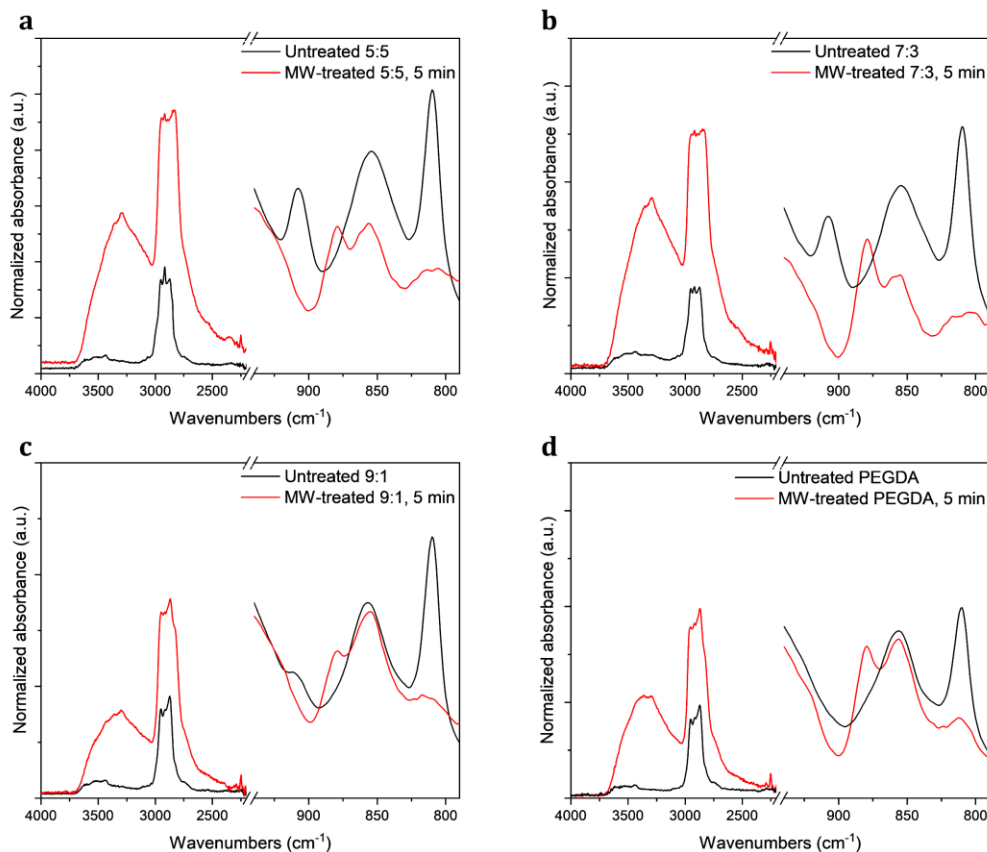


Figure 4-10. **Characterization of the different 3D printed PEGDA250/GMA samples (by the FTIR spectroscopy technique) after the microwave-induced functionalization.** The tests were performed using the PEI600 solution for 5 minutes on (a) 5:5, (b) 7:3, (c) 9:1, and (d) 10:0 PEGDA250/GMA samples. The FTIR spectra show the decreasing of the acrylate and epoxy-related bands at  $905\text{ cm}^{-1}$  and  $810\text{ cm}^{-1}$ , respectively, after the MW treatment. Besides, the appearance of a new region (between  $3600$  and  $2800\text{ cm}^{-1}$ ) is observed. This new region can be related to the linking of primary and secondary amines, as reported in the literature.<sup>493</sup>

PEI600 solution was selected again as an initial reference for performing MW-assisted functionalization on 5:5 PEGDA250/GMA samples (those with higher glycidyl proportion), decreasing the reaction times starting from 5 minutes down to 10 seconds. The results are plotted in Figure 4-11. The tests showed that 30 seconds of microwave reaction was enough for functionalizing the 5:5 samples. This assumption was corroborated by the complete disappearance of the glycidyl band at  $905\text{ cm}^{-1}$  and the appearance of the amine-related bands in the region between  $3600$  and  $2800\text{ cm}^{-1}$ , see Figure 4-11.a.

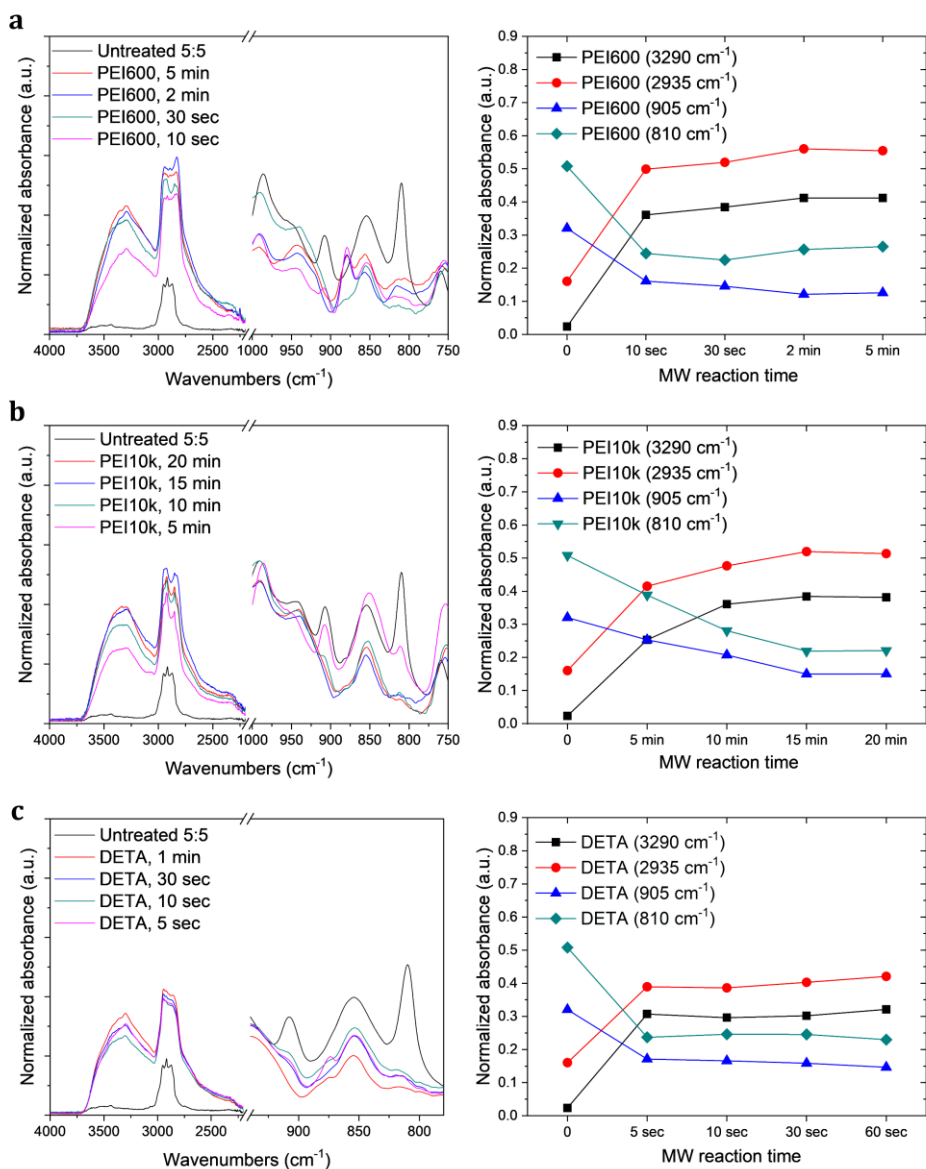


Figure 4-11. **Characterization of the different 3D printed PEGDA250/GMA samples (by the FTIR spectroscopy technique) after the microwave-induced functionalization using the three amine-based solutions.** ATR-FTIR spectra of 5:5 PEGDA250/GMA samples after different MW reaction times using (a) the PEI600 solution, (b) the PEI10k solution, and (c) the DETA solution. On the right of each FTIR graph, the curves of the evolution of the normalized absorbance intensity as a function of the MW reaction time is shown for the three amines-based solutions following the infra-red bands related to the amines (at 3290  $\text{cm}^{-1}$  and 2935  $\text{cm}^{-1}$ ), to glycidyl groups (at 905  $\text{cm}^{-1}$ ) and the acrylate double-bond (at 810  $\text{cm}^{-1}$ ) 'calibrated' considering the thermal contribution of the MW radiation. The minimum reaction time can be abstracted from the spectra by analyzing the required time to induce the highest acrylate/epoxy conversion as possible: 30 seconds using DETA and PEI600, and 5 minutes using PEI10k.

In these conditions, the samples ended up with good surface integrity, see Figure 4-7.e. The degree of functionalization did not change significantly at additional reaction times (see the curve to the right of Figure 4-11.a).

Therefore, in downstream experiments, 30 seconds was established as the MW treatment time for functionalizing the PEGDA250/GMA samples using the PEI600 solution. The same MW treatment strategy was repeated for 5:5 PEGDA250/GMA samples using both the PEI10k and the DETA solutions to find a compromise between surface modification and sample integrity. Using the PEI10k solution, we predicted that the reaction would take place at a longer MW reaction time, mainly due to the steric hindrance of the polymer backbone of PEI10k.<sup>488</sup> Therefore, in this case, the MW-assisted surface modification was evaluated by increasing the MW reaction times, starting from 5 minutes. The minimum MW treatment time using the PEI10k solution was found to be 15 minutes, Figure 4-11.b. Even so, at 15 minutes of MW irradiation time, the samples ended up with a significant brittle character. There was no further variation, at longer irradiation times, in the IR signal associated with the peaks of interest (see the curve to the right of Figure 4-11.b, which represents the FTIR curves intensities 'calibrated' considering the thermal contribution of MW). Hence, for future experiments in which the functionalization with PEI10K is required, particular care is necessary for handling the treated samples. In the case of the highly reactive DETA molecules, the shorter MW reaction time for modifying the sample's surface using the DETA solution was found to be 30 seconds, as observed in Figure 4-11.c. The 5:5 PEGDA250/GMA samples ended up with good surface integrity after MW treatment.

As mentioned before, the acrylate conversion might be influenced by the system's heating due to the microwave radiation. Therefore, the microwave radiation's thermal contribution was evaluated by performing MW treatments on pristine PEGDA250 (higher acrylate content) and 5:5 PEGDA250/GMA (higher glycidyl content). For this test, only acetonitrile was used for the MW-treatment (with no amines) for 30 seconds and 15 minutes; see resulting FTIR spectra in Figure 4-12.a,b. There was a similar band reduction at  $810\text{ cm}^{-1}$  after 30 sec of MW radiation (nearly 50 % of acrylic double-bond conversion) for both samples. The further reduction resulted in negligible for longer MW radiation times (15 minutes). Most importantly, under these conditions, there was no conversion of the epoxy groups (band at  $905\text{ cm}^{-1}$ ) for 5:5 samples, confirming that the epoxy conversion observed in the functionalization steps was only due to the amines' reaction. The thermal contribution by the microwave irradiation results was used to 'calibrate' the FTIR spectra's intensity (see Figure 4-11) and calculate the acrylate double-bond conversion (due to amines) in downstream experiments.

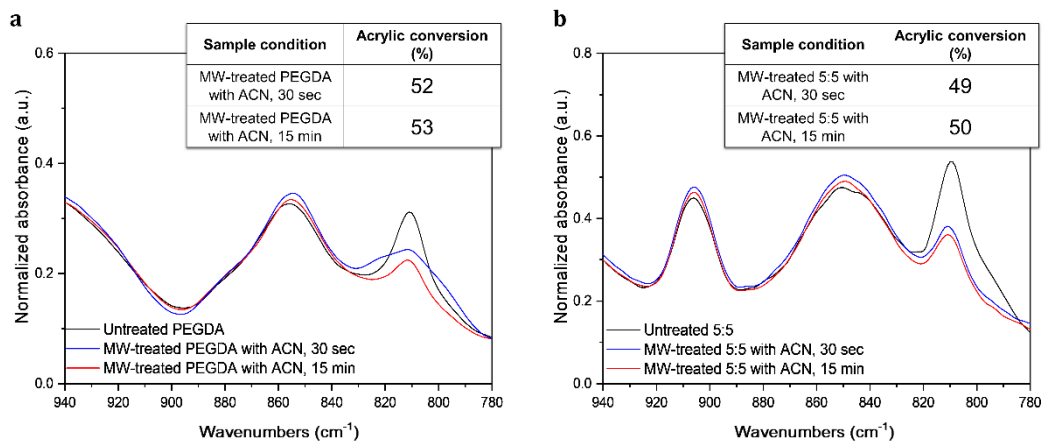


Figure 4-12. **Characterization of the 3D printed samples after MW-treatment without amine molecules presence.** Normalized ATR-FTIR spectra of (a) PEGDA250 and (b) 5:5 PEGDA250/GMA samples after MW treatment in acetonitrile for 30 sec and 15 min compared to untreated samples. After the MW-treatment, the acrylate groups partially react while the epoxy functionality does not. The inset tables show the acrylate double-bond conversion after each MW treatment.

Once the minimum MW reaction times were established for functionalizing the 5:5 PEGDA250/GMA samples, the rest of the samples were treated using the treatment conditions. The results are summarized in Table 4-2 and plotted in Figure 4-13, showing the IR spectra of signals under investigation.

Table 4-2. Acrylate double-bond and epoxy conversions of 3D printed PEGDA250/GMA and pristine PEGDA250 samples before and after microwave-assisted functionalization with DETA solution (30 sec of MW time), PEI600 solution (30 sec of MW time), and PEI10k solution (15 min of MW time). Infrared spectra of the signals of interest for the different PEGDA250 and GMA samples are shown in Figure 4-13.

Samples	As 3D printed	After microwave treatments					
	Acrylate conversion (%) <sup>a)</sup>	Acrylate conversion (%) <sup>b)</sup>			Epoxy conversion (%)		
		DETA	PEI600	PEI10k	DETA	PEI600	PEI10k
PEGDA250	82	97	97	96	-	-	-
9:1 PEGDA250/GMA	83	98	99	99	96	96	94
7:3 PEGDA250/GMA	85	99	99	99	98	95	93
5:5 PEGDA250/GMA	90	99	99	99	99	99	98

a) The acrylate conversion was evaluated following the C=C signal at 810 cm<sup>-1</sup>.

b) The epoxy conversion was evaluated following the glycidyl band at 905 cm<sup>-1</sup>.

The acrylate conversion increases significantly (up to near 100 %) after the MW treatments, and the extent of such conversion depends on the sample's composition and the type of amines used. The ring-opening reaction took place with values near 100 %. The slight differences in the epoxy conversion between the samples are related to the type of amines used. The differences observed can be related to the topological restriction of the aliphatic amines used, which hinders access to N-H bonds, and to the different reactivity of primary and secondary amines as it was demonstrated elsewhere.<sup>145</sup>

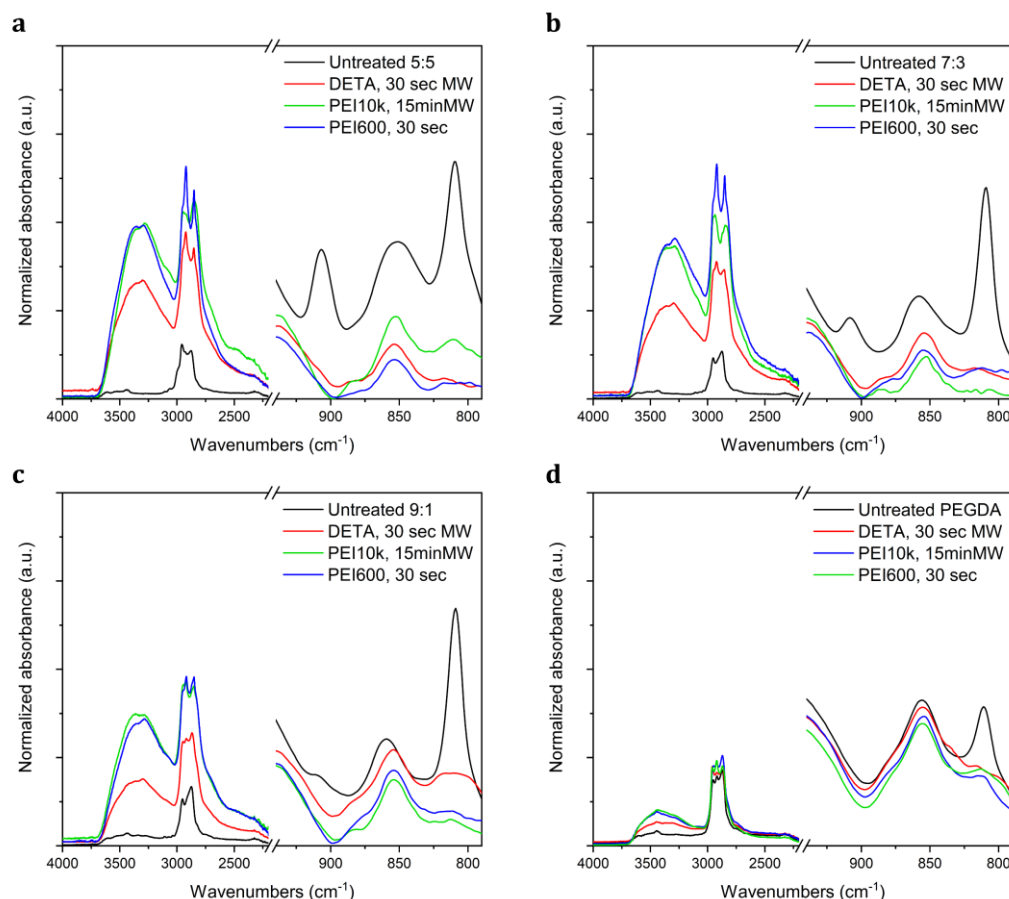


**Figure 4-13. Characterization by the FTIR spectroscopy technique of the different 3D printed PEGDA250/GMA samples after the microwave-induced functionalization step (at the minimum treatment times) using the three amine-based solutions.** Normalized ATR-FTIR spectra of (a) 5:5, (b) 7:3, (c) 9:1 PEGDA250/GMA, and (d) PEGDA250 samples after the MW treatment using the PEI600 solution, the PEI10k solution, and the DETA solution. Samples with more epoxy content presented the greatest amine-related absorbance intensity; such amine-related region also depends on the type of the amine used, reaching higher intensity values for the biggest hyperbranched amines PEI600 and PEI10k.

Figure 4-14.a shows the evolution of the absorbance intensity obtained from Figure 4-13 associated with N-H bonds (3600-3200  $\text{cm}^{-1}$  region) and C-H bonds (3000-2800  $\text{cm}^{-1}$  region) from treated PEGDA250/GMA samples. Some trends can be observed: (1) the formulation with higher glycidyl content



reacts with more amine molecules, producing a considerable increase in the amine-related regions' absorbance intensity due to a higher amount of amine groups on the sample's surface. (2) The absorbance intensity of these regions is greater according to the type of amine used, reaching higher values for the biggest hyperbranched amines PEI600 and PEI10k. Static contact angle measurements were performed on both untreated and MW-treated samples to evaluate the changes in the materials' surface properties; results are shown in Figure 4-14.b and resumed in Table 4-3. In a first vision, there was a dependence between GMA content and surface wettability for untreated samples. It was observed that the contact angle value was raised by increasing the GMA content in the copolymer structures ranging from  $81.8^\circ \pm 1.9$  for PEGDA250 samples to  $114.6^\circ \pm 2.4$  for 5:5 PEGDA250/GMA samples.

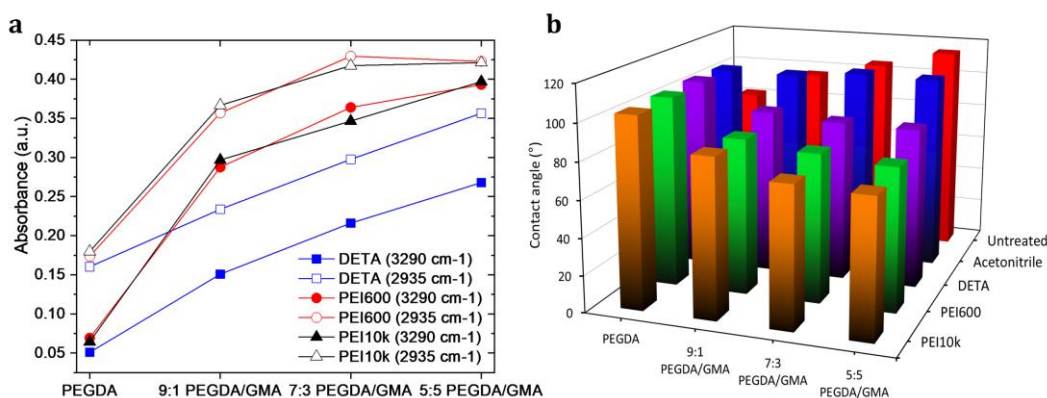


Figure 4-14. **Surface properties changes of the untreated and MW-treated 3D printed PEGDA250/GMA samples.** (a) normalized absorbance intensity as a function of the PEGDA250/GMA weight ratios after the different microwave treatments. Filled symbols refer to the 3600-3200  $\text{cm}^{-1}$  region's absorbance, associated with amines' N-H bond stretching. Empty symbols refer to the 3000-2800  $\text{cm}^{-1}$  region's absorbance associated with the C-H bond. The graph displays that samples with a higher content of epoxy reach the greatest amine-related absorbance intensity and that such amine-related region also depends on the type of the amine used, reaching higher intensity values for the biggest hyperbranched amines PEI600 and PEI10k. (b) Histogram showing the static contact angle of untreated and MW-treated samples as a function of the PEGDA250/GMA weight ratios and after the different MW-treatment treatments. The higher the epoxy content is, the higher is the amount of linked amine, and therefore, a lower contact angle presents the sample. The MW treatments were performed following the optimized irradiation times, 30 seconds using PEI600 and DETA solutions, 15 minutes using PEI10k solution, and 15 minutes using acetonitrile uniquely.

After the MW functionalization with amines, there were changes in the PEGDA250/GMA samples' surface wettability. As showed in Figure 4-14.b, the contact angles decreased more using the hyperbranched amines with higher molecular weight (PEI10k and PEI600) than using smaller amines molecules (DETA). This increase in the sample's hydrophilicity is caused by the incorporation of hydrophilic amines on the sample's surfaces through the

reaction with the glycidyl groups, and it is indeed more evident for 5:5 PEGDA250/GMA samples (higher amount of glycidyl groups). It is interesting to note that the contact angle value for all PEGDA250/GMA samples treated with only acetonitrile (without amine) at both 30 sec and 15 min is over 100° (Table 4-3). This trend can probably be attributed to the surface physical-mechanical changes produced by the microwave irradiation, creating small irregularities over the sample's surface.<sup>494</sup> This latest result further highlights the effect of the linked aliphatic amines on the MW-treated samples by inducing a more hydrophilic behavior.

Table 4-3. The untreated and MW-treated samples' average contact angle with different weight ratios between PEGDA250 and GMA monomers and after the MW-treatments. The MW treatments were performed following the optimized irradiation times, 30 seconds using PEI600 and DETA solutions, 15 minutes using PEI10k solution. The results for 15 minutes of MW treatment using acetonitrile uniquely are shown as well.

<b>Sample condition</b>	<b>PEGDA250</b>	<b>9:1 PEGDA250/GMA</b>	<b>7:3 PEGDA250/GMA</b>	<b>5:5 PEGDA250/GMA</b>
Untreated	81.80 ± 1.91	96.51 ± 1.91	105.30 ± 1.91	114.57 ± 2.42
DETA	105.02 ± 1.24	90.47 ± 1.31	87.86 ± 1.58	87.37 ± 1.45
PEI600	104.17 ± 1.78	84.98 ± 1.26	80.80 ± 1.48	77.67 ± 1.77
PEI10k	103.39 ± 1.13	85.84 ± 1.53	75.95 ± 1.69	74.25 ± 1.72
Acetonitrile 30 sec	105.3 ± 2.1	105.9 ± 2.7	104.23 ± 2.3	109.1 ± 2.93
Acetonitrile 15 min	104.53 ± 2.30	104.09 ± 2.84	107.41 ± 0.56	106.43 ± 1.68

### *Antibacterial tests*

Aiming to produce suitable structures and devices for medical applications, one of the most requested characteristics is antibacterial behavior, especially when the object enters direct contact with human elements.<sup>240,450,495</sup> This property plays a fundamental role in mitigating the risk of disease infection related to the proliferation of bacteria, such as bioimplants and biomedical systems, increasing their operating life.<sup>496</sup> Avoiding bacteria proliferation is also of great interest in other day-by-day applications such as water and air purification purposes or antimicrobial packaging in the food industry.<sup>497-501</sup> Considering the antibacterial activity of amine molecules,<sup>458,484-487</sup> the next step was to evaluate the microbial behavior of the PEGDA250/GMA samples MW-treated with the linear amine, DETA, and the two types of branched polyethylene imines, PEI600 and PEI10k against *Staphylococcus aureus*. This gram-positive model was chosen as it is responsible for many skin and soft-tissue infection diseases.<sup>468,469</sup> Firstly, as

verified in the previous section, the MW-treatment compromised some samples (especially 5:5 PEGDA250/GMA samples), showing significant deterioration after the functionalization step. This aspect can adversely affect the antibacterial studies since if the samples break easily under any slight mechanical action, the results may not be reproducible. Based on this observation, the 5:5 PEGDA250/GMA samples were discarded for antibacterial tests. Thereby, preliminary antibacterial tests were performed on MW-treated 7:3, 9:1 PEGDA250/GMA, and PEGDA250 samples. After *S. aureus* incubating over the samples for 1 hour, the bacteria solution was removed, and the samples were covered with fresh PBS media. Finally, the bacteria cultures were allowed to proliferate for 48 hours. The bacteria integrity was evidenced by the live/dead assay. This test examines the bacteria cells' membrane status, staining green when they are intact or red when the membrane is compromised. The live and dead bacteria images were obtained and recorded using a fluorescence microscope.

Figure 4-15.a shows the living and dead bacteria's fluorescence images, in terms of the sample composition and the amines solution used, incubated after 48 hours over the MW-treated samples. The bacteria proliferation over the samples ostensibly depends on the amine used for the experiments. From a general perspective, the first observation is that the bacteria proliferation was reduced for all samples treated with the amine-based solutions compared to those without microwave treatment. As anticipated, the samples treated with hyperbranched amines resulted in many dead bacteria, though with the amine lower molecular weight (DETA), the MW-treated samples presented good antibacterial behavior. Nevertheless, it is interesting to note that the treated samples' antibacterial action does not significantly depend on the starting sample's composition.

As observed in Figure 4-15.b-d, the surface covered by dead bacteria is similar independently of the starting samples' composition, either with PEGDA250 alone or with GMA content. What resulted more crucial was the type of amine used, lineal or hyperbranched, which directly impacted the living of bacteria as reported elsewhere.<sup>502-504</sup> These data suggest that the samples' antibacterial effect can be efficiently induced through microwave reaction even without epoxy (GMA) groups on the samples' surface. The unreacted acrylate groups are enough to link amine molecules and induce antimicrobial effects against the *S. aureus* bacteria model. Nevertheless, the incorporation of epoxy moieties on the samples can be the appropriate method for better controlling the exposed functional groups on the samples' surface, thus not depending on the possibly unreacted acrylate groups after the polymerization process.

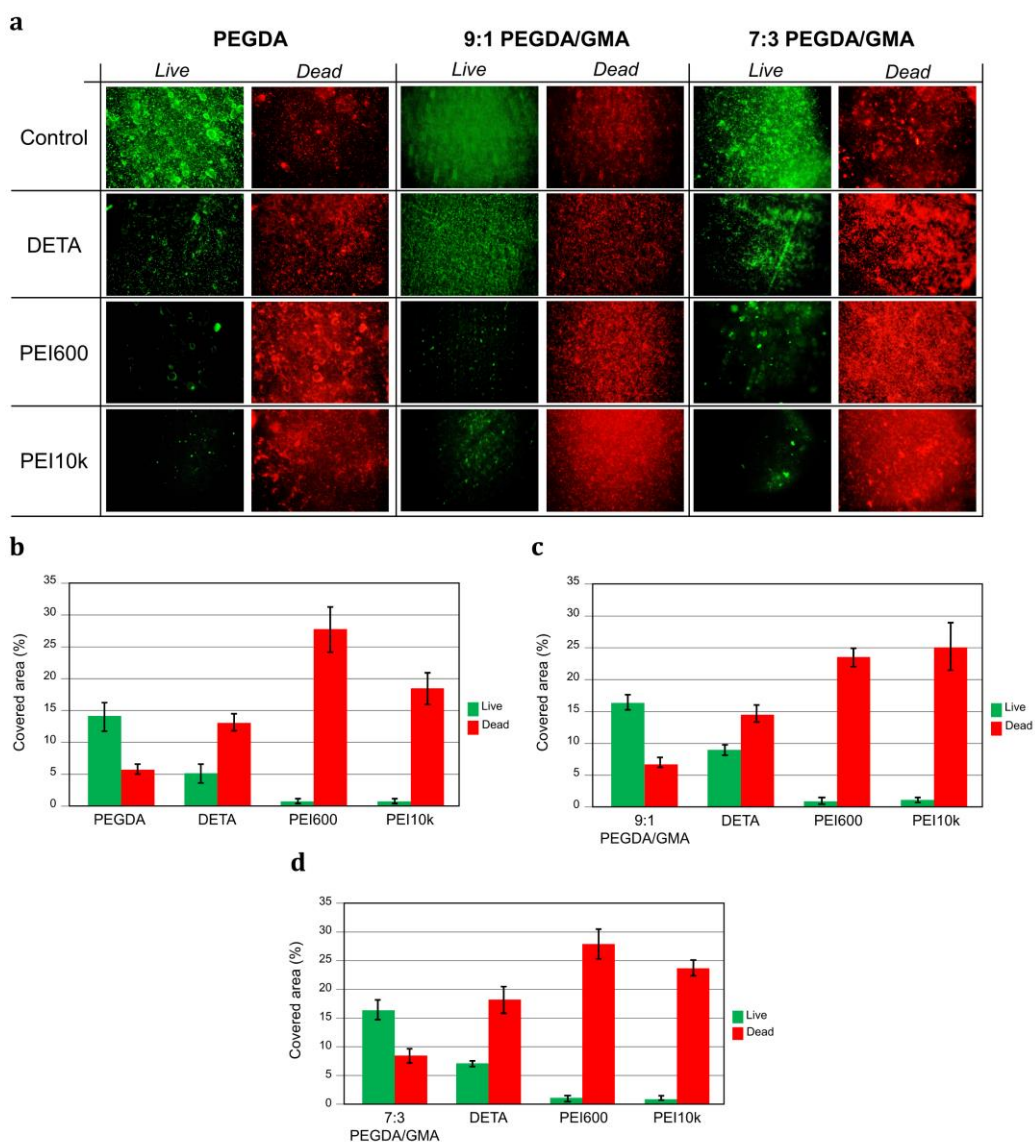


**Figure 4-15. Live and dead *Staphylococcus aureus* bacteria over the untreated and MW-treated 3D printed samples.** The images represent the number of live bacteria (green-colored) and dead bacteria (red-colored) onto the sample's surface. (a) Images (20x) of live/dead bacteria after incubation for 48 hours, over PEGDA250, 9:1, and 7:3 PEGDA250/GMA samples before (control samples) and after the different MW-treatment using the DETA, PEI600, and PEI10k solutions. Bacteria surface covered area (%) of live and dead bacteria over the (b) PEGDA250, (c) 9:1, and (d) 7:3 PEGDA250/GMA samples. The images show that the bacteria proliferation mainly depends on the type of amine used; the samples treated with hyperbranched amines (PEI) resulted in more dead bacteria (redder colored), confirming the surface treatment with amines confers antibacterial properties to the printed samples.

### 4.3.3. Conclusion.

In conclusion, a series of photopolymers made from different PEGDA250 and GMA monomers concentrations (5:5, 7:3, 9:1, and 10:0, respectively) were successfully printed, obtaining complex-shaped hybrid polymeric objects. These 3D parts presented unreacted epoxy groups used to perform surface modification in a suitable post-printing protocol. In particular, the samples were functionalized with aliphatic polyamine solutions upon microwave irradiation. This chemical functionalization was achieved via the nucleophilic attack of the N atom's electron pair to glycidyl groups and some unreacted acrylate groups. The amines used were DETA, PEI600, and PEI10k, characterized by the differences in architecture and reactivity. The MW-treated samples presented notable changes in their surface properties due to the surface linking of amines, which was evaluated via the ATR-FTIR method and static contact angle analysis. After optimizing the functionalization conditions, the samples ended up with good structural integrity, except the 5:5 PEGDA250/GMA samples, where the brittleness led to a marked deterioration after the microwave treatment.

By considering the amines' antimicrobial activity, the antibacterial behavior of the MW-functionalized parts was tested against *Staphylococcus aureus*, a bacteria model responsible for many skin infection diseases. The MW-treated samples presented a more potent antibacterial effect compared to untreated samples. The highest antibacterial characteristics were achieved using hyperbranched molecules for the surface modifications. However, with low-molecular-weight amine (DETA), a potent antimicrobial effect was also induced on the PEGDA250/GMA samples. The samples' antibacterial characteristics depended on the type of amine used but not on the starting sample composition. The unreacted acrylate double bonds were enough for inducing antibacterial features through the chemical link with amines. However, incorporating epoxy moieties could be preferred to control the functional groups over the sample's surface and thus do not depend exclusively on the eventual unreacted acrylate double bonds.

#### 4.4. Conclusions of the chapter.

The methodology presented in both parts of Chapter 4 showed how 3D printed samples' surface properties could be adjusted either by exploiting the unreacted acrylate groups or by incorporating functional elements in the printable formulation that can be exploited after the polymerization process. Both strategies can be used for linking molecules such as carboxyl and amines groups on the samples in a dedicated procedure. By performing the suitable post-3D printing protocol, one can selectively functionalize structures in green UV-mediated ways (Part I) or inducing strong antibacterial properties on objects by a fast method upon microwave radiation (Part II). Both functionalization strategies can be applied on customized 3D printed fluidic devices to add unique surface features to the channels' surface and increase the biomedical field's possible applications. For example, one can imagine microfluidic systems made of the PEGDA250-based photopolymer introduced in Part II. Through a suitable microwave treatment, the properties of the device's channels can be changed by chemically linking amine molecules. This idea could increase the 3D printed fluidic device's capability since amines are of particular interest for grafting biomolecules.<sup>505</sup> Indeed, as a concept, using the PEGDA250-based photopolymer in Part II (PEGDA250 + 1 wt.% BAPO + 0.01 wt.% DR1-MA), complex-shaped fluidic devices were 3D printed, see Figure 4-16. Both 3D printed objects consisted of microfluidic chips that hosted a helical-shaped channel of 1x1 mm. Besides, suppose a second resin, such as the PDMS-based presented in Chapter 3, is integrated into this system type; the possibilities can be further expanded and produce vastly interesting micro-fluidic systems.

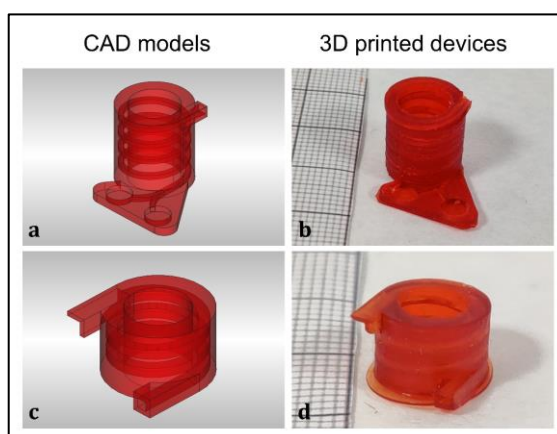


Figure 4-16. **3D printed of complex-shaped fluidic devices.** (a) CAD design and (b) photograph of a complex-shaped microfluidic chip consisting of a helical-shaped channel of 1x1 mm with two different outputs directed to a small well each. (c) CAD design and (d) photograph of a complex-shaped microfluidic chip consisting of a helical-shaped channel of 1x1 mm. The red-colored appearance was due to the dye used (DR1- MA at 0.01 wt.%), which increased the printing resolution for achieving the desired geometry.



## Chapter 5

# Integrated functionalities:

A functional dye for 3D printable resins.

### 5.1. Outline and motivation.

The following paragraphs are based on the original research article titled "*Three-Dimensional Printed Photoluminescent Polymeric Waveguides.*" The paper was published in ACS Applied Materials & Interfaces scientific journal from the American Chemical Society, ISSN: 19448244.<sup>421</sup>

As reported in the previous chapters, 3D printed structures with specific characteristics can be obtained through vat polymerization 3D printing techniques when the suitable elements are adequately selected and mixed during the resin preparation and by performing the suitable post-3D printing protocols. Other methods to introduce unique properties into the printed pieces can be followed by adding functional fillers or additives to the photopolymer (e.g., carbonous or ceramic particles, pigments, and even biomolecules such as enzymes and antibodies) for enhancing the properties of the printed objects.<sup>203,449</sup> However, one of the factors to consider when using such additives is the photopolymer's homogeneity, a common problem if the added components present a low affinity with the rest of the formulation



constituents. Therefore, to successfully transfer the envisioned characteristics and features from the additives to the printed parts, the photopolymer must be as homogeneous and stable as possible, at least, during the entire printing process. Another aspect is that the resin's viscosity could considerably increase at certain additives content, which might cause problems during the printing step (due to the resin's low flowability), leading to 3D printing processing defects and poor mechanical properties.<sup>150,158,208</sup> Moreover, additives can also absorb the incident light, changing the photopolymer's optical feature significantly (e.g., light penetration during the 3D printing step) and affecting the final printing resolution.

While additives might improve some parts' properties, it is essential to employ such components correctly for obtaining precise and reliable 3D printed structures. When suitable additives (either dyes or fillers) are adequately used, it could be feasible to transfer their distinctive properties to the printed parts, e.g., electrical, mechanical, or optical.<sup>506</sup> For example, by incorporating carbon nanotubes (CNTs) or silver nanoparticles into a printable resin, the polymeric parts' conductivity could increase by several orders of magnitude.<sup>150,167,209</sup> Silver nanoparticles can also be used to impart antibacterial properties to the polymerized parts.<sup>160</sup> Similarly, by adding quaternary ammonium compounds, 3D printed parts with enhanced antibacterial properties can be obtained.<sup>109</sup>

Other types of additives, such as dyes, can also introduce functionalities to the printed parts when added correctly.<sup>412</sup> Dyes are typically added (at low concentration) into a 3D printable resin, aiming at increase the accuracy during the printing step, which is achieved by limiting the penetration of light (z-axis) and regulating the diffusion of the light laterally (X-Y plane) during the printing process.<sup>152,153</sup> Hence, a suitable functional dye can improve the printing accuracy and introduce unique characteristics to the printed object.<sup>148</sup> For example, using azo-type organic dyes (e.g., such as methyl red (MR)), the mechanical properties of 3D printed objects can be reversibly tuned thermally or upon laser irradiation at 532 nm by taking advantage of the cis-trans isomerism behavior of these compounds (characterized by a stimulus-responsive R-N=N-R' bond).<sup>152,155,156</sup> Likewise, using a disperse red one dye but methacrylate, another azo-compound type, the gas permeability toward carbon dioxide and oxygen of the 3D printed pieces can be locally modified upon green-emitting laser irradiation by inducing cis-trans switching of the dye molecules.<sup>157</sup> Moreover, the dye used, having a methacrylate functionality, remained covalently linked to the polymeric backbone during the 3D printing, allowing the fabrication of long-time stable devices. By following a similar approach, this chapter will present a methodology to produce printed structures through DLP-3D printing methods with tailored optical features by adding a functional dye into the printable photopolymers. The functional dye

employed in this investigation is an amino derivative of 7-nitrobenzo-2-oxa-1,3-diazole (NBD) functionalized with a methacrylic double bond (see Figure 5-1.c). NBD compounds have been extensively utilized in different fields since their introduction, particularly in the pharmaceutical and biomedical fields, for labeling biological units.<sup>507</sup> The interest in NBD compounds mainly relies on that their synthetic precursors, the 4-Chloro-7-nitrobenzo-2-oxa-1,3-diazole (NBD-Cl) and 4-fluoro-7-nitrobenzo-2-oxa-1,3-diazole (NBD-F), can easily react with thiols or amines groups, generating highly fluorescent and stable NBD products. In general, NBD-Cl is more widely used due to its low cost despite its slightly lower reactivity towards amine and amino acids compared to NBD-F.<sup>508,509</sup> <sup>510</sup> Due to its fluorescent characteristics, NBD compounds have been employed in widespread analytical biosensing applications as agents to label proteins, amino acids, nucleotide, and sugar derivatives amines, natural bases as well as antibiotic drugs. The fluorescent labeling of such compounds serves as a fast method for monitoring various analytical processes by observing their intrinsic emissive properties compared to the native biological models.<sup>511,512</sup>

The NBD dye, used as a fundamental additive in the printable formulation, might give fluorescence characteristics to 3D printed parts that can be used as optical waveguides (or optical transmitters) capable of guiding the luminescence. Optical waveguides are dielectric structures used to confine and guide wavelengths between their two extremes in the infrared or visible range of the electromagnetic spectrum.<sup>513</sup> These devices can be fabricated with glass, plastic, or semiconductor materials. An example of these devices is optical fibers used in optical telecommunications, composed of a circular core or central region surrounded by a transparent cladding part and a protective coating.<sup>514</sup> Optical waveguides can also be planar-type or strip where the core part, a layer, is sandwiched between two cladding layers, creating a "two-dimensional" waveguide. Optical waveguides (planar or circular) are structures where the light travels along the core part by the total internal reflection (TIR) effect, which is based on the difference between the core's refractive index (optically denser medium) and its surface or cladding part with lower refractive index, allowing to guide the excited light from the light source to the end of the waveguide.<sup>515</sup> According to the mode of light propagation, they can be divided into two subclasses: multi-mode waveguides, structures that support the propagation of multiple light modes, and single-mode waveguides where is only propagated a single mode of light, the transverse mode (plane perpendicular to the radiations propagation direction of the electromagnetic field). These optical devices are of particular interest in communications since they are not as susceptible to strong electromagnetic fields as some of their existing electrical and electronic counterparts. Optical waveguides can also be found in the medical and chemical fields for fluorescence-based biosensing applications. The devices are used as a

platform for the biochemical receptor, transmitting the light and the generated signal to a photodetector converting it into an electrical signal.<sup>516-519</sup> Although optical biosensors cannot compete against current laboratory procedures, they are easier to use, cheaper, require lesser samples, and allow the real-time monitoring of analytes, being widely used in environmental analysis, food safety, and medical diagnostics.<sup>520</sup> In this context, optical waveguides produced from polymers are of particular interest since using such material, more complex and miniaturized optical waveguides with customized features can be produced compared to the well-established glass materials.<sup>521</sup> Moreover, in contrast to inorganic materials, polymers can be more easily processed, enabling the possibility to tune the final refractive index of the structure at lower costs.<sup>522,523</sup> Polymeric optical waveguides (POWs) can be produced through different processes according to the achievable performance and resolution: hot embossing, flexographic printing, and laser ablation, photolithography, methods that involve multiples, and, in some cases, intricate steps of production. Besides, they are limited to in-plane configurations or, in the best cases, require repeated developing or etchings steps for producing multilayered optical waveguides.<sup>524-527</sup>

The 3D printing versatilities might be exploited as a valuable alternative for producing customized and precise polymeric optical waveguides in fewer steps than conventional fabrication methods. Indeed, the literature reports few 3D printed optical structures, such as the work presented by Udofia et al.<sup>528</sup> In this work, the authors developed a series of complex-shaped optical waveguides using flexible and optically transparent thermoplastic polymer (ballistic gel) through a custom-made  $\mu$ -extrusion 3D printer. The researchers obtained 3D printed polymeric waveguides with minimum dimensional features of about 154  $\mu\text{m}$ , display great optical transparency above 98 %, and low transmission losses of about  $\sim 0.22 \text{ dBcm}^{-1}$ . Moreover, they presented nonplanar and complex-shaped devices for different applications, such as combiner circuits on both planar and 3D conformal surfaces. As Udofia and coworkers detailed, their innovative extrusion-based 3D printing method could be used for developing low-cost optical circuits, complex optical devices, and other innovative optical applications that were not possible before, which will potentially have a significant impact on the optical industry. Other examples of 3D printed polymeric waveguides are introduced by Lorang et al., which fabricated optical waveguides in arbitrary planar and nonplanar configurations by co-extruding two photocurable resins in a core-fugitive shell extrusion-based printing approach.<sup>529</sup> The co-extrusion method allowed the researchers to pattern hybrid organic-inorganic optical waveguides in different forms: linear, curved, and out-of-plane. The polymeric waveguides presented a nearly cylindrical shape and low optical loss in the visible spectrum. The researchers could also print up to six polymeric optical waveguides coupled to three different LEDs with good optical performances

by following such an approach. Optical systems using vat 3D printing have also been reported.<sup>530</sup> In the Swargiaryand coworkers' work, they developed optical waveguides from a commercial clear photopolymer (Hex-polymer PX-8880) with dimensional features small as 200  $\mu\text{m}$  with promising results in terms of light confinement compare to bigger waveguides. The changes in the refractive index of such 3D printed optical waveguides were tested toward deionized water, isopropanol, and glycerol in liquid and gas states, showing a good response of the devices in terms of optical transmission, indicating that the printed waveguides could be implemented as environmental sensors.<sup>531</sup> Considering 3D printing methods' capabilities in terms of resin preparation and freedom of fabrication, this chapter will demonstrate how by using a photoluminescent NBD-derivate compound as a dye into a photopolymer, complex-shaped 3D printed structures could be fabricated through vat 3D printing with the desired optical features owing to the photoluminescent characteristic of the NBD compound (as represented in Figure 5-1). These printed devices could be used as optical waveguides and light splitters by correctly transferring the NBD dye properties to the printed devices. Moreover, these NBD-containing 3D printed waveguides could maintain the sensitivity against solvents of different polarity, enabling the use of these devices as polarity sensors.

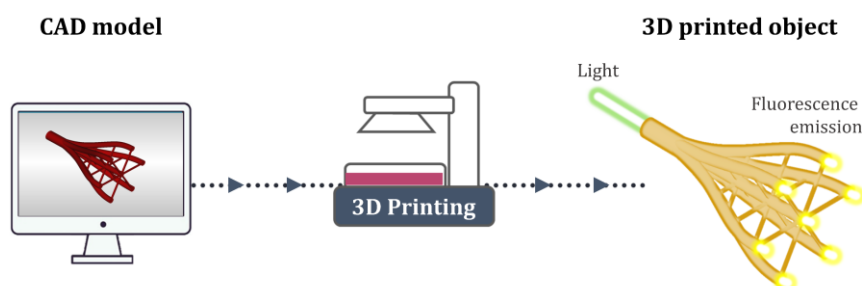


Figure 5-1. **3D printing of optical waveguides.** Illustration of the 3D printing of optical waveguides using NBD-dye as a functional component of the photocurable formulation. The fabrication process starts from the CAD modeling, passing through the light-based 3D printing step and obtaining the printed structure.

### 5.1.1. Experimental section.

#### Materials

As a reactive monomer, bisphenol A ethoxylate diacrylate (**BEDA**,  $M_n \sim 512$  g/mol, EO/phenol 2) was used. As a photoinitiator, phenyl bis(2,4,6-trimethylbenzoyl)phosphine oxide (**BAPO**, 97 %) was used. Other substances such as acetonitrile (**ACN**,  $\geq 99.8\%$ ), ethanol (**EtOH**, 99.8 %), dichloromethane (**DCM**,  $\geq 99.8\%$ ), N,N-dimethylformamide (**DMF**, 99.8%), toluene (99.8 %), 4-Chloro-7-nitrobenzo-2-oxa-1,3-di-azole (98%), triethylamine, methacryloyl chloride (97 %), ethyl acetate (99.8 %) and 2-(N-methyl) aminoethanol ( $\geq 99.8\%$ ) were also used. All reagents and substances were purchased from Merck Company (Darmstadt, Germany) and used as received. The chemical structures of the components used for the resin preparation are shown in Figure 5-2.

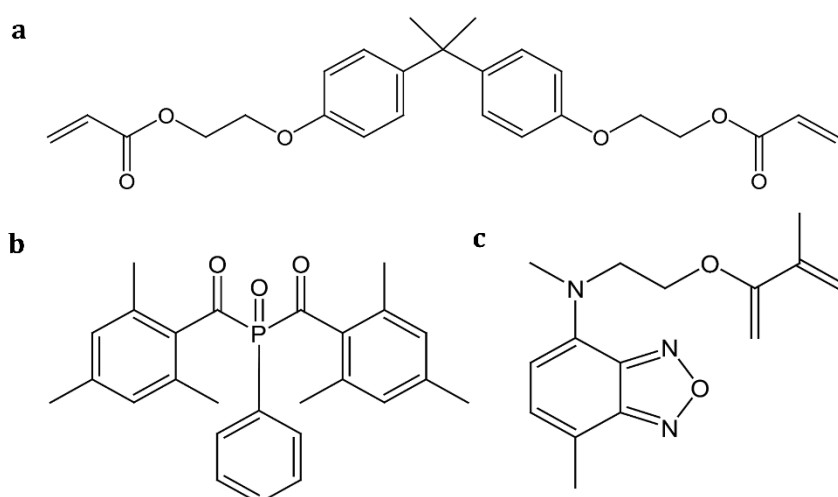


Figure 5-2. **Chemical structures of the chemical reagents used.** (a) bisphenol A ethoxylate diacrylate (**BEDA**) monomer, (b) phenyl bis(2,4,6-trimethylbenzoyl) phosphine oxide (**BAPO**) photoinitiator. (c) 4-(N-Methyl-N 9-ethanol) amino-7-nitrobenzo-2-oxa-1,3-diazole derivate dye with methacrylate functionality (**NBD-MA**).

#### Synthesis of NBD-MA dye

The syntheses of the 4-(N-Methyl-N 9-ethanol) amino-7-nitrobenzo-2-oxa-1,3-diazole (NBD-NEtOH) and the methacrylate derivate of NBD (NBD-MA) were performed by P. Bosch (ICTP-CSIC, Spain) as a part of research collaborations. However, a brief description of the synthesis routes is described. 250 mg (1.2 mmol) of 4-Chloro-7-nitrobenzo-2-oxa-1,3-di-azole

and 15 mL of ethanol were introduced in a microwave glass tube of 30 mL of maximum capacity; then 240  $\mu$ L (1.5 mmol) of 2-(N-methyl) aminoethanol was slowly added to the solution under mechanical stirring. The glass tube was hermetically sealed with a silicone septum. The system was subjected to microwave radiation for 3 minutes at 90 °C. Finally, the glass tube was kept at room temperature, and crystals of NBD-NEtOH were slowly formed, as observed by the formation of bright orange powder. The amount of compound obtained was 285 mg, with a 75 % yield of purity. NBD-NEtOH:  $^1\text{H}$  NMR ( $\text{CDCl}_3$ ):  $\delta$  = 8.46 (d, Har, J = 9.02 Hz), 6.18 (d, Har, J = 9.02 Hz), 4.35 (t,  $\text{CH}_2\text{O}$ , J = 5.29 Hz), 4.06 (t,  $\text{CH}_2\text{-N}$ , J = 5.29 Hz), 3.65 (s, OH), 3.52 ppm (s,  $\text{CH}_3\text{-N}$ ).

Standard acylation of NBD-EtOH was performed, as is described in previous work.<sup>532</sup> First, in a round-bottomed three-necked flask, 0.5 g (1.7 mmol) of the NBD-NEtOH, 0.2 g (2 mmol) of triethylamine, and 20 mL of dichloromethane with toluene (80:20 vol. %) were mixed. The mixture was cooled in a water-ice bath, and 0.23 g (2 mmol) of methacryloyl chloride, solved in 5 mL of dichloromethane, was slowly added to the stirred solution. After 10 h, the solvent was eliminated under reduced pressure; the solid was dissolved in dichloromethane and purified through a silica gel column using a dichloromethane mixture with ethyl acetate (80:20 vol.%) as eluent. An orange oil product was obtained, which was crystallized in ether and dried until constant weight. NBD-MA:  $^1\text{H}$  NMR ( $\text{CDCl}_3$ ):  $\delta$  = 8.46 (d, Har, J = 9.02 Hz), 6.32 (d,  $\text{CH}_2\text{-C}$ , J = 1.56 Hz), 6.18 (d, Har, J = 9.02 Hz), 5.95 (d,  $\text{CH}_2\text{-C}$ , J = 1.56 Hz), 4.53 (m,  $\text{CH}_2$ ), 3.49 ppm (s,  $\text{CH}_3\text{-N}$ ).

#### *Preparation of the photoluminescent photopolymers*

Three different formulations containing NBD-MA dye were prepared with 0.01, 0.005, and 0.001 wt.% of dye concentration. The resins were prepared as follows: First, NBD-MA and BAPO were dissolved in acetonitrile by 20 minutes of sonication (130  $\text{mg}\cdot\text{mL}^{-1}$  dye per ACN). Then, the BEDA monomer was added and mixed by 10 minutes of sonication. Moreover, a neat formulation with no NBD-MA amount was also prepared for the characterization tests. All formulations were prepared with two (2) wt.% of BAPO.

#### *Digital light processing DLP-3D printer*

The printing equipment used is a DLP-3D Printer-HD 2.0 (Robot Factory). This printer has a projector with a resolution of 50  $\mu\text{m}$  (1920 $\times$ 480 $\times$ 1080 pixels) and a build area of 100 $\times$ 56.25 $\times$ 150 $\text{mm}^3$ . The Z resolution range from 10 to 100  $\mu\text{m}$ . The power density of the light source is set up at 10  $\text{mW}\cdot\text{cm}^{-2}$ . The irradiation time for the first six (6) layers of the object was 8 seconds to guarantee an appropriate adhesion to the building

platform. The irradiation times were slightly varied according to the amount of NBD-MA dye in the formulation, ranging from 1 to 1.3 seconds per layer. After the printing step, 3 minutes of UV post-curing process in the air was performed on the sample using a broad-band medium-pressure mercury lamp (Robot Factory, a UV power density of 5 mW/cm<sup>2</sup>).

### *Characterization methods*

An Anton Paar Monowave 300 microwave reactor provided with an infrared sensor (IR pyrometer) was used for synthesizing the photoluminescent dye. The reaction was performed under magnetic stirring inside a pressure-resistant 30 mL glass tube sealed with silicone septum.

Real-time photo-rheological tests were performed to measure the changes in the viscoelastic material properties during polymerization. The experiments were carried out using an Anton Paar rheometer (Physica MCR 302) configured in parallel mode with the lower plate consisting of 20 mm quartz and the upper parallel plate consisting of 20 mm aluminum. A Hamamatsu LC8 lamp was used to study the photopolymerization process. It is equipped with a visible bulb and a cutoff filter below 400 nm, and an 8 mm light guide. During the tests, the light irradiation was initiated after 60 seconds to stabilize the system before the photopolymerization process (light intensity set at 10 mW/cm<sup>2</sup>), and the gap between the two parallel plates was set at 100  $\mu$ m. The measurements were performed at 25 °C, at 1% of strain amplitude, and at a constant shear frequency of 1 rad/s. The variations in the viscoelastic moduli of the photopolymer during polymerization were measured against exposure time. Viscosity measurements were also performed with this instrument in parallel-plate mode with a gap of 0.1 mm between both plates. The shear rate range was set up from 0.1 to 100 s<sup>-1</sup>.

For the differential scanning calorimetry (DSC) measurements, a system apparatus (DSC1 STARe) of TA Instruments equipped with a low-temperature probe was used. The experiments were performed at a heating rate of 10 °C/min between 20 and 100 °C.

An FT-IR spectrometer (Nicolet iS50, Thermo Scientific, Milano, IT) was used to calculate the acrylate double bond conversion on both liquid photopolymers and polymerized objects. The spectra were collected on an attenuated total reflectance (ATR) system (Smart iTX). For the FTIR experiments, the spectra were collected with a resolution of 2 cm<sup>-1</sup>, averaging 32 scans for each spectrum, wavenumbers range 650 – 4000 cm<sup>-1</sup>. The acrylate double bond (C=C) conversion was monitored by following the decrease of the peak at 1640 cm<sup>-1</sup>. The acrylate signals were normalized using the constant signal at 1510 cm<sup>-1</sup>, corresponding to the stretch of the aromatic ring of the acrylate resin.

DMA measurements were performed using a Triton Technology TTDMA. The tests were performed on 3D printed films with a thickness, 200  $\mu\text{m}$ . The samples' mechanical response was evaluated from  $-40$  to  $70$   $^{\circ}\text{C}$  with a heating rate of  $3$   $^{\circ}\text{C}/\text{min}$ , a frequency of  $1$  Hz, and  $20$   $\mu\text{m}$  of strain. According to the literature, the polymerized parts' crosslinking density was calculated from  $E'$  rubbery plateau value.<sup>474</sup>

The insoluble (or crosslinked) fractions of the samples were calculated following the standard ASTM D2765–84 test procedure.<sup>428</sup> The samples were kept in a metal mesh, precisely weighed, and later submitted to extraction with chloroform ( $\text{CHCl}_3$ ) for 24 hours at room temperature to remove the unbounded components. Then, the samples were dried overnight at  $80$   $^{\circ}\text{C}$ , and the insoluble fraction percentage was determined as the weight difference before and after solvent extraction (relative error =  $\pm 1\%$ ).

The optical characterization of the 3D printed structures was performed using a laser setup arranged explicitly for this work see Figure 5-3. The configuration comprised a pulsed doubled Ti: Sapphire laser beam (Tsunami Spectra-Physics), with a pulse width of  $10$  ps, a repetition rate of  $80$  MHz set at  $490$  nm, which was expanded through a beam expander (BE) to obtain a  $2$  mm wide Gaussian beam. For the fluorescence analysis, an imaging system was placed composed of a low numerical aperture objective (OBJ, Olympus MD plan 5, NA =  $0.1$ ), a long pass edge filter (EF) with cutting wavelength  $550$  nm (Thorlabs FEL550) to cut off the scattered laser light, and a lens (L1 – focal length  $f = 50$  mm) that produces an image of the focal plane of the objective on a monochromatic CMOS camera (Thorlabs DCC1240M). For the fluorescence analysis of the swelled sample, on the orthogonal optical axis, the light is spectrally filtered with an edge filter for laser radiation and collected into a fibered dispersive spectrometer (Ocean Optics USB2000+). The optical characterizations were performed at the vibrational & nano-optical spectroscopy laboratory by Angelo Angelini (Post-doctoral researcher) and Francesca Frascella (Post-doctoral researcher), both from Polytechnic of Turin.

UV–vis spectroscopy measurements were conducted using a double-beam Lambda 40 instrument (PerkinElmer Italia, Milano, Italy) in the range between  $200 - 600$  nm, at  $480$  nm/min scan step. The tests were performed on solid films (thickness  $50$   $\mu\text{m}$ ) coated on a glass slide. The possible dye photodegradation was evaluated by collecting UV-vis spectra on an NBD-MA solution in acetonitrile ( $0.015$  mg/mL) before and after 3 minutes of direct UV irradiating the solution. This technique was also used to analyze the extracting chloroform solutions from the insoluble fraction test.



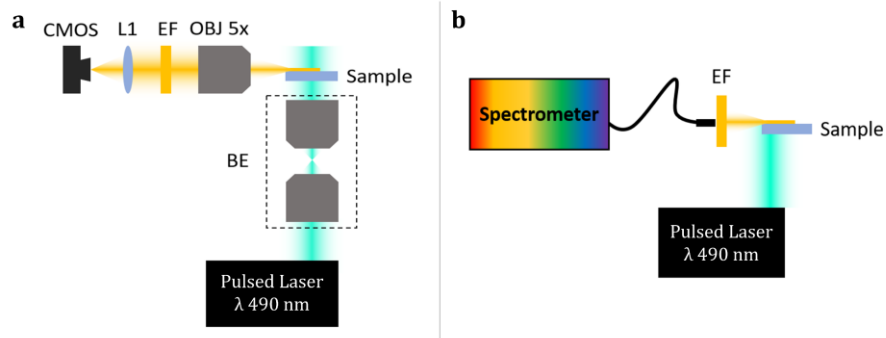


Figure 5-3. **Representation of the two laser configurations used to characterize the 3D printed waveguides.** (a) Orthogonal fluorescence setup and (b) Fluorescence setup for the swelled samples.

### 5.1.2. Results and discussion.

The first step for the development of this work was the synthesis of the NBD-based functional dye. The selection of NBD derivate compound as a functional dyed was based on two interesting features considering the objective of this investigation:

1. It presents appropriate absorption and emission characteristics: with a charge transfer (CT) intense absorption band in the red region (max.  $\lambda_{\text{abs}} = 440\text{--}475\text{ nm}$ ) and intense fluorescence emission in the yellow-green region ( $\lambda_{\text{em}} = 497\text{--}526\text{ nm}$ ).<sup>533</sup>
2. The fluorescence emission of 7-nitrobenzo-2-oxa-1,3-diazole (NBD) amino derivatives depends on the medium's viscosity and polarity since the twisted intramolecular charge transfer (TICT) mechanism; hence, its fluorescence quantum yield increases as rigidity increases.<sup>534</sup>

The synthesis route for obtaining the NBD-EtOH precursor is a well-established method, and it was described years ago.<sup>534</sup> However, here, a different route that improves the synthesis considerably is described. NBD-EtOH compound was produced via microwave irradiation. Through this method, the reaction time is shortened from 2 hours to 2 minutes, the use of inert atmosphere (in argon), toxic solvents and reactants (ethanol, toluene, and triethylamine), and multiple and laborious steps of purification are avoided; indeed, the product crystallizes pure in the reaction medium with a purity yield comparable to the obtained product through conventional methods. Subsequently, the NBD-EtOH compound was subjected to a methacrylation process following the method reported by Alonso and coworkers.<sup>532</sup> In this way, the NBD carrying (meth)acrylate functionalities (NBD-MA) could remain covalently linked to the polymeric material after the 3D printing step, obtaining printed parts with stable photoluminescent properties by avoiding the long-term unwanted leaking of this functional dye. Moreover, the NBD dye's solvatochromism property could be transferred to the printed part by copolymerization.<sup>535</sup> The solvatochromism is the phenomenon by which a solute (the dye) changes its emission spectrum when dispersed in various solvents. The way in which the spectrum of emission of the dye changes is related to the polarity of the solvent used (more specifically, to the dielectric constant and hydrogen bonding). Dyes with negative solvatochromism are those with blue or hypsochromic shift (the emission shift toward inferior wavelengths) when the solvent's polarity increases. The positive ones are those with a red or bathochromic shift (the emission shift toward higher wavelengths) when the solvent's polarity increases. Therefore, if the NBD compound remains chemically linked to the printed parts, they can give them photoluminescent properties and present solvatochromic

characteristics, enabling their utilization as solvents polarity sensors, as expected.<sup>536</sup>

The obtained NBD-MA dye was then added into BEDA monomer, with 2 wt.% of BAPO, at different concentrations. BEDA monomer has been selected since it has been previously used for preparing printable resins with excellent results,<sup>152,416</sup> while BAPO photoinitiator choice was based on its strong absorption around 405 nm,<sup>151,422</sup> which is where the printer's projector light emits. Some preliminary studies were carried out to explore BEDA-based formulation properties' effect when the NBD-MA dye is added. The resin's viscosity needs to be suitable not to compromise the piece's production during 3D printing since highly viscous resins might not cover, in time, the vat area to create the subsequent layers. Even though a novel 3D printing methodology has been developed for processing high viscous resins,<sup>208</sup> here, it is desired to maintain a low viscosity for operating with any commercial 3D printer. Therefore, the viscosity of the formulations was initially evaluated.

All the formulations presented a Newtonian behavior: the shear rate does not influence the viscosity of the formulations, and only small variations are observed at low shear rate due to the sensibility of the instrument, see Figure 5-4.a. The average viscosity calculated between 1 and 100 s<sup>-1</sup> for Neat BEDA formulation and BEDA-based formulations with NBD-MA concentrations of 0.001, 0.005, and 0.01 wt.% is reported in Table 5-1.

Table 5-1. Viscosity values at 25 °C (average value), acrylate conversion (%) after visible light irradiation for 10 seconds and after UV irradiation for 180 seconds, glass transition temperature T<sub>g</sub> (°C), and gel fraction (%) for Neat BEDA formulation and BEDA-based formulations with NBD-MA concentration of 0.001 wt.%, 0.005 wt.%, and 0.01 wt.%. All formulations contained 2 wt.% of BAPO. Crosslinking densities were calculated from the DMA experiments.

Formulation	Viscosity (Pa*s)	Acrylate conversion		Insoluble fraction (%) <sup>c)</sup>	T <sub>g</sub> (°C) <sup>d)</sup>	Crosslinking density (mmol/mol) <sup>e)</sup>
		(%) <sup>a)</sup>	(%) <sup>b)</sup>			
Neat BEDA	0.08	97	98	92	49	12.5
0.001 wt.% NBD-MA	0.10	97	98	92	47	12
0.005 wt.% NBD-MA	0.09	94	98	91	46	11
0.01 wt.% NBD-MA	0.11	85	92	89	40	10

<sup>a)</sup> after visible light irradiation <sup>b)</sup> after UV light irradiation, <sup>c)</sup> measured after 24h of extraction in chloroform, <sup>d)</sup> T<sub>g</sub> obtained from DSC, <sup>e)</sup> calculated from the rubbery plateau in DMA tests.

As observed, NBD-MA dye's presence had no relevant influence on the viscosity of printable formulations, which is considerably lower than usually acceptable values for commercial DLP 3D-printers.<sup>537</sup> Moving to photorheological tests, in Figure 5-4.b, the curves of storage modulus (G') and

loss modulus ( $G''$ ) versus irradiation time for neat BEDA formulation and with NBD-MA dye contents (0.001, 0.005, and 0.01 wt.%) are reported. The plots showed similar reaction times ( $G' = G''$ ) for all the formulations, which indicates that the addition of NBD-MA does not strongly modify the printability. For all formulations, the transition of  $G'$  and  $G''$  occurred after 10 seconds of illumination.

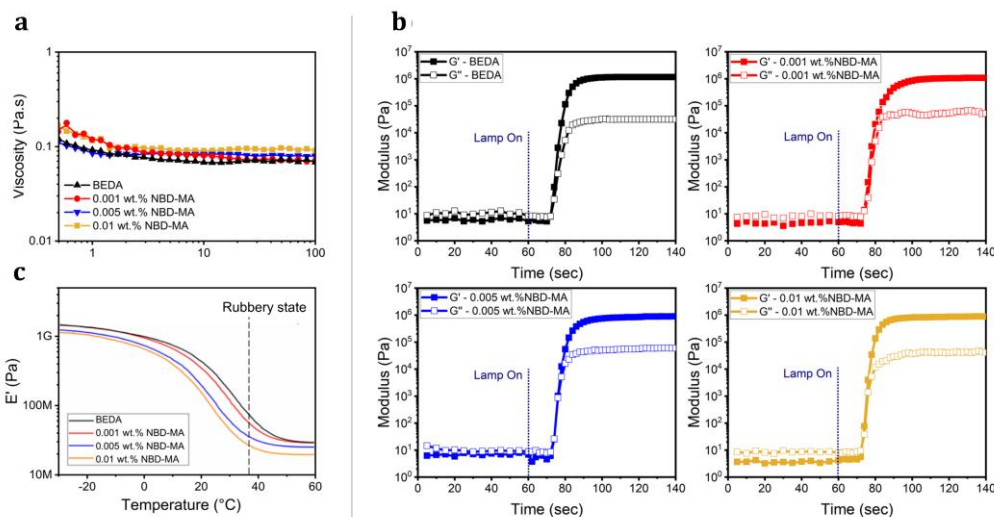


**Figure 5-4. Characterization of the different BEDA-based photocurable resins showing the effect on the formulation properties by adding the NBD-MA dye into the formulation.** (a) Viscosity values (at 25°C) of the formulations at different NBD-MA concentrations (0.001, 0.005, and 0.01 wt.%) were similar in the shear rate range between 1 and 100 s<sup>-1</sup>. (b) Storage- $G'$  (full symbols) and Loss- $G''$  (empty symbols) moduli versus irradiation time where is observed similar reaction times (the point where  $G'$  crosses  $G''$ ) for the BEDA-based formulations at different NBD-MA dye concentration. (c) Elastic modulus curves versus temperature for the four BEDA-based formulations obtained from DMA experiments where the differences of the storage modulus ( $E'$ ) in the rubbery state ( $E'_r$ ) can be observed. This piece of information can be correlated to the polymeric matrix's crosslinking density by the conventional theory of rubber elasticity, which results in a lower crosslinked density for samples with a lower value of  $E'$  in the rubbery state.

By the ATR-FTIR technique, the acrylate double bond conversions were evaluated on the samples films obtained from the photorheological experiments; the results are reported in see Table 5-1 and supported by Figure 5-5. As observed, the films made with a higher concentration of NBD-MA dye reached a slightly lower degree of acrylate conversion after visible irradiation, which increases to higher values after UV irradiation. The difference in conversion is related to the fact that the NBD-MA dye absorbs part of the incident light during the visible irradiation, competing with the BAPO in the light absorption. This competition produced a decrease in the efficiency of photoinitiation and hence the final double bond conversion.<sup>148</sup> Nevertheless, the acrylate conversions reached are adequate for 3D printing since it is

sufficient to reach the gelation point during this step for enabling the object shaping.<sup>171</sup>

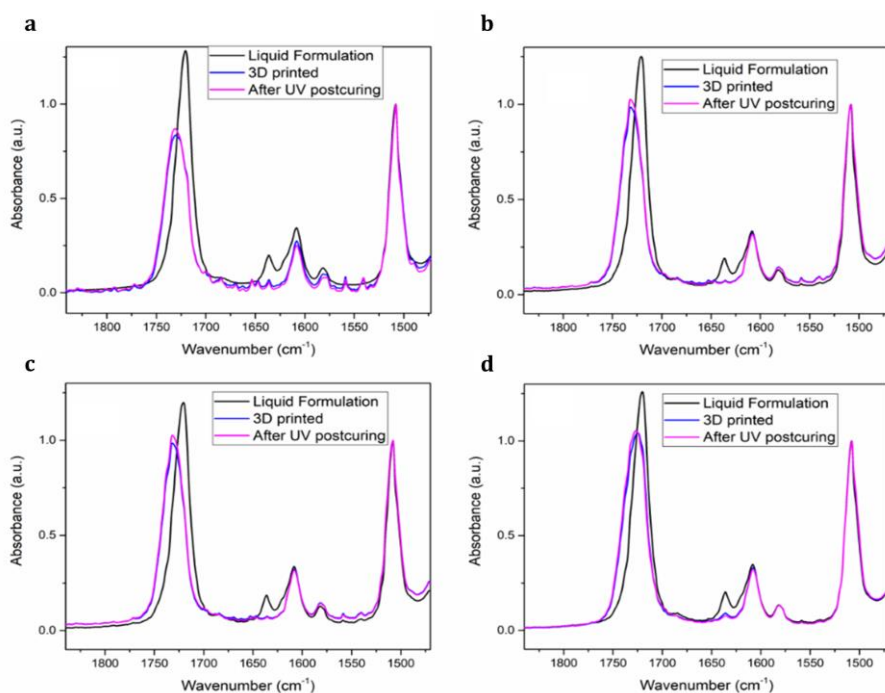


**Figure 5-5. Conversion of the acrylate double-bond groups of the BEDA-based formulations by observing the peak reduction at 1635 cm<sup>-1</sup>.** The spectra were collected through the Fourier transformed infrared (FTIR) technique after subjecting to diverse irradiation conditions the four BEDA-based formulations: (a) neat BEDA formulation with not NBDA-MA content and BEDA-based formulations with (b) 0.001 wt.%, (c) 0.005 wt.%, and (d) 0.01 wt.% of NBD-MA concentration. The acrylate groups' peak area was normalized using a constant signal in the spectra corresponding to the aromatic ring stretch centered at 1510 cm<sup>-1</sup>. All formulations contained two (2) wt.% of BAPO as the photoinitiator.

The insoluble fraction was also evaluated for all BEDA-based samples after UV irradiation, results reported in Table 5-1. The extent of the insoluble fraction was slightly lower for formulations with higher NBD-MA concentration, which is in line with the infrared evaluations reported above. The presence of NBD-MA also had a slight influence on the glass transition temperature of the polymeric parts. A decrease in  $T_g$  values was observed by increasing the amount of NBD-MA dye, which can be explained considering the decrease of crosslinking density when the dye content is higher, resulting in a looser and slightly more flexible network (Table 5-1). The lower crosslinked density might again be related to lower acrylate conversion and the fact that NBD-MA copolymerizes with BEDA, resulting in more extensive polymeric networks, as confirmed by a lower value of  $E'$  in the rubbery plateau (Figure 5-4.c).<sup>474</sup> UV-Visible spectra were also collected from uncured liquid resins and after polymerizing the same formulation (with visible and UV light) to

check the dye's possible photodegradation under light irradiation. Figure 5-6.a reports the spectrum taken on the neat BEDA sample.

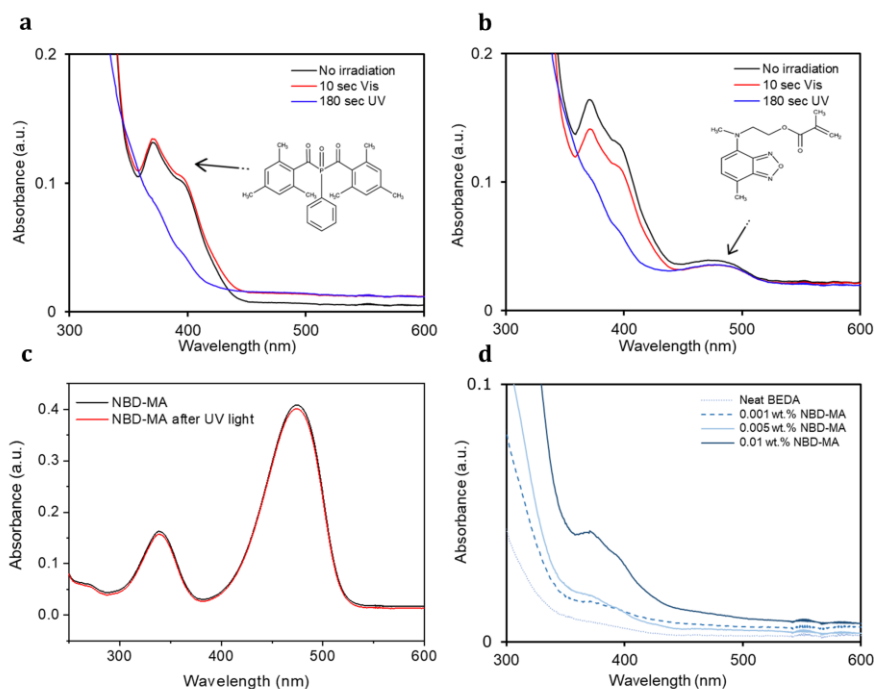


**Figure 5-6. Characterization of the BEDA-based photocurable resins through the UV-Vis technique.** The BAPO consumption and the non-degradation of the NBD-MA dye after visible and UV irradiation (for 10 sec and 180 sec, respectively) are shown. (a) UV-Vis spectra collected on 50  $\mu\text{m}$  films made of BEDA-based formulation with not NBD-MA content. (b) UV-Vis spectra collected on 50  $\mu\text{m}$  films made of BEDA-based formulation with 0.01 wt.% NBD-MA. (c) UV-Vis spectra of NBD-MA dye in acetonitrile before and after UV light irradiation. (d) The polymerized BEDA-based samples were immersed in chloroform for 24 h (for the insoluble fraction experiments). The extracting solvents were analyzed through the UV-VIS test to observe the residuals components and the successful copolymerization of the NBD-MA dye with the polymeric BEDA matrix.

As it is possible to observe, the liquid formulation showed a broad absorption band between 350 nm and 420 nm, which belongs to the BAPO photoinitiator. After visible irradiation, this band slightly decreased ( $\lambda > 400$  nm), which completely disappeared after UV irradiation, indicating the complete photocleavage of the BAPO photoinitiator. In samples containing NBD-MA dye, another clear peak appeared at 480 nm (Figure 5-6.b), related to the dye absorption. For these samples, the band relative to the BAPO disappeared after the UV irradiation step. The NBD-MA absorption peak was not affected by visible and UV light irradiation, indicating that the NBD-MA no photodegrade in these conditions. The latter observation was confirmed through UVS-vis experiments by irradiating the dye compound directly, diluted in acetonitrile (0.015 mg/mL), with UV light. No changes in its absorption spectrum were observed; see Figure 5-6.c. Accordingly, the NBD-

MA dye is stable during the photocrosslinking process, and it should maintain its photoluminescence properties after the 3D printing step. Finally, the effective integration of NBD-MA dye by copolymerizing with the polymeric network was evaluated through UV-Vis analysis. The tests were performed on the extracting chloroform solvent used for the insoluble fractions tests; the results are shown in Figure 5-6.d. The extracted chloroform used for the neat BEDA samples did not show any absorption band; in contrast, the chloroform used for the samples with NBD-MA showed a band in the range between 360 nm and 420 nm, which is associated with the unreacted BAPO photoinitiator, as previously mentioned. The BAPO-related band increases as higher are the dye content in the printable formulations due to the conflict in light absorption between both compounds. It is essential to highlight that no absorption band was observed at a longer wavelength, indicating that NBD-MA (480 nm) was not extracted by chloroform and remained copolymerized with the polymeric network, as desired. As observed, the NBD-MA compound might effectively operate as a suitable dye for 3D printable photopolymers (competing with BAPO), and it could be copolymerized to the final photo-crosslinked material. Conversely, a misuse of NBD-MA dye quantity might hinder the acrylate conversion and the final crosslinking density, producing weaker material.

The next step was to use the prepared photopolymers for producing 3D printed complex-shaped structures. In particular, the formulations (2 wt.% of BAPO and different NBD-MA concentrations: 0.001, 0.005, and 0.01 wt.%) were used to 3D-print optical waveguides with photoluminescent features owing to the NBD-MA properties. Initially, the intention was to determine the NBD-MA concentration that ensures the best 3D printing resolution exhibiting at the same time excellent optical transmission. For this purpose, straight waveguides with a circular section of 2.8 mm and a length of 30 mm were 3D printed, and the fluorescence intensity of them was measured in an end-fire coupling configuration, as described in Figure 5-3.a. The excitation was provided by a laser beam aligned orthogonally to the waveguide direction to ensure no propagation of the excitation beam inside the waveguides, allowing a better localization of the fluorescence source. The waveguide's fluorescence signal presented a sublinear dependence (when the excitation point is faced with the objective coupled to the CMOS camera) concerning the dye concentration, probably due to saturation effects (Figure 5-7.a, direct collection). While the fluorescence signal propagated through the waveguide when the excitation point is placed at the opposite side of the collection arm in a remote collection configuration, see Figure 5-7.b. The transmittivity here is described as the ratio between the fluorescence intensity  $I_1$  calculated in the direct collection of the waveguide and the fluorescence intensity  $I_2$  calculated in the remote collection.

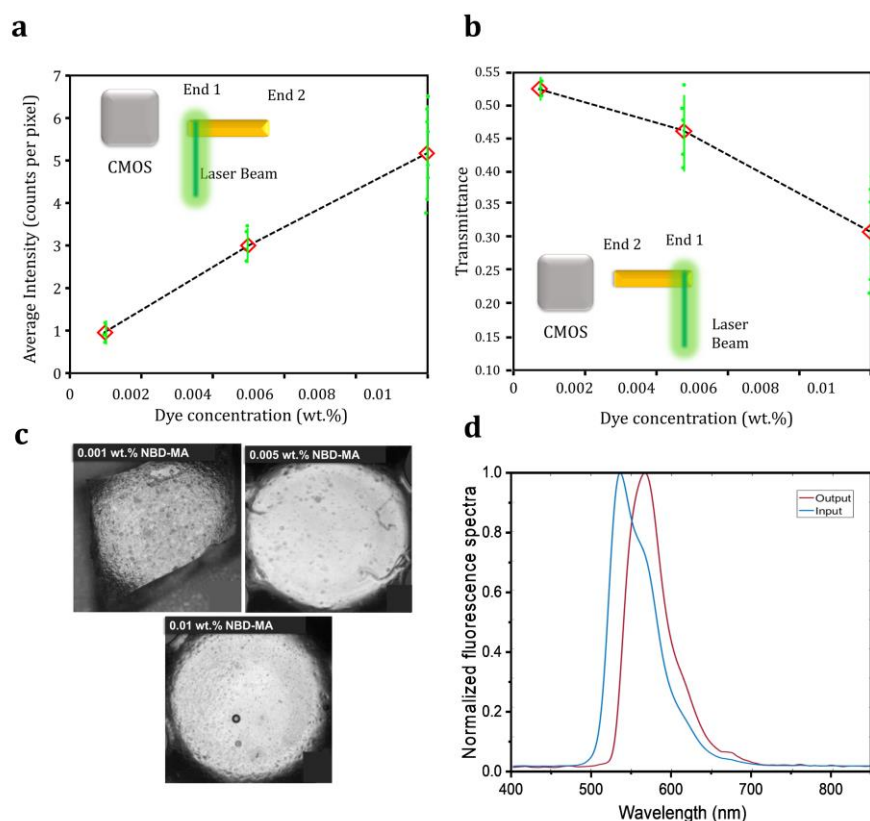


**Figure 5-7. Optical characterization and printing resolution of the 3D printed samples obtained from the different BEDA-based formulations.** (a) the 3D printed structures' fluorescence intensity was measured (in an end-fire configuration), varying the NBD-MA dye concentration; the graph shows a sublinear dependence between the dye concentration and the fluorescence signal intensity of the samples. (b) The transmittance ( $T$ ) of the 3D printed waveguides was measured varying the NBD-MA content, showing a lower waveguide's transmissivity at higher dye content. Green circles represent the experimental data, and green lines represent the average intensity values (red diamonds). (c-e) Photographs of the 3D printed waveguides showing the poorest printing resolution at lower NBD-MA dye concentration. (f) Differences in the printed devices' fluorescence signals when the spectra are collected at the input (blue curve) and the output (red curve) of the waveguides.

Moreover, Figure 5-7.b indicates that higher NBD-MA concentration leads to lower waveguide's transmissivity, suggesting the re-absorption of the dye compound's fluorescence signal. This hypothesis was confirmed by the fluorescence spectra collected in the direct and remote configuration, as presented in Figure 5-7.f. On the other hand, it was evident that lower amounts of dye led to poor printing resolution by observing the fabricated waveguides (Figure 5-7.c-e). While at higher amounts of the dye (0.005 and 0.01 wt.% of NBD-MA), 3D printed waveguides with good printing accuracy (maintaining the round section shape) were obtained.

The guiding performance of more complex-shaped 3D printed structures was also evaluated. For this purpose, a series of Y-shaped waveguides were 3D printed using the BEDA-based photopolymer containing 0.005 wt.% of NBD-



MA dye. The structures were produced (this time, with different aperture angles ( $\alpha$ ), namely 30°, 40° 50°, and 60°, and with square segments of 2x2 mm<sup>2</sup>; see Figure 5-8.a. The preference to produce such relatively large samples was based on the easiness of fabrication and characterization, and due to the multimodal nature of the considered waveguides, it does not expect significant variations in the transmittance. As foreseen for the total internal reflection, the waveguide's higher transmittance would be reached at a lower aperture angle ( $\alpha$ ). Precisely, at angles lower than 40.7°, that is the critical angle obtained from the BEDA's datasheet with a refractive index of 1.534 at a wavelength of 589 nm at room temperature. The transmittance was determined as the relationship between fluorescence collected in the remote setup and the direct setup's fluorescence. Figure 5-8.a indicates that the transmittance was almost steady below 40° and drops to zero beyond the critical angle value, as anticipated. Waveguide with  $\alpha = 40^\circ$  guided light until the end facet, as observed in Figure 5-8.a, appearing brilliant in the inset image. The waveguide's end facet with  $\alpha = 60^\circ$  looked dark in Figure 5-8.a (inset photograph), meaning that light is no longer guided and vanished from the intersection point. The balance between the two outputs has been evaluated, and the experimental data are reported in Table 5-2.

Table 5-2. Light transmittances of 3D printed Y-splitters made from the BEDA-based formulation with 0.005 wt.% of NBD-MA. The letters a and b refer to two different samples used for the measurements.

Y-junction	30°		40°		50°		60°	
	a	b	a	b	a	b	a	b
Lateral 1*	1,19	1,17	0,84	1,21	0,80	0,67	0,28	0,29
Lateral 2*	1,05	1,10	1,12	1,15	0,67	0,82	0,29	0,36

\* average counts per pixel

For the next experiments, a series of 3D printed 1x7 branching optical waveguides with circular cross-sections were produced from the photopolymer with 0.005 wt.% of NBD-MA since it presented the most suitable compromise between printability, transmittance, and photoluminescence features. Figure 5-8.b details the CAD design of these waveguides, and Figure 5-8.c shows the 3D printed parts. The shape of the 1x7 waveguides relies on a rectilinear input arm of diameter 2.8 mm, a central rectilinear output arm of diameter 1.6 mm, surrounded by six non-rectilinear output arms (with a diameter of 1.6 mm). The exterior arms are equidistantly separated from the central arm, creating a perimeter with different diameters and angles (Figure 5-8.c). Relatively large devices were made to simplify the samples' handling during the experiments; however, smaller structures were also produced, reaching resolutions of 600  $\mu\text{m}$  see (Figure 5-8.e-h). The light transmission ratio between later arms (TL) and central arm (TC) is presented in Figure 5-8.d. As more extensive is the splitter, the percentage of light guided

in lateral arms is lower; though, there was no sudden decrease in transmission since their smoother shapes. The previous results demonstrated that 3D printing could be effectively used for fabricating complex-shaped optical devices.

Finally, the applicability of these devices as a polarity sensor was studied. Contemplating some dyes' well-known solvatochromism, particularly this NBD dye,<sup>196,534</sup> aiming to transfer these dye properties into a 3D printed bulk device. The experiments on the 3D printed solid devices were performed by swelling the samples in different solvents using a handmade fluorescence setup, as described in Figure 5-3.b. The dye's fluorescence signal inside the solid polymer was evaluated and compared when the dye is exposed to different solvents as reported in the literature<sup>532-534</sup>, see Figure 5-9.a. The dye emission is red-shifted with a maximum emission wavelength of about 535 nm (the literature indicates the dye emission is 514 nm in toluene or 519 nm in chloroform<sup>532-534</sup>), and a band appeared around 565 nm. Such results could be associated with the NBD moieties' aggregation inside the highly crosslinked solid matrix, producing a new fluorescent species due, for instance, to dipolar interactions arising from electronic excitation. Either simple dimeric (excimers) or multimeric (J-aggregates) association might cause a bathochromic shift in the fluorescence emission spectra. The formation of J-aggregates of NBD molecules in confined media has been previously reported,<sup>510</sup> and the new fluorescence emission found for planar aromatic molecules through the so-called Aggregated Induced Emission phenomenon (AIE) is well known.<sup>538</sup>

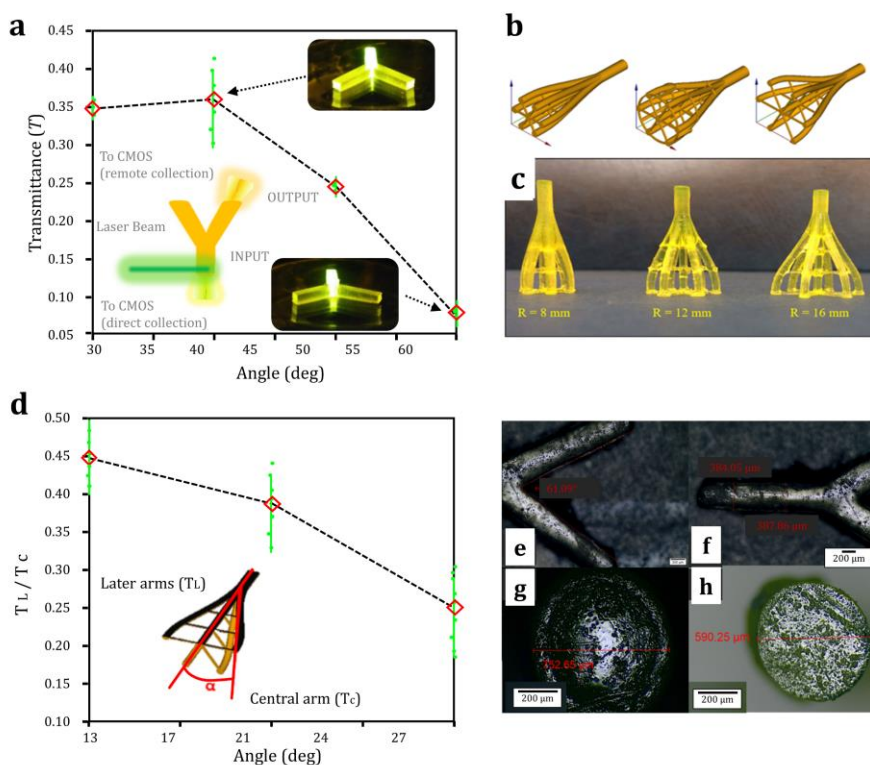


**Figure 5-8. Optical characterization and the smallest printing resolution of complex-shaped 3D printed structures with 0.005 wt.% of NBD-MA dye.** (a) Transmittance measured through one branch of the Y-shaped 3D printed waveguide as a function of the aperture angle  $\alpha$  where is verified that the light is no longer guided at aperture angles above 40 degrees by observing the drops in its transmittance signal. The inset shows a schematic view of the experimental setup and the fluorescence photographs of the waveguides illuminated at one of their end branches. (b) CAD model images and (c) picture of the complex-shaped 3D printed optical waveguides with circular cross-section and different radii (aperture angles). (d) the light transmission ratio of the 3D printed optical waveguides between later arms (TL) and central arm (TC) as a function of the radius of the external circumference. (e) angle and (f) X-Y dimension evaluation of the smallest Y-shaped 3D printed splitters, (g) dimension evaluation of the input arm, and (h) lateral arm. Both objects were produced with the formulation containing 0.05 wt.% of NBD-MA.

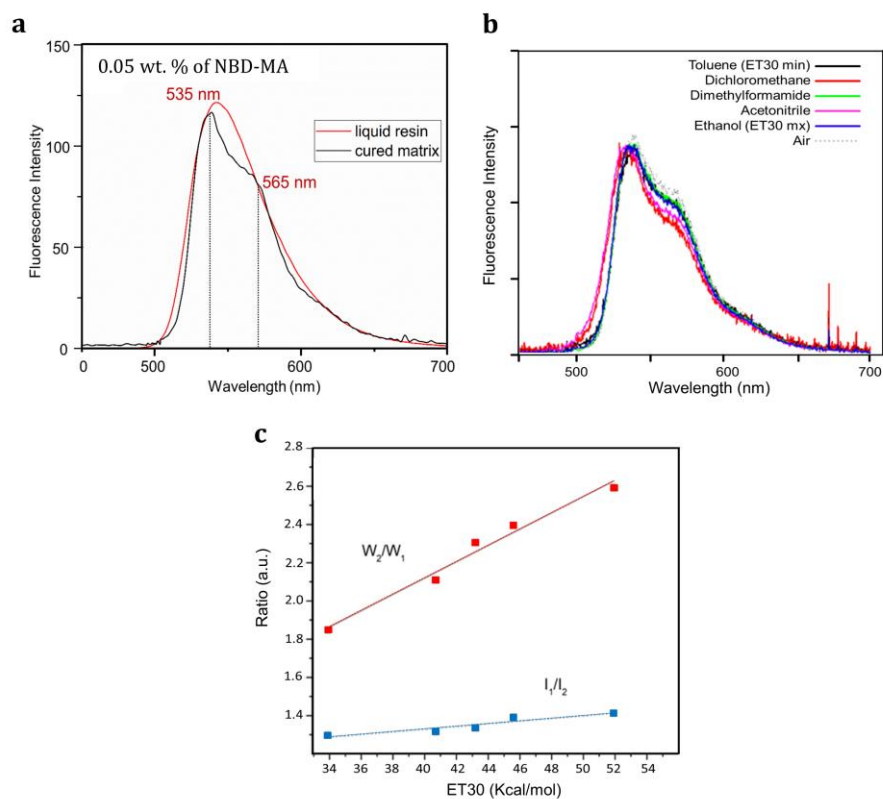
Since the dye was copolymerized with the polymeric network and cannot be extracted, the emission spectra on swollen samples in solvents with different polarity parameters (ET30) were recorded.<sup>536</sup> In particular, toluene, dichloromethane, dimethylformamide, acetonitrile, and ethanol were used. The devices were immersed in different solvents for 5 minutes, and subtle changes in the emission band were observed as a function of the microenvironment's polarity inside the swollen optical waveguide; the results are reported in Table 5-3 and Figure 5-9.b.

Table 5-3. Fluorescence spectra data for all the solvents used as a polarity test bench for the 3D printed waveguides. Solvent uptake in 5 minutes in 3D printed structures.

Solvent	ET30 (Kcal.mol <sup>-1</sup> )	W <sub>2</sub> /W <sub>1</sub> <sup>a)</sup>	I <sub>1</sub> /I <sub>2</sub>	Solvent uptake (mmol.gr <sup>-1</sup> ) <sup>b)</sup>
Toluene	33.9	1.87	1.298	0.15
Dichloromethane	40.7	2.11	1.315	0.48
Dimethylformamide	43.2	2.30	1.335	0.43
Acetonitrile	45.6	2.39	1.392	0.60
Ethanol	51.9	2.59	1.412	0.18

<sup>a)</sup>  $w$  is the full width at half maximum height, <sup>b)</sup> mmol of solvent absorbed per gram of sample after 5 min.

As the solvent's polarity increases, the spectra of swollen samples showed a bathochromic shift of the individual NBD molecules' emission band, as shown in Figure 5-9.b. The band corresponds to the aggregates does not change in its position. Furthermore, a substantial decrease in the relative intensity of the shoulder concerning the intensity at maximum wavelength is observed, see Figure 5-9.c, which is consistent with the assumption that the band corresponds to emission from dye aggregates. As the solvent penetrates the network, the aggregates are partially destroyed by solvation. Moreover, a decrease in the aggregate's emission band's width was found, confirming the behavior above-described (Figure 5-9.c). Although the number of solvents studied is relatively limited, they cover a considerable interval of polarity. The linearity found for both parameters is quite satisfying; therefore, these findings are exciting since they support the possible application of these printed devices only as waveguides and as polarity sensors.



**Figure 5-9. Optical characterization of the 3D printed BEDA-based structures when exposed to different solvent vapors.** (a) Fluorescence spectra of the NBD-MA dye in the liquid BEDA resin (at 0.05 wt.% of concentration) compared to the fluorescence spectra of the NBD-MA dye when the BEDA resin is polymerized, showing the differences in the two spectra due to the NBD moieties' aggregation inside the solid polymeric matrix. (b) Fluorescence spectra of swollen samples in different solvents, showing a bathochromic shift of the emission band of individual NBD molecules. (c) variation of the fluorescence emission band of swollen 3D printed structures in the different solvents represented as the ratio of the signal intensities ( $I_1/I_2$ ) and the full widths half-maximum height of the signal ( $W_2/W_1$ ). Subscripts 1 and 2 refer to peaks assigned to individual NBD molecules and aggregates, respectively.

### 5.1.3. Conclusion.

In Chapter 5, 3D printable materials' capabilities were implemented through the customization of a printable photopolymer. Specifically, during the photopolymer preparation, a functional dye (NBD-MA) was included as a fundamental additive to increase the printing resolution (obtaining well-defined complex geometries) and impart specific functionalities to the printed structures. When the appropriate amount of the NBD-MA dye was used, 3D printed photoluminescent waveguides and splitters were obtained (see Figure 5-10). Moreover, the dye compound was copolymerized with the polymeric network after the printing process and not degraded, transferring its properties to the printed objects. The fabricated optical devices were demonstrated to guide the dye's luminescence up to an angle of 40°. Finally, since the synthesized dye was copolymerized with the polymeric network, the NBD-MA dye's solvatochromic properties were successfully transferred to the printed structures, enabling the use of these waveguides as solvent polarity sensors.

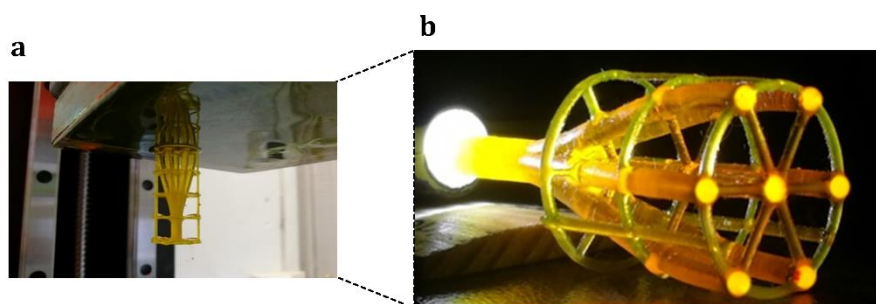


Figure 5-10. **3D printed optical waveguide made from BEDA formulation containing 0.005 wt.% of NBD-dye.** (a) Photograph of the device once is finished the 3D printing step. (b) the optical device while guiding the light upon direct illumination.

The 3D printed optical structures introduced in this chapter presented the desired characteristics and properties by mixing the appropriate components during the resin preparation phase. Although these optical objects still require further optical tests to a broader characterization, the ease of producing them at low cost and in a short time following our methodology could offer new opportunities for the realization of complex integrated optical circuits or other advanced applications.<sup>539</sup> Optical devices with unique features and geometry can be manufactured through 3D printing, which could greatly impact the optical communication industry.

# Final considerations and Conclusions

This manuscript presented different approaches for obtaining customized biocompatible and functional structures by optimizing the photopolymers preparation for vat 3D printing and performing the suitable post-printing procedures. The results reported in this thesis demonstrated how selecting the suitable components for the photocurable polymer preparation and performing the right post-printing procedures, structures with the tailored characteristics could be obtained according to the looked-for application.

In the first experimental part, Chapter 3, different acrylate-based photopolymers were prepared and used to print objects with enhanced biomedical characteristics tailoring the printable materials composition and carrying out suitable post-printing treatments. The printed parts presented good optical transparency, appropriate mechanical properties, suitable chemical resistance or stability, and tunable surface qualities, useful for biological applications. Some of the developed photopolymers were used for obtaining objects for cell growth with good viability results, while others, based on acrylate-polydimethylsiloxane (PDMS) material, was used for producing complex-shaped and truly three-dimensional microfluidic chips with similar characteristics to the conventional PDMS material used for this purpose, the Sylgard 189. The different strategies in terms of materials used, post-printing treatments, and 3D printed freedom of design showed in Chapter

3 could contribute to the development of practical and precise microfluidic devices. In the second experimental section, the printed parts' surface properties were modified by linking other functional groups with biomedical interest. Two approaches were followed; first, in Part I, Chapter 4, the surface properties were modified by exploiting the unreacted acrylate groups after the 3D printing step of the PDMS-based photopolymer. In this way, other functional groups, i.e., carboxylic moieties, were chemically linked to those exposed groups during the necessary UV post-curing step via photon-grafting functionalization. The second strategy was based on incorporating functional elements in the printable photopolymer that, after the printing process, can be used for linking amine molecules through microwave irradiation (Part II, Chapter 4), obtaining thus structures with strong antibacterial properties on behalf of the amine molecules. In the last experimental part, Chapter 5, precise and complex-shaped optical structures were obtained by adding a photoluminescent dye into the printable photopolymer. The objects' optical performances, such as light guiding and photoluminescent properties, can be tailored by adjusting the dye concentration. The dye was copolymerized with the polymeric network during the printing step, and therefore, its properties were effectively transferred to the printed part, enabling the use of these 3D printed waveguides as solvent polarity sensors. The optical properties displayed by these unique devices may potentially cover applications in integrated optical platforms, with customized shapes and tailored optical properties, and analytical medical and chemical fields for biosensing applications and multiplexed detection.

As seen, customized 3D printed structures with tailored properties can be manufactured through vat polymerization 3D printing by properly selecting the components for the photocurable formulation and exploiting the freedom of design that 3D printing techniques offer. From this point of view, possible applications in the (bio)medical field might be wide-ranging, including biomedical scenarios where the integration of microfluidic systems with multi-well plates is desired. Vat polymerization 3D printing can be used for the realization of such specific configurations from a structural point of view (for example, using different materials with various features in a single printing process); also by properly adjusting the properties of the parts for creating these 3D printed platforms with different and engineered surface properties that can be adapted to various applications, see Illustration 1. Acting on these two fronts, one can imagine the production of tailor-made three-dimensional devices for performing chemical screening in static liquid environments (multiwell plates approach) and analysis with controlling dynamic fluid (microfluidic devices approach). Several investigations have been reported in recent times about this subject, describing how the integration of both systems could enable the automation of specific analysis, such as fish embryo toxicity tests, enzymatic assays, and drug screening on



tumor cell lines.<sup>274,540-548</sup> These high-throughput devices can considerably reduce laborious and time-consuming manual manipulation of specimens and solutions and the cost of laboratory protocols. Moreover, due to the continuous development of materials and technology for the medical field, these 3D printed systems could be envisaged among the new generation of futuristic 'smart' devices in point-of-care medicine, which involves cost-effective personalized and mobile health care, that can be useful, particularly in remote and resource-deficient areas.<sup>287</sup>

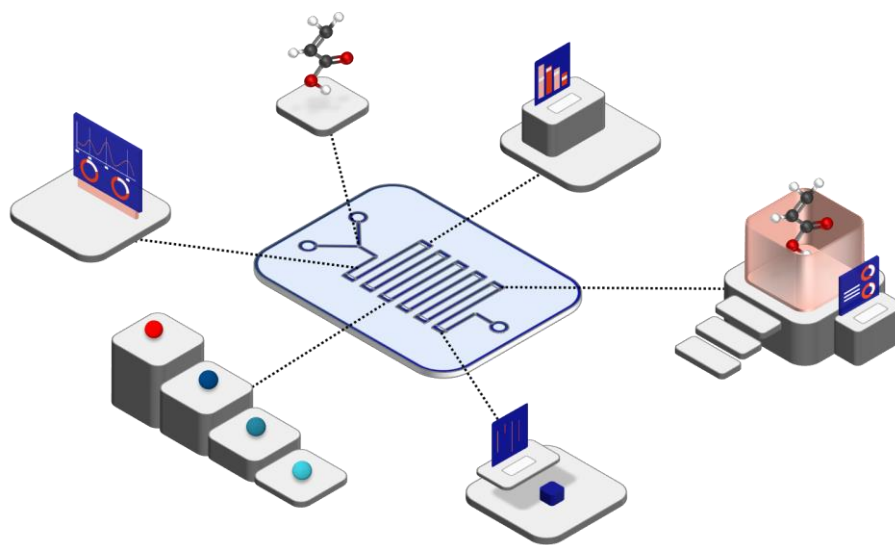


**Illustration 1: Representation of an engineered microfluidic platform where each channel's section presents different surface characteristics.**



# References

- (1) Santos, C.; Mehrsai, A.; Barros, A. C.; Araújo, M.; Ares, E. Towards Industry 4.0: An Overview of European Strategic Roadmaps. *Procedia Manuf.* **2017**, *13*, 972–979. <https://doi.org/10.1016/j.promfg.2017.09.093>.
- (2) Dilberoglu, U. M.; Gharehpapagh, B.; Yaman, U.; Dolen, M. The Role of Additive Manufacturing in the Era of Industry 4.0. *Procedia Manuf.* **2017**, *11* (June), 545–554. <https://doi.org/10.1016/j.promfg.2017.07.148>.
- (3) Ngo, T. D.; Kashani, A.; Imbalzano, G.; Nguyen, K. T. Q.; Hui, D. Additive Manufacturing (3D Printing): A Review of Materials, Methods, Applications and Challenges. *Composites Part B: Engineering*. 2018. <https://doi.org/10.1016/j.compositesb.2018.02.012>.
- (4) Anglani, G. 3D Printed Capsules for Self-Healing Concrete Applications. **2019**, No. June. <https://doi.org/10.21012/fc10.235356>.
- (5) de Leon, A. C.; Chen, Q.; Palaganas, N. B.; Palaganas, J. O.; Manapat, J.; Advincula, R. C. High Performance Polymer Nanocomposites for Additive Manufacturing Applications. *React. Funct. Polym.* **2016**, *103*, 141–155. <https://doi.org/10.1016/j.reactfunctpolym.2016.04.010>.
- (6) Berman, B. 3-D Printing: The New Industrial Revolution. *Bus. Horiz.* **2012**, *55* (2), 155–162. <https://doi.org/10.1016/j.bushor.2011.11.003>.
- (7) Mehrpouya, M.; Dehghanghadikolaei, A.; Fotovvati, B.; Vosooghnia, A.; Emamian, S. S.; Gisario, A. The Potential of Additive Manufacturing in the Smart Factory Industrial 4.0: A Review. *Appl. Sci.* **2019**, *9* (18). <https://doi.org/10.3390/app9183865>.
- (8) Gebler, M.; Schoot Uiterkamp, A. J. M.; Visser, C. A Global Sustainability Perspective on 3D Printing Technologies. *Energy Policy* **2014**. <https://doi.org/10.1016/j.enpol.2014.08.033>.

- (9) Ford, S.; Despeisse, M. Additive Manufacturing and Sustainability: An Exploratory Study of the Advantages and Challenges. *J. Clean. Prod.* **2016**, *137*, 1573–1587. <https://doi.org/10.1016/j.jclepro.2016.04.150>.
- (10) Thomas, D. S.; Gilbert, S. W. Costs and Cost Effectiveness of Additive Manufacturing: A Literature Review and Discussion. In *Additive Manufacturing: Costs, Cost Effectiveness and Industry Economics*; 2015.
- (11) Matos, F.; Godina, R.; Jacinto, C.; Carvalho, H.; Ribeiro, I.; Peças, P. Additive Manufacturing: Exploring the Social Changes and Impacts. *Sustain.* **2019**. <https://doi.org/10.3390/su11143757>.
- (12) ASTM International. *ASTM F2792-12a, Standard Terminology for Additive Manufacturing Technologies*; West Conshohocken, PA, 2012. <https://doi.org/10.1520/F2792-12A2>.
- (13) Chong, L.; Ramakrishna, S.; Singh, S. A Review of Digital Manufacturing-Based Hybrid Additive Manufacturing Processes. *Int. J. Adv. Manuf. Technol.* **2018**, *95* (5–8), 2281–2300. <https://doi.org/10.1007/s00170-017-1345-3>.
- (14) Kodama, H. Automatic Method for Fabricating a Three-Dimensional Plastic Model with Photo-Hardening Polymer. *Rev. Sci. Instrum.* **1981**. <https://doi.org/10.1063/1.1136492>.
- (15) Gupta, V.; Nesterenko, P.; Paull, B. *3D Printing in Chemical Sciences: Applications Across Chemistry*; The Royal Society of Chemistry, 2019. <https://doi.org/10.1039/9781788015745>.
- (16) Hull, C. W. Apparatus for Production of Three-Dimensional Objects By Stereolithography. *Patent* **1984**, No. 19, 16.
- (17) Deckard, C. R. ; Beaman, J. J. ; Darrah, J. F. Method and Apparatus for Producing Parts by Selective Sintering. *U.S. Pat. 4,863,538* **1992**.
- (18) Beaman, J. J.; Deckard, C. R. Selective Laser Sintering With Assisted Powder Handling. *Google Patents* **1990**.
- (19) Bourell, D. L.; Marcus, H. L.; Barlow, J. W.; Beaman, J. J.; Deckard, C. R. Multiple Material Systems for Selective Beam Sintering, 1990.
- (20) Crump, S. Apparatus and Method for Creating Three-Dimensional Objects - Patent, 1992. [https://doi.org/10.2116/bunsekikagaku.28.3\\_195](https://doi.org/10.2116/bunsekikagaku.28.3_195).
- (21) Mordor Intelligence. 3D Printing Market - Growth, Trends, and Forecasts (2020 - 2025) <https://www.mordorintelligence.com/industry-reports/3d-printing-market>.
- (22) 3D systems, N. R. 3D Systems Opens New Advanced Additive Manufacturing Center in Pinerolo, Italy. *Clinical Toxicology*. Rock Hill, South Carolina April 11, 2019. <https://doi.org/10.3109/15563657408988018>.
- (23) Sculpteo. The State of 3D Printing <https://www.sculpteo.com/en/ebooks/state-of-3d-printing-report->

2020/.

- (24) Liu, R.; Wang, Z.; Sparks, T.; Liou, F.; Newkirk, J. Aerospace Applications of Laser Additive Manufacturing. In *Laser Additive Manufacturing: Materials, Design, Technologies, and Applications*; 2017. <https://doi.org/10.1016/B978-0-08-100433-3.00013-0>.
- (25) Reith, M.; Franke, M.; Schloffer, M.; Körner, C. Processing 4th Generation Titanium Aluminides via Electron Beam Based Additive Manufacturing – Characterization of Microstructure and Mechanical Properties. *Materialia* **2020**. <https://doi.org/10.1016/j.mtla.2020.100902>.
- (26) Uhlmann, E.; Kersting, R.; Klein, T. B.; Cruz, M. F.; Borille, A. V. Additive Manufacturing of Titanium Alloy for Aircraft Components. In *Procedia CIRP*; 2015. <https://doi.org/10.1016/j.procir.2015.08.061>.
- (27) DebRoy, T.; Wei, H. L.; Zuback, J. S.; Mukherjee, T.; Elmer, J. W.; Milewski, J. O.; Beese, A. M.; Wilson-Heid, A.; De, A.; Zhang, W. Additive Manufacturing of Metallic Components – Process, Structure and Properties. *Progress in Materials Science*. 2018. <https://doi.org/10.1016/j.pmatsci.2017.10.001>.
- (28) Deloitte. 3D opportunity for aerospace and defense <https://www2.deloitte.com/us/en/insights/focus/3d-opportunity/additive-manufacturing-3d-opportunity-in-aerospace.html>.
- (29) Nickels, L. AM and Aerospace: An Ideal Combination. *Met. Powder Rep.* **2015**, *70* (6), 300–303. <https://doi.org/10.1016/j.mprp.2015.06.005>.
- (30) Materialise. A 63% Lighter Titanium Aerospace Part <https://www.materialise.com/en/cases/a-63-lighter-titanium-aerospace-part> (accessed Sep 20, 2020).
- (31) Beamler, A. M. Business cases: 3D printing in the automotive industry <https://www.beamler.com/3d-printing-in-the-automotive-industry/>.
- (32) Porsche Communication for journalists. Classic parts from a 3D printer <https://newsroom.porsche.com/en/company/porsche-classic-3d-printer-spare-parts-sls-printer-production-cars-innovative-14816.html>.
- (33) Nichols, M. R. How Does the Automotive Industry Benefit from 3D Metal Printing? *Met. Powder Rep.* **2019**, *74* (5), 257–258. <https://doi.org/10.1016/j.mprp.2019.07.002>.
- (34) Ni, J.; Ling, H.; Zhang, S.; Wang, Z.; Peng, Z.; Benyshek, C.; Zan, R.; Miri, A. K.; Li, Z.; Zhang, X.; Lee, J.; Lee, K. J.; Kim, H. J.; Tebon, P.; Hoffman, T.; Dokmeci, M. R.; Ashammakhi, N.; Li, X.; Khademhosseini, A. Three-Dimensional Printing of Metals for Biomedical Applications. *Mater. Today Bio* **2019**, *3* (May). <https://doi.org/10.1016/j.mtbio.2019.100024>.
- (35) Sarment, D. P.; Al-Shammari, K.; Kazor, C. E. Stereolithographic Surgical Templates for Placement of Dental Implants in Complex Cases. *Int. J. Periodontics Restorative Dent.* **2003**.

<https://doi.org/10.11607/prd.00.0527>.

- (36) Yan, Q.; Dong, H.; Su, J.; Han, J.; Song, B.; Wei, Q.; Shi, Y. A Review of 3D Printing Technology for Medical Applications. *Engineering* **2018**, *4* (5), 729–742. <https://doi.org/10.1016/j.eng.2018.07.021>.
- (37) Lee Ventola, C. Medical Applications for 3D Printing: Current and Projected Uses. *P T* **2014**, *39* (10), 704–711.
- (38) Mondschein, R. J.; Kanitkar, A.; Williams, C. B.; Verbridge, S. S.; Long, T. E. Polymer Structure-Property Requirements for Stereolithographic 3D Printing of Soft Tissue Engineering Scaffolds. *Biomaterials* **2017**, *140*, 170–188. <https://doi.org/10.1016/j.biomaterials.2017.06.005>.
- (39) Williams, F. C.; Hammer, D. A.; Wentland, T. R.; Kim, R. Y. Immediate Teeth in Fibulas: Planning and Digital Workflow With Point-of-Care 3D Printing. *J. Oral Maxillofac. Surg.* **2020**, *78* (8), 1320–1327. <https://doi.org/10.1016/j.joms.2020.04.006>.
- (40) Jardini, A. L.; Larosa, M. A.; de Carvalho Zavaglia, C. A.; Bernardes, L. F.; Lambert, C. S.; Kharmandayan, P.; Calderoni, D.; Maciel Filho, R. Customised Titanium Implant Fabricated in Additive Manufacturing for Craniomaxillofacial Surgery: This Paper Discusses the Design and Fabrication of a Metallic Implant for the Reconstruction of a Large Cranial Defect. *Virtual Phys. Prototyp.* **2014**, *9* (2), 115–125. <https://doi.org/10.1080/17452759.2014.900857>.
- (41) Kang, H. G. 3D-Printed Personalized Titanium Implant Design, Manufacturing and Verification for Bone Tumor Surgery of Forearm. *Biomed. J. Sci. Tech. Res.* **2018**, *10* (3), 7796–7801. <https://doi.org/10.26717/bjstr.2018.10.001950>.
- (42) Wong, K. C. 3D-Printed Patient-Specific Applications in Orthopedics. *Orthop. Res. Rev.* **2016**, *8* (October), 57–66. <https://doi.org/10.2147/ORR.S99614>.
- (43) Gemalmaz, H. C.; Sariyılmaz, K.; Ozkunt, O.; Sungur, M.; Kaya, I.; Dikici, F. Postoperative Mechanical Alignment Analysis of Total Knee Replacement Patients Operated with 3D Printed Patient Specific Instruments: A Prospective Cohort Study. *Acta Orthop. Traumatol. Turc.* **2019**, *53* (5), 323–328. <https://doi.org/10.1016/j.aott.2019.02.001>.
- (44) Goldstein, T.; Oreste, A.; Hutnick, G.; Chory, A.; Chehata, V.; Seldin, J.; Gallo, M. D.; Bloom, O. A Pilot Study Testing a Novel 3D Printed Amphibious Lower Limb Prosthesis in a Recreational Pool Setting. *PM R* **2020**, *12* (8), 783–793. <https://doi.org/10.1002/pmrj.12293>.
- (45) Apis-Cor. Groundbreaking project <https://www.apis-cor.com/dubai-project> (accessed Oct 25, 2019).
- (46) Mantihal, S.; Kobun, R.; Lee, B. B. 3D Food Printing of as the New Way of Preparing Food: A Review. *Int. J. Gastron. Food Sci.* **2020**, *22* (September), 100260. <https://doi.org/10.1016/j.ijgfs.2020.100260>.
- (47) Sun, J.; Zhou, W.; Yan, L.; Huang, D.; Lin, L. ya. Extrusion-Based Food Printing for Digitalized Food Design and Nutrition Control. *J. Food Eng.*

- 2018**, *220*, 1–11. <https://doi.org/10.1016/j.jfoodeng.2017.02.028>.
- (48) Wu, P.; Wang, J.; Wang, X. A Critical Review of the Use of 3-D Printing in the Construction Industry. *Autom. Constr.* **2016**, *68*, 21–31. <https://doi.org/10.1016/j.autcon.2016.04.005>.
- (49) He, C.; Zhang, M.; Fang, Z. 3D Printing of Food: Pretreatment and Post-Treatment of Materials. *Crit. Rev. Food Sci. Nutr.* **2020**, *60* (14), 2379–2392. <https://doi.org/10.1080/10408398.2019.1641065>.
- (50) Liu, L.; Meng, Y.; Dai, X.; Chen, K.; Zhu, Y. 3D Printing Complex Egg White Protein Objects: Properties and Optimization. *Food Bioprocess Technol.* **2019**, *12* (2), 267–279. <https://doi.org/10.1007/s11947-018-2209-z>.
- (51) Lanaro, M.; Forrestal, D. P.; Scheurer, S.; Slinger, D. J.; Liao, S.; Powell, S. K.; Woodruff, M. A. 3D Printing Complex Chocolate Objects: Platform Design, Optimization and Evaluation. *J. Food Eng.* **2017**, *215*, 13–22. <https://doi.org/10.1016/j.jfoodeng.2017.06.029>.
- (52) Sun, J.; Zhou, W.; Huang, D.; Fuh, J. Y. H.; Hong, G. S. An Overview of 3D Printing Technologies for Food Fabrication. *Food Bioprocess Technol.* **2015**, *8* (8), 1605–1615. <https://doi.org/10.1007/s11947-015-1528-6>.
- (53) Karyappa, R.; Hashimoto, M. Chocolate-Based Ink Three-Dimensional Printing (Ci3DP). *Sci. Rep.* **2019**, *9* (1), 1–11. <https://doi.org/10.1038/s41598-019-50583-5>.
- (54) Liu, Z.; Zhang, M.; Bhandari, B.; Wang, Y. 3D Printing: Printing Precision and Application in Food Sector. *Trends Food Sci. Technol.* **2017**, *69*, 83–94. <https://doi.org/10.1016/j.tifs.2017.08.018>.
- (55) Joshi, S.; Rawat, K.; C, K.; Rajamohan, V.; Mathew, A. T.; Koziol, K.; Kumar Thakur, V.; A.S.S, B. 4D Printing of Materials for the Future: Opportunities and Challenges. *Appl. Mater. Today* **2020**, *18*, 100490. <https://doi.org/10.1016/j.apmt.2019.100490>.
- (56) Rafiee, M.; Farahani, R. D.; Therriault, D. Multi-Material 3D and 4D Printing: A Survey. *Adv. Sci.* **2020**, *7* (12), 1–26. <https://doi.org/10.1002/advs.201902307>.
- (57) Korger, M.; Bergschneider, J.; Lutz, M.; Mahltig, B.; Finsterbusch, K.; Rabe, M. Possible Applications of 3D Printing Technology on Textile Substrates. *IOP Conf. Ser. Mater. Sci. Eng.* **2016**, *141* (1). <https://doi.org/10.1088/1757-899X/141/1/012011>.
- (58) Mawale, M. B.; Kuthe, A. M.; Dahake, S. W. Additive Layered Manufacturing: State-of-the-Art Applications in Product Innovation. *Concurr. Eng. Res. Appl.* **2016**, *24* (1), 94–102. <https://doi.org/10.1177/1063293X15613111>.
- (59) Cao, Y.; Zhang, G.; Zhang, Y.; Yue, M.; Chen, Y.; Cai, S.; Xie, T.; Feng, X. Direct Fabrication of Stretchable Electronics on a Polymer Substrate with Process-Integrated Programmable Rigidity. *Adv. Funct. Mater.* **2018**, *28* (50), 1–9. <https://doi.org/10.1002/adfm.201804604>.
- (60) Chatterjee, K.; Ghosh, T. K. 3D Printing of Textiles: Potential Roadmap to Printing with Fibers. *Adv. Mater.* **2020**, *32* (4), 1–24.

<https://doi.org/10.1002/adma.201902086>.

- (61) Zastrow, M. The New 3D Printing. *Nature* **2020**, *578* (February), 20–24.
- (62) Pérez, M.; Carou, D.; Rubio, E. M.; Teti, R. Current Advances in Additive Manufacturing. *Procedia CIRP* **2020**, *88*, 439–444. <https://doi.org/10.1016/j.procir.2020.05.076>.
- (63) Dehghanhadikolaei, A.; Namdari, N.; Mohammadian, B. Additive Manufacturing Methods : A Brief Overview. **2018**, No. September.
- (64) Pham, D. T.; Gault, R. S. A Comparison of Rapid Prototyping Technologies. *Int. J. Mach. Tools Manuf.* **1998**, *38* (10–11), 1257–1287. [https://doi.org/10.1016/S0890-6955\(97\)00137-5](https://doi.org/10.1016/S0890-6955(97)00137-5).
- (65) Chen, D.; Heyer, S.; Ibbotson, S.; Salonitis, K.; Steingrímsson, J. G.; Thiede, S. Direct Digital Manufacturing: Definition, Evolution, and Sustainability Implications. *J. Clean. Prod.* **2015**. <https://doi.org/10.1016/j.jclepro.2015.05.009>.
- (66) Zhou, L. Y.; Fu, J.; He, Y. A Review of 3D Printing Technologies for Soft Polymer Materials. *Adv. Funct. Mater.* **2020**, *2000187*, 1–38. <https://doi.org/10.1002/adfm.202000187>.
- (67) Gross, B. C.; Erkal, J. L.; Lockwood, S. Y.; Chen, C.; Spence, D. M. Evaluation of 3D Printing and Its Potential Impact on Biotechnology and the Chemical Sciences. **2014**.
- (68) Zhao, J.; Hussain, M.; Wang, M.; Li, Z.; He, N. Embedded 3D Printing of Multi-Internal Surfaces of Hydrogels. *Addit. Manuf.* **2020**, *32* (September 2019), 101097. <https://doi.org/10.1016/j.addma.2020.101097>.
- (69) ISO; ASTM. ISO/ASTM 52900 Additive Manufacturing — General Principles — Terminology. In *International Standards*; 2015. <https://doi.org/10.1520/ISOASTM52900-15>.
- (70) Stansbury, J. W.; Idacavage, M. J. 3D Printing with Polymers: Challenges among Expanding Options and Opportunities. *Dent. Mater.* **2016**, *32* (1), 54–64. <https://doi.org/10.1016/j.dental.2015.09.018>.
- (71) Ng, W. L.; Lee, J. M.; Zhou, M.; Chen, Y. W.; Lee, K. X. A.; Yeong, W. Y.; Shen, Y. F. Vat Polymerization-Based Bioprinting - Process, Materials, Applications and Regulatory Challenges. *Biofabrication* **2020**, *12* (2). <https://doi.org/10.1088/1758-5090/ab6034>.
- (72) Li, W.; Mille, L. S.; Robledo, J. A.; Uribe, T.; Huerta, V.; Zhang, Y. S. Recent Advances in Formulating and Processing Biomaterial Inks for Vat Polymerization-Based 3D Printing. *Adv. Healthc. Mater.* **2020**, *9* (15), 1–18. <https://doi.org/10.1002/adhm.202000156>.
- (73) Braun, D.; Cherdron, H.; Rehahn, M.; Ritter, H.; Voit, B. *Polymer Synthesis: Theory and Practice: Fundamentals, Methods, Experiments, Fifth Edition*; 2013. <https://doi.org/10.1007/978-3-642-28980-4>.
- (74) Odian, G. *Principles of Polymerization*, 3rd Edit.; John Wiley & Sons Inc: New York, USA, 1991.
- (75) Minsk, L. M.; Van Deusen, W. P.; Robertson, E. M. Photosensitization of



Polymeric Cinnamic Acid Esters, 1952.

- (76) Crivello, J. V. Photopolymerization. In *Polymer Science: A Comprehensive Reference, 10 Volume Set*; 2012. <https://doi.org/10.1016/B978-0-444-53349-4.00123-0>.
- (77) Yu, C.; Schimelman, J.; Wang, P.; Miller, K. L.; Ma, X.; You, S.; Guan, J.; Sun, B.; Zhu, W.; Chen, S. Photopolymerizable Biomaterials and Light-Based 3D Printing Strategies for Biomedical Applications. *Chem. Rev.* **2020**. <https://doi.org/10.1021/acs.chemrev.9b00810>.
- (78) Crivello, J. V.; Reichmanis, E. Photopolymer Materials and Processes for Advanced Technologies. **2014**.
- (79) Narupai, B.; Nelson, A. 100th Anniversary of Macromolecular Science Viewpoint: Macromolecular Materials for Additive Manufacturing. *ACS Macro Lett.* **2020**, 627–638. <https://doi.org/10.1021/acsmacrolett.0c00200>.
- (80) Felix, J. F.; Barros, R. A.; De Azevedo, W. M.; Da Silva, E. F. X-Ray Irradiation: A Non-Conventional Route for the Synthesis of Conducting Polymers. *Synth. Met.* **2011**. <https://doi.org/10.1016/j.synthmet.2010.11.017>.
- (81) Chen, Z.; Wang, X.; Li, S.; Liu, S.; Miao, H.; Wu, S. Near-Infrared Light Driven Photopolymerization Based On Photon Upconversion. *ChemPhotoChem*. 2019. <https://doi.org/10.1002/cptc.201900007>.
- (82) Li, Z.; Chen, H.; Wang, C.; Chen, L.; Liu, J.; Liu, R. Efficient Photopolymerization of Thick Pigmented Systems Using Upconversion Nanoparticles-Assisted Photochemistry. *J. Polym. Sci. Part A Polym. Chem.* **2018**, 56 (9), 994–1002. <https://doi.org/10.1002/pola.28969>.
- (83) Fantino, E.; Vitale, A.; Quaglio, M.; Cocuzza, M.; Pirri, C. F.; Bongiovanni, R. Blue and UV Combined Photolithographic Polymerization for the Patterning of Thick Structures. *Chem. Eng. J.* **2015**, 267 (May), 65–72. <https://doi.org/10.1016/j.cej.2014.12.088>.
- (84) Masson, F.; Decker, C.; Andre, S.; Andrieu, X. UV-Curable Formulations for UV-Transparent Optical Fiber Coatings: I. Acrylic Resins. *Prog. Org. Coatings* **2004**, 49 (1), 1–12. [https://doi.org/10.1016/S0300-9440\(03\)00122-X](https://doi.org/10.1016/S0300-9440(03)00122-X).
- (85) Steyrer, B.; Neubauer, P.; Liska, R.; Stampfl, J. Visible Light Photoinitiator for 3D-Printing of Tough Methacrylate Resins. *Materials (Basel)*. **2017**, 10 (12), 1–11. <https://doi.org/10.3390/ma10121445>.
- (86) Fouassier, J. P.; Allonas, X.; Burget, D. Photopolymerization Reactions under Visible Lights: Principle, Mechanisms and Examples of Applications. *Prog. Org. Coatings* **2003**. [https://doi.org/10.1016/S0300-9440\(03\)00011-0](https://doi.org/10.1016/S0300-9440(03)00011-0).
- (87) Sangermano, M.; Razza, N.; Crivello, J. V. Cationic UV-Curing: Technology and Applications. *Macromol. Mater. Eng.* **2014**, 299 (7), 775–793. <https://doi.org/10.1002/mame.201300349>.
- (88) Allonas, X. Photopolymerization, Cationic. In *Encyclopedia of Polymer*

- Science and Technology*; 2019.  
<https://doi.org/10.1002/0471440264.pst491.pub2>.
- (89) Fouassier, J. P.; Lalevée, J. *Photoinitiators for Polymer Synthesis*; 2012.  
<https://doi.org/10.1002/9783527648245>.
- (90) Zhao, T.; Li, X.; Yu, R.; Zhang, Y.; Yang, X.; Zhao, X.; Wang, L.; Huang, W. Silicone–Epoxy-Based Hybrid Photopolymers for 3D Printing. *Macromol. Chem. Phys.* **2018**, *219* (10), 1–10.  
<https://doi.org/10.1002/macp.201700530>.
- (91) Sangermano, M.; Acosta Ortiz, R.; Garcia Valdez, A. E.; Berlanga Duarte, L.; Amerio, E.; Priola, A.; Rizza, G. Developments of Organic-Inorganic Hybrid Free Radical-Cationic Dual Cured Coatings. *Polym. Bull.* **2008**, *59*, 865–872. <https://doi.org/10.1007/s00289-007-0833-2>.
- (92) Yagci, Y.; Jockusch, S.; Turro, N. J. Photoinitiated Polymerization: Advances, Challenges, and Opportunities. *Macromolecules* **2010**, *43* (15), 6245–6260. <https://doi.org/10.1021/ma1007545>.
- (93) Fouassiers, J. P.; Lalevée, J. *Photoinitiators for Polymer Synthesis*; Wiley-VCH Verlag & Co. KGaA: Weinheim, Germany, 2012.
- (94) Andrzejewska, E. Photopolymerization Kinetics of Multifunctional Monomers. *Progress in Polymer Science (Oxford)*. 2001.  
[https://doi.org/10.1016/S0079-6700\(01\)00004-1](https://doi.org/10.1016/S0079-6700(01)00004-1).
- (95) Pascault, J. P.; Sautereau, H.; Verdu, J.; Williams, R. J. J. *Thermosetting Polymers*; Marcel Dekker Inc: New York, USA, 2002.
- (96) Lammel-Lindemann, J.; Dourado, I. A.; Shanklin, J.; Rodriguez, C. A.; Catalani, L. H.; Dean, D. Photocrosslinking-Based 3D Printing of Unsaturated Polyesters from Isosorbide: A New Material for Resorbable Medical Devices. *Bioprinting* **2020**.  
<https://doi.org/10.1016/j.bprint.2019.e00062>.
- (97) Scott, P. J.; Meenakshisundaram, V.; Hegde, M.; Kasprzak, C. R.; Winkler, C. R.; Feller, K. D.; Williams, C. B.; Long, T. E. 3D Printing Latex: A Route to Complex Geometries of High Molecular Weight Polymers. *ACS Appl. Mater. Interfaces* **2020**. <https://doi.org/10.1021/acscami.9b19986>.
- (98) Leonards, H.; Engelhardt, S.; Hoffmann, A.; Pongratz, L.; Schriever, S.; Bläsius, J.; Wehner, M.; Gillner, A. Advantages and Drawbacks of Thiol-Ene Based Resins for 3D-Printing. In *Laser 3D Manufacturing II*; 2015.  
<https://doi.org/10.1117/12.2081169>.
- (99) Bagheri, A.; Jin, J. Photopolymerization in 3D Printing. *ACS Appl. Polym. Mater.* **2019**, *1* (4), 593–611.  
<https://doi.org/10.1021/acsapm.8b00165>.
- (100) Decker, C.; Jenkins, A. D. Kinetic Approach of O<sub>2</sub> Inhibition in Ultraviolet and Laser-Induced Polymerizations. *Macromolecules* **1985**.  
<https://doi.org/10.1021/ma00148a034>.
- (101) Ligon, S. C.; Husár, B.; Wutzel, H.; Holman, R.; Liska, R. Strategies to Reduce Oxygen Inhibition in Photoinduced Polymerization. *Chem. Rev.* **2014**, *114* (1), 577–589. <https://doi.org/10.1021/cr3005197>.

- (102) Studer, K.; Decker, C.; Beck, E.; Schwalm, R. Overcoming Oxygen Inhibition in UV-Curing of Acrylate Coatings by Carbon Dioxide Inerting, Part I. *Prog. Org. Coatings* **2003**, *48* (1), 92–100. [https://doi.org/10.1016/S0300-9440\(03\)00120-6](https://doi.org/10.1016/S0300-9440(03)00120-6).
- (103) Zhao, Z.; Mu, X.; Wu, J.; Qi, H. J.; Fang, D. Effects of Oxygen on Interfacial Strength of Incremental Forming of Materials by Photopolymerization. *Extrem. Mech. Lett.* **2016**, *9*, 108–118. <https://doi.org/10.1016/j.eml.2016.05.012>.
- (104) Cheng, Y.-L.; Kao, H.-L. Study on Visible-Light-Curable Polycaprolactone and Poly(Ethylene Glycol) Diacrylate for LCD-Projected Maskless Additive Manufacturing System. In *Light Manipulating Organic Materials and Devices II*; 2015. <https://doi.org/10.1117/12.2188047>.
- (105) Kim, S. H.; Yeon, Y. K.; Lee, J. M.; Chao, J. R.; Lee, Y. J.; Seo, Y. B.; Sultan, M. T.; Lee, O. J.; Lee, J. S.; Yoon, S. Il; Hong, I. S.; Khang, G.; Lee, S. J.; Yoo, J. J.; Park, C. H. Precisely Printable and Biocompatible Silk Fibroin Bioink for Digital Light Processing 3D Printing. *Nat. Commun.* **2018**, *9* (1), 1–14. <https://doi.org/10.1038/s41467-018-03759-y>.
- (106) Moszner, N.; Salz, U. New Developments of Polymeric Dental Composites. *Prog. Polym. Sci.* **2001**, *26* (4), 535–576. [https://doi.org/10.1016/S0079-6700\(01\)00005-3](https://doi.org/10.1016/S0079-6700(01)00005-3).
- (107) Charton, C.; Colon, P.; Pla, F. Shrinkage Stress in Light-Cured Composite Resins: Influence of Material and Photoactivation Mode. *Dent. Mater.* **2007**, *23* (8), 911–920. <https://doi.org/10.1016/j.dental.2006.06.034>.
- (108) Kuang, X.; Zhao, Z.; Chen, K.; Fang, D.; Kang, G.; Qi, H. J. High-Speed 3D Printing of High-Performance Thermosetting Polymers via Two-Stage Curing. *Macromol. Rapid Commun.* **2018**, *39* (7), 1–8. <https://doi.org/10.1002/marc.201700809>.
- (109) Li, Z.; Wang, C.; Qiu, W.; Liu, R. Antimicrobial Thiol–Ene–Acrylate Photosensitive Resins for DLP 3D Printing. *Photochem. Photobiol.* **2019**, No. 32, 1219–1229. <https://doi.org/10.1111/php.13099>.
- (110) Oesterreicher, A.; Wiener, J.; Roth, M.; Moser, A.; Gmeiner, R.; Edler, M.; Pinter, G.; Griesser, T. Tough and Degradable Photopolymers Derived from Alkyne Monomers for 3D Printing of Biomedical Materials. *Polym. Chem.* **2016**. <https://doi.org/10.1039/c6py01132b>.
- (111) Griffini, G.; Invernizzi, M.; Levi, M.; Natale, G.; Postiglione, G.; Turri, S. 3D-Printable CFR Polymer Composites with Dual-Cure Sequential IPNs. *Polymer (Guildf)*. **2016**, *91*, 174–179. <https://doi.org/10.1016/j.polymer.2016.03.048>.
- (112) Lantean, S.; Roppolo, I.; Sangermano, M.; Pirri, C. F.; Chiappone, A. Development of New Hybrid Acrylic/Epoxy DLP-3D Printable Materials. *Inventions* **2018**, *3* (2), 1–13. <https://doi.org/10.3390/inventions3020029>.
- (113) Shanmugam, S.; Xu, J.; Boyer, C. Light-Regulated Polymerization under near-Infrared/Far-Red Irradiation Catalyzed by Bacteriochlorophyll A. *Angew. Chemie - Int. Ed.* **2016**.

<https://doi.org/10.1002/anie.201510037>.

- (114) Corrigan, N.; Xu, J.; Boyer, C. A Photoinitiation System for Conventional and Controlled Radical Polymerization at Visible and NIR Wavelengths. *Macromolecules* **2016**. <https://doi.org/10.1021/acs.macromol.6b00542>.
- (115) Al Mousawi, A.; Poriel, C.; Dumur, F.; Toufaily, J.; Hamieh, T.; Fouassier, J. P.; Lalevée, J. Zinc Tetraphenylporphyrin as High Performance Visible Light Photoinitiator of Cationic Photosensitive Resins for LED Projector 3D Printing Applications. *Macromolecules* **2017**. <https://doi.org/10.1021/acs.macromol.6b02596>.
- (116) Xu, J.; Shanmugam, S.; Fu, C.; Aguey-Zinsou, K. F.; Boyer, C. Selective Photoactivation: From a Single Unit Monomer Insertion Reaction to Controlled Polymer Architectures. *J. Am. Chem. Soc.* **2016**. <https://doi.org/10.1021/jacs.5b12408>.
- (117) Hong, B. M.; Park, S. A.; Park, W. H. Effect of Photoinitiator on Chain Degradation of Hyaluronic Acid. *Biomater. Res.* **2019**. <https://doi.org/10.1186/s40824-019-0170-1>.
- (118) Zhang, J.; Lalevée, J.; Zhao, J.; Graff, B.; Stenzel, M. H.; Xiao, P. Dihydroxyanthraquinone Derivatives: Natural Dyes as Blue-Light-Sensitive Versatile Photoinitiators of Photopolymerization. *Polym. Chem.* **2016**. <https://doi.org/10.1039/c6py01550f>.
- (119) Santini, A.; Gallegos, I. T.; Felix, C. M. Photoinitiators in Dentistry: A Review. *Primary dental journal.* **2013**. <https://doi.org/10.1308/205016814809859563>.
- (120) Kuno, I.; Takeshi, E. A Review of the Development of Radical Photopolymerization Initiators Used for Designing Light-Curing Dental Adhesives and Resin Composites. *Dental Materials Journal.* **2010**. <https://doi.org/10.4012/dmj.2009-137>.
- (121) Lalevée, J.; Morlet-Savary, F.; Dietlin, C.; Graff, B.; Fouassier, J. P. Photochemistry and Radical Chemistry under Low Intensity Visible Light Sources: Application to Photopolymerization Reactions. *Molecules* **2014**. <https://doi.org/10.3390/molecules190915026>.
- (122) Sangermano, M.; Roppolo, I.; Chiappone, A. New Horizons in Cationic Photopolymerization. *Polymers.* **2018**. <https://doi.org/10.3390/polym10020136>.
- (123) Kaur, M.; Srivastava, A. K. Photopolymerization: A Review. *Journal of Macromolecular Science - Polymer Reviews.* **2002**. <https://doi.org/10.1081/MC-120015988>.
- (124) Kutall, C.; Grutsch, P. A.; Yang, D. B. A Novel Strategy for Photoinitiated Anionic-Polymerization. *Macromolecules* **1991**, *24* (26), 6872–6873. <https://doi.org/10.1021/ma00026a016>.
- (125) Palmer, B. J.; Kutal, C.; Billing, R.; Hennig, H. A New Photoinitiator for Anionic Polymerization. *Macromolecules.* **1995**. <https://doi.org/10.1021/ma00108a078>.

- (126) Wang, Y. H.; Wan, P. Ketoprofen as a Photoinitiator for Anionic Polymerization. *Photochem. Photobiol. Sci.* **2015**. <https://doi.org/10.1039/c4pp00454j>.
- (127) Rahal, M.; Mokbel, H.; Gra, B.; Toufaily, J.; Hamieh, T.; Lalev, J. Mono vs. Difunctional Coumarin as Photoinitiators in Photocomposite Synthesis and 3D Printing. *Catalysts* **2020**, *10* (1202), 1–18. <https://doi.org/doi:10.3390/catal10101202>.
- (128) Nguyen, A. K.; Goering, P. L.; Elespuru, R. K.; Das, S. S.; Narayan, R. J. The Photoinitiator Lithium Phenyl (2,4,6-Trimethylbenzoyl) Phosphinate with Exposure to 405 Nm Light Is Cytotoxic to Mammalian Cells but Not Mutagenic in Bacterial Reverse Mutation Assays. *Polymers (Basel)*. **2020**, *12* (1489), 1–13. <https://doi.org/10.3390/polym12071489>.
- (129) Tomal, W.; Ortyl, J. Water-Soluble Photoinitiators in Biomedical Applications. *Polymers (Basel)*. **2020**, *12* (1073), 1–30. <https://doi.org/10.3390/POLYM12051073>.
- (130) Eren, T. N.; Gencoglu, T.; Abdallah, M.; Lalevée, J.; Avci, D. A Water Soluble and Highly Reactive Bisphosphonate Functionalized Thioxanthone-Based Photoinitiator. *Eur. Polym. J.* **2020**, *135*, 109906. <https://doi.org/10.1016/j.eurpolymj.2020.109906>.
- (131) Breloy, L.; Negrell, C.; Mora, A. S.; Li, W. S. J.; Brezová, V.; Caillol, S.; Versace, D. L. Vanillin Derivative as Performing Type I Photoinitiator. *Eur. Polym. J.* **2020**, *132*, 109727. <https://doi.org/10.1016/j.eurpolymj.2020.109727>.
- (132) Love, D. M.; Fairbanks, B. D.; Bowman, C. N. Evaluation of Aromatic Thiols as Photoinitiators. *Macromolecules* **2020**, *53* (13), 5237–5247. <https://doi.org/10.1021/acs.macromol.0c00757>.
- (133) Liu, S.; Chen, H.; Zhang, Y.; Sun, K.; Xu, Y.; Morlet-Savary, F.; Graff, B.; Noirbent, G.; Pigot, C.; Brunel, D.; Nechab, M.; Gignes, D.; Xiao, P.; Dumur, F.; Lalevée, J. Monocomponent Photoinitiators Based on Benzophenone-Carbazole Structure for LED Photoinitiating Systems and Application on 3D Printing. *Polymers (Basel)*. **2020**, *12* (1394), 1–15. <https://doi.org/10.3390/polym12061394>.
- (134) Lim, K. S.; Galarraga, J. H.; Cui, X.; Lindberg, G. C. J.; Burdick, J. A.; Woodfield, T. B. F. Fundamentals and Applications of Photo-Cross-Linking in Bioprinting. *Chem. Rev.* **2020**. <https://doi.org/10.1021/acs.chemrev.9b00812>.
- (135) Besse, V.; Derbanne, M. A.; Pham, T. N.; Cook, W. D.; Le Pluart, L. Photopolymerization Study and Adhesive Properties of Self-Etch Adhesives Containing Bis(Acyl)Phosphine Oxide Initiator. *Dent. Mater.* **2016**. <https://doi.org/10.1016/j.dental.2016.01.005>.
- (136) Ravve, A. *Light-Associated Reactions of Synthetic Polymers*; Springer US, 2006.
- (137) Ayub, N. F.; Hashim, S.; Jamaluddin, J.; Adrus, N. New UV LED Curing Approach for Polyacrylamide and Poly(: N -Isopropylacrylamide) Hydrogels. *New J. Chem.* **2017**. <https://doi.org/10.1039/c7nj00176b>.

- (138) Mucci, V.; Vallo, C. Efficiency of 2,2-Dimethoxy-2-Phenylacetophenone for the Photopolymerization of Methacrylate Monomers in Thick Sections. *J. Appl. Polym. Sci.* **2012**. <https://doi.org/10.1002/app.34473>.
- (139) Park, H. K.; Shin, M.; Kim, B.; Park, J. W.; Lee, H. A Visible Light-Curable yet Visible Wavelength-Transparent Resin for Stereolithography 3D Printing. *NPG Asia Mater.* **2018**, *10* (4), 82–89. <https://doi.org/10.1038/s41427-018-0021-x>.
- (140) Fairbanks, B. D.; Schwartz, M. P.; Bowman, C. N.; Anseth, K. S. Photoinitiated Polymerization of PEG-Diacrylate with Lithium Phenyl-2,4,6-Trimethylbenzoylphosphinate: Polymerization Rate and Cytocompatibility. *Biomaterials* **2009**, *30* (35), 6702–6707. <https://doi.org/10.1016/j.biomaterials.2009.08.055>.
- (141) Wang, K.; Yang, K.; Yu, Q. Novel Polymeric Photoinitiators with Side-Chain Benzophenone: Facile Synthesis and Photopolymerization Properties without Coinitiator. *Prog. Org. Coatings* **2014**. <https://doi.org/10.1016/j.porgcoat.2014.06.026>.
- (142) Matsushima, H.; Hait, S.; Li, Q.; Zhou, H.; Shirai, M.; Hoyle, C. E. Non-Extractable Photoinitiators Based on Thiol-Functionalized Benzophenones and Thioxanthenes. *Eur. Polym. J.* **2010**. <https://doi.org/10.1016/j.eurpolymj.2010.03.003>.
- (143) Chen, Y. C.; Ferracane, J. L.; Prahl, S. A. Quantum Yield of Conversion of the Photoinitiator Camphorquinone. *Dent. Mater.* **2007**. <https://doi.org/10.1016/j.dental.2006.06.005>.
- (144) Stemmelen, M.; Pessel, F.; Lapinte, V.; Caillol, S.; Habas, J. P.; Robin, J. J. A Fully Biobased Epoxy Resin from Vegetable Oils: From the Synthesis of the Precursors by Thiol-Ene Reaction to the Study of the Final Material. *J. Polym. Sci. Part A Polym. Chem.* **2011**, *49* (11), 2434–2444. <https://doi.org/10.1002/pola.24674>.
- (145) González, G.; Fernández-Francos, X.; Serra, À.; Sangermano, M.; Ramis, X. Environmentally-Friendly Processing of Thermosets by Two-Stage Sequential Aza-Michael Addition and Free-Radical Polymerization of Amine-Acrylate Mixtures. *Polym. Chem.* **2015**, *6*, 6987–6997. <https://doi.org/10.1039/C5PY00906E>.
- (146) Kokkinis, D.; Schaffner, M.; Studart, A. R. Multimaterial Magnetically Assisted 3D Printing of Composite Materials. *Nat. Commun.* **2015**, *6*. <https://doi.org/10.1038/ncomms9643>.
- (147) Kuo, A. P.; Bhattacharjee, N.; Lee, Y. S.; Castro, K.; Kim, Y. T.; Folch, A. High-Precision Stereolithography of Biomicrofluidic Devices. *Adv. Mater. Technol.* **2019**, *1800395* (4), 1–11. <https://doi.org/10.1002/admt.201800395>.
- (148) Wang, F.; Chong, Y.; Wang, F. K.; He, C. Photopolymer Resins for Luminescent Three-Dimensional Printing. *J. Appl. Polym. Sci.* **2017**, *134* (32), 1–8. <https://doi.org/10.1002/app.44988>.
- (149) Schuster, M.; Turecek, C.; Kaiser, B.; Stampfl, J.; Liska, R.; Varga, F. Evaluation of Biocompatible Photopolymers I: Photoreactivity and

- Mechanical Properties of Reactive Diluents. *J. Macromol. Sci. Part A Pure Appl. Chem.* **2007**, *44* (5), 547–557. <https://doi.org/10.1080/10601320701235958>.
- (150) Gonzalez, G.; Chiappone, A.; Roppolo, I.; Fantino, E.; Bertana, V.; Perrucci, F.; Scaltrito, L.; Pirri, F.; Sangermano, M. Development of 3D Printable Formulations Containing CNT with Enhanced Electrical Properties. *Polymer (Guildf)*. **2016**, *109*, 246–253. <https://doi.org/10.1016/j.polymer.2016.12.051>.
- (151) Manzano, J. S.; Weinstein, Z. B.; Sadow, A. D.; Slowing, I. I. Direct 3D Printing of Catalytically Active Structures. *ACS Catal.* **2017**, *7* (11), 7567–7577. <https://doi.org/10.1021/acscatal.7b02111>.
- (152) Roppolo, I.; Chiappone, A.; Angelini, A.; Stassi, S.; Frascella, F.; Pirri, C. F.; Ricciardi, C.; Descrovi, E. 3D Printable Light-Responsive Polymers. *Mater. Horizons* **2017**, *4* (3), 396–401. <https://doi.org/10.1039/c7mh00072c>.
- (153) Gong, H.; Bickham, B. P.; Woolley, A. T.; Nordin, G. P. Custom 3D Printer and Resin for 18 Mm × 20 Mm Microfluidic Flow Channels. *Lab a Chip* **2017**. <https://doi.org/10.1039/C7LC00644F>.
- (154) Ni, R.; Qian, B.; Liu, C.; Liu, X.; Qiu, J. Three-Dimensional Printing of Hybrid Organic/Inorganic Composites with Long Persistence Luminescence. *Opt. Mater. Express* **2018**, *8* (9), 2823–2831. [https://doi.org/10.1016/S0920-9964\(12\)70638-2](https://doi.org/10.1016/S0920-9964(12)70638-2).
- (155) Merino, E.; Ribagorda, M. Control over Molecular Motion Using the Cis-Trans Photoisomerization of the Azo Group. *Beilstein Journal of Organic Chemistry*. 2012. <https://doi.org/10.3762/bjoc.8.119>.
- (156) Wagner-Wysiecka, E.; Łukasik, N.; Biernat, J. F.; Luboch, E. Azo Group(s) in Selected Macrocyclic Compounds. *Journal of Inclusion Phenomena and Macrocyclic Chemistry*. 2018. <https://doi.org/10.1007/s10847-017-0779-4>.
- (157) Gillono, M.; Roppolo, I.; Frascella, F.; Scaltrito, L.; Pirri, C. F.; Chiappone, A. CO<sub>2</sub> Permeability Control in 3D Printed Light Responsive Structures. *Appl. Mater. Today* **2020**, *18*. <https://doi.org/10.1016/j.apmt.2019.100470>.
- (158) Weng, Z.; Zhou, Y.; Lin, W.; Senthil, T.; Wu, L. Structure-Property Relationship of Nano Enhanced Stereolithography Resin for Desktop SLA 3D Printer. *Compos. Part A Appl. Sci. Manuf.* **2016**, *88*, 234–242. <https://doi.org/10.1016/j.compositesa.2016.05.035>.
- (159) Lin, D.; Jin, S.; Zhang, F.; Wang, C.; Wang, Y.; Zhou, C.; Cheng, G. J. 3D Stereolithography Printing of Graphene Oxide Reinforced Complex Architectures. *Nanotechnology* **2015**, *26* (43). <https://doi.org/10.1088/0957-4484/26/43/434003>.
- (160) Chen, S.; Yang, J.; Jia, Y. G.; Lu, B.; Ren, L. A Study of 3D-Printable Reinforced Composite Resin: PMMA Modified with Silver Nanoparticles Loaded Cellulose Nanocrystal. *Materials (Basel)*. **2018**, *11* (12). <https://doi.org/10.3390/ma11122444>.

- (161) Moniruzzaman, M.; Winey, K. I. Polymer Nanocomposites Containing Carbon Nanotubes. *Macromolecules* **2006**, *39* (16), 5194–5205. <https://doi.org/10.1021/ma060733p>.
- (162) Chen, H.; Muthuraman, H.; Stokes, P.; Zou, J.; Liu, X.; Wang, J.; Huo, Q.; Khondaker, S. I.; Zhai, L. Dispersion of Carbon Nanotubes and Polymer Nanocomposite Fabrication Using Trifluoroacetic Acid as a Co-Solvent. *Nanotechnology* **2007**, *18*, 415606. <https://doi.org/10.1088/0957-4484/18/41/415606>.
- (163) González-Henríquez, C. M.; Pizarro, G. del C.; Sarabia-Vallejos, M. A.; Terraza, C. A.; López-Cabaña, Z. E. In Situ-Preparation and Characterization of Silver-HEMA/PEGDA Hydrogel Matrix Nanocomposites: Silver Inclusion Studies into Hydrogel Matrix. *Arab. J. Chem.* **2014**. <https://doi.org/10.1016/j.arabjc.2014.11.012>.
- (164) Tenório-Neto, E. T.; Guilherme, M. R.; Winkler, M. E. G.; Cardozo-Filho, L.; Beneti, S. C.; Rubira, A. F.; Kunita, M. H. Synthesis and Characterization of Silver Nanoparticle Nanocomposite Thin Films with Thermally Induced Surface Morphology Changes. *Mater. Lett.* **2015**, *159* (July), 118–121. <https://doi.org/10.1016/j.matlet.2015.06.095>.
- (165) Jankauskaite, V.; Lazauskas, A.; Gri Konis, E.; Lisauskaite, A.; Ukiene, K. UV-Curable Aliphatic Silicone Acrylate Organic–Inorganic Hybrid Coatings with Antibacterial Activity. *Molecules* **2017**, *22* (6). <https://doi.org/10.3390/molecules22060964>.
- (166) Nazar, R.; Sangermano, M.; Vitale, A.; Bongiovanni, R. Silver Polymer Nanocomposites by Photoreduction of AgNO<sub>3</sub> and Simultaneous Photocrosslinking of the Acrylic Matrix: Effect of PVP on Ag Particle Formation. *J. Polym. Eng.* **2018**, *38* (8), 803–809. <https://doi.org/10.1515/polyeng-2017-0156>.
- (167) Fantino, E.; Chiappone, A.; Roppolo, I.; Manfredi, D.; Bongiovanni, R.; Pirri, C. F.; Calignano, F. 3D Printing of Conductive Complex Structures with In Situ Generation of Silver Nanoparticles. *Adv. Mater.* **2016**, *18*, 3712–3717. <https://doi.org/10.1002/adma.201505109>.
- (168) Chiappone, A.; Fantino, E.; Roppolo, I.; Lorusso, M.; Manfredi, D.; Fino, P.; Pirri, C. F.; Calignano, F. 3D Printed PEG-Based Hybrid Nanocomposites Obtained by Sol-Gel Technique. *ACS Appl. Mater. Interfaces* **2016**, *acsami.5b12578*. <https://doi.org/10.1021/acsami.5b12578>.
- (169) Fantino, E.; Chiappone, A.; Calignano, F.; Fontana, M.; Pirri, F.; Roppolo, I. In Situ Thermal Generation of Silver Nanoparticles in 3D Printed Polymeric Structures. *Materials (Basel)*. **2016**, *9* (7), 589. <https://doi.org/10.3390/ma9070589>.
- (170) Li, J.; Wu, C.; Chu, P. K.; Gelinsky, M. 3D Printing of Hydrogels: Rational Design Strategies and Emerging Biomedical Applications. *Mater. Sci. Eng. R Reports* **2020**, *140* (January), 100543. <https://doi.org/10.1016/j.mser.2020.100543>.
- (171) Melchels, F. P. W.; Feijen, J.; Grijpma, D. W. A Review on Stereolithography and Its Applications in Biomedical Engineering.



- Biomaterials* **2010**, *31* (24), 6121–6130.  
<https://doi.org/10.1016/j.biomaterials.2010.04.050>.
- (172) Juskova, P.; Ollitrault, A.; Serra, M.; Viovy, J. L.; Malaquin, L. Resolution Improvement of 3D Stereo-Lithography through the Direct Laser Trajectory Programming: Application to Microfluidic Deterministic Lateral Displacement Device. *Anal. Chim. Acta* **2018**.  
<https://doi.org/10.1016/j.aca.2017.11.062>.
- (173) Ikuta, K.; Hirowatari, K. Real Three Dimensional Micro Fabrication Using Stereo Lithography and Metal Molding. In *Proceedings IEEE Micro Electro Mechanical Systems*; Fort Lauderdale, FL, USA, 1993; pp 42–27.  
<https://doi.org/10.1109/MEMSYS.1993.296949>.
- (174) Liu, Y.; Hu, Q.; Zhang, F.; Tuck, C.; Irvine, D.; Hague, R.; He, Y.; Simonelli, M.; Rance, G. A.; Smith, E. F.; Wildman, R. D. Additive Manufacture of Three Dimensional Nanocomposite Based Objects through Multiphoton Fabrication. *Polymers (Basel)*. **2016**, *8* (9), 325.  
<https://doi.org/10.3390/polym8090325>.
- (175) Wang, X.; Jiang, M.; Zhou, Z.; Gou, J.; Hui, D. 3D Printing of Polymer Matrix Composites: A Review and Prospective. *Compos. Part B Eng.* **2017**, *110*, 442–458. <https://doi.org/10.1016/j.compositesb.2016.11.034>.
- (176) DeSimone, J.; Sarnulski, E.; Ermoshkin, A.; DeSimone, P. Rapid 3D Continuous Printing of Casting Molds for Metals and Other Materials. WO 2015/080888A2, 2015.
- (177) Quan, H.; Zhang, T.; Xu, H.; Luo, S.; Nie, J.; Zhu, X. Photo-Curing 3D Printing Technique and Its Challenges. *Bioactive Materials*. 2020.  
<https://doi.org/10.1016/j.bioactmat.2019.12.003>.
- (178) Xing, J. F.; Zheng, M. L.; Duan, X. M. Two-Photon Polymerization Microfabrication of Hydrogels: An Advanced 3D Printing Technology for Tissue Engineering and Drug Delivery. *Chem. Soc. Rev.* **2015**.  
<https://doi.org/10.1039/c5cs00278h>.
- (179) Felipe-Mendes, C.; Ruiz-Rubio, L.; Vilas-Vilela, J. L. Biomaterials Obtained by Photopolymerization: From UV to Two Photon. *Emergent Mater.* **2020**, *3* (4), 453–468. <https://doi.org/10.1007/s42247-020-00114-0>.
- (180) Zhou, X.; Hou, Y.; Lin, J. A Review on the Processing Accuracy of Two-Photon Polymerization. *AIP Adv.* **2015**.  
<https://doi.org/10.1063/1.4916886>.
- (181) Nguyen, A. K.; Narayan, R. J. Two-Photon Polymerization for Biological Applications. *Materials Today*. 2017.  
<https://doi.org/10.1016/j.mattod.2017.06.004>.
- (182) Serbin, J.; Ovsianikov, A.; Chichkov, B. Fabrication of Woodpile Structures by Two-Photon Polymerization and Investigation of Their Optical Properties. *Opt. Express* **2004**.  
<https://doi.org/10.1364/opex.12.005221>.
- (183) Swanson, W. K.; Kremer, S. D. Three Dimensional Systems. US Patent

4078229, 1975.

- (184) Kuebler, S. M.; Ananthavel, S.; Rumi, M.; Marder, S. R.; Perry, J. W.; Barlow, S.; Cumpston, B. H.; Dyer, D. L.; Ehrlich, J. E.; Erskine, L. L.; Heikal, A.; Lee, I. S. Two-Photon Polymerization Initiators for Threedimensional Optical Data Storage and Microfabrication. **1998**, *1653*, 1998–1998.
- (185) Erskine, L. L.; Heikal, A. a; Kuebler, S. M.; Rumi, M.; Wu, X.; Marder, S. R.; Perry, J. W. Two-Photon Polymerization Initiators for Three-Dimensional Optical Data Storage and Microfabrication. *Solid State Phys.* **1999**, *398* (March), 51–54. <https://doi.org/10.1038/17989>.
- (186) Liu, R.; Chen, H.; Li, Z.; Shi, F.; Liu, X. Extremely Deep Photopolymerization Using Upconversion Particles as Internal Lamps. *Polym. Chem.* **2016**, *7* (14), 2457–2463. <https://doi.org/10.1039/c6py00184j>.
- (187) Hudson, D. E.; Hudson, D. O.; Winingar, J. M.; Richardson, B. D. Penetration of Laser Light at 808 and 980 Nm in Bovine Tissue Samples. *Photomed. Laser Surg.* **2013**. <https://doi.org/10.1089/pho.2012.3284>.
- (188) Gibson, I.; Rosen, D.; Stucker, B. *Additive Manufacturing Technologies: 3D Printing, Rapid Prototyping, and Direct Digital Manufacturing*; 2015. [https://doi.org/10.1007/978-981-13-8281-9\\_2](https://doi.org/10.1007/978-981-13-8281-9_2).
- (189) Infuehr, R.; Stampfl, J.; Krivec, S.; Liska, R.; Lichtenegger, H.; Satzinger, V.; Schmidt, V.; Matsko, N.; Grogger, W. 3D-Structuring of Optical Waveguides with Two Photon Polymerization. *MRS Proc.* **2009**, *1179* (1), 1179-BB01-07. <https://doi.org/10.1557/PROC-1179-BB01-07>.
- (190) Whitby, R.; Ben-Tal, Y.; MacMillan, R.; Janssens, S.; Raymond, S.; Clarke, D.; Jin, J.; Kay, A.; Simpson, M. C. Photoinitiators for Two-Photon Polymerisation: Effect of Branching and Viscosity on Polymerisation Thresholds. *RSC Adv.* **2017**, *7* (22), 13232–13239. <https://doi.org/10.1039/c6ra27176f>.
- (191) Bhattacharya, I.; Kelly, B.; Shusteff, M.; Spadaccini, C.; Taylor, H. Computed Axial Lithography: Volumetric 3D Printing of Arbitrary Geometries (Conference Presentation); 2018. <https://doi.org/10.1117/12.2307780>.
- (192) Kelly, B. E.; Bhattacharya, I.; Heidari, H.; Shusteff, M.; Spadaccini, C. M.; Taylor, H. K. Volumetric Additive Manufacturing via Tomographic Reconstruction. *Science* (80-. ). **2019**. <https://doi.org/10.1126/science.aau7114>.
- (193) Kelly, B. E.; Bhattacharya, I.; Shusteff, M.; Taylor, H. K.; Spaddacini, C. M. Computed Axial Lithography for Rapid Volumetric 3D Additive Manufacturing. In *Solid Freeform Fabrication 2017: Proceedings of the 28th Annual International Solid Freeform Fabrication Symposium - An Additive Manufacturing Conference, SFF 2017*; 2020.
- (194) Bernal, P. N.; Delrot, P.; Loterie, D.; Li, Y.; Malda, J.; Moser, C.; Levato, R. Biofabrication: Volumetric Bioprinting of Complex Living-Tissue Constructs within Seconds (Adv. Mater. 42/2019). *Adv. Mater.* **2019**. <https://doi.org/10.1002/adma.201970302>.

- (195) Yang, J.; Vitale, A.; Bongiovanni, R.; Nie, J. Synthesis and Characterization of Siloxane Photopolymers Used for Microfluidic Devices. *New J. Chem.* **2015**, *39* (4), 2532–2540. <https://doi.org/10.1039/c4nj01773k>.
- (196) Reichardt, C. Solvatochromic Dyes as Solvent Polarity Indicators. *Chem. Rev.* **1994**. <https://doi.org/10.1021/cr00032a005>.
- (197) Boldrini, B.; Cavalli, E.; Painelli, A.; Terenziani, F. Polar Dyes in Solution: A Joint Experimental and Theoretical Study of Absorption and Emission Band Shapes. *J. Phys. Chem. A* **2002**, *106* (26), 6286–6294. <https://doi.org/10.1021/jp020031b>.
- (198) Priimagi, A.; Kaivola, M.; Virkki, M.; Rodríguez, F. J.; Kauranen, M. Suppression of Chromophore Aggregation in Amorphous Polymeric Materials: Towards More Efficient Photoresponsive Behavior. *J. Nonlinear Opt. Phys. Mater.* **2010**. <https://doi.org/10.1142/S0218863510005091>.
- (199) Kausar, A. A Review of High Performance Polymer Nanocomposites for Packaging Applications in Electronics and Food Industries. *Journal of Plastic Film and Sheeting*. **2020**. <https://doi.org/10.1177/8756087919849459>.
- (200) Zhang, Y.; Li, H.; Yang, X.; Zhang, T.; Zhu, K.; Si, W.; Liu, Z.; Sun, H. Additive Manufacturing of Carbon Nanotube-Photopolymer Composite Radar Absorbing Materials. *Polym. Compos.* **2018**, *39*, E671–E676. <https://doi.org/10.1002/pc.24117>.
- (201) Ahn, D.; Stevens, L. M.; Zhou, K.; Page, Z. A. Rapid High-Resolution Visible Light 3D Printing. *ACS Cent. Sci.* **2020**. <https://doi.org/10.1021/acscentsci.0c00929>.
- (202) Jeong, H. J.; Yang, J.; Kim, J. T.; Seol, S. K. Three-Dimensional Printing of Highly Conductive Carbon Nanotube Microarchitectures with Fluid Ink. **2016**. <https://doi.org/10.1021/acsnano.6b04771>.
- (203) Campbell, T. A.; Ivanova, O. S. 3D Printing of Multifunctional Nanocomposites. *Nano Today* **2013**, *8* (2), 119–120. <https://doi.org/10.1016/j.nantod.2012.12.002>.
- (204) Khoo, Z. X.; Teoh, J. E. M.; Liu, Y.; Chua, C. K.; Yang, S.; An, J.; Leong, K. F.; Yeong, W. Y. 3D Printing of Smart Materials: A Review on Recent Progresses in 4D Printing. *Virtual Phys. Prototyp.* **2015**. <https://doi.org/10.1080/17452759.2015.1097054>.
- (205) Manapat, J. Z.; Chen, Q.; Ye, P.; Advincula, R. C. 3D Printing of Polymer Nanocomposites via Stereolithography. *Macromolecular Materials and Engineering*. **2017**. <https://doi.org/10.1002/mame.201600553>.
- (206) Sano, Y.; Matsuzaki, R.; Ueda, M.; Todoroki, A.; Hirano, Y. 3D Printing of Discontinuous and Continuous Fibre Composites Using Stereolithography. *Addit. Manuf.* **2018**. <https://doi.org/10.1016/j.addma.2018.10.033>.
- (207) Varghese, G.; Moral, M.; Castro-García, M.; López-López, J. J.; Marín-Rueda, J. R.; Yagüe-Alcaraz, V.; Hernández-Afonso, L.; Ruiz-Morales, J. C.;

- Canales-Vázquez, J. Fabrication and Characterisation of Ceramics via Low-Cost DLP 3D Printing. *Boletín la Soc. Española Cerámica y Vidr.* **2018**. <https://doi.org/10.1016/j.bsecv.2017.09.004>.
- (208) Song, S. Y.; Park, M. S.; Lee, D.; Lee, J. W.; Yun, J. S. Optimization and Characterization of High-Viscosity ZrO<sub>2</sub> Ceramic Nanocomposite Resins for Supportless Stereolithography. *Mater. Des.* **2019**, *180*, 107960. <https://doi.org/10.1016/j.matdes.2019.107960>.
- (209) Mu, Q.; Wang, L.; Dunn, C. K.; Kuang, X.; Duan, F.; Zhang, Z.; Qi, H. J.; Wang, T. Digital Light Processing 3D Printing of Conductive Complex Structures. *Addit. Manuf.* **2017**, *18* (September), 74–83. <https://doi.org/10.1016/j.addma.2017.08.011>.
- (210) Palaganas, J. O.; Palaganas, N. B.; Ramos, L. J. I.; David, C. P. C. 3D Printing of Covalent Functionalized Graphene Oxide Nanocomposite via Stereolithography. *ACS Appl. Mater. Interfaces* **2019**, *11* (49), 46034–46043. <https://doi.org/10.1021/acsmi.9b12071>.
- (211) Li, J.; Wang, L.; Dai, L.; Zhong, L.; Liu, B.; Ren, J.; Xu, Y. Synthesis and Characterization of Reinforced Acrylate Photosensitive Resin by 2-Hydroxyethyl Methacrylate-Functionalized Graphene Nanosheets for 3D Printing. *J. Mater. Sci.* **2018**, *53* (3), 1874–1886. <https://doi.org/10.1007/s10853-017-1432-8>.
- (212) Klikovits, N.; Sinaweil, L.; Knaack, P.; Koch, T.; Stampfl, J.; Gorsche, C.; Liska, R. UV-Induced Cationic Ring-Opening Polymerization of 2-Oxazolines for Hot Lithography. *ACS Macro Lett.* **2020**, *9* (4), 546–551. <https://doi.org/10.1021/acsmacrolett.0c00055>.
- (213) Dall'Argine, C.; Hochwallner, A.; Klikovits, N.; Liska, R.; Stampf, J.; Sangermano, M. Hot-Lithography SLA-3D Printing of Epoxy Resin. *Macromol. Mater. Eng.* **2020**, *2000325*, 1–6. <https://doi.org/10.1002/mame.202000325>.
- (214) Steyrer, B.; Busetti, B.; Harakály, G.; Liska, R.; Stampfl, J. Hot Lithography vs. Room Temperature DLP 3D-Printing of a Dimethacrylate. *Addit. Manuf.* **2018**, *21* (January), 209–214. <https://doi.org/10.1016/j.addma.2018.03.013>.
- (215) Lantada, A. D.; De Blas Romero, A.; Schwentenwein, M.; Jellinek, C.; Homa, J. Lithography-Based Ceramic Manufacture (LCM) of Auxetic Structures: Present Capabilities and Challenges. *Smart Mater. Struct.* **2016**, *25* (5). <https://doi.org/10.1088/0964-1726/25/5/054015>.
- (216) Hofmann, B. K. Holey Graphene for Energy Storage. *ECS Meet. Abstr.* **2017**, 330–334. <https://doi.org/10.1149/ma2017-01/12/774>.
- (217) Revilla-León, M.; Meyers, M. J.; Zandinejad, A.; Özcan, M. A Review on Chemical Composition, Mechanical Properties, and Manufacturing Work Flow of Additively Manufactured Current Polymers for Interim Dental Restorations. *J. Esthet. Restor. Dent.* **2019**, *31* (1), 51–57. <https://doi.org/10.1111/jerd.12438>.
- (218) Esposito Corcione, C.; Striani, R.; Montagna, F.; Cannoletta, D. Organically Modified Montmorillonite Polymer Nanocomposites for

- Stereolithography Building Process. *Polym. Adv. Technol.* **2015**, 26 (1), 92–98. <https://doi.org/10.1002/pat.3425>.
- (219) Lee, J. H.; Prud'homme, R. K.; Aksay, I. a. Cure Depth in Photopolymerization: Experiments and Theory. *J. Mater. Res.* **2001**, 16 (12), 3536–3544. <https://doi.org/10.1557/JMR.2001.0485>.
- (220) Moore, B. K.; Platt, J. A.; Borges, G.; Chu, T. M. G.; Katsilieri, I. Depth of Cure of Dental Resin Composites: ISO 4049 Depth and Microhardness of Types of Materials and Shades. *Oper. Dent.* **2008**. <https://doi.org/10.2341/07-104>.
- (221) Garcia, D.; Yaman, P.; Dennison, J.; Neiva, G. F. Polymerization Shrinkage and Depth of Cure of Bulk Fill Flowable Composite Resins. *Oper. Dent.* **2014**. <https://doi.org/10.2341/12-484-L>.
- (222) Hofstetter, C.; Orman, S.; Baudis, S.; Stampfl, J. Combining Cure Depth and Cure Degree, a New Way to Fully Characterize Novel Photopolymers. *Addit. Manuf.* **2018**. <https://doi.org/10.1016/j.addma.2018.09.025>.
- (223) Heller, C.; Schwentenwein, M.; Russmueller, G.; Varga, F.; Stampfl, J.; Liska, R. Vinyl Esters: Low Cytotoxicity Monomers for the Fabrication of Biocompatible 3D Scaffolds by Lithography Based Additive Manufacturing. *J. Polym. Sci. Part A Polym. Chem.* **2009**. <https://doi.org/10.1002/pola.23734>.
- (224) Benjamin, A. D.; Abbasi, R.; Owens, M.; Olsen, R. J.; Walsh, D. J.; Lefevre, T. B.; Wilking, J. N. Light-Based 3D Printing of Hydrogels with High-Resolution Channels. *Biomed. Phys. Eng. Express* **2019**. <https://doi.org/10.1088/2057-1976/aad667>.
- (225) Aimar, A.; Palermo, A.; Innocenti, B. The Role of 3D Printing in Medical Applications: A State of the Art. *J. Healthc. Eng.* **2019**, 2019. <https://doi.org/10.1155/2019/5340616>.
- (226) Li, H.; Fan, W.; Zhu, X. Three-Dimensional Printing: The Potential Technology Widely Used in Medical Fields. *Journal of Biomedical Materials Research - Part A*. **2020**. <https://doi.org/10.1002/jbm.a.36979>.
- (227) Mathew, E.; Pitzanti, G.; Larrañeta, E.; Lamprou, D. A. Three-Dimensional Printing of Pharmaceuticals and Drug Delivery Devices. *Pharmaceutics* **2020**, 12 (3), 1–9. <https://doi.org/10.3390/pharmaceutics12030266>.
- (228) Pellizzari, M.; Jam, A.; Tschon, M.; Fini, M.; Lora, C.; Benedetti, M. A 3D-Printed Ultra-Low Young ' s Modulus  $\beta$  -Ti Alloy for Biomedical Applications. **2020**, 1–16.
- (229) Hao, Y. L.; Li, S. J.; Yang, R. Biomedical Titanium Alloys and Their Additive Manufacturing. *Rare Metals*. **2016**. <https://doi.org/10.1007/s12598-016-0793-5>.
- (230) Harun, W. S. W.; Kamariah, M. S. I. N.; Muhamad, N.; Ghani, S. A. C.; Ahmad, F.; Mohamed, Z. A Review of Powder Additive Manufacturing Processes for Metallic Biomaterials. *Powder Technology*. **2018**.

<https://doi.org/10.1016/j.powtec.2017.12.058>.

- (231) Stenlund, P.; Kurosu, S.; Koizumi, Y.; Suska, F.; Matsumoto, H.; Chiba, A.; Palmquist, A. Osseointegration Enhancement by Zr Doping of Co-Cr-Mo Implants Fabricated by Electron Beam Melting. *Addit. Manuf.* **2015**. <https://doi.org/10.1016/j.addma.2015.02.002>.
- (232) Koizumi, Y.; Okazaki, A.; Chiba, A.; Kato, T.; Takezawa, A. Cellular Lattices of Biomedical Co-Cr-Mo-Alloy Fabricated by Electron Beam Melting with the Aid of Shape Optimization. *Addit. Manuf.* **2016**. <https://doi.org/10.1016/j.addma.2016.06.001>.
- (233) Salmi, M.; Tuomi, J.; Paloheimo, K. S.; Björkstrand, R.; Paloheimo, M.; Salo, J.; Kontio, R.; Mesimäki, K.; Mäkitie, A. A. Patient-Specific Reconstruction with 3D Modeling and DMLS Additive Manufacturing. *Rapid Prototyp. J.* **2012**, *18* (3), 209–214. <https://doi.org/10.1108/13552541211218126>.
- (234) Petrovskaya, T. S.; Toropkov, N. E.; Mironov, E. G.; Azarmi, F. 3D Printed Biocompatible Polylactide-Hydroxyapatite Based Material for Bone Implants. *Mater. Manuf. Process.* **2018**. <https://doi.org/10.1080/10426914.2018.1476764>.
- (235) Seidenstuecker, M.; Kerr, L.; Bernstein, A.; Mayr, H. O.; Suedkamp, N. P.; Gadow, R.; Krieg, P.; Latorre, S. H.; Thomann, R.; Syrowatka, F.; Esslinger, S. 3D Powder Printed Bioglass and  $\beta$ -Tricalcium Phosphate Bone Scaffolds. *Materials (Basel)*. **2017**. <https://doi.org/10.3390/ma11010013>.
- (236) Chen, Z.; Li, Z.; Li, J.; Liu, C.; Lao, C.; Fu, Y.; Liu, C.; Li, Y.; Wang, P.; He, Y. 3D Printing of Ceramics: A Review. *Journal of the European Ceramic Society*. 2019. <https://doi.org/10.1016/j.jeurceramsoc.2018.11.013>.
- (237) Goyos-Ball, L.; García-Tuñón, E.; Fernández-García, E.; Díaz, R.; Fernández, A.; Prado, C.; Saiz, E.; Torrecillas, R. Mechanical and Biological Evaluation of 3D Printed 10CeTzP-Al<sub>2</sub>O<sub>3</sub> Structures. *J. Eur. Ceram. Soc.* **2017**. <https://doi.org/10.1016/j.jeurceramsoc.2017.03.012>.
- (238) Leukers, B.; Gülkan, H.; Irsen, S. H.; Milz, S.; Tille, C.; Schieker, M.; Seitz, H. Hydroxyapatite Scaffolds for Bone Tissue Engineering Made by 3D Printing. In *Journal of Materials Science: Materials in Medicine*; 2005. <https://doi.org/10.1007/s10856-005-4716-5>.
- (239) Zeng, Y.; Yan, Y.; Yan, H.; Liu, C.; Li, P.; Dong, P.; Zhao, Y.; Chen, J. 3D Printing of Hydroxyapatite Scaffolds with Good Mechanical and Biocompatible Properties by Digital Light Processing. *J. Mater. Sci.* **2018**, *53* (9), 6291–6301. <https://doi.org/10.1007/s10853-018-1992-2>.
- (240) Weisman, J. a; Nicholson, J.; Tappa, K.; Jammalamadak, U.; Wilson, C.; Mills, D. Antibiotic and Chemotherapeutic Enhanced Three-Dimensional Printer Filaments and Constructs for Biomedical Applications. *Int. J. Nanomedicine* **2015**, *10*, 357–370. <https://doi.org/10.2147/IJN.S74811>.
- (241) Geven, M. A.; Varjas, V.; Kamer, L.; Wang, X.; Peng, J.; Eglin, D.; Grijpma,

- D. W. Fabrication of Patient Specific Composite Orbital Floor Implants by Stereolithography. *Polym. Adv. Technol.* **2015**, *26* (12), 1433–1438. <https://doi.org/10.1002/pat.3589>.
- (242) González-Henríquez, C. M.; Sarabia-Vallejos, M. A.; Rodríguez-Hernández, J. Polymers for Additive Manufacturing and 4D-Printing: Materials, Methodologies, and Biomedical Applications. *Prog. Polym. Sci.* **2019**, *94*, 57–116. <https://doi.org/10.1016/j.progpolymsci.2019.03.001>.
- (243) Hofmann, M. 3D Printing Gets a Boost and Opportunities with Polymer Materials. *ACS Macro Letters.* **2014**. <https://doi.org/10.1021/mz4006556>.
- (244) Murphy, S. V.; Atala, A. 3D Bioprinting of Tissues and Organs. *Nat. Biotechnol.* **2014**, *32* (8), 773–785. <https://doi.org/10.1038/nbt.2958>.
- (245) Knowlton, S.; Yenilmez, B.; Tasoglu, S. Towards Single-Step Biofabrication of Organs on a Chip via 3D Printing. *Trends Biotechnol.* **2016**, *34* (9), 685–688. <https://doi.org/10.1016/j.tibtech.2016.06.005>.
- (246) Bhattacharjee, N.; Urrios, A.; Kang, S.; Folch, A. The Upcoming 3D-Printing Revolution in Microfluidics. *Lab Chip* **2016**, *16* (10), 1720–1742. <https://doi.org/10.1039/C6LC00163G>.
- (247) Ho, C. M. B.; Ng, S. H.; Li, K. H. H.; Yoon, Y.-J. 3D Printed Microfluidics for Biological Applications. *Lab Chip* **2015**, *15* (18), 3627–3637. <https://doi.org/10.1039/C5LC00685F>.
- (248) Cavallo, L.; Marcianò, A.; Cicciù, M.; Oteri, G. 3D Printing beyond Dentistry during COVID 19 Epidemic: A Technical Note for Producing Connectors to Breathing Devices. *Prosthesis* **2020**, *2*, 46–52. <https://doi.org/doi:10.3390/prosthesis2020005>.
- (249) Tino, R.; Moore, R.; Antoline, S.; Ravi, P.; Wake, N.; Ionita, C. N.; Morris, J. M.; Decker, S. J.; Sheikh, A.; Rybicki, F. J.; Chepelev, L. L. COVID-19 and the Role of 3D Printing in Medicine. *3D Print. Med.* **2020**. <https://doi.org/10.1186/s41205-020-00064-7>.
- (250) Salmi, M.; Akmal, J. S.; Pei, E.; Wolff, J.; Jaribion, A.; Khajavi, S. H. 3D Printing in COVID-19: Productivity Estimation of the Most Promising Open Source Solutions in Emergency Situations. *Appl. Sci.* **2020**, *10* (11). <https://doi.org/10.3390/app10114004>.
- (251) Ishack, S.; Lipner, S. R. Applications of 3D Printing Technology to Address COVID-19–Related Supply Shortages. *Am. J. Med.* **2020**, *133* (7), 771–773. <https://doi.org/https://doi.org/10.1016/j.amjmed.2020.04.002>.
- (252) Peker, A.; Aydin, L.; Kucuk, S.; Ozkoc, G.; Cetinarslan, B.; Canturk, Z.; Selek, A. Additive Manufacturing and Biomechanical Validation of a Patient-Specific Diabetic Insole. *Polym. Adv. Technol.* **2020**, *31* (5), 988–996. <https://doi.org/10.1002/pat.4832>.
- (253) Trenfield, S. J.; Awad, A.; Madla, C. M.; Hatton, G. B.; Firth, J.; Goyanes, A.; Gaisford, S.; Basit, A. W. Shaping the Future: Recent Advances of 3D

- Printing in Drug Delivery and Healthcare. *Expert Opin. Drug Deliv.* **2019**, *16* (10), 1081–1094. <https://doi.org/10.1080/17425247.2019.1660318>.
- (254) Tappa, K.; Jammalamadaka, U. Novel Biomaterials Used in Medical 3D Printing Techniques. *J. Funct. Biomater.* **2018**, *9* (1). <https://doi.org/10.3390/jfb9010017>.
- (255) Arun, M.; Sathishkumar, N.; Nithesh Kumar, K.; Ajai, S. S.; Aswin, S. Development of Patient Specific Bio-Polymer Incisor Teeth by 3D Printing Process: A Case Study. *Mater. Today Proc.* **2020**, No. xxxx. <https://doi.org/10.1016/j.matpr.2020.04.367>.
- (256) Guillaume, O.; Geven, M. A.; Varjas, V.; Varga, P.; Gehweiler, D.; Stadelmann, V. A.; Smidt, T.; Zeiter, S.; Sprecher, C.; Bos, R. R. M.; Grijpma, D. W.; Alini, M.; Yuan, H.; Richards, G. R.; Tang, T.; Qin, L.; Yuxiao, L.; Jiang, P.; Eglin, D. Orbital Floor Repair Using Patient Specific Osteoinductive Implant Made by Stereolithography. *Biomaterials* **2020**, *233* (December 2019). <https://doi.org/10.1016/j.biomaterials.2019.119721>.
- (257) Ock, J.; Gwon, E.; Kim, D. hwan; Kim, S. hoon; Kim, N. Patient-Specific and Hyper-Realistic Phantom for an Intubation Simulator with a Replaceable Difficult Airway of a Toddler Using 3D Printing. *Sci. Rep.* **2020**, *10* (1), 1–12. <https://doi.org/10.1038/s41598-020-67575-5>.
- (258) Kaschwich, M.; Horm, M.; Matthiensen, S.; Stahlberg, E.; Behrendt, C.-A.; Matysiak, F.; Bouchagiar, J.; Dell, A.; Ellebrecht, D.; Bayer, A.; Kleemann, M. Accuracy Evaluation of Patient-Specific 3D-Printed Aortic Anatomy Mark. *J. Neurol. Sci.* **2020**, 116544. <https://doi.org/10.1016/j.jaanat.2020.151629>.
- (259) Chandak, P.; Byrne, N.; Coleman, A.; Karunanithy, N.; Carmichael, J.; Marks, S. D.; Stojanovic, J.; Kessarar, N.; Mamode, N. Patient-Specific 3D Printing: A Novel Technique for Complex Pediatric Renal Transplantation. *Ann. Surg.* **2019**, *269* (2), e18–e23. <https://doi.org/10.1097/SLA.0000000000003016>.
- (260) Mobaraki, M.; Ghaffari, M.; Yazdanpanah, A.; Luo, Y.; Mills, D. K. Bioinks and Bioprinting: A Focused Review. *Bioprinting* **2020**, *18* (May), e00080. <https://doi.org/10.1016/j.bprint.2020.e00080>.
- (261) Lee, C. Y.; Wang, W. T.; Liu, C. C.; Fu, L. M. Passive Mixers in Microfluidic Systems: A Review. *Chemical Engineering Journal*. 2016. <https://doi.org/10.1016/j.cej.2015.10.122>.
- (262) He, Y.; Yang, F.; Zhao, H.; Gao, Q.; Xia, B.; Fu, J. Research on the Printability of Hydrogels in 3D Bioprinting. *Sci. Rep.* **2016**, *6*, 29977. <https://doi.org/10.1038/srep29977>.
- (263) Stanton, M. M.; Samitier, J.; Sánchez, S. Bioprinting of 3D Hydrogels. *Lab Chip* **2015**, *15* (15), 3111–3115. <https://doi.org/10.1039/C5LC90069G>.
- (264) Leucht, A.; Volz, A. C.; Rogal, J.; Borchers, K.; Kluger, P. J. Advanced Gelatin-Based Vascularization Bioinks for Extrusion-Based Bioprinting of Vascularized Bone Equivalents. *Sci. Rep.* **2020**, *10* (1), 5330 |. <https://doi.org/10.1038/s41598-020-62166-w>.



- (265) Boularaoui, S.; Al Hussein, G.; Khan, K. A.; Christoforou, N.; Stefanini, C. An Overview of Extrusion-Based Bioprinting with a Focus on Induced Shear Stress and Its Effect on Cell Viability. *Bioprinting* **2020**, *20* (May), e00093. <https://doi.org/10.1016/j.bprint.2020.e00093>.
- (266) Gillispie, G.; Prim, P.; Copus, J.; Fisher, J.; Mikos, A. G.; Yoo, J. J.; Atala, A.; Lee, S. J. Assessment Methodologies for Extrusion-Based Bioink Printability. *Biofabrication* **2020**, *12* (2), 022003. <https://doi.org/10.1088/1758-5090/ab6f0d>.
- (267) Ning, L.; Chen, X. A Brief Review of Extrusion-Based Tissue Scaffold Bio-Printing. *Biotechnol. J.* **2017**, *12* (8), 1600671. <https://doi.org/10.1002/biot.201600671>.
- (268) Ozbolat, I. T.; Hospodiuk, M. Current Advances and Future Perspectives in Extrusion-Based Bioprinting. *Biomaterials* **2016**, *76*, 321–343. <https://doi.org/10.1016/j.biomaterials.2015.10.076>.
- (269) Thakare, K.; Wei, X.; Jerpseth, L.; Bhardwaj, A.; Qin, H.; Pei, Z. Feasible Regions of Bioink Composition, Extrusion Pressure, and Needle Size for Continuous Extrusion-Based Bioprinting. *J. Manuf. Sci. Eng.* **2020**, *142* (12), 124501–1. <https://doi.org/10.1115/1.4048000>.
- (270) Emmermacher, J.; Spura, D.; Cziommer, J.; Kilian, D.; Wollborn, T.; Fritsching, U.; Steingroewer, J.; Walther, T.; Gelinsky, M.; Lode, A. Engineering Considerations on Extrusion-Based Bioprinting: Interactions of Material Behavior, Mechanical Forces and Cells in the Printing Needle. *Biofabrication* **2020**, *12* (2), 025022. <https://doi.org/10.1088/1758-5090/ab7553>.
- (271) Kim, M. H.; Nam, S. Y. Assessment of Coaxial Printability for Extrusion-Based Bioprinting of Alginate-Based Tubular Constructs. *Bioprinting* **2020**, *20* (April), e00092. <https://doi.org/10.1016/j.bprint.2020.e00092>.
- (272) Ahn, S. H.; Lee, J.; Park, S. A.; Kim, W. D. Three-Dimensional Bio-Printing Equipment Technologies for Tissue Engineering and Regenerative Medicine. *Tissue Eng. Regen. Med.* **2016**, *13* (6), 663–676. <https://doi.org/10.1007/s13770-016-0148-1>.
- (273) Gao, B.; Yang, Q.; Zhao, X.; Jin, G.; Ma, Y.; Xu, F. 4D Bioprinting for Biomedical Applications. *Trends Biotechnol.* **2016**, *34* (9), 746–756. <https://doi.org/10.1016/j.tibtech.2016.03.004>.
- (274) Zhu, F.; Wigh, A.; Friedrich, T.; Devaux, A.; Bony, S.; Nugegoda, D.; Kaslin, J.; Wlodkowic, D. Automated Lab-on-a-Chip Technology for Fish Embryo Toxicity Tests Performed under Continuous Microperfusion (MFET). *Environ. Sci. Technol.* **2015**, *49* (24), 14570–14578. <https://doi.org/10.1021/acs.est.5b03838>.
- (275) Valentin, T. M.; Dubois, E. M.; Machnicki, C. E.; Bhaskar, D.; Cui, F. R.; Wong, I. Y. 3D Printed Self-Adhesive PEGDA-PAA Hydrogels as Modular Components for Soft Actuators and Microfluidics. *Polym. Chem.* **2019**, *10* (16), 2015–2028. <https://doi.org/10.1039/c9py00211a>.
- (276) Alessandri, K.; Feyeux, M.; Gurchenkov, B.; Delgado, C.; Trushko, A;

- Krause, K. H.; Vignjević, D.; Nassoy, P.; Roux, A. A 3D Printed Microfluidic Device for Production of Functionalized Hydrogel Microcapsules for Culture and Differentiation of Human Neuronal Stem Cells (HNSC). *Lab Chip* **2016**, *16* (9), 1593–1604. <https://doi.org/10.1039/c6lc00133e>.
- (277) Beauchamp, M. J.; Nordin, G. P.; Woolley, A. T. Moving from Millifluidic to Truly Microfluidic Sub-100-µm Cross-Section 3D Printed Devices. *Anal. Bioanal. Chem.* **2017**, *409* (18), 4311–4319. <https://doi.org/10.1007/s00216-017-0398-3>.
- (278) Lake, M.; Arciso, C.; Cowdrick, K.; Storey, T.; Zhang, S.; Zartman, J.; Hoelzle, D. Microfluidic Device Design, Fabrication, and Testing Protocols. *Protocol Exchange*. 2015, pp 1–26. <https://doi.org/10.1038/protex.2015.069>.
- (279) Mehling, M.; Tay, S. Microfluidic Cell Culture. *Current Opinion in Biotechnology*. 2014, pp 95–102. <https://doi.org/10.1016/j.copbio.2013.10.005>.
- (280) Fujii, T. PDMS-Based Microfluidic Devices for Biomedical Applications. *Microelectron. Eng.* **2002**, *61–62*, 907–914. [https://doi.org/10.1016/S0167-9317\(02\)00494-X](https://doi.org/10.1016/S0167-9317(02)00494-X).
- (281) Whitesides, G. M.; Tang, S. K. Y. Fluidic Optics. **2006**, 6329, 63290A. <https://doi.org/10.1117/12.681672>.
- (282) Lee, C. Y.; Chang, C. L.; Wang, Y. N.; Fu, L. M. Microfluidic Mixing: A Review. *International Journal of Molecular Sciences*. 2011. <https://doi.org/10.3390/ijms12053263>.
- (283) Castillo-León, J. *Microfluidics and Lab-on-a-Chip Devices: History and Challenges*; Castillo-León, J., Winnie E, S., Eds.; Lab-on-a-Chip Devices and Micro-Total Analysis Systems. Springer, Cham, 2015. [https://doi.org/10.1007/978-3-319-08687-3\\_1](https://doi.org/10.1007/978-3-319-08687-3_1).
- (284) Whitesides, G. M. The Origins and the Future of Microfluidics. *Nature* **2006**, *442* (7101), 368–373. <https://doi.org/10.1038/nature05058>.
- (285) Paegel, B. M.; Blazej, R. G.; Mathies, R. A. Microfluidic Devices for DNA Sequencing: Sample Preparation and Electrophoretic Analysis. *Curr. Opin. Biotechnol.* **2003**, *14* (1), 42–50. [https://doi.org/10.1016/S0958-1669\(02\)00004-6](https://doi.org/10.1016/S0958-1669(02)00004-6).
- (286) Scott Mellors, J.; Jorabchi, K.; M. Smith, L.; Michael Ramsey, J. Integrated Microfluidic Device for Automated Single Cell Analysis Using Electrophoretic Separation and Electrospray Ionization Mass Spectrometry. *Anal. Chem.* **2010**, *82* (3), 967–973. <https://doi.org/10.1021/ac902218y>.
- (287) Vashist, S. K.; Lippa, P. B.; Yeo, L. Y.; Ozcan, A.; Luong, J. H. T. Emerging Technologies for Next-Generation Point-of-Care Testing. *Trends Biotechnol.* **2015**, *33* (11), 692–705. <https://doi.org/10.1016/j.tibtech.2015.09.001>.
- (288) Myers, F. B.; Lee, L. P. Innovations in Optical Microfluidic Technologies for Point-of-Care Diagnostics. *Lab Chip* **2008**, *8* (12), 2015–2031.

<https://doi.org/10.1039/b812343h>.

- (289) Nge, P. N.; Rogers, C. I.; Woolley, A. T. Advances in Microfluidic Materials, Functions, Integration, and Applications. *Chem. Rev.* **2013**, *113* (4), 2550–2583. <https://doi.org/10.1021/cr300337x>.
- (290) Fior, R.; Kwok, J.; Malfatti, F.; Sbaizero, O.; Lal, R. Biocompatible Optically Transparent MEMS for Micromechanical Stimulation and Multimodal Imaging of Living Cells. *Ann. Biomed. Eng.* **2015**, *43* (8), 1841–1850. <https://doi.org/10.1007/s10439-014-1229-8>.
- (291) Ren, K.; Zhou, J.; Wu, H. Materials for Microfluidic Chip Fabrication. *Acc. Chem. Res.* **2013**, *46* (11), 2396–2406. <https://doi.org/10.1021/ar300314s>.
- (292) Ren, K.; Zhou, J.; Wu, H. Materials for Microfluidic Chip Fabrication. *Acc. Chem. Res.* **2013**, *46* (11), 2396–2406. <https://doi.org/10.1021/ar300314s>.
- (293) Halldorsson, S.; Lucumi, E.; Gómez-Sjöberg, R.; Fleming, R. M. T. Advantages and Challenges of Microfluidic Cell Culture in Polydimethylsiloxane Devices. *Biosens. Bioelectron.* **2015**, *63*, 218–231. <https://doi.org/10.1016/j.bios.2014.07.029>.
- (294) Mata, A.; Fleischman, A. J.; Roy, S. Characterization of Polydimethylsiloxane (PDMS) Properties for Biomedical Micro/Nanosystems. *Biomed. Microdevices* **2005**, *7* (4), 281–293. <https://doi.org/10.1007/s10544-005-6070-2>.
- (295) Johnston, I. D.; McCluskey, D. K.; Tan, C. K. L.; Tracey, M. C. Mechanical Characterization of Bulk Sylgard 184 for Microfluidics and Microengineering. *J. Micromechanics Microengineering* **2014**, *24* (3). <https://doi.org/10.1088/0960-1317/24/3/035017>.
- (296) McDonald, J. C.; Duffy, D. C.; Anderson, J. R.; Chiu, D. T.; Wu, H.; Schueller, O. J. A.; Whitesides, G. M. Fabrication of Microfluidic Systems in Poly(Dimethylsiloxane). *Electrophoresis* **2000**, *21* (1), 27–40. [https://doi.org/10.1002/\(sici\)1522-2683\(20000101\)21:1<27::aid-elps27>3.3.co;2-3](https://doi.org/10.1002/(sici)1522-2683(20000101)21:1<27::aid-elps27>3.3.co;2-3).
- (297) Regehr, K. J.; Domenech, M.; Koepsel, J. T.; Carver, K. C.; Ellison-Zelski, S. J.; Murphy, W. L.; Schuler, L. A.; Alarid, E. T.; Beebe, D. J. Biological Implications of Polydimethylsiloxane-Based Microfluidic Cell Culture. *Lab on a Chip*. 2009. <https://doi.org/10.1039/b903043c>.
- (298) Yu, L.; Li, C. M.; Liu, Y.; Gao, J.; Wang, W.; Gan, Y. Flow-through Functionalized PDMS Microfluidic Channels with Dextran Derivative for ELISAs. *Lab Chip* **2009**, *9* (9), 1243–1247. <https://doi.org/10.1039/b816018j>.
- (299) Zhang, Z. L.; Crozatier, C.; Le Berre, M.; Chen, Y. In Situ Bio-Functionalization and Cell Adhesion in Microfluidic Devices. *Microelectron. Eng.* **2005**, *78–79* (1–4), 556–562. <https://doi.org/10.1016/j.mee.2004.12.071>.
- (300) Xu, J.; Gleason, K. K. Conformal, Amine-Functionalized Thin Films by

- Initiated Chemical Vapor Deposition (ICVD) for Hydrolytically Stable Microfluidic Devices. *Chem. Mater.* **2010**. <https://doi.org/10.1021/cm903156a>.
- (301) Yu, X.; Xiao, J.; Dang, F. Surface Modification of Poly(Dimethylsiloxane) Using Ionic Complementary Peptides to Minimize Nonspecific Protein Adsorption. *Langmuir* **2015**, *31* (21), 5891–5898. <https://doi.org/10.1021/acs.langmuir.5b01085>.
- (302) Hu, S.; Ren, X.; Bachman, M.; Sims, C. E.; Li, G. P.; Allbritton, N. Surface Modification of Poly(Dimethylsiloxane) Microfluidic Devices by Ultraviolet Polymer Grafting. *Anal. Chem.* **2002**. <https://doi.org/10.1021/ac025700w>.
- (303) Ginn, B. T.; Steinbock, O. Polymer Surface Modification Using Microwave-Oven-Generated Plasma. *Langmuir* **2003**. <https://doi.org/10.1021/la034138h>.
- (304) Hui, A. Y. N.; Wang, G.; Lin, B.; Chan, W. T. Microwave Plasma Treatment of Polymer Surface for Irreversible Sealing of Microfluidic Devices. *Lab Chip* **2005**. <https://doi.org/10.1039/b504271b>.
- (305) Goda, T.; Konno, T.; Takai, M.; Ishihara, K. Synthesis and Characterization on Polydimethylsiloxane Grafted with Poly(2-Methacryloyloxyethyl Phosphorylcholine) by Photo-Induced Radical Polymerization. In *Polymer Preprints, Japan*; 2005.
- (306) Kurkuri, M. D.; Al-Ejeh, F.; Shi, J. Y.; Palms, D.; Prestidge, C.; Griesser, H. J.; Brown, M. P.; Thierry, B. Plasma Functionalized PDMS Microfluidic Chips: Towards Point-of-Care Capture of Circulating Tumor Cells. *J. Mater. Chem.* **2011**. <https://doi.org/10.1039/c1jm10317b>.
- (307) Kuang, J.; Messersmith, P. B. Universal Surface-Initiated Polymerization of Antifouling Zwitterionic Brushes Using a Mussel-Mimetic Peptide Initiator. *Langmuir* **2012**, *28* (18), 7258–7266. <https://doi.org/10.1021/la300738e>.
- (308) Wong, I.; Ho, C. M. Surface Molecular Property Modifications for Poly(Dimethylsiloxane) (PDMS) Based Microfluidic Devices. *Microfluidics and Nanofluidics*. 2009. <https://doi.org/10.1007/s10404-009-0443-4>.
- (309) Zhang, J.; Chen, Y.; Brook, M. A. Facile Functionalization of PDMS Elastomer Surfaces Using Thiol – Ene Click Chemistry. **2013**. <https://doi.org/10.1021/la403425d>.
- (310) Sterner, O.; Serrano, A.; Mieszkin, S.; Zürcher, S.; Tosatti, S.; Callow, M. E.; Callow, J. A.; Spencer, N. D. Photochemically Prepared, Two-Component Polymer-Concentration Gradients. *Langmuir* **2013**. <https://doi.org/10.1021/la402168z>.
- (311) Minko, S. Chapter 11 Grafting on Solid Surfaces: ‘Grafting to’ and ‘Grafting from’ Methods. In *Polymer Surfaces and Interfaces: Characterization, Modification and Applications*; Stamm, M., Ed.; 2008. [https://doi.org/10.1007/978-3-540-73864-0\\_11](https://doi.org/10.1007/978-3-540-73864-0_11).

- (312) Zdyrko, B.; Luzinov, I. Polymer Brushes by the “Grafting to” Method. *Macromol. Rapid Commun.* **2011**, *32* (12), 859–869. <https://doi.org/10.1002/marc.201100162>.
- (313) Larnaudie, S. C.; Brendel, J. C.; Jolliffe, K. A.; Perrier, S. Cyclic Peptide-Polymer Conjugates: Grafting-to vs Grafting-From. *J. Polym. Sci. Part A Polym. Chem.* **2016**, *54* (7), 1003–1011. <https://doi.org/10.1002/pola.27937>.
- (314) Mazloomi-Rezvani, M.; Salami-Kalajahi, M.; Roghani-Mamaqani, H. “Grafting to” Approach for Surface Modification of AuNPs with RAFT-Mediated Synthesized Smart Polymers: Stimuli-Responsive Behaviors of Hybrid Nanoparticles. *J. Phys. Chem. Solids* **2018**, *123* (July), 183–190. <https://doi.org/10.1016/j.jpcs.2018.08.002>.
- (315) Sangermano, M.; Razza, N. Light Induced Grafting-from Strategies as Powerful Tool for Surface Modification. *Express Polym. Lett.* **2019**, *13* (2), 135–145. <https://doi.org/10.3144/expresspolymlett.2019.13>.
- (316) Dietliker, K.; Grützmacher, H.; Rentsch, D.; Wang, J.; Fantino, E.; Chiappone, A.; Lorusso, M.; Pirri, C. F.; Shao, F.; Roppolo, I. All-in-One Cellulose Nanocrystals for 3D Printing of Nanocomposite Hydrogels. *Angew. Chemie Int. Ed.* **2017**, *57* (9), 2353–2356. <https://doi.org/10.1002/anie.201710951>.
- (317) Rubio, N.; Au, H.; Leese, H. S.; Hu, S.; Clancy, A. J.; Shaffer, M. S. P. Grafting from versus Grafting to Approaches for the Functionalization of Graphene Nanoplatelets with Poly(Methyl Methacrylate). *Macromolecules* **2017**, *50* (18), 7070–7079. <https://doi.org/10.1021/acs.macromol.7b01047>.
- (318) Ebara, M.; Hoffman, J. M.; Stayton, P. S.; Hoffman, A. S. Surface Modification of Microfluidic Channels by UV-Mediated Graft Polymerization of Non-Fouling and “smart” Polymers. *Radiat. Phys. Chem.* **2007**, *76* (8–9), 1409–1413. <https://doi.org/10.1016/j.radphyschem.2007.02.072>.
- (319) Marazzi, M.; Wibowo, M.; Gattuso, H.; Dumont, E.; Roca-Sanjuán, D.; Monari, A. Hydrogen Abstraction by Photoexcited Benzophenone: Consequences for DNA Photosensitization. *Phys. Chem. Chem. Phys.* **2016**. <https://doi.org/10.1039/c5cp07938a>.
- (320) Taskin, O. S.; Temel, B. A.; Tasdelen, M. A.; Yagci, Y. Synthesis of Block Copolymers by Selective H-Abstraction and Radical Coupling Reactions Using Benzophenone/Benzhydrol Photoinitiating System. *Eur. Polym. J.* **2015**, *62*, 304–311. <https://doi.org/10.1016/j.eurpolymj.2014.07.007>.
- (321) Walling, C.; Gibian, M. J. Hydrogen Abstraction Reactions by the Triplet States of Ketones. *J. Am. Chem. Soc.* **1965**. <https://doi.org/10.1021/ja01093a014>.
- (322) Nesvadba, P. *Radical Polymerization in Industry*; 2012. <https://doi.org/10.1002/9781119953678.rad080>.
- (323) Hu, S.; Ren, X.; Bachman, M.; Sims, C. E.; Li, G. P.; Allbritton, N. L. Surface-Directed, Graft Polymerization within Microfluidic Channels. *Anal. Chem.*

- 2004**, 76 (7), 1865–1870. <https://doi.org/10.1021/ac049937z>.
- (324) Schneider, M. H.; Kozlov, B.; Willaime, H.; Tran, Y.; Rezgui, F.; Tabeling, P. Wettability Patterning in Microfluidic Systems By Poly ( Acrylic Acid ) Graft Polymerization. *Anal. Chem.* **2010**, 82 (21), 8848–8855.
- (325) Carlborg, C. F.; Haraldsson, T.; Oberg, K.; Malkoch, M.; Van der Wijngaart, W. Beyond PDMS: Off-Stoichiometry Thiol-Ene (OSTE) Based Soft Lithography for Rapid Prototyping of Microfluidic Devices. *Lab Chip* **2011**, 11, 3136–3147. <https://doi.org/10.1039/c1lc20388f>.
- (326) Pardon, G.; Saharil, F.; Karlsson, J. M.; Supekar, O.; Carlborg, C. F.; van der Wijngaart, W.; Haraldsson, T. Rapid Mold-Free Manufacturing of Microfluidic Devices with Robust and Spatially Directed Surface Modifications. *Microfluid. Nanofluidics* **2014**, 17 (4), 773–779. <https://doi.org/10.1007/s10404-014-1351-9>.
- (327) Jo, B.; Van Lerberghe, L. M.; Motsegood, K. M.; Beebe, D. J. Three-Dimensional Micro-Channel Fabrication in Polydimethylsiloxane (PDMS) Elastomer. *J. Microelectromechanical Syst.* **2000**, 9 (1), 76–81.
- (328) Li Jeon, N.; Chiu, D. T.; Wargo, C. J.; Wu, H.; Choi, I. S.; Anderson, J. R.; Whitesides, G. M. Design and Fabrication of Integrated Passive Valves and Pumps for Flexible Polymer 3-Dimensional Microfluidic Systems. *Biomed. Microdevices* **2002**, 4 (2), 117–121.
- (329) Wu, H.; Odom, T. W.; Chiu, D. T.; Whitesides, G. M. Fabrication of Complex Three-Dimensional Microchannel Systems in PDMS. *J. Am. Chem. Soc.* **2003**, 125 (2), 554–559. <https://doi.org/10.1021/ja021045y>.
- (330) Anderson, J. R.; Chiu, D. T.; Jackman, R. J.; Chemiavskaya, O.; McDonald, J. C.; Wu, H.; Whitesides, S. H.; Whitesides, G. M. Fabrication of Topologically Complex Three-Dimensional Microfluidic Systems in PDMS by Rapid Prototyping. *Anal. Chem.* **2000**, 72 (14), 3158–3164. <https://doi.org/10.1021/ac9912294>.
- (331) Villegas, M.; Cetinic, Z.; Shakeri, A.; Didar, T. F. Fabricating Smooth PDMS Microfluidic Channels from Low-Resolution 3D Printed Molds Using an Omniphobic Lubricant-Infused Coating. *Anal. Chim. Acta* **2018**, 1000, 248–255. <https://doi.org/10.1016/j.aca.2017.11.063>.
- (332) Credi, C.; Griffini, G.; Levi, M.; Turri, S. Biotinylated Photopolymers for 3D-Printed Unibody Lab-on-a-Chip Optical Platforms. *Small* **2018**, 14 (1), 1–8. <https://doi.org/10.1002/sml.201702831>.
- (333) Zhu, F.; Macdonald, N.; Skommer, J.; Wlodkowic, D. Biological Implications of Lab-on-a-Chip Devices Fabricated Using Multi-Jet Modelling and Stereolithography Processes. *SPIE Microtechnologies* **2015**, 9518, 951808. <https://doi.org/10.1117/12.2180743>.
- (334) Chiadò, A.; Palmara, G.; Chiappone, A.; Tanzanu, C.; Pirri, C. F.; Roppolo, I.; Frascella, F. A Modular 3D Printed Lab-on-a-Chip for Early Cancer Detection. *Lab Chip* **2020**, 20 (3), 665–674. <https://doi.org/10.1039/c9lc01108k>.
- (335) Panjan, P.; Virtanen, V.; Sesay, A. M. Towards Microbioprocess Control:

- An Inexpensive 3D Printed Microbioreactor with Integrated Online Real-Time Glucose Monitoring. *Analyst* **2018**, *143* (16), 3926–3933. <https://doi.org/10.1039/c8an00308d>.
- (336) Weisgrab, G.; Ovsianikov, A.; Costa, P. F. Functional 3D Printing for Microfluidic Chips. *Adv. Mater. Technol.* **2019**, *4* (10). <https://doi.org/10.1002/admt.201900275>.
- (337) Macdonald, N. P.; Cabot, J. M.; Smejkal, P.; Guijt, R. M.; Paull, B.; Breadmore, M. C. Comparing Microfluidic Performance of Three-Dimensional (3D) Printing Platforms. *Anal. Chem.* **2017**, *89* (7), 3858–3866. <https://doi.org/10.1021/acs.analchem.7b00136>.
- (338) Rimington, R. P.; Capel, A. J.; Christie, S. D. R.; Lewis, M. P. Biocompatible 3D Printed Polymers: Via Fused Deposition Modelling Direct C2C12 Cellular Phenotype in Vitro. *Lab Chip* **2017**, *17* (17), 2982–2993. <https://doi.org/10.1039/c7lc00577f>.
- (339) Nyberg, E.; Rindone, A.; Dorafshar, A.; Grayson, W. L. Comparison of 3D-Printed Poly- $\epsilon$ -Caprolactone Scaffolds Functionalized with Tricalcium Phosphate, Hydroxyapatite, Bio-Oss, or Decellularized Bone Matrix. *Tissue Eng. - Part A* **2017**. <https://doi.org/10.1089/ten.tea.2016.0418>.
- (340) Raeisdasteh Hokmabad, V.; Davaran, S.; Ramazani, A.; Salehi, R. Design and Fabrication of Porous Biodegradable Scaffolds: A Strategy for Tissue Engineering. *J. Biomater. Sci. Polym. Ed.* **2017**, *28* (16), 1797–1825. <https://doi.org/10.1080/09205063.2017.1354674>.
- (341) Kotz, F.; Mader, M.; Dellen, N.; Risch, P.; Kick, A.; Helmer, D.; Rapp, B. E. Fused Deposition Modeling of Microfluidic Chips in Polymethylmethacrylate. *Micromachines* **2020**, *11* (9), 5–8. <https://doi.org/10.3390/mi11090873>.
- (342) Nelson, M. D.; Ramkumar, N.; Gale, B. K. Flexible, Transparent, Sub-100 Mm Microfluidic Channels with Fused Deposition Modeling 3D-Printed Thermoplastic Polyurethane. *J. Micromechanics Microengineering* **2019**, *29* (9). <https://doi.org/10.1088/1361-6439/ab2f26>.
- (343) Castiaux, A. D.; Pinger, C. W.; Hayter, E. A.; Bunn, M. E.; Martin, R. S.; Spence, D. M. PolyJet 3D-Printed Enclosed Microfluidic Channels without Photocurable Supports. *Anal. Chem.* **2019**. <https://doi.org/10.1021/acs.analchem.9b01302>.
- (344) BMF Materials Inc. Industrial Micro-Precision 3D Printers <https://bmf3d.com/>.
- (345) Ge, Q.; Li, Z.; Wang, Z.; Kowsari, K.; Zhang, W.; He, X.; Zhou, J.; Fang, N. X. Projection Micro Stereolithography Based 3D Printing and Its Applications. *Int. J. Extrem. Manuf.* **2020**, *2* (2). <https://doi.org/10.1088/2631-7990/ab8d9a>.
- (346) Bressan, L. P.; Lima, T. M.; da Silveira, G. D.; da Silva, J. A. F. Low-Cost and Simple FDM-Based 3D-Printed Microfluidic Device for the Synthesis of Metallic Core-Shell Nanoparticles. *SN Appl. Sci.* **2020**, *2* (5), 1–8. <https://doi.org/10.1007/s42452-020-2768-2>.

- (347) Bressan, L. P.; Robles-Najar, J.; Adamo, C. B.; Quero, R. F.; Costa, B. M. C.; de Jesus, D. P.; da Silva, J. A. F. 3D-Printed Microfluidic Device for the Synthesis of Silver and Gold Nanoparticles. *Microchem. J.* **2019**, *146* (February), 1083–1089. <https://doi.org/10.1016/j.microc.2019.02.043>.
- (348) Gaal, G.; Mendes, M.; de Almeida, T. P.; Piazzetta, M. H. O.; Gobbi, Â. L.; Riul, A.; Rodrigues, V. Simplified Fabrication of Integrated Microfluidic Devices Using Fused Deposition Modeling 3D Printing. *Sensors Actuators, B Chem.* **2017**, *242*, 35–40. <https://doi.org/10.1016/j.snb.2016.10.110>.
- (349) Romanov, V.; Samuel, R.; Chaharlang, M.; Jafek, A. R.; Frost, A.; Gale, B. K. FDM 3D Printing of High-Pressure, Heat-Resistant, Transparent Microfluidic Devices. *Anal. Chem.* **2018**, *90* (17), 10450–10456. <https://doi.org/10.1021/acs.analchem.8b02356>.
- (350) Li, F.; Macdonald, N. P.; Guijt, R. M.; Breadmore, M. C. Using Printing Orientation for Tuning Fluidic Behavior in Microfluidic Chips Made by Fused Deposition Modeling 3D Printing. *Anal. Chem.* **2017**, *89* (23), 12805–12811. <https://doi.org/10.1021/acs.analchem.7b03228>.
- (351) Li, F.; Macdonald, N. P.; Guijt, R. M.; Breadmore, M. C. Increasing the Functionalities of 3D Printed Microchemical Devices by Single Material, Multimaterial, and Print-Pause-Print 3D Printing. *Lab on a Chip*. Royal Society of Chemistry **2019**, pp 35–49. <https://doi.org/10.1039/c8lc00826d>.
- (352) Vidakis, N.; Petousis, M.; Vaxevanidis, N.; Kechagias, J. Surface Roughness Investigation of Poly-Jet 3D Printing. *Mathematics* **2020**, *8* (10), 1758. <https://doi.org/10.3390/math8101758>.
- (353) Lee, J. M.; Zhang, M.; Yeong, W. Y. Characterization and Evaluation of 3D Printed Microfluidic Chip for Cell Processing. *Microfluid. Nanofluidics* **2016**, *20* (1), 1–15. <https://doi.org/10.1007/s10404-015-1688-8>.
- (354) Mansur, E. A.; YE, M.; WANG, Y.; DAI, Y. A State-of-the-Art Review of Mixing in Microfluidic Mixers. *Chinese J. Chem. Eng.* **2008**. [https://doi.org/10.1016/S1004-9541\(08\)60114-7](https://doi.org/10.1016/S1004-9541(08)60114-7).
- (355) Enders, A.; Siller, I. G.; Urmann, K.; Hoffmann, M. R.; Bahnemann, J. 3D Printed Microfluidic Mixers—A Comparative Study on Mixing Unit Performances. *Small* **2019**, *15* (2), 1–9. <https://doi.org/10.1002/smll.201804326>.
- (356) Waheed, S.; Cabot, J. M.; Macdonald, N. P.; Lewis, T.; Guijt, R. M.; Paull, B.; Breadmore, M. C. 3D Printed Microfluidic Devices: Enablers and Barriers. *Lab Chip* **2016**, *16* (11), 1993–2013. <https://doi.org/10.1039/C6LC00284F>.
- (357) Chen, C.; Mehl, B. T.; Munshi, A. S.; Townsend, A. D.; Spence, D. M.; Martin, R. S. 3D-Printed Microfluidic Devices: Fabrication, Advantages and Limitations - a Mini Review. *Analytical Methods*. **2016**. <https://doi.org/10.1039/c6ay01671e>.
- (358) Tothill, A. M.; Partridge, M.; James, S. W.; Tatam, R. P. Fabrication and



- Optimisation of a Fused Filament 3D-Printed Microfluidic Platform. *J. Micromechanics Microengineering* **2017**, *27* (3). <https://doi.org/10.1088/1361-6439/aa5ae3>.
- (359) Keating, S. J.; Gariboldi, M. I.; Patrick, W. G.; Sharma, S.; Kong, D. S.; Oxman, N. 3D Printed Multimaterial Microfluidic Valve. *PLoS One* **2016**, *11* (8), 1–12. <https://doi.org/10.1371/journal.pone.0160624>.
- (360) Sochol, R. D.; Sweet, E.; Glick, C. C.; Venkatesh, S.; Avetisyan, A.; Ekman, K. F.; Raulinaitis, A.; Tsai, A.; Wienkers, A.; Korner, K.; Hanson, K.; Long, A.; Hightower, B. J.; Slatton, G.; Burnett, D. C.; Massey, T. L.; Iwai, K.; Lee, L. P.; Pister, K. S. J.; Lin, L. 3D Printed Microfluidic Circuitry via Multijet-Based Additive Manufacturing. *Lab Chip* **2016**, *16* (4), 668–678. <https://doi.org/10.1039/c5lc01389e>.
- (361) Sweet, E.; Mehta, R.; Xu, Y.; Jew, R.; Lin, R.; Lin, L. Finger-Powered Fluidic Actuation and Mixing: Via MultiJet 3D Printing. *Lab Chip* **2020**, *20* (18), 3375–3385. <https://doi.org/10.1039/d0lc00488j>.
- (362) Walczak, R.; Adamski, K.; Kubicki, W. Inkjet 3D Printed Chip for Capillary Gel Electrophoresis. *Sensors Actuators, B Chem.* **2018**, *261*, 474–480. <https://doi.org/10.1016/j.snb.2018.01.174>.
- (363) Ligon, S. C.; Liska, R.; Stampfl, J.; Gurr, M.; Mülhaupt, R. Polymers for 3D Printing and Customized Additive Manufacturing. *Chem. Rev.* **2017**, *117* (15), 10212–10290. <https://doi.org/10.1021/acs.chemrev.7b00074>.
- (364) Farahani, R. D.; Dubé, M.; Therriault, D. Three-Dimensional Printing of Multifunctional Nanocomposites: Manufacturing Techniques and Applications. *Adv. Mater.* **2016**, 5794–5821. <https://doi.org/10.1002/adma.201506215>.
- (365) Guerra, M. G.; Volpone, C.; Galantucci, L. M.; Percoco, G. Photogrammetric Measurements of 3D Printed Microfluidic Devices. *Addit. Manuf.* **2018**, *21* (February), 53–62. <https://doi.org/10.1016/j.addma.2018.02.013>.
- (366) Park, C.; Han, Y. D.; Kim, H. V.; Lee, J.; Yoon, H. C.; Park, S. Double-Sided 3D Printing on Paper towards Mass Production of Three-Dimensional Paper-Based Microfluidic Analytical Devices (3D-MPADs). *Lab Chip* **2018**, *18* (11), 1533–1538. <https://doi.org/10.1039/c8lc00367j>.
- (367) Ruiz, C.; Kadimisetty, K.; Yin, K.; Mauk, M. G.; Zhao, H.; Liu, C. Fabrication of Hard-Soft Microfluidic Devices Using Hybrid 3D Printing. *Micromachines* **2020**, *11* (6), 1–11. <https://doi.org/10.3390/M11060567>.
- (368) Costa, P. F.; Albers, H. J.; Linsen, J. E. A.; Middelkamp, H. H. T.; Van Der Hout, L.; Passier, R.; Van Den Berg, A.; Malda, J.; Van Der Meer, A. D. Mimicking Arterial Thrombosis in a 3D-Printed Microfluidic: In Vitro Vascular Model Based on Computed Tomography Angiography Data. *Lab Chip* **2017**, *17* (16), 2785–2792. <https://doi.org/10.1039/c7lc00202e>.
- (369) Heo, P.; Ramakrishnan, S.; Coleman, J.; Rothman, J. E.; Fleury, J. B.; Pincet, F. Highly Reproducible Physiological Asymmetric Membrane with Freely Diffusing Embedded Proteins in a 3D-Printed Microfluidic Setup.

- Small* **2019**, *15* (21), 1–13. <https://doi.org/10.1002/sml.201900725>.
- (370) Manzanares Palenzuela, C. L.; Pumera, M. (Bio)Analytical Chemistry Enabled by 3D Printing: Sensors and Biosensors. *TrAC - Trends Anal. Chem.* **2018**, *103*, 110–118. <https://doi.org/10.1016/j.trac.2018.03.016>.
- (371) Wales, D. J.; Cao, Q.; Kastner, K.; Karjalainen, E.; Newton, G. N.; Sans, V. 3D-Printable Photochromic Molecular Materials for Reversible Information Storage. *Adv. Mater.* **2018**, *30* (26), 1–7. <https://doi.org/10.1002/adma.201800159>.
- (372) Kang, H. W.; Lee, I. H.; Cho, D. W. Development of an Assembly-Free Process Based on Virtual Environment for Fabricating 3D Microfluidic Systems Using Microstereolithography Technology. *J. Manuf. Sci. Eng. Trans. ASME* **2004**, *126* (4), 766–771. <https://doi.org/10.1115/1.1811116>.
- (373) Zhu, F.; Macdonald, N. P.; Cooper, J. M.; Wlodkovic, D. Additive Manufacturing of Lab-on-a-Chip Devices: Promises and Challenges. *Micro/Nano Mater. Devices, Syst.* **2013**, *8923*, 892344. <https://doi.org/10.1117/12.2033400>.
- (374) Au, A. K.; Lee, W.; Folch, A. Mail-Order Microfluidics: Evaluation of Stereolithography for the Production of Microfluidic Devices. *Lab Chip* **2014**, *14* (7), 1294–1301. <https://doi.org/10.1039/c3lc51360b>.
- (375) Shallan, A. I.; Smejkal, P.; Corban, M.; Guijt, R. M.; Breadmore, M. C. Cost-Effective Three-Dimensional Printing of Visibly Transparent Microchips within Minutes. *Anal. Chem.* **2014**, *86* (6), 3124–3130. <https://doi.org/10.1021/ac4041857>.
- (376) Lee, W.; Kwon, D.; Choi, W.; Jung, G. Y.; Au, A. K.; Folch, A.; Jeon, S. 3D-Printed Micro Fluidic Device for the Detection of Pathogenic Bacteria Using Size-Based Separation in Helical Channel with Trapezoid Cross-Section. *Sci. Rep.* **2015**, *5*, 1–7. <https://doi.org/10.1038/srep07717>.
- (377) Beauchamp, M. J.; Gong, H.; Woolley, A. T.; Nordin, G. P. 3D Printed Microfluidic Features Using Dose Control in X, Y, and Z Dimensions. *Micromachines* **2018**, *9* (7). <https://doi.org/10.3390/mi9070326>.
- (378) Männel, M. J.; Selzer, L.; Bernhardt, R.; Thiele, J. Optimizing Process Parameters in Commercial Micro-Stereolithography for Forming Emulsions and Polymer Microparticles in Nonplanar Microfluidic Devices. *Adv. Mater. Technol.* **2019**, *4* (1), 1–10. <https://doi.org/10.1002/admt.201800408>.
- (379) Takenaga, S.; Schneider, B.; Erbay, E.; Biselli, M.; Schnitzler, T.; Schöning, M. J.; Wagner, T. Fabrication of Biocompatible Lab-on-Chip Devices for Biomedical Applications by Means of a 3D-Printing Process. *Phys. Status Solidi Appl. Mater. Sci.* **2015**, *212* (6), 1347–1352. <https://doi.org/10.1002/pssa.201532053>.
- (380) Gong, H.; Beauchamp, M.; Perry, S.; Woolley, A.; Nordin, G. Optical Approach to Resin Formulation for 3D Printed Microfluidics. *RSC Adv.* **2015**, *5* (129), 106621–106632.

<https://doi.org/10.1039/C5RA23855B>.

- (381) Parker, E. K.; Nielsen, A. V.; Beauchamp, M. J.; Almughamsi, H. M.; Nielsen, J. B.; Sonker, M.; Gong, H.; Nordin, G. P.; Woolley, A. T. 3D Printed Microfluidic Devices with Immunoaffinity Monoliths for Extraction of Preterm Birth Biomarkers. *Anal. Bioanal. Chem.* **2019**, *411* (21), 5405–5413. <https://doi.org/10.1007/s00216-018-1440-9>.
- (382) Beauchamp, M. J.; Nielsen, A. V.; Gong, H.; Nordin, G. P.; Woolley, A. T. 3D Printed Microfluidic Devices for Microchip Electrophoresis of Preterm Birth Biomarkers. *Anal. Chem.* **2019**, *91* (11), 7418–7425. <https://doi.org/10.1021/acs.analchem.9b01395>.
- (383) Rogers, C. I.; Qaderi, K.; Woolley, A. T.; Nordin, G. P. 3D Printed Microfluidic Devices with Integrated Valves. *Biomicrofluidics* **2015**, *9* (1), 1–9. <https://doi.org/10.1063/1.4905840>.
- (384) Gong, H.; Woolley, A. T.; Nordin, G. P. High Density 3D Printed Microfluidic Valves, Pumps, and Multiplexers. *Lab Chip* **2016**, *16* (13), 2450–2458. <https://doi.org/10.1039/c6lc00565a>.
- (385) Lee, Y. S.; Bhattacharjee, N.; Folch, A. 3D-Printed Quake-Style Microvalves and Micropumps. *Lab Chip* **2018**, *18* (8), 1207–1214. <https://doi.org/10.1039/c8lc00001h>.
- (386) Au, A. K.; Bhattacharjee, N.; Horowitz, L. F.; Chang, T. C.; Folch, A. 3D-Printed Microfluidic Automation. *Lab Chip* **2015**, *15* (8), 1934–1941. <https://doi.org/10.1039/c5lc00126a>.
- (387) Wang, Z.; Martin, N.; Hini, D.; Mills, B.; Kim, K. Rapid Fabrication of Multilayer Microfluidic Devices Using the Liquid Crystal Display-Based Stereolithography 3D Printing System. *3D Print. Addit. Manuf.* **2017**, *4* (3), 156–164. <https://doi.org/10.1089/3dp.2017.0028>.
- (388) Kotz, F.; Risch, P.; Helmer, D.; Rapp, B. E. Highly Fluorinated Methacrylates for Optical 3D Printing of Microfluidic Devices. *Micromachines* **2018**, *9* (3). <https://doi.org/10.3390/mi9030115>.
- (389) Yeung, C.; Chen, S.; King, B.; Lin, H.; King, K.; Akhtar, F.; Diaz, G.; Wang, B.; Zhu, J.; Sun, W.; Khademhosseini, A.; Emaminejad, S. A 3D-Printed Microfluidic-Enabled Hollow Microneedle Architecture for Transdermal Drug Delivery. *Biomicrofluidics* **2019**, *13* (6). <https://doi.org/10.1063/1.5127778>.
- (390) Chen, Z.; Han, J. Y.; Shumate, L.; Fedak, R.; DeVoe, D. L. High Throughput Nanoliposome Formation Using 3D Printed Microfluidic Flow Focusing Chips. *Adv. Mater. Technol.* **2019**, *4* (6), 1–9. <https://doi.org/10.1002/admt.201800511>.
- (391) Bhattacharjee, N.; Parra-Cabrera, C.; Kim, Y. T.; Kuo, A. P.; Folch, A. Desktop-Stereolithography 3D-Printing of a Poly(Dimethylsiloxane)-Based Material with Sylgard-184 Properties. *Adv. Mater.* **2018**, *30* (22), 1–7. <https://doi.org/10.1002/adma.201800001>.
- (392) Zips, S.; Hiendlmeier, L.; Weiß, L. J. K.; Url, H.; Teshima, T. F.; Schmid, R.; Eblenkamp, M.; Mela, P.; Wolfrum, B. Biocompatible, Flexible, and

- Oxygen-Permeable Silicone-Hydrogel Material for Stereolithographic Printing of Microfluidic Lab-On-A-Chip and Cell-Culture Devices. *ACS Appl. Polym. Mater.* **2020**. <https://doi.org/10.1021/acsapm.0c01071>.
- (393) Lee, J. Y.; An, J.; Chua, C. K. Fundamentals and Applications of 3D Printing for Novel Materials. *Appl. Mater. Today* **2017**, *7*, 120–133. <https://doi.org/10.1016/j.apmt.2017.02.004>.
- (394) Layani, M.; Wang, X.; Magdassi, S. Novel Materials for 3D Printing by Photopolymerization. *Adv. Mater.* **2018**, *30* (41), 1–7. <https://doi.org/10.1002/adma.201706344>.
- (395) Andrews, L. S.; Clary, J. J. Review of the Toxicity of Multifunctional Acrylates. *J. Toxicol. Environ. Health* **1986**. <https://doi.org/10.1080/15287398609530916>.
- (396) Zhu, F.; Skommer, J.; Friedrich, T.; Kaslin, J.; Wlodkowic, D. 3D Printed Polymers Toxicity Profiling: A Caution for Biodevice Applications. In *SPIE Micro+Nano Materials, Devices, and Applications Symposium*; Sidney, Australia. <https://doi.org/10.1117/12.2202392>.
- (397) Zhang, R.; Larsen, N. B. Stereolithographic Hydrogel Printing of 3D Culture Chips with Biofunctionalized Complex 3D Perfusion Networks. *Lab Chip* **2017**, *17* (24), 4273–4282. <https://doi.org/10.1039/c7lc00926g>.
- (398) Pawar, A. A.; Saada, G.; Cooperstein, I.; Larush, L.; Jackman, J. A.; Tabaei, S. R.; Cho, N. J.; Magdassi, S. High-Performance 3D Printing of Hydrogels by Water-Dispersible Photoinitiator Nanoparticles. *Sci. Adv.* **2016**, *2* (4). <https://doi.org/10.1126/sciadv.1501381>.
- (399) Zhang, Y.; An, D.; Pardo, Y.; Chiu, A.; Song, W.; Liu, Q.; Zhou, F.; McDonough, S. P.; Ma, M. High-Water-Content and Resilient PEG-Containing Hydrogels with Low Fibrotic Response. *Acta Biomater.* **2017**, *53*, 100–108. <https://doi.org/10.1016/j.actbio.2017.02.028>.
- (400) Kim, Y. S.; Cho, K.; Lee, H. J.; Chang, S.; Lee, H.; Kim, J. H.; Koh, W. G. Highly Conductive and Hydrated PEG-Based Hydrogels for the Potential Application of a Tissue Engineering Scaffold. *React. Funct. Polym.* **2016**, *109*, 15–22. <https://doi.org/10.1016/j.reactfunctpolym.2016.09.003>.
- (401) González-Henríquez, C. M.; Rodríguez-Umanzor, F. E.; Almagro-Correa, J.; Sarabia-Vallejos, M. A.; Martínez-Campos, E.; Esteban-Lucía, M.; del Campo-García, A.; Rodríguez-Hernández, J. Biocompatible Fluorinated Wrinkled Hydrogel Films with Antimicrobial Activity. *Mater. Sci. Eng. C* **2020**, *114* (March), 111031. <https://doi.org/10.1016/j.msec.2020.111031>.
- (402) Männel, M. J.; Fischer, C.; Thiele, J. A Non-Cytotoxic Resin for Micro-Stereolithography for Cell Cultures of HUVECs. *Micromachines* **2020**, *11* (3). <https://doi.org/10.3390/mi11030246>.
- (403) Warr, C.; Valdoz, J. C.; Bickham, B. P.; Knight, C. J.; Franks, N. A.; Chartrand, N.; Van Ry, P. M.; Christensen, K. A.; Nordin, G. P.; Cook, A. D. Biocompatible PEGDA Resin for 3D Printing. *ACS Appl. Bio Mater.* **2020**, *3*, 2239–2244. <https://doi.org/10.1021/acsabm.0c00055>.

- (404) Mehta, V.; Rath, S. N. 3D Printed Microfluidic Devices: A Review Focused on Four Fundamental Manufacturing Approaches and Implications on the Field of Healthcare. *Bio-Design Manuf.* **2021**. <https://doi.org/10.1007/s42242-020-00112-5>.
- (405) MicronInc. FDA Approved 3D Printer Resins <https://www.microndental.com/regulatory/fda-approved-cleared-3d-printer-resins> (accessed Oct 30, 2019).
- (406) Piironen, K.; Haapala, M.; Talman, V.; Järvinen, P.; Sikanen, T. Cell Adhesion and Proliferation on Common 3D Printing Materials Used in Stereolithography of Microfluidic Devices. *Lab Chip* **2020**, *20* (13), 2372–2382. <https://doi.org/10.1039/d0lc00114g>.
- (407) MacDonald, N. P.; Zhu, F.; Hall, C. J.; Reboud, J.; Crosier, P. S.; Patton, E. E.; Wlodkowic, D.; Cooper, J. M. Assessment of Biocompatibility of 3D Printed Photopolymers Using Zebrafish Embryo Toxicity Assays. *Lab Chip* **2016**, *16* (2), 291–297. <https://doi.org/10.1039/c5lc01374g>.
- (408) Kreß, S.; Schaller-Ammann, R.; Feiel, J.; Friedl, J.; Kasper, C.; Egger, D. 3D Printing of Cell Culture Devices: Assessment and Prevention of the Cytotoxicity of Photopolymers for Stereolithography. *Materials (Basel)*. **2020**, *13* (13). <https://doi.org/10.3390/ma13133011>.
- (409) Rimington, R. P.; Capel, A. J.; Player, D. J.; Bibb, R. J.; Christie, S. D. R.; Lewis, M. P. Feasibility and Biocompatibility of 3D-Printed Photopolymerized and Laser Sintered Polymers for Neuronal, Myogenic, and Hepatic Cell Types. *Macromol. Biosci.* **2018**, *1800113*, 1–12. <https://doi.org/10.1002/mabi.201800113>.
- (410) Alifui-Segbaya, F.; Varma, S.; Lieschke, G. J.; George, R. Biocompatibility of Photopolymers in 3D Printing. *3D Print. Addit. Manuf.* **2017**, *4* (4), 185–191. <https://doi.org/10.1089/3dp.2017.0064>.
- (411) Carve, M.; Wlodkowic, D. 3D-Printed Chips: Compatibility of Additive Manufacturing Photopolymeric Substrata with Biological Applications. *Micromachines* **2018**, *9* (2). <https://doi.org/10.3390/mi9020091>.
- (412) Schuster, M.; Turecek, C.; Kaiser, B.; Stampfl, J.; Liska, R.; Varga, F. Evaluation of Biocompatible Photopolymers I: Photoreactivity and Mechanical Properties of Reactive Diluents. *J. Macromol. Sci. Part A Pure Appl. Chem.* **2007**, *44* (5), 547–557. <https://doi.org/10.1080/10601320701235958>.
- (413) Urrios, A.; Parra-Cabrera, C.; Bhattacharjee, N.; Gonzalez-Suarez, A. M.; Rigat-Brugarolas, L. G.; Nallapatti, U.; Samitier, J.; Deforest, C. A.; Posas, F.; Garcia-Cordero, J. L.; Folch, A. 3D-Printing of Transparent Bio-Microfluidic Devices in PEG-DA. *Lab Chip* **2016**, *16* (12), 2287–2294. <https://doi.org/10.1039/c6lc00153j>.
- (414) Zhang, Y. Post-3D Printing Modification for Improved Biomedical Applications. *Int. J. Bioprinting* **2017**, *3* (2). <https://doi.org/10.18063/ijb.2017.02.001>.
- (415) Wang, X.; Cai, X.; Guo, Q.; Zhang, T.; Kobe, B.; Yang, J. I3DP, a Robust 3D Printing Approach Enabling Genetic Post-Printing Surface Modification.

- Chem. Commun.* **2013**, 49 (86), 10064–10066.  
<https://doi.org/10.1039/c3cc45817b>.
- (416) Stassi, S.; Fantino, E.; Calmo, R.; Chiappone, A.; Gillono, M.; Scaiola, D.; Pirri, C. F.; Ricciardi, C.; Chiadò, A.; Roppolo, I. Polymeric 3D Printed Functional Microcantilevers for Biosensing Applications. *ACS Appl. Mater. Interfaces* **2017**, 9 (22), 19193–19201.  
<https://doi.org/10.1021/acsami.7b04030>.
- (417) Amin, R.; Knowlton, S.; Hart, A.; Yenilmez, B.; Ghaderinezhad, F.; Katebifar, S.; Messina, M.; Khademhosseini, A.; Tasoglu, S. 3D-Printed Microfluidic Devices. *Biofabrication* **2016**, 8 (2), 022001.  
<https://doi.org/10.1088/1758-5090/8/2/022001>.
- (418) Chen, L.; Yan, C.; Zheng, Z. Functional Polymer Surfaces for Controlling Cell Behaviors. *Mater. Today* **2018**, 21 (1), 38–59.  
<https://doi.org/10.1016/j.mattod.2017.07.002>.
- (419) Gonzalez, G.; Baruffaldi, D.; Martinengo, C.; Angelini, A.; Chiappone, A.; Roppolo, I.; Pirri, F. C.; Frascella, F. Materials Testing for the Development of Biocompatible Devices through Vat-Polymerization 3D Printing. *Nanomaterials* **2020**, 10 (9), 1788.  
<https://doi.org/10.3390/nano10091788>.
- (420) Wu, K. C.; Halloran, J. W. Photopolymerization Monitoring of Ceramic Stereolithography Resins by FTIR Methods. *J. Mater. Sci.* **2005**, 40 (1), 71–76. <https://doi.org/10.1007/s10853-005-5689-y>.
- (421) Frascella, F.; González, G.; Bosch, P.; Angelini, A.; Chiappone, A.; Sangermano, M.; Pirri, C. F.; Roppolo, I. Three-Dimensional Printed Photoluminescent Polymeric Waveguides. *ACS Appl. Mater. Interfaces* **2018**, 10 (45), 39319–39326.  
<https://doi.org/10.1021/acsami.8b16036>.
- (422) Wang, X.; Schmidt, F.; Hanaor, D.; Kamm, P. H.; Li, S.; Gurlo, A. Additive Manufacturing of Ceramics from Pre-ceramic Polymers: A Versatile Stereolithographic Approach Assisted by Thiol-Ene Click Chemistry. *Addit. Manuf.* **2019**, 27 (February), 80–90.  
<https://doi.org/10.1016/j.ADDMA.2019.02.012>.
- (423) Pawar, A. A.; Saada, G.; Cooperstein, I.; Larush, L.; Jackman, J. A.; Tabaei, S. R.; Cho, N. J.; Magdassi, S. High-Performance 3D Printing of Hydrogels by Water-Dispersible Photoinitiator Nanoparticles. *Sci. Adv.* **2016**, 2 (4), 1–8. <https://doi.org/10.1126/sciadv.1501381>.
- (424) Popal, M.; Volk, J.; Leyhausen, G.; Geurtsen, W. Cytotoxic and Genotoxic Potential of the Type I Photoinitiators BAPO and TPO on Human Oral Keratinocytes and V79 Fibroblasts. *Dent. Mater.* **2018**.  
<https://doi.org/10.1016/j.dental.2018.09.015>.
- (425) Bail, R.; Patel, A.; Yang, H.; Rogers, C. M.; Rose, F. R. A. J.; Segal, J. I.; Ratchev, S. M. The Effect of a Type I Photoinitiator on Cure Kinetics and Cell Toxicity in Projection-Microstereolithography. *Procedia CIRP* **2013**, 5, 222–225. <https://doi.org/10.1016/j.procir.2013.01.044>.
- (426) Clark, E. A.; Alexander, M. R.; Irvine, D. J.; Roberts, C. J.; Wallace, M. J.;

- Sharpe, S.; Yoo, J.; Hague, R. J. M.; Tuck, C. J.; Wildman, R. D. 3D Printing of Tablets Using Inkjet with UV Photoinitiation. *Int. J. Pharm.* **2017**, *529* (1–2), 523–530. <https://doi.org/10.1016/j.ijpharm.2017.06.085>.
- (427) Abdallah, M. N.; Light, N.; Amin, W. M.; Retrouvey, J. M.; Cerruti, M.; Tamimi, F. Development of a Composite Resin Disclosing Agent Based on the Understanding of Tooth Staining Mechanisms. *J. Dent.* **2014**, *42* (6), 697–708. <https://doi.org/10.1016/j.jdent.2014.03.004>.
- (428) New, N.; Dictionary, C. Standard Test Methods for Determination of Gel Content and Swell Ratio of Crosslinked Ethylene Plastics. *Annu. B. ASTM Stand.* **2005**.
- (429) Yang, X.; Li, K.; Zhang, X.; Liu, C.; Guo, B.; Wen, W.; Gao, X. Nanofiber Membrane Supported Lung-on-a-Chip Microdevice for Anti-Cancer Drug Testing. *Lab Chip* **2018**. <https://doi.org/10.1039/c7lc01224a>.
- (430) Guo, K.; Cao, Y.; Li, Z.; Zhou, X.; Ding, R.; Chen, K.; Liu, Y.; Qiu, Y.; Wu, Z.; Fang, M. Glycine Metabolomic Changes Induced by Anticancer Agents in A549 Cells. *Amino Acids* **2020**, *52* (5), 793–809. <https://doi.org/10.1007/s00726-020-02853-0>.
- (431) Gonzalez, G.; Chiappone, A.; Dietliker, K.; Pirri, C. F.; Roppolo, I. Fabrication and Functionalization of 3D Printed Polydimethylsiloxane-Based Microfluidic Devices Obtained through Digital Light Processing. *Adv. Mater. Technol.* **2020**, *5* (9), 2000374. <https://doi.org/10.1002/admt.202000374>.
- (432) Halldorsson, S.; Lucumi, E.; Gómez-sjöberg, R.; Fleming, R. M. T. Biosensors and Bioelectronics Advantages and Challenges of Micro Fluidic Cell Culture in Polydimethylsiloxane Devices. *Biosens. Bioelectron.* **2015**, *63*, 218–231. <https://doi.org/10.1016/j.bios.2014.07.029>.
- (433) Bishop, G. W. 3D Printed Microfluidic Devices. In *Microfluidics for Biologists: Fundamentals and Applications*; Chandra, D. K., Ajeet, K., Eds.; 2016; pp 103–113. <https://doi.org/3D prin>.
- (434) Abdollahi, S.; Markvicka, E. J.; Majidi, C.; Feinberg, A. W. 3D Printing Silicone Elastomer for Patient-Specific Wearable Pulse Oximeter. *Adv. Healthc. Mater.* **2020**, *9* (15), 1–9. <https://doi.org/10.1002/adhm.201901735>.
- (435) Hinton, T. J.; Hudson, A.; Pusch, K.; Lee, A.; Feinberg, A. W. 3D Printing PDMS Elastomer in a Hydrophilic Support Bath via Freeform Reversible Embedding. *ACS Biomater. Sci. Eng.* **2016**, *2* (10), 1781–1786. <https://doi.org/10.1021/acsbiomaterials.6b00170>.
- (436) Ozbolat, V.; Dey, M.; Ayan, B.; Povilianskas, A.; Demirel, M. C.; Ozbolat, I. T. 3D Printing of PDMS Improves Its Mechanical and Cell Adhesion Properties. *ACS Biomater. Sci. Eng.* **2018**, *4* (2), 682–693. <https://doi.org/10.1021/acsbiomaterials.7b00646>.
- (437) Cunningham, A. F.; Misteli, K.; Dietliker, K.; Grimm, B. Liquid Bisacrylphosphine Oxide Photoinitiator. WO2015 / 004566, 2015.

- (438) Palaganas, J.; de Leon, A. C.; Mangadlao, J.; Palaganas, N.; Mael, A.; Lee, Y. J.; Lai, H. Y.; Advincula, R. Facile Preparation of Photocurable Siloxane Composite for 3D Printing. *Macromol. Mater. Eng.* **2017**, *302* (5), 1–9. <https://doi.org/10.1002/mame.201600477>.
- (439) Taylor, P.; Singer, I. L.; Kohl, J. G.; Patterson, M. Mechanical Aspects of Silicone Coatings for Hard Foulant Control. *Biofouling J. Bioadhesion Biofilm Res.* **2009**, *16* ((2-4)), 301–309.
- (440) Artus, B. G. R. J.; Jung, S.; Zimmermann, J.; Gautschi, H.; Marquardt, K.; Seeger, S. Silicone Nanofilaments and Their Application as Superhydrophobic Coatings. **2006**, 2758–2762. <https://doi.org/10.1002/adma.200502030>.
- (441) Yeh, S. B.; Chen, C. S.; Chen, W. Y.; Huang, C. J. Modification of Silicone Elastomer with Zwitterionic Silane for Durable Antifouling Properties. *Langmuir* **2014**. <https://doi.org/10.1021/la502486e>.
- (442) Sirrine, J. M.; Zlatanovic, A.; Meenakshisundaram, V.; Messman, J. M.; Williams, C. B.; Dvornic, P. R.; Long, T. E. 3D Printing Amorphous Polysiloxane Terpolymers via Vat Photopolymerization. *Macromol. Chem. Phys.* **2019**, *220* (4), 1–9. <https://doi.org/10.1002/macp.201800425>.
- (443) Taki, K.; Watanabe, Y.; Tanabe, T.; Ito, H.; Ohshima, M. Oxygen Concentration and Conversion Distributions in a Layer-by-Layer UV-Cured Film Used as a Simplified Model of a 3D UV Inkjet Printing System. *Chem. Eng. Sci.* **2017**, *158* (October 2016), 569–579. <https://doi.org/10.1016/j.ces.2016.10.050>.
- (444) Fang, N.; Sun, C.; Zhang, X. Diffusion-Limited Photopolymerization in Scanning Micro-Stereolithography. *Appl. Phys. A Mater. Sci. Process.* **2004**, *79* (8), 1839–1842. <https://doi.org/10.1007/s00339-004-2938-x>.
- (445) Liao, Y.; Song, J.; Li, E.; Luo, Y.; Shen, Y.; Chen, D.; Cheng, Y.; Xu, Z.; Sugioka, K.; Midorikawa, K. Rapid Prototyping of Three-Dimensional Microfluidic Mixers in Glass by Femtosecond Laser Direct Writing. *Lab Chip* **2012**, *12* (4), 746–749. <https://doi.org/10.1039/c2lc21015k>.
- (446) Zirath, H.; Rothbauer, M.; Spitz, S.; Bachmann, B.; Jordan, C.; Müller, B.; Ehgartner, J.; Priglinger, E.; Mühleder, S.; Redl, H.; Holnthoner, W.; Harasek, M.; Mayr, T.; Ertl, P. Every Breath You Take: Non-Invasive Real-Time Oxygen Biosensing in Two- and Three-Dimensional Microfluidic Cell Models. *Front. Physiol.* **2018**, *9* (JUL), 1–12. <https://doi.org/10.3389/fphys.2018.00815>.
- (447) Lee, J. N.; Park, C.; Whitesides, G. M. Solvent Compatibility of Poly(Dimethylsiloxane)-Based Microfluidic Devices. *Anal. Chem.* **2003**, *75* (23), 6544–6554. <https://doi.org/10.1021/ac0346712>.
- (448) Toro, C.; Thibert, A.; De Boni, L.; Masunov, A. E.; Hernández, F. E. Fluorescence Emission of Disperse Red 1 in Solution at Room Temperature. *J. Phys. Chem. B* **2008**, *112* (3), 929–937. <https://doi.org/10.1021/jp076026v>.



- (449) Mandon, C. A.; Blum, L. J.; Marquette, C. A. Adding Biomolecular Recognition Capability to 3D Printed Objects. *Anal. Chem.* **2016**, *88* (21), 10767–10772. <https://doi.org/10.1021/acs.analchem.6b03426>.
- (450) Santos, M. R. E.; Fonseca, A. C.; Mendonça, P. V.; Branco, R.; Serra, A. C.; Morais, P. V.; Coelho, J. F. J. Recent Developments in Antimicrobial Polymers: A Review. *Materials (Basel)*. **2016**, *9* (7). <https://doi.org/10.3390/MA9070599>.
- (451) Sugiura, S.; Edahiro, J. ichi; Sumaru, K.; Kanamori, T. Surface Modification of Polydimethylsiloxane with Photo-Grafted Poly(Ethylene Glycol) for Micropatterned Protein Adsorption and Cell Adhesion. *Colloids Surfaces B Biointerfaces* **2008**, *63* (2), 301–305. <https://doi.org/10.1016/j.colsurfb.2007.12.013>.
- (452) Zhang, Z.; Feng, X.; Xu, F.; Liu, X.; Liu, B. F. “Click” Chemistry-Based Surface Modification of Poly(Dimethylsiloxane) for Protein Separation in a Microfluidic Chip. *Electrophoresis* **2010**, *31* (18), 3129–3136. <https://doi.org/10.1002/elps.201000208>.
- (453) Cai, D.; Neyer, A.; Kuckuk, R.; Heise, H. M. Raman, Mid-Infrared, near-Infrared and Ultraviolet–Visible Spectroscopy of PDMS Silicone Rubber for Characterization of Polymer Optical Waveguide Materials. *J. Mol. Struct.* **2010**, *976* (1–3), 274–281. <https://doi.org/10.1016/J.MOLSTRUC.2010.03.054>.
- (454) Lee, W.; Lee, T. G.; Koh, W.-G. Grafting of Poly(Acrylic Acid) on the Poly(Ethylene Glycol) Hydrogel Using Surface-Initiated Photopolymerization for Covalent Immobilization of Collagen. *J. Ind. Eng. Chem* **2007**, *13* (7), 1195–1200.
- (455) Akkahat, P.; Mekboonsonglarp, W.; Kiatkamjornwong, S.; Hoven, V. P. Surface-Grafted Poly(Acrylic Acid) Brushes as a Precursor Layer for Biosensing Applications: Effect of Graft Density and Swellability on the Detection Efficiency. *Langmuir* **2012**. <https://doi.org/10.1021/la204542e>.
- (456) Lim, S. L.; Ooi, C. W.; Tan, W. S.; Chan, E. S.; Ho, K. L.; Tey, B. T. Biosensing of Hepatitis B Antigen with Poly(Acrylic Acid) Hydrogel Immobilized with Antigens and Antibodies. *Sensors Actuators, B Chem.* **2017**. <https://doi.org/10.1016/j.snb.2017.06.003>.
- (457) Sun, H.; Wang, H.; Bai, W.; Bao, L.; Lin, J.; Li, Y. Sensitive Electrogenerated Chemiluminescence Biosensing Method for the Determination of DNA Hydroxymethylation Based on Ru(Bpy)<sub>3</sub><sup>2+</sup>-Doped Silica Nanoparticles Labeling and MoS<sub>2</sub>-Poly(Acrylic Acid) Nanosheets Modified Electrode. *Talanta* **2019**, *191* (May 2018), 350–356. <https://doi.org/10.1016/j.talanta.2018.08.070>.
- (458) Oh, J.; Kim, S. J.; Oh, M. K.; Khan, A. Antibacterial Properties of Main-Chain Cationic Polymers Prepared through Amine-Epoxy “Click” Polymerization. *RSC Adv.* **2020**, *10* (45), 26752–26755. <https://doi.org/10.1039/d0ra04625f>.
- (459) Malekshahinezhad, K.; Ahmadi-khaneghah, A.; Behniafar, H. Amine-

- Functionalized TiO<sub>2</sub> Nanoparticles Covalently Loaded into Epoxy Networks via Thermal and Microwave Curing Processes. *Macromol. Res.* **2020**, *28* (6), 567–572. <https://doi.org/10.1007/s13233-020-8067-3>.
- (460) Hubbard, R. L.; Tyler, D. R.; Thompson, B. An Empirically Derived Model for Further Increasing Microwave Curing Rates of Epoxy-Amine Polymerizations. *J. Appl. Polym. Sci.* **2020**, *138* (1), 1–7. <https://doi.org/10.1002/app.49635>.
- (461) Johnston, K.; Pavuluri, S. K.; Leonard, M. T.; Desmulliez, M. P. Y.; Arrighi, V. Microwave and Thermal Curing of an Epoxy Resin for Microelectronic Applications. *Thermochim. Acta* **2015**, *616*, 100–109. <https://doi.org/10.1016/j.tca.2015.08.010>.
- (462) Hou, A.; Wang, X.; Wu, L. Effect of Microwave Irradiation on the Physical Properties and Morphological Structures of Cotton Cellulose. *Carbohydr. Polym.* **2008**. <https://doi.org/10.1016/j.carbpol.2008.05.011>.
- (463) Das, S.; Mukhopadhyay, A. K.; Datta, S.; Basu, D. Prospects of Microwave Processing: An Overview. *Bulletin of Materials Science*. 2009, pp 1–13.
- (464) Escalante, J.; Carrillo-Morales, M.; Linzaga, I. Michael Additions of Amines to Methyl Acrylates Promoted by Microwave Irradiation. *Molecules* **2008**, *13* (2), 340–347.
- (465) Mirabedini, S. M.; Rahimi, H.; Hamedifar, S.; Mohsen Mohseni, S. Microwave Irradiation of Polypropylene Surface: A Study on Wettability and Adhesion. *Int. J. Adhes. Adhes.* **2004**, *24* (2), 163–170. <https://doi.org/10.1016/j.ijadhadh.2003.09.004>.
- (466) Mohandas, H.; Sivakumar, G.; Kasi, P.; Jaganathan, S. K.; Supriyanto, E. Microwave-Assisted Surface Modification of Metallocene Polyethylene for Improving Blood Compatibility. *Biomed Res. Int.* **2013**, *2013*. <https://doi.org/10.1155/2013/253473>.
- (467) Mallakpour, S.; Zadehnazari, A. A Facile, Efficient, and Rapid Covalent Functionalization of Multi-Walled Carbon Nanotubes with Natural Amino Acids under Microwave Irradiation. *Prog. Org. Coatings* **2014**, *77* (3), 679–684. <https://doi.org/10.1016/j.porgcoat.2013.12.003>.
- (468) Wang, J.; Li, J.; Guo, G.; Wang, Q.; Tang, J.; Zhao, Y.; Qin, H.; Wahafu, T.; Shen, H.; Liu, X.; Zhang, X. Silver-Nanoparticles-Modified Biomaterial Surface Resistant to Staphylococcus: New Insight into the Antimicrobial Action of Silver. *Sci. Rep.* **2016**. <https://doi.org/10.1038/srep32699>.
- (469) Li, B.; Webster, T. J. Bacteria Antibiotic Resistance: New Challenges and Opportunities for Implant-Associated Orthopedic Infections. *J. Orthop. Res.* **2018**, *36* (1), 22–32. <https://doi.org/10.1002/jor.23656>.
- (470) Ondusko, D. S.; Nolt, D. Staphylococcus Aureus. *Pediatr. Rev.* **2018**. <https://doi.org/10.1542/pir.2017-0224>.
- (471) Román, F.; Colomer, P.; Calventus, Y.; Hutchinson, J. M. Study of Hyperbranched Poly(Ethyleneimine) Polymers of Different Molecular Weight and Their Interaction with Epoxy Resin. *Materials (Basel)*. **2018**, *11* (3), 1–26. <https://doi.org/10.3390/ma11030410>.

- (472) De Ruiter, B.; El-Ghayoury, A.; Hofmeier, H.; Schubert, U. S.; Manea, M. Two-Step Curing Processes for Coating Application. *Prog. Org. Coatings* **2006**, *55* (2), 154–159. <https://doi.org/10.1016/j.porgcoat.2005.09.011>.
- (473) Fu, Y. R.; Ma, Y. Z.; Di, G. Bin; Guo, S. Q.; Jin, H. P. Applications of FTIR on Epoxy Resins – Identification, Monitoring the Curing Process, Phase Separation and Water Uptake. *Oilf. Chem.* **1999**, *16* (3), 208.
- (474) Chiappone, A.; Jeremias, S.; Bongiovanni, R.; Schönhoff, M. NMR Study of Photo-Crosslinked Solid Polymer Electrolytes: The Influence of Monofunctional Oligoethers. *J. Polym. Sci. Part B Polym. Phys.* **2013**, *51* (21), 1571–1580. <https://doi.org/10.1002/polb.23371>.
- (475) Lu, H.; Stansbury, J. W.; Nie, J.; Berchtold, K. A.; Bowman, C. N. Development of Highly Reactive Mono-(Meth)Acrylates as Reactive Diluents for Dimethacrylate-Based Dental Resin Systems. *Biomaterials* **2005**, *26* (12), 1329–1336. <https://doi.org/10.1016/j.biomaterials.2004.04.041>.
- (476) Kalita, P.; Pegu, C. D.; Dutta, P.; Baruah, P. K. Room Temperature Solvent Free Aza-Michael Reactions over Nano-Cage Mesoporous Materials. *J. Mol. Catal. A Chem.* **2014**, *394*, 145–150. <https://doi.org/10.1016/j.molcata.2014.06.031>.
- (477) Muzammil, E. M.; Khan, A.; Stuparu, M. C. Post-Polymerization Modification Reactions of Poly(Glycidyl Methacrylate)S. *RSC Adv.* **2017**, *7* (88), 55874–55884. <https://doi.org/10.1039/c7ra11093f>.
- (478) Lin, Z.; Ma, Y.; Zhao, C.; Chen, R.; Zhu, X.; Zhang, L.; Yan, X.; Yang, W. An Extremely Simple Method for Fabricating 3D Protein Microarrays with an Anti-Fouling Background and High Protein Capacity. *Lab Chip* **2014**, *14* (14), 2505–2514. <https://doi.org/10.1039/c4lc00223g>.
- (479) Allmér, K.; Hult, A.; Rånby, B. Surface Modification of Polymers. II. Grafting with Glycidyl Acrylates and the Reactions of the Grafted Surfaces with Amines. *J. Polym. Sci. Part A Polym. Chem.* **1989**. <https://doi.org/10.1002/pola.1989.080270516>.
- (480) Denq, B.-L.; Hu, Y.-S.; Chen, L.-W.; Chiu, W.-Y.; Wu, T.-R. The Curing Reaction and Physical Properties of DGEBA/DETA Epoxy Resin Blended with Propyl Ester Phosphazene. *J. Appl. Polym. Sci.* **1999**, *74* (1), 229–237. [https://doi.org/doi:10.1002/\(SICI\)1097-4628\(19991003\)74:1<229::AID-APP28>3.0.CO;2-C](https://doi.org/doi:10.1002/(SICI)1097-4628(19991003)74:1<229::AID-APP28>3.0.CO;2-C).
- (481) Liu, C.; Bai, R.; Hong, L. Diethylenetriamine-Grafted Poly(Glycidyl Methacrylate) Adsorbent for Effective Copper Ion Adsorption. *J. Colloid Interface Sci.* **2006**, *303* (1), 99–108. <https://doi.org/10.1016/j.jcis.2006.07.057>.
- (482) Santiago, D.; Fernández-Francos, X.; Ramis, X.; Salla, J. M.; Sangermano, M. Comparative Curing Kinetics and Thermal-Mechanical Properties of DGEBA Thermosets Cured with a Hyperbranched Poly(Ethyleneimine) and an Aliphatic Triamine. *Thermochim. Acta* **2011**, *526* (1–2), 9–21. <https://doi.org/10.1016/j.tca.2011.08.016>.

- (483) Shen, Z.; Chen, Y.; Frey, H.; Stiriba, S. E. Complex of Hyperbranched Polyethylenimine with Cuprous Halide as Recoverable Homogeneous Catalyst for the Atom Transfer Radical Polymerization of Methyl Methacrylate. *Macromolecules* **2006**.  
<https://doi.org/10.1021/ma052418t>.
- (484) Shani, S.; Friedman, M.; Steinberg, D. Relation between Surface Activity and Antibacterial Activity of Amine-Fluorides. *Int. J. Pharm.* **1996**.  
[https://doi.org/10.1016/0378-5173\(95\)04299-7](https://doi.org/10.1016/0378-5173(95)04299-7).
- (485) Gibney, K. A.; Sovadinova, I.; Lopez, A. I.; Urban, M.; Ridgway, Z.; Caputo, G. A.; Kuroda, K. Poly(Ethylene Imine)s as Antimicrobial Agents with Selective Activity. *Macromol. Biosci.* **2012**.  
<https://doi.org/10.1002/mabi.201200052>.
- (486) Meng, X.; Xing, R.; Liu, S.; Yu, H.; Li, K.; Qin, Y.; Li, P. Molecular Weight and PH Effects of Aminoethyl Modified Chitosan on Antibacterial Activity in Vitro. *Int. J. Biol. Macromol.* **2012**.  
<https://doi.org/10.1016/j.ijbiomac.2012.01.018>.
- (487) Kabara, J. J.; Conley, A. J.; Truant, J. P. Relationship of Chemical Structure and Antimicrobial Activity of Alkyl Amides and Amines. *Antimicrob. Agents Chemother.* **1972**. <https://doi.org/10.1128/AAC.2.6.492>.
- (488) Mather, B. D.; Viswanathan, K.; Miller, K. M.; Long, T. E. Michael Addition Reactions in Macromolecular Design for Emerging Technologies. *Prog. Polym. Sci.* **2006**, *31*, 488–531.
- (489) Gao, H.; Elsabahy, M.; Giger, E. V.; Li, D.; Prud'Homme, R. E.; Leroux, J. C. Aminated Linear and Star-Shape Poly(Glycerol Methacrylate)s: Synthesis and Self-Assembling Properties. *Biomacromolecules* **2010**.  
<https://doi.org/10.1021/bm901241k>.
- (490) Escalante, J.; Díaz-Coutiño, F. D. Synthesis of Gamma-Nitro Aliphatic Methyl Esters via Michael Additions Promoted by Microwave Irradiation. *Molecules* **2009**, *14* (4), 1595–1604.  
<https://doi.org/10.3390/molecules14041595>.
- (491) Bilecka, I.; Niederberger, M. Microwave Chemistry for Inorganic Nanomaterials Synthesis. *Nanoscale* **2010**.  
<https://doi.org/10.1039/b9nr00377k>.
- (492) Wang, M.; Xu, J.; Zhou, X.; Tan, T. Preparation and Characterization of Polyethyleneimine Modified Ion-Exchanger Based on Poly(Methacrylate-Co-Ethylene Dimethacrylate) Monolith. *J. Chromatogr. A* **2007**. <https://doi.org/10.1016/j.chroma.2007.02.032>.
- (493) Vukoje, I. D.; Džunuzović, E. S.; Vodnik, V. V.; Dimitrijević, S.; Ahrenkiel, S. P.; Nedeljković, J. M. Synthesis, Characterization, and Antimicrobial Activity of Poly(GMA-Co-EGDMA) Polymer Decorated with Silver Nanoparticles. *J. Mater. Sci.* **2014**, *49* (19), 6838–6844.  
<https://doi.org/10.1007/s10853-014-8386-x>.
- (494) Jaganathan, S. K.; Balaji, A.; Vellayappan, M. V.; Subramanian, A. P.; John, A. A.; Asokan, M. K.; Supriyanto, E. Review: Radiation-Induced Surface Modification of Polymers for Biomaterial Application. *J. Mater. Sci.* **2015**,

- 50 (5), 2007–2018. <https://doi.org/10.1007/s10853-014-8718-x>.
- (495) Wang, S.; Li, R.; Qing, Y.; Wei, Y.; Wang, Q.; Zhang, T.; Sun, C.; Qin, Y.; Li, D.; Yu, J. Antibacterial Activity of Ag-Incorporated Zincosilicate Zeolite Scaffolds Fabricated by Additive Manufacturing. *Inorg. Chem. Commun.* **2019**, *105* (March), 31–35. <https://doi.org/10.1016/j.inoche.2019.04.026>.
- (496) Zuniga, J. M. 3D Printed Antibacterial Prostheses. *Appl. Sci.* **2018**, *8* (9), 1–10. <https://doi.org/10.3390/app8091651>.
- (497) Jain, P.; Pradeep, T. Potential of Silver Nanoparticle-Coated Polyurethane Foam as an Antibacterial Water Filter. *Biotechnol. Bioeng.* **2005**. <https://doi.org/10.1002/bit.20368>.
- (498) Sinde, E.; Carballo, J. Attachment of Salmonella Spp. and Listeria Monocytogenes to Stainless Steel, Rubber and Polytetrafluorehtylene: The Influence of Free Energy and the Effect of Commercial Sanitizers. *Food Microbiol.* **2000**. <https://doi.org/10.1006/fmic.2000.0339>.
- (499) Liao, C.; Li, Y.; Tjong, S. C. Bactericidal and Cytotoxic Properties of Silver Nanoparticles. *Int. J. Mol. Sci.* **2019**, *20* (2). <https://doi.org/10.3390/ijms20020449>.
- (500) Capita, R.; Alonso-Calleja, C. Antibiotic-Resistant Bacteria: A Challenge for the Food Industry. *Crit. Rev. Food Sci. Nutr.* **2013**. <https://doi.org/10.1080/10408398.2010.519837>.
- (501) Shi, X.; Zhu, X. Biofilm Formation and Food Safety in Food Industries. *Trends Food Sci. Technol.* **2009**. <https://doi.org/10.1016/j.tifs.2009.01.054>.
- (502) Endo, Y.; Tani, T.; Kodama, M. Antimicrobial Activity of Tertiary Amine Covalently Bonded to a Polystyrene Fiber. *Appl. Environ. Microbiol.* **1987**. <https://doi.org/10.1128/aem.53.9.2050-2055.1987>.
- (503) Qiu, Y.; Chan, S. T.; Lin, L.; Shek, T. L.; Tsang, T. F.; Barua, N.; Zhang, Y.; Ip, M.; Chan, P. K. sheung; Blanchard, N.; Hanquet, G.; Zuo, Z.; Yang, X.; Ma, C. Design, Synthesis and Biological Evaluation of Antimicrobial Diarylimine and –Amine Compounds Targeting the Interaction between the Bacterial NusB and NusE Proteins. *Eur. J. Med. Chem.* **2019**. <https://doi.org/10.1016/j.ejmech.2019.05.090>.
- (504) Alan, J.; Meyers, P. E. T.; Data, R. U. S. A. Method of Inhibiting the Growth of Bacteria and Fungi Using Organosilicon Amines, 1975.
- (505) Boulares-Pender, A.; Prager-Duschke, A.; Eisner, C.; Buchmeiser, M. R. Surface-Functionalization of Plasma-Treated Polystyrene by Hyperbranched Polymers and Use in Biological Applications. *J. Appl. Polym. Sci.* **2009**. <https://doi.org/10.1002/app.29849>.
- (506) Paul, D. R.; Robeson, L. M. Polymer Nanotechnology: Nanocomposites. *Polymer (Guildf)*. **2008**, *49* (15), 3187–3204. <https://doi.org/10.1016/j.polymer.2008.04.017>.
- (507) Chattopadhyay, A. Chemistry and Biology of N-(7-Nitrobenz-2-Oxa-1,3-Diazol-4-Yl)-Labeled Lipids: Fluorescent Probes of Biological and Model

- Membranes. *Chem. Phys. Lipids* **1990**, *53* (1), 1–15. [https://doi.org/10.1016/0009-3084\(90\)90128-E](https://doi.org/10.1016/0009-3084(90)90128-E).
- (508) Mazères, S.; Schram, V.; Tocanne, J. F.; Lopez, A. 7-Nitrobenz-2-Oxa-1,3-Diazole-4-Yl-Labeled Phospholipids in Lipid Membranes: Differences in Fluorescence Behavior. *Biophys. J.* **1996**, *71* (1), 327–335. [https://doi.org/10.1016/S0006-3495\(96\)79228-7](https://doi.org/10.1016/S0006-3495(96)79228-7).
- (509) Watanabe, Y.; Imai, K. Sensitive Detection of Amino Acids in Human Serum and Dried Blood Disc of 3 Mm Diameter for Diagnosis of Inborn Errors of Metabolism. *J. Chromatogr. B Biomed. Sci. Appl.* **1984**. [https://doi.org/10.1016/0378-4347\(84\)80035-3](https://doi.org/10.1016/0378-4347(84)80035-3).
- (510) Sasaki, H.; White, S. H. A Novel Fluorescent Probe That Senses the Physical State of Lipid Bilayers. *Biophys. J.* **2009**. <https://doi.org/10.1016/j.bpj.2009.03.003>.
- (511) Sakanyan, V.; Hulin, P.; Alves De Sousa, R.; Silva, V. A. O.; Hambarzumyan, A.; Nedellec, S.; Tomasoni, C.; Logé, C.; Pineau, C.; Roussakis, C.; Fleury, F.; Artaud, I. Activation of EGFR by Small Compounds through Coupling the Generation of Hydrogen Peroxide to Stable Dimerization of Cu/Zn SOD1. *Sci. Rep.* **2016**, *6* (February). <https://doi.org/10.1038/srep21088>.
- (512) Shi, T. H.; Huang, Y. L.; Chen, C. C.; Pi, W. C.; Hsu, Y. L.; Lo, L. C.; Chen, W. Y.; Fu, S. L.; Lin, C. H. Andrographolide and Its Fluorescent Derivative Inhibit the Main Proteases of 2019-NCoV and SARS-CoV through Covalent Linkage. *Biochem. Biophys. Res. Commun.* **2020**, No. xxxx. <https://doi.org/10.1016/j.bbrc.2020.08.086>.
- (513) Ghandehari, M. Optical Waveguides. In *Smart Sensors, Measurement and Instrumentation*; 2018. [https://doi.org/10.1007/978-3-319-70715-0\\_2](https://doi.org/10.1007/978-3-319-70715-0_2).
- (514) Kikuchi, K. Fundamentals of Coherent Optical Fiber Communications. *Journal of Lightwave Technology.* 2016. <https://doi.org/10.1109/JLT.2015.2463719>.
- (515) Benito-Peña, E.; Valdés, M. G.; Glahn-Martínez, B.; Moreno-Bondi, M. C. Fluorescence Based Fiber Optic and Planar Waveguide Biosensors. A Review. *Anal. Chim. Acta* **2016**, *943*, 17–40. <https://doi.org/10.1016/j.aca.2016.08.049>.
- (516) Liu, L.; Zhou, X.; Wilkinson, J. S.; Hua, P.; Song, B.; Shi, H. Integrated Optical Waveguide-Based Fluorescent Immunosensor for Fast and Sensitive Detection of Microcystin-LR in Lakes: Optimization and Analysis. *Sci. Rep.* **2017**, *7* (1), 1–9. <https://doi.org/10.1038/s41598-017-03939-8>.
- (517) Fan, X.; White, I. M.; Shopova, S. I.; Zhu, H.; Suter, J. D.; Sun, Y. Sensitive Optical Biosensors for Unlabeled Targets: A Review. *Analytica Chimica Acta.* 2008. <https://doi.org/10.1016/j.aca.2008.05.022>.
- (518) Cooper, M. A. Optical Biosensors in Drug Discovery. *Nature Reviews Drug Discovery.* 2002. <https://doi.org/10.1038/nrd838>.

- (519) Leung, A.; Shankar, P. M.; Mutharasan, R. A Review of Fiber-Optic Biosensors. *Sensors and Actuators, B: Chemical*. 2007. <https://doi.org/10.1016/j.snb.2007.03.010>.
- (520) Taitt, C. R.; Anderson, G. P.; Ligler, F. S. Evanescent Wave Fluorescence Biosensors: Advances of the Last Decade. *Biosens. Bioelectron.* **2016**, *76*, 103–112. <https://doi.org/10.1016/j.bios.2015.07.040>.
- (521) Oh, M. C.; Chu, W. S.; Shin, J. S.; Kim, J. W.; Kim, K. J.; Seo, J. K.; Lee, H. K.; Noh, Y. O.; Lee, H. J. Polymeric Optical Waveguide Devices Exploiting Special Properties of Polymer Materials. *Opt. Commun.* **2016**, *362*, 3–12. <https://doi.org/10.1016/j.optcom.2015.07.079>.
- (522) Ma, H.; Jen, A. K. Y.; Dalton, L. R. Polymer-Based Optical Waveguides: Materials, Processing, and Devices. *Adv. Mater.* **2002**, *14* (19), 1339–1365. [https://doi.org/10.1002/1521-4095\(20021002\)14:19<1339::AID-ADMA1339>3.0.CO;2-O](https://doi.org/10.1002/1521-4095(20021002)14:19<1339::AID-ADMA1339>3.0.CO;2-O).
- (523) Oh, M.; Chu, W.; Shin, J.; Kim, J.; Kim, K. Polymeric Optical Waveguide Devices Exploiting Special Properties of Polymer Materials. *Opt. Commun.* **2016**, *362*, 3–12. <https://doi.org/10.1016/j.optcom.2015.07.079>.
- (524) Wolfer, T.; Bollgruen, P.; Mager, D.; Overmeyer, L.; Korvink, J. G. Printing and Preparation of Integrated Optical Waveguides for Optronics Sensor Networks. *Mechatronics* **2016**, *34*, 119–127. <https://doi.org/10.1016/j.mechatronics.2015.05.004>.
- (525) Giacon, V. M.; Da Silva Padilha, G.; Bartoli, J. R. Fabrication and Characterization of Polymeric Optical by Plasmafluorination Process. *Optik (Stuttg.)*. **2015**, *126* (1), 74–76. <https://doi.org/10.1016/j.ijleo.2014.08.152>.
- (526) Bollgruen, P.; Gleissner, U.; Wolfer, T.; Megnin, C.; Mager, D.; Overmeyer, L.; Korvink, J. G.; Hanemann, T. Ink-Jet Printed Fluorescent Materials as Light Sources for Planar Optical Waveguides on Polymer Foils. *Opt. Eng.* **2016**, *55* (10), 107107. <https://doi.org/10.1117/1.oe.55.10.107107>.
- (527) Bollgruen, P.; Wolfer, T.; Gleissner, U.; Mager, D.; Megnin, C.; Overmeyer, L.; Hanemann, T.; Korvink, J. G. Ink-Jet Printed Optical Waveguides. *Flex. Print. Electron.* **2017**, *2* (4), 045003. <https://doi.org/https://doi.org/10.1088/2058-8585/aa8ed6>  
Manuscript.
- (528) Nseowo Udofia, E.; Zhou, W. 3D Printed Optics with a Soft and Stretchable Optical Material. *Addit. Manuf.* **2020**, *31* (July 2019). <https://doi.org/10.1016/j.addma.2019.100912>.
- (529) Lorang, D. J.; Tanaka, D.; Spadaccini, C. M.; Rose, K. A.; Cherepy, N. J.; Lewis, J. A. Photocurable Liquid Core-Fugitive Shell Printing of Optical Waveguides. *Adv. Mater.* **2011**, *23* (43), 5055–5058. <https://doi.org/10.1002/adma.201102411>.
- (530) Swargiary, K.; Jarutatsanangkoon, P.; Suwanich, P.; Jolivot, R.; Mohammed, W. S. Single-Step 3D-Printed Integrated Optical System and Its Implementation for a Sensing Application Using Digital Light

- Processing Technology. *Appl. Opt.* **2020**, *59* (1), 122. <https://doi.org/10.1364/ao.59.000122>.
- (531) Sharma, K.; Bora, T.; Mohammed, W. S. Effect of Solvent Absorption on the Optical Properties of 3D Printed Methacrylate Waveguide. *Opt. Laser Technol.* **2021**, *134* (August 2020), 106573. <https://doi.org/10.1016/j.optlastec.2020.106573>.
- (532) Alonso, A.; Catalina, F.; Salvador, E. F.; Peinado, C. Synthesis of Amphiphilic Random Copolymers and Fluorescence Study of Their Association Behavior in Water. *Macromol. Chem. Phys.* **2001**, *202* (11), 2293–2299. [https://doi.org/10.1002/1521-3935\(20010701\)202:11<2293::AID-MACP2293>3.0.CO;2-W](https://doi.org/10.1002/1521-3935(20010701)202:11<2293::AID-MACP2293>3.0.CO;2-W).
- (533) Peinado, C.; Salvador, E. F.; Baselga, J.; Catalina, F. Fluorescent Probes for Monitoring the UV Curing of Acrylic Adhesives, 1: FTIR and Fluorescence in Real Time. *Macromol. Chem. Phys.* **2001**. [https://doi.org/10.1002/1521-3935\(20010601\)202:9<1924::AID-MACP1924>3.0.CO;2-C](https://doi.org/10.1002/1521-3935(20010601)202:9<1924::AID-MACP1924>3.0.CO;2-C).
- (534) Fery-Forgues, S.; Fayet, J. P.; Lopez, A. Drastic Changes in the Fluorescence Properties of NBD Probes with the Polarity of the Medium: Involvement of a TICT State? *J. Photochem. Photobiol. A Chem.* **1993**. [https://doi.org/10.1016/1010-6030\(93\)85048-D](https://doi.org/10.1016/1010-6030(93)85048-D).
- (535) Marini, A.; Muñoz-Losa, A.; Biancardi, A.; Mennucci, B. What Is Solvatochromism? *J. Phys. Chem. B* **2010**, *114* (51), 17128–17135. <https://doi.org/10.1021/jp1097487>.
- (536) Cerón-Carrasco, J. P.; Jacquemin, D.; Laurence, C.; Planchat, A.; Reichardt, C.; Sraïdi, K. Solvent Polarity Scales: Determination of New ET(30) Values for 84 Organic Solvents. *J. Phys. Org. Chem.* **2014**. <https://doi.org/10.1002/poc.3293>.
- (537) Chen, J. Y.; Hwang, J. V.; Ao-Ieong, W. S.; Lin, Y. C.; Hsieh, Y. K.; Cheng, Y. L.; Wang, J. Study of Physical and Degradation Properties of 3D-Printed Biodegradable, Photocurable Copolymers, PGSA-Co-PEGDA and PGSA-Co-PCLDA. *Polymers (Basel)*. **2018**, *10* (11). <https://doi.org/10.3390/polym10111263>.
- (538) Hong, Y.; Lam, J. W. Y.; Tang, B. Z. Aggregation-Induced Emission. *Chem. Soc. Rev.* **2011**. <https://doi.org/10.1039/c1cs15113d>.
- (539) Muñoz, J.; Pumera, M. 3D-Printed Biosensors for Electrochemical and Optical Applications. *TrAC - Trends Anal. Chem.* **2020**, *128*. <https://doi.org/10.1016/j.trac.2020.115933>.
- (540) Lagoy, R. C.; Albrecht, D. R. Automated Fluid Delivery from Multiwell Plates to Microfluidic Devices for High-Throughput Experiments and Microscopy. *Sci. Rep.* **2018**, *8* (1), 1–10. <https://doi.org/10.1038/s41598-018-24504-x>.
- (541) Wei, X.; Do, V. Q.; Pham, S. V.; Martins, D.; Song, Y. A. A Multiwell-Based Detection Platform with Integrated PDMS Concentrators for Rapid Multiplexed Enzymatic Assays. *Sci. Rep.* **2018**, *8* (1), 1–11. <https://doi.org/10.1038/s41598-018-29065-7>.



- (542) Virumbrales-Muñoz, M.; Ayuso, J. M.; Olave, M.; Monge, R.; De Miguel, D.; Martínez-Lostao, L.; Le Gac, S.; Doblare, M.; Ochoa, I.; Fernandez, L. J. Multiwell Capillarity-Based Microfluidic Device for the Study of 3D Tumour Tissue-2D Endothelium Interactions and Drug Screening in Co-Culture Models. *Sci. Rep.* **2017**, *7* (1), 1–15. <https://doi.org/10.1038/s41598-017-12049-4>.
- (543) Bale, S. S.; Borenstein, J. T. Microfluidic Cell Culture Platforms to Capture Hepatic Physiology and Complex Cellular Interactions. *Drug Metab. Dispos.* **2018**, *46* (11), 1638–1646. <https://doi.org/10.1124/dmd.118.083055>.
- (544) Gheibi, P.; Son, K. J.; Stybayeva, G.; Revzin, A. Harnessing Endogenous Signals from Hepatocytes Using a Low Volume Multi-Well Plate. *Integr. Biol. (United Kingdom)* **2017**, *9* (5), 427–435. <https://doi.org/10.1039/c7ib00010c>.
- (545) Veliz, D. S.; Zhang, H.; Toivakka, M. Stacking up: A New Approach for Cell Culture Studies. *Biomater. Sci.* **2019**, *7* (8), 3249–3257. <https://doi.org/10.1039/c8bm01694a>.
- (546) Brennan, M. D.; Rexius-Hall, M. L.; Eddington, D. T. A 3D-Printed Oxygen Control Insert for a 24-Well Plate. *PLoS One* **2015**, *10* (9), 1–9. <https://doi.org/10.1371/journal.pone.0137631>.
- (547) Li, H.; Garner, T.; Diaz, F.; Wong, P. K. A Multiwell Microfluidic Device for Analyzing and Screening Nonhormonal Contraceptive Agents. *Small* **2019**, *15* (28), 1–7. <https://doi.org/10.1002/sml.201901910>.
- (548) Wang, H.; Khodaparast, S.; Carroll, J.; Kelly, C.; Robles, E. S. J.; Cabral, J. T. A Microfluidic-Multiwell Platform for Rapid Phase Mapping of Surfactant Solutions. *Rev. Sci. Instrum.* **2020**, *91* (4). <https://doi.org/10.1063/1.5144770>.

# Appendix A

## List of figures

Figure 1-1. <b>Illustration of the seven (7) steps involved in a typical 3D printing process.</b> .....	3
Figure 1-2. <b>Example of how 3D printing can be used to produce customized and complex-shaped structures difficult or laborious to create with other conventional manufacturing methods from a simple digital CAD model.</b> .....	5
Figure 1-3. <b>Examples of 3D printing in the biomedical sector.</b> (a) Representation of the production flow of metallic parts optimized for weight reduction of up to 63%. <sup>30</sup> (b) 3D printed cabin bracket using a titanium alloy for the Airbus A350 XWB. <sup>29</sup> (c) bioimplants and prosthesis obtained through 3D printing. <sup>39-44</sup> (d) 640 m <sup>2</sup> building produced from <i>Apis Cor</i> company. <sup>45</sup> (e) 3D printed structure made of chocolate. <sup>46</sup> (f) flow plan for developing specific food items with the required nutrient features. <sup>47</sup> .....	7
Figure 1-4. <b>The seven Additive Manufacturing classification and its mains advantages and drawbacks.</b> <sup>56,65</sup> .....	10
Figure 1-5. <b>Publications per year using vat polymerization or similar terms (as detailed in the legend inset) from 1990 to 2020.</b> (a) N° publications per year in which the keywords appear at least once during the article's full text. (b) N° of	

publications per year in which the keywords appear in the scientific article's title or the abstract. Data obtained from the dimensions.ai database.....	11
Figure 1-6. <b>Principle of polymer formation.</b> (a) Common macromolecular polymer structures. (b) Illustration of the free-radical-based photocuring process. The initial system is a mixture of monomers/oligomers and a photoinitiator, in which under light exposure, the photoinitiator is decomposed, generating reactive species. In the beginning, these reactive species promote the interaction between the prepolymer chains. At last, the interaction between chains continues until the formation of the final polymer is completed.....	13
Figure 1-7. <b>Schematic representation of the different steps of the chain-growth polymerization reaction.</b> .....	15
Figure 1-8. <b>Examples of most common free-radical (meth)acrylate-based monomers and oligomers used for vat polymerization 3D printing</b> .....	16
Figure 1-9. <b>Examples of some of the compounds used as photoinitiators in photopolymerization processes.</b> 2,2-dimethoxy-2-phenylacetophenone ( <b>HMMP</b> ), phenyl bis (2,4,6-trimethylbenzoyl)-phosphine oxide ( <b>BAPO</b> ), 7,8-Dimethyl-10-ribitylisoalloxazine ( <b>Riboflavin</b> ), 1,4-Bis(pentylamino)anthracene-9,10-dione ( <b>solvent blue 14</b> ), and (3S,4S, 21R)-9-ethenyl-14-ethyl-21-(methoxycarbonyl)-4,8,13,18-tetramethyl-20-oxo-3-phorbinepropanoic acid ( <b>Pheophorbide-a</b> ).....	19
Figure 1-10. <b>Example of homolytic <math>\alpha</math>-bond cleavage of phenyl bis (2,4,6 trimethyl benzoyl)-phosphine oxide.</b> <sup>135</sup> .....	19
Figure 1-11. <b>Representation of the most representative Vat 3D printing and 3D printing techniques by photopolymerization.</b> (a) Stereolithography (SL). (b) Digital light processing 3D printing (DLP). (c) Typical two-photon polymerization setup. <sup>182</sup> (d) Computed axial lithography (CAL). .....	25
Figure 2-1. <b>Examples of medical applications of polymeric 3D printing.</b> (a) Alignment of the patient-specific teeth followed by the incisor teeth' processing in a mesh mixer software for obtaining the biocompatible PLA 3D printed incisor teeth. <sup>40</sup> (b) Above: the 3D digital model of a patient orbit, showing the procedure followed: I) analysis and II) elimination/ patterning of the pseudo-hole, III) locating the fracture zone, IV) the implant position is colored in magenta; below is shown the 3D printed pieces obtained from the CAD model. The parts were produced from polytrimethylene carbonate (PTMC) methacrylate with various nanohydroxyapatite (nHAp) amounts into the resin. <sup>25</sup> (c) Interaction with the 3D printed models providing an immediate appreciation of the patients' anatomical situation, informing planning and subsequent surgery. <sup>44</sup> .....	33
Figure 2-2. <b>Representation of the (a) soft lithography procedure compared to (b) vat polymerization 3D printing for producing microfluidic devices.</b> .....	36

Figure 2-3. **Photo-mediated surface modifications of polydimethylsiloxane chips.** (a) Contact angle measurements on PEGDA-grafted and pNIPAAm-grafted PDMS surface at 20 °C and 40 °C, the photograph below shows the changes in wettability of the pNIPAAm-grafted PDMS at both temperatures.<sup>105</sup>. (b) Contact angle measurements of the different OSTE PDMS material with different surface wettability after UV-mediated polymerization. (c) UV patterning of the microfluidic chips exploiting the allyl and thiol groups of the microchannel's surface, which is appreciated by the difference in the meniscus behavior when a green-colored liquid is led flow.<sup>112</sup>..... 39

Figure 2-4. **3D printed milli- and microfluidic chips fabricated by Fused Filament Fabrication (FFF)-3D printing methods.** (a) 3D printed chips in PMMA. 1) Microchip cascade for mixing of yellow/blue-dyed water. 2) 3D printed chip with a square channel of 600x600 μm. 3) improved mixer structure of 600x600 μm channel. 4) 3D printed channel produced around a straight channel, using an aqueous fluorescent dye. For the four images, the scale bar is 10 mm.<sup>128</sup> (b) Transparent 3D printed microfluidic chips made of polyurethane (TPU) images showing a) the flexibility, 2) the transparency of the chip, and 3) mIMCD3 cells behavior where a characteristic cobblestone appearance was observed in both control wells, and 3D printed TPU (scale bars = 100 μm).<sup>129</sup>. (c) Microscopic photographs of the laminar fluid flow inside 500x500 μm channel toward a 750 μm x 500 μm channel, where yellow/blue dyed water is passed at 25 μL/min through microfluidic chips fabricated with FDM at 0°, 30°, 60°, and 90° of filament orientation, Eden (Polyjet), and Miicraft+ (DLP-SLA), respectively. Plots of distance vs. mixing ratio demonstrated the diffusion through the laminar flow channel at 25, 50, and 100 μL/min.<sup>137</sup>..... 42

Figure 2-5. **3D printed milli- and microfluidic chips fabricated by Polyjet-3D printing methods.** a) Scanning electron microscope (SEM) images of the 3D printed channels through 1-3) PolyJet printing and 4-6) FDM 3D printing where is depicted the surface roughness features between both techniques.<sup>140</sup> b) Photographs of the 3D printed microfluidic mixers: 1) Caterpillar mixer, 2) enhanced Caterpillar mixer, 3) Tesla-like mixer, and 4) HC mixer. Next to each image is shown the calculated mixing performances (from simulation tests) as a mixer length function.<sup>142</sup> c) 3D printed microfluidic multichannel valves made of 1) a single material and 2) a multi-material.<sup>147</sup> d) 3D printed DNA-inspired fluidic devices that comprise eight fluidic channels (750 μm in diameter) filled with distinct dye-colored solution.<sup>148</sup>. e) Working principle of a finger-powered two-fluid FPA prototype for fluid mixing two distinct dyed-colored solutions.<sup>150</sup>..... 45

Figure 2-6. **3D printed milli- and microfluidic chips fabricated by vat polymerization-3D printing methods.** (a) 3D printed microfluidic with helical microchannel used for separating pathogenic *E. coli* bacteria (linked to magnetic

nanoparticles clusters) taking advantage of the Dean forces within the channel's trapezoidal cross-section.<sup>165</sup> (b) photograph of the microchannel obtained (height of about 18  $\mu\text{m}$ ) from the three (3) wt. % NPS into PEGDA-based resin.<sup>62</sup> (c) photograph showing the effect of the 3D printed particles trappers positioned at different zones of the microchannel: traps positioned 1) in the center of the channels, 2) staggered along the sides of the channel, 3) staggered along the sides, and in the middle of the channel, 4) traps partially formed after 500 ms of light exposure with no bead capture, 5) particle captured in well-formed traps after 750 ms of exposure, 6) overexposed traps after 1000 ms.<sup>166</sup> (d) nonplanar 3D printed flow-focusing device: 1) representation of the microfluidic flow cell chip, 2) CAD image of the flow cell model; 3) photograph of the printed chip using R11 resin, and 4) diameter of the droplet generated depending on the flow rate ratio (FRR) of dispersed and continuous water-oil phases.<sup>167</sup> ..... 49

**Figure 2-7. Examples of 3D printed microfluidic valves and pumps fabricated by vat polymerization-3D printing methods.** (a) Schematic view of the 3D design. 1) Top view and 2) side illustration view of the valve design. The control chamber (in green color) and fluidic chamber (blue color) are voids in the 3D printed device. The control chamber has 2 access ports to enable it to be drained after printing. Pressure can be applied through both ports to actuate the valve, or one channel can be sealed, and pressure applied through the other to actuate the valve. Pressurized membrane (black dotted line) shows valve closure.<sup>172</sup> (b) 3D printed multiplexer devices. 1) schematic view of the multiplexer working principles and CAD design. Next to the design images is displayed the multiplexer's bottom view fabricated according to the CAD design. From 2) to 3) is shown the arbitrary 3-to-2 multiplexing.<sup>173</sup> c) Design of the printed valve. 1) photograph of the single-valve device. Schematics of a valve unit when it is open (2) and closed (3). Micrographs of the valve unit when it is open (4) and closed (5).<sup>175</sup> ..... 51

**Figure 2-8. Examples of 3D printed milli- and microfluidic chips fabricated by vat polymerization-3D printing methods.** (a) 3D printed perfluoropolyether (PFEP) microfluidic chip: 1) front view of the gradient mixing chip (scale bar: 2 mm) with channel 2) 800  $\mu\text{m}$  x 800  $\mu\text{m}$  filled with black ink (scale bar: 500  $\mu\text{m}$ ), 3) isometric view of the gradient mixing chip (scale bar: 2 mm) with channel 4) 600  $\mu\text{m}$  x 600  $\mu\text{m}$  filled with black ink (scale bar: 500  $\mu\text{m}$ ), 5) lateral view of the 800  $\mu\text{m}$  channel width at the inlet and 6) in the middle (scale bar: 250 $\mu\text{m}$ ), 7) lateral view of the 600  $\mu\text{m}$  channel width at the inlet and 8) in the middle (scale bar: 250 $\mu\text{m}$ ).<sup>177</sup> (b) 3D printed microfluidic-enabled hollow microneedle devices: 1) CAD model and representation of the SL-3D printing method, 2) the printed device composed with 3) three microfluidic inlets converging into a 3D spiral mixing chamber and a 4) hollow microneedle array outlet.<sup>178</sup> (c) 3D printed microfluidic: (1) the device with integrated connectors, (2) cross-sectional image of the chips showing the

internal microchannel structure, and (3) micrograph image (scale bar 1 mm) of the device with details of the asymmetric focusing channels.<sup>179</sup> (d) Microfluidic devices obtained using a methacrylate-polydimethylsiloxane oligomer. 1) photograph of a PDMS-based microfluidic device with 500  $\mu\text{m}$  wide channels printed with a commercial 385 nm SL machine. 2) a central stream of yellow dye (9 mL/h) flanked by two streams of blue dye (9 mL/h each) produces a heterogeneous laminar flow (9 mL h<sup>-1</sup>) in the 3D printed PDMS-based microfluidic chip.<sup>180</sup>..... 53

**Figure 3-1. CAD design representation of a multi-material fluidic chip.** The device consists of two wells connected with a millifluidic channel (1 mm diameter). ..... 63

**Figure 3-2. Chemical structures of the chemical reagents used.** (a) polyethylene glycol diacrylate (PEGDA250), (b) 1,6-hexanediol diacrylate (HDDA), (c) bisphenol A ethoxylate diacrylate (BEDA), and (d) phenyl bis(2,4,6-trimethylbenzoyl)phosphine oxide (BAPO)..... 66

**Figure 3-3. Characterization of the six different acrylate resins.** (a) Storage modulus ( $G'$ ) versus irradiation time, where is observed the similarities between reaction times of PEGDA250, BEDA, and HDDA resins with 0.2 or 1 wt.% of BAPO. (b) Zoomed  $G'$  curve once the visible lamp is on. (c) UV-vis spectra collected on 100  $\mu\text{m}$  thick printed disks made of PEGDA250, BEDA, and HDDA resin with 0.2 wt.% (continue lines) and 1 wt.% (dashed line) of BAPO. The curves show a greater shoulder (related to the BAPO photoinitiator) between 350 and 420 nm for samples with the higher (1 wt.%) content of the photoinitiator, indicating more leaching out of the unreacted BAPO. (d) recorded UV-Vis spectrum from the extracting solvent used to calculate the insoluble gel fraction of the 3D printed parts, showing a higher released BAPO photoinitiator..... 72

**Figure 3-4. CAD model and photographs of the printed wells.** (a) Isometric view of the CAD model showing the dimensions of 24- and 96-well-like designs. (b) Photograph of the 3D printed 24-well-like objects from each prepared acrylate-based photopolymer, showing the good transparency of the bottom of the well. (c) Top-view and (d) frontal-view of a 3D printed 24-well-like object (P-0.2) compared to a 24-multiwell plate..... 73

**Figure 3-5. MTT assay results showing the seeded A549 cells onto the three types of printed samples.** The graphs show the optical density (OD) of the cells grown on the printed wells after each of the four different washing protocols: sonication in ethanol, sonication in acetone, incubation in ethanol, and incubation in acetone for samples made from (a) PEGDA250, (b) HDDA, and (c) BEDA photopolymers (containing either 0.2 wt.% and 1 wt.% of the BAPO photoinitiator). The cell viability is measured after 24 and 48 hours. The results were compared to conventional cell culture on PS plate. Error bars mean standard deviation (c)

Photograph of the washed samples where optical and mechanical characteristics of the 3D printed disks made from the six photopolymers and after the four washing protocols are displayed. The photograph shows that PEGDA samples better resisted the washing treatments. ....75

Figure 3-6. **Environmental Scanning Electron Microscope (ESEM) images collected from the 3D printed samples with 0.2 wt.% of BAPO.** The images show the difference between the cultured A549 cells on the different samples: on the BEDA (B-0.2) samples, the cells presented a rounded apotheosis aspect. The cells presented epithelial appearances on the HDDA (H-0.2) and the PEGDA250 (P-0.2) samples. Three different images were recorded for each sample type: samples without cells (as is) and with A549 cells at different degrees of magnification as reported in the images. ....76

Figure 3-7. **UV-Vis spectrum collected from the ethanol used for the overnight washing step of PEGDA250 with 0.2 wt.% of BAPO.** The curve shows no BAPO-related shoulder (the region between 350 and 420 nm) appeared in the analysis. The inset table shows the weight losses of P-0.2 samples after different washing protocols in ethanol and chloroform. ....77

Figure 3-8. **Cell viability and proliferation on the 3D printed wells made from PEGDA 250 with 0.2 wt.% of BAPO.** (a) Phase-contrast and live/dead staining images from the cultured A549 cells on the 3D printed wells after different sterilization methods: autoclave, ethanol, and UV light either with or without water pre-treatment. The scale bar denotes 100  $\mu\text{m}$  for all images. Covered area (%) by the living and dead cells onto the 3D printed wells after the different sterilization types, and either (b) without or with (c) water pre-treatment. The histograms show a better cell proliferation on samples previously treated with water (overnight) and UV-sterilized. ....78

Figure 3-9. Chemical structures of the reagents used. (a) TegoRAD 2800® (TRAD), (b) dispersed red one methacrylate (DR1-MA), and (c) the BAPO derivate photoinitiator (BAPO-Si). ....83

Figure 3-10. **Characterization of TRAD formulation components.** (a) Absorbance spectrum similarities between the BAPO-Si photoinitiator and the BAPO 819 photoinitiator. (b) absorbance spectrum of the DR1-MA showing a great absorption in the region of 405 nm, the printer's light emission. (c) storage ( $G'$ ) and loss ( $G''$ ) moduli curves against visible light times of TRAD resin varying the BAPO-si concentration and (d) moduli crossover ( $G'=G''$ ) of the TRAD resin at different concentrations of BAPO-si. These curves show that 0.6 wt.% of BAPO-si were enough to prepare a TRAD formulation with good reactivity as possible without changing the formulation optical features. (e) normalized ATR-FTIR spectra of the TRAD formulation at different conditions, with (f) the area of interest

zoomed in the region between 1300-1150  $\text{cm}^{-1}$  where is shown the acrylate double bond decrease in the range 1220-1170  $\text{cm}^{-1}$  after visible and UV light irradiation.

..... 88

**Figure 3-11. CAD design illustration and photographs of different 3D printed fluidic chips and samples.** (a) 3D printed microfluidic chip with an s-shaped channel of 800  $\mu\text{m}$  in diameter, where the channel is filled with green colored water. (b) Two 3D printed wells connected by a  $1 \times 1 \text{ mm}^2$  square section channel. (c) trapezoidal 3D printed microfluidic chip with a  $1 \times 1 \text{ mm}^2$  channel square section. (d) photograph of the two-3D printed 96-wells showing the bottom's transparency with 500  $\mu\text{m}$  thickness, (e) a 3D printed strip ( $20 \times 5 \times 1 \text{ mm}^3$ ), showing the material's excellent stretchability when wrapped around a 3 mm diameter cylinder. Photograph (10x) of the smallest microchannel achieved in (f) XY-plane and (g) Z-axis. (h) CAD design (lateral and top views), and a photograph of the 3D printed trapezoidal microfluidic device with a dye liquid passing through its channel ( $1 \times 1 \text{ mm}^2$ )..... 90

**Figure 3-12. Characterization of the 3D printed TRAD-based samples by the FTIR technique.** (a) Acrylate double-bond conversion (%) of the 3D printed samples and after different UV post-curing times (in the air), obtained by following the decrease of the peak at  $1196 \text{ cm}^{-1}$  after the different radiation conditions. (b) Full normalized ATR-FTIR spectra of 3D printed TRAD samples followed by 5 min of UV post-curing treatment compared to the liquid formulation, where the acrylate-related band decreased after the UV post-curing step. (c) Shows the region between  $1800-1100 \text{ cm}^{-1}$ . ..... 92

**Figure 3-13. Solvent compatibility of the 3D printed based samples toward common organic compounds.** (a,b) Swelling percentage (wt.%) versus time (min) curves for 3D printed TRAD samples after immersion in different solvents. (c) Scatter plot of the swelling percentage (wt.%) versus extracted resin percentage (wt.%) for 3D-printed TRAD samples after 24-hours of immersion in different solvents. (d) UV- VIS spectra of the acetone used to extract unreacted material from 3DP TRAD samples, in which after 5 hours of washing in acetone, the analyzed solution did not show any trace of unreacted substance (either photoinitiator or dye)..... 94

**Figure 3-14. Mechanical characterization of the 3D printed TRAD samples.** Stress (MPa) versus elongation at break (%) curves for (a) only 3D printed TRAD samples and (b) TRAD samples after 5 min of UV post-curing treatment. (c) photograph of one of the 3D printed TRAD samples used for the mechanical test (dog-bone with a gauge length of 20 mm). The UTS and young modulus values were higher for UV post-cured samples than just 3D printed samples, while elongation values at break were quite similar. .... 96



Figure 3-15. **3D printed bi-material fluidic chip.** (a) The devices were fabricated from a PEGDA250 formulation containing + 1 wt. % BAPO (the bottom of the chips) and the TRAD formulation with + 0.6 wt. % BAPO-Si + 0.01 wt. % DR1-MA dye (the rest of the chip). (b) Frontal view of the bi-material chip where is observed the distinction between both materials used. (c) top view of the chip showing the good transparency of the bottom of it. The bottom of the chip is 500  $\mu\text{m}$  thick. The device consists of two wells connected by a millifluidic channel of 1x1  $\text{mm}^2$  section. .... 98

Figure 4-1. **Representation of the two functionalization strategies presented in Chapter 4.** Each strategy is based on chemically linking active molecules to the printed structures through a dedicated post-3D printing treatment following: (a) UV-induced approach or (b) microwave-induced approach..... 101

Figure 4-2. **Representation of the surface modification by UV light.** A few drops of the acrylic-based grafting solution are deposited over the sample surface; then, the system is UV irradiated for a certain time. The sample surface remained chemically modified after the UV-induced treatment. .... 105

Figure 4-3. **Surface properties changes of the TRAD samples after the UV-induced grating surface modification.** (a) Contact angle measurements from untreated and UV-treated samples (at different irradiation times) showing a decrease of the contact angle after the UV-grafting surface modification. (b) ATR-FTIR spectra of untreated and UV-treated samples (at different irradiation times) where the presence of linked carboxylic acid groups over the samples can be observed by analyzing the increase in spectra regions of 3500-2500  $\text{cm}^{-1}$  (associated to O-H stretch) and 1760-1690  $\text{cm}^{-1}$  associated to the carbonyl group, confirming the surface modification. (c) Normalized spectra from the TRAD samples after the different UV-induced grafting treatments showing the peak used for normalizing the spectra centered at 790  $\text{cm}^{-1}$  peak that corresponds to the Si-C asymmetrical bending or rocking vibration..... 106

Figure 4-4. **Representation of the UV-induced surface modification of 3D printed TRAD samples.** (a) Representation of the surface modification carried out inside the inner chamber of a 3D printed TRAD samples, where on the right side of the image displays the contact angle decrease after functionalizing step compared to the untreated sample can be observed. (b) CAD designs and a photograph of a 3D printed chip with an internal chamber filled with green colored water is shown. (c) Representation of the UV-induced surface modifications in an S-shaped millifluidic chip. The test showed the channel's selective functionalization by observing, in the same channel, the hydrophobic behavior (part of the channel with no treatment) and the hydrophilic behavior of the treated part of the channel. (d)

CAD designs and a photograph of the S-shaped 3D printed chip filled half with green colored water and a half with silicon oil..... 107

Figure 4-5. **Chemical structures of the chemical reagents used.** (a) polyethylene glycol diacrylate (PEGDA250). (b) glycidyl methacrylate (GMA). (c) phenyl bis(2,4,6-trimethylbenzoyl) phosphine oxide (BAPO). (d) disperse red one methacrylate (DR1-MA). (e) diethylenetriamine (DETA). (f) hyperbranched polyethyleneimine (PEI). ..... 112

Figure 4-6. **Representative chart example of a microwave treatment performed on one of the samples used in this work.** The graph shows the different parameters during the microwave treatment, such as the power (W) and pressure (bar) given from the reactor to the system to reach the desired temperature ( $^{\circ}\text{C}$ ) during a specific time (t). ..... 114

Figure 4-7. **Images of the microwave-induced surface modification of the 3D printed structures made from PEGDA250/GMA resins.** (a) An image that outlines the surface functionalization procedure with microwaves of 3D printed PEGDA250/GMA structures using amine-based solutions. (b) Photo of 3D printed disks (150  $\mu\text{m}$  thick and 9 mm in diameter) obtained from 5:5, 7:3, 9:1, and 10:0 PEGDA250/GMA formulations. (c) A complex-shaped 3D printed structure (10x10x10  $\text{mm}^3$ ) obtained from 7:3 PEGDA250/GMA formulation displaying the good resolution achieved. (d) MW-treated 3D printed samples with the PEI600 solution for 5 minutes where the sample's damage after the treatment is shown. (e) MW-treated samples in the PEI600 solution for 30 seconds showing the sample suffered no damage. All the formulations contained 1 wt.% of BAPO and 0.01 wt.% of DR1-MA dye ..... 118

Figure 4-8. **Characterization of the 3D printed samples by the FTIR spectroscopy technique for determining the available functional groups.** In the graph, the acrylate and epoxy functional groups can be observed at 810  $\text{cm}^{-1}$  and 905  $\text{cm}^{-1}$  respectively. The available functionalities might potentially be used for linking additional molecules (e.g., amines). Normalize FTIR spectra of liquid formulations, and 3D printed samples made of (a) 5:5 PEGDA250/GMA, (b) 7:3 PEGDA250/GMA, (c) 9:1 PEGDA250/GMA, and (d) pristine PEGDA250 mixtures with 1 wt.% of BAPO. The spectra were normalized using the carbonyl ( $\text{C}=\text{O}$ ) signal centered at 1720  $\text{cm}^{-1}$ . ..... 119

Figure 4-9. **Characterization of the 3D printed samples (by the FTIR spectroscopy technique) after functionalization under mechanical stirring and certain temperature conditions.** The FTIR spectra curves show the decreasing of the acrylate and epoxy-related bands at 905  $\text{cm}^{-1}$  and 810  $\text{cm}^{-1}$ , respectively, for the treated samples. The tests were performed on 5:5 PEGDA250/GMA samples using (a) DETA solution, (b) PEI600 solution and (c) PEI10k solution; the tests were run

at 24, 48, and 96 hours at room temperature ( $T = 25^{\circ}\text{C}$ ) under continuous mechanical stirring. Even though the reaction took place in this condition, the reaction times can be lengthy. (d) FTIR results from 5:5 PEGDA250/GMA treated with the PEI10k solution at  $60^{\circ}\text{C}$  under continuous mechanical stirring for 24 and 48 hours, where it can be observed that the conversion of the functional groups might be boosted by increasing the system temperature. .... 121

**Figure 4-10. Characterization of the different 3D printed PEGDA250/GMA samples (by the FTIR spectroscopy technique) after the microwave-induced functionalization.** The tests were performed using the PEI600 solution for 5 minutes on (a) 5:5, (b) 7:3, (c) 9:1, and (d) 10:0 PEGDA250/GMA samples. The FTIR spectra show the decreasing of the acrylate and epoxy-related bands at  $905\text{ cm}^{-1}$  and  $810\text{ cm}^{-1}$ , respectively, after the MW treatment. Besides, the appearance of a new region (between  $3600$  and  $2800\text{ cm}^{-1}$ ) is observed. This new region can be related to the linking of primary and secondary amines, as reported in the literature.<sup>60</sup> ..... 123

**Figure 4-11. Characterization of the different 3D printed PEGDA250/GMA samples (by the FTIR spectroscopy technique) after the microwave-induced functionalization using the three amine-based solutions.** ATR-FTIR spectra of 5:5 PEGDA250/GMA samples after different MW reaction times using (a) the PEI600 solution, (b) the PEI10k solution, and (c) the DETA solution. On the right of each FTIR graph, the curves of the evolution of the normalized absorbance intensity as a function of the MW reaction time is shown for the three amines-based solutions following the infra-red bands related to the amines (at  $3290\text{ cm}^{-1}$  and  $2935\text{ cm}^{-1}$ ), to glycidyl groups (at  $905\text{ cm}^{-1}$ ) and the acrylate double-bond (at  $810\text{ cm}^{-1}$ ) 'calibrated' considering the thermal contribution of the MW radiation. The minimum reaction time can be abstracted from the spectra by analyzing the required time to induce the highest acrylate/epoxy conversion as possible: 30 seconds using DETA and PEI600, and 5 minutes using PEI10k. .... 124

**Figure 4-12. Characterization of the 3D printed samples after MW-treatment without amine molecules presence.** Normalized ATR-FTIR spectra of (a) PEGDA250 and (b) 5:5 PEGDA250/GMA samples after MW treatment in acetonitrile for 30 sec and 15 min compared to untreated samples. After the MW-treatment, the acrylate groups partially react while the epoxy functionality does not. The inset tables show the acrylate double-bond conversion after each MW treatment. .... 126

**Figure 4-13. Characterization by the FTIR spectroscopy technique of the different 3D printed PEGDA250/GMA samples after the microwave-induced functionalization step (at the minimum treatment times) using the three amine-based solutions.** Normalized ATR-FTIR spectra of (a) 5:5, (b) 7:3, (c) 9:1

PEGDA250/GMA, and (d) PEGDA250 samples after the MW treatment using the PEI600 solution, the PEI10k solution, and the DETA solution. Samples with more epoxy content presented the greatest amine-related absorbance intensity; such amine-related region also depends on the type of the amine used, reaching higher intensity values for the biggest hyperbranched amines PEI600 and PEI10k..... 127

**Figure 4-14. Surface properties changes of the untreated and MW-treated 3D printed PEGDA250/GMA samples.** (a) normalized absorbance intensity as a function of the PEGDA250/GMA weight ratios after the different microwave treatments. Filled symbols refer to the 3600-3200  $\text{cm}^{-1}$  region's absorbance, associated with amines' N-H bond stretching. Empty symbols refer to the 3000-2800  $\text{cm}^{-1}$  region's absorbance associated with the C-H bond. The graph displays that samples with a higher content of epoxy reach the greatest amine-related absorbance intensity and that such amine-related region also depends on the type of the amine used, reaching higher intensity values for the biggest hyperbranched amines PEI600 and PEI10k. (b) Histogram showing the static contact angle of untreated and MW-treated samples as a function of the PEGDA250/GMA weight ratios and after the different MW-treatment treatments. The higher the epoxy content is, the higher is the amount of linked amine, and therefore, a lower contact angle presents the sample. The MW treatments were performed following the optimized irradiation times, 30 seconds using PEI600 and DETA solutions, 15 minutes using PEI10k solution, and 15 minutes using acetonitrile uniquely..... 128

**Figure 4-15. Live and dead *Staphylococcus aureus* bacteria over the untreated and MW-treated 3D printed samples.** The images represent the number of live bacteria (green-colored) and dead bacteria (red-colored) onto the sample's surface. (a) Images (20x) of live/dead bacteria after incubation for 48 hours, over PEGDA250, 9:1, and 7:3 PEGDA250/GMA samples before (control samples) and after the different MW-treatment using the DETA, PEI600, and PEI10k solutions. Bacteria surface covered area (%) of live and dead bacteria over the (b) PEGDA250, (c) 9:1, and (d) 7:3 PEGDA250/GMA samples. The images show that the bacteria proliferation mainly depends on the type of amine used; the samples treated with hyperbranched amines (PEI) resulted in more dead bacteria (redder colored), confirming the surface treatment with amines confers antibacterial properties to the printed samples. .... 131

**Figure 4-16. 3D printed of complex-shaped fluidic devices.** (a) CAD design and (b) photograph of a complex-shaped microfluidic chip consisting of a helical-shaped channel of 1x1 mm with two different outputs directed to a small well each. (c) CAD design and (d) photograph of a complex-shaped microfluidic chip consisting of a helical-shaped channel of 1x1 mm. The red-colored appearance was due to the dye used (DR1- MA at 0.01 wt.%), which increased the printing resolution for achieving the desired geometry. .... 133

Figure 5-1. **3D printing of optical waveguides.** Illustration of the 3D printing of optical waveguides using NBD-dye as a functional component of the photocurable formulation. The fabrication process starts from the CAD modeling, passing through the light-based 3D printing step and obtaining the printed structure. .139

Figure 5-2. **Chemical structures of the chemical reagents used.** (a) bisphenol A ethoxylate diacrylate (BEDA) monomer, (b) phenyl bis(2,4,6-trimethylbenzoyl) phosphine oxide (BAPO) photoinitiator. (c) 4-(N-Methyl-N 9-ethanol) amino-7-nitrobenzo-2-oxa-1,3-diazole derivate dye with methacrylate functionality (NBD-MA). ..... 140

Figure 5-3. **Representation of the two laser configurations used to characterize the 3D printed waveguides.** (a) Orthogonal fluorescence setup and (b) Fluorescence setup for the swelled samples..... 144

Figure 5-4. **Characterization of the different BEDA-based photocurable resins showing the effect on the formulation properties by adding the NBD-MA dye into the formulation.** (a) Viscosity values (at 25°C) of the formulations at different NBD-MA concentrations (0.001, 0.005, and 0.01 wt.%) were similar in the shear rate range between 1 and 100 s<sup>-1</sup>. (b) Storage-G' (full symbols) and Loss-G'' (empty symbols) moduli versus irradiation time where is observed similar reaction times (the point where G' crosses G'') for the BEDA-based formulations at different NBD-MA dye concentration. (c) Elastic modulus curves versus temperature for the four BEDA-based formulations obtained from DMA experiments where the differences of the storage modulus (E') in the rubber state (E'<sub>r</sub>) can be observed. This piece of information can be correlated to the polymeric matrix's crosslinking density by the conventional theory of rubber elasticity, which results in a lower crosslinked density for samples with a lower value of E' in the rubbery state. .... 147

Figure 5-5. **Conversion of the acrylate double-bond groups of the BEDA-based formulations by observing the peak reduction at 1635 cm<sup>-1</sup>.** The spectra were collected through the Fourier transformed infrared (FTIR) technique after subjecting to diverse irradiation conditions the four BEDA-based formulations: (a) neat BEDA formulation with not NBDA-MA content and BEDA-based formulations with (b) 0.001 wt.%, (c) 0.005 wt.%, and (d) 0.01 wt.% of NBD-MA concentration. The acrylate groups' peak area was normalized using a constant signal in the spectra corresponding to the aromatic ring stretch centered at 1510 cm<sup>-1</sup>. All formulations contained two (2) wt.% of BAPO as the photoinitiator... 148

Figure 5-6. **Characterization of the BEDA-based photocurable resins through the UV-Vis technique.** The BAPO consumption and the non-degradation of the NBD-MA dye after visible and UV irradiation (for 10 sec and 180 sec, respectively) are shown. (a) UV-Vis spectra collected on 50 μm films made of BEDA-based formulation with not NBD-MA content. (b) UV-Vis spectra collected on 50 μm

films made of BEDA-based formulation with 0.01 wt.% NBD-MA. (c) UV-Vis spectra of NBD-MA dye in acetonitrile before and after UV light irradiation. (d) The polymerized BEDA-based samples were immersed in chloroform for 24 h (for the insoluble fraction experiments). The extracting solvents were analyzed through the UV-VIS test to observe the residuals components and the successful copolymerization of the NBD-MA dye with the polymeric BEDA matrix..... 149

**Figure 5-7. Optical characterization and printing resolution of the 3D printed samples obtained from the different BEDA-based formulations.** (a) the 3D printed structures' fluorescence intensity was measured (in an end-fire configuration), varying the NBD-MA dye concentration; the graph shows a sublinear dependence between the dye concentration and the fluorescence signal intensity of the samples. (b) The transmittance ( $T$ ) of the 3D printed waveguides was measured varying the NBD-MA content, showing a lower waveguide's transmissivity at higher dye content. Green circles represent the experimental data, and green lines represent the average intensity values (red diamonds). (c-e) Photographs of the 3D printed waveguides showing the poorest printing resolution at lower NBD-MA dye concentration. (f) Differences in the printed devices' fluorescence signals when the spectra are collected at the input (blue curve) and the output (red curve) of the waveguides. .... 151

**Figure 5-8. Optical characterization and the smallest printing resolution of complex-shaped 3D printed structures with 0.005 wt.% of NBD-MA dye.** (a) Transmittance measured through one branch of the Y-shaped 3D printed waveguide as a function of the aperture angle  $\alpha$  where is verified that the light is no longer guided at aperture angles above 40 degrees by observing the drops in its transmittance signal. The inset shows a schematic view of the experimental setup and the fluorescence photographs of the waveguides illuminated at one of their end branches. (b) CAD model images and (c) picture of the complex-shaped 3D printed optical waveguides with circular cross-section and different radii (aperture angles). (d) the light transmission ratio of the 3D printed optical waveguides between later arms (TL) and central arm (TC) as a function of the radius of the external circumference. (e) angle and (f) X-Y dimension evaluation of the smallest Y-shaped 3D printed splitters, (g) dimension evaluation of the input arm, and (h) lateral arm. Both objects were produced with the formulation containing 0.05 wt.% of NBD-MA. .... 154

**Figure 5-9. Optical characterization of the 3D printed BEDA-based structures when exposed to different solvent vapors.** (a) Fluorescence spectra of the NBD-MA dye in the liquid BEDA resin (at 0.05 wt.% of concentration) compared to the fluorescence spectra of the NBD-MA dye when the BEDA resin is polymerized, showing the differences in the two spectra due to the NBD moieties' aggregation inside the solid polymeric matrix. (b) Fluorescence spectra of swollen samples in

different solvents, showing a bathochromic shift of the emission band of individual NBD molecules. (c) variation of the fluorescence emission band of swollen 3D printed structures in the different solvents represented as the ratio of the signal intensities ( $I_1/I_2$ ) and the full widths half-maximum height of the signal ( $W_2/W_1$ ). Subscripts 1 and 2 refer to peaks assigned to individual NBD molecules and aggregates, respectively..... 156

**Figure 5-10. 3D printed optical waveguide made from BEDA formulation containing 0.005 wt.% of NBD-dye.** (a) Photograph of the device once is finished the 3D printing step. (b) the optical device while guiding the light upon direct illumination..... 157

## List of tables

Table 1-1. Most common type I and type II free radical photoinitiators for vat polymerization 3D printing.....	20
Table 2-1. Some of the most used materials in 3D printing for biomedical applications.....	32
Table 2-2. Comparison between the three most used polymeric 3D printing technologies (FDM, PolyJet, and Vat polymerization) for the manufacture of microfluidic chips in terms of materials used, energy source required for joining material, benefits, and drawbacks of each technology, small features reached and application in the biomedical field. ....	41
Table 3-1. Composition and nomenclature of the home-made acrylate resins, average viscosity values at 25 ° C, 3D printing settings used for each formulation with a slicing thickness of 50 µm, insoluble gel fraction (%), and acrylate conversion of the 3D printed objects.....	70
Table 3-2. Acrylate conversion (%) for TRAD formulation after visible light irradiation (10 seconds), 3D printing with similar irradiation conditions followed by 5 minutes of UV post-curing irradiation, and some mechanical properties of the 3D printed TRAD samples compared to those values for classical PDMS Sylgard 184 taken from literature. TRAD formulation contained 0.6 wt.% of BAPO-Si and 0.1 wt.% of DR1-MA.....	89
Table 3-3. Swelling percentage (wt.%) of 3D printed TRAD samples after immersion for 24 hours and 1 hour and extracted resin percentage (wt.%) of samples after 24 hours of immersion in different solvents at 25°C. ....	93
Table 4-1. Weight percent (%), molar acrylate/epoxy ratio for each PEGDA250 and GMA formulation, and the 3D printing settings used for each formulation with 50 µm of slicing thickness.....	113
Table 4-2. Acrylate double-bond and epoxy conversions of 3D printed PEGDA250/GMA and pristine PEGDA250 samples before and after microwave-assisted functionalization with DETA solution (30 sec of MW time), PEI600 solution (30 sec of MW time), and PEI10k solution (15 min of MW time). Infrared spectra of the signals of interest for the different PEGDA250 and GMA samples are shown in Figure 4-12. ....	126
Table 4-3. The untreated and MW-treated samples' average contact angle with different weight ratios between PEGDA250 and GMA monomers and after the MW-treatments. The MW treatments were performed following the optimized	



irradiation times, 30 seconds using PEI600 and DETA solutions, 15 minutes using PEI10k solution. The results for 15 minutes of MW treatment using acetonitrile uniquely are shown as well. .... 129

Table 5-1. Viscosity values at 25 °C (average value), acrylate conversion (%) after visible light irradiation for 10 seconds and after UV irradiation for 180 seconds, glass transition temperature  $T_g$  (°C), and gel fraction (%) for Neat BEDA formulation and BEDA-based formulations with NBD-MA concentration of 0.001 wt.%, 0.005 wt.%, and 0.01 wt.%. All formulations contained 2 wt.% of BAPO. Crosslinking densities were calculated from the DMA experiments. .... 146

Table 5-2. Light transmittances of 3D printed Y-splitters made from the BEDA-based formulation with 0.005 wt.% of NBD-MA. The letters a and b refer to two different samples used for the measurements. .... 152

Table 5-3. Fluorescence spectra data for all the solvents used as a polarity test bench for the 3D printed waveguides. Solvent uptake in 5 minutes in 3D printed structures. .... 155

## List of publications and conferences from the author

### Peer-reviewed publications

- **Gonzalez, G.**; Baruffaldi, D; Martinengo C.; Angelini A., Chiappone A.; Roppolo, I.; Pirri, C.F.; Frascella F. “Materials testing for the development of biocompatible devices through vat-polymerization 3D printing.” *Nanomaterials (MDPI)*, **2020**, 10 (9), p. 1788-1791, doi: doi:10.3390/nano10091788.
- **Gonzalez, G.**; Chiappone, A.; Dietliker, K.; Pirri, C.F.; Roppolo, I. “Fabrication and Functionalization of 3D Printed Polydimethylsiloxane-Based Microfluidic Devices Obtained through Digital Light Processing.” *Adv. Mater. Technol.*, **2020**, 5 (9), 2000374, doi: 10.1002/admt.202000374.
- Frascella, F.; **Gonzalez, G.**; Bosch, P.; Angelini, A.; Chiappone, A.; Sangermano, M.; Pirri, C.F.; Roppolo, I. “Three-Dimensional Printed Photoluminescent Polymeric Waveguides.” *ACS Appl. Mater. Interfaces*, **2018**, 10 (45), p. 39319–39326, doi:10.1021/acsami.8b16036.

### Related to side research topics

- **Gonzalez, G.**; Chiappone, A.; Roppolo, I.; Fantino, E.; Bertana V.; Perrucci F.; Scaltrito L.; Pirri F.; Sangermano M. “Development of 3D printable formulations containing CNT with enhanced electrical properties.” *Polymer.*, **2017**, 109, p. 246–253, doi: 10.1016/j.polymer.2016.12.051.
- **Gonzalez, G.**; Fernandez X.; Serra A.; Sangermano M.; Ramis X. “Environmentally-friendly processing of thermosets by two-stage sequential aza-Michael addition and free-radical polymerization of amine–acrylate mixtures.” *Polymer Chemistry*, **2015**, 6, p. 6987-6997, doi: 10.1039/C5PY00906E.

## **Abroad research activities**

- Antibacterial activity studies of amine-functionalized 3D printed devices, Institute of Polymers Science and Technology (ICTP-CSIC), Madrid, Spain, October 1-December 20.

## **Conferences and workshops attended**

- *Three-dimensional printed photoluminescent polymeric waveguides*, Poster presentation at the 14<sup>th</sup> IEEE Nanotechnology Materials and Devices Conference, KTH, Stockholm, Sweden, October 27-30, 2019.
- *Three-dimensional printed photoluminescent polymeric waveguides*, Oral presentation at the Material in the Next Decade Workshop, INSTM, Favignana, Italy, September 18-20, 2019.
- *3D printed microfluidics and multiwell for biological applications*, Oral presentation at Converging Micro-nano-bio Technologies towards Integrated Biomedical Systems seminar, Fondazione Bruno Kessler, Trento, Italy, February 27-March 1, 2019
- *Novel 3D printable materials*, Oral and Poster presentation at Advanced Materials for High Growth Industries Workshop, CoACH, Turin, Italy October 3-4, 2018.

# Appendix B

## Characterization techniques

Through this doctoral dissertation, multiple techniques were employed to carry out different experiments and characterize the materials used. Herein, in Appendix B, those techniques are introduced.

### **Spectroscopy techniques.**

#### **Ultraviolet-Visible (UV-VIS) spectroscopy.**

The UV-Vis spectroscopy determines the radiation absorbed or transmitted by a solution containing an undetermined amount of solute compared to the same substance with a known solute concentration. The absorption/transmittance difference between both types of substance is collected by the instrument (the spectrophotometer). The UV-vis experiment uses electromagnetic radiation (light) in the regions between near-ultraviolet (UVB) and near-infrared (NIR), i.e., 200 to 800 nm. The irradiation absorbed in this region of the spectrum from the sample's molecules generates electronic transitions that can be determined (and quantified) from the instrument's detector. This absorption provokes the valence electrons' promotion from the basilar state, at lower energy, to an excited state of higher energy. When the UV-Vis irradiation passes through the solution containing an absorbent analyte, the incident light intensity ( $I_0$ ) is attenuated ( $I$ ); the light fraction that passed the solution is known as transmittance ( $T$ ) and follows  $T = I/I_0$ . Absorbance ( $A$ ) is more frequently used than  $T$  ( $A = -\log T$ ) since it is proportionally associated with the analyte concentration according to the Beer-Lambert law:  $A = \epsilon \cdot l \cdot c$ , where  $\epsilon$  is the molar absorptivity coefficient,  $l$  is the optical path, and  $c$  is the absorbent species' concentration, the analyte. The UV-vis microscopy techniques were used in this

doctoral dissertation to evaluate the absorbance range of different compositions and solutions.

### **Fourier transformed infrared (FTIR) spectroscopy.**

The FTIR spectroscopy is mainly used to measure the light absorption of a specific sample (liquid, solid, and gas) in the mid-infrared range of the electromagnetic spectrum, specifically in the range between 4000 to 400  $\text{cm}^{-1}$  wavenumbers (wavelengths from 2.5 to 25  $\mu\text{m}$ ), where most of the common organic and inorganic compounds absorb. Here, the samples' vibrational energy level shifts are measured by the transition from the ground state to an excited state in the radiation range. By Fourier transform mathematician operations, the raw data is converted into the final spectrum, composed of multiple peaks where the absorption intensity is associated with the change of a molecule's dipole moment. The vibrational energy gap provides the frequency of the absorption peak. The number of absorption peaks is related to the number of vibrational freedoms of the molecule. During the FTIR analysis, an attenuated total reflectance (ATR) accessory might be used to measure samples' properties (solid or liquid) at a surface level rather than the entire bulk of the material. In this case, the IR signal slightly penetrates inside the sample's surface, of around 1-2 micrometers. During this doctoral dissertation, the FTIR experiment was used to characterize the samples by following the change of the peaks related to functional groups (e.g., acrylate moieties) at different conditions. The spectra are normalized using a reference signal; the parameters selected are reported through the manuscript.

### **Microplate reader.**

Microplate readers are instruments used in the pharmaceutical and biotechnological field for detecting biological and chemical components. The samples are placed in a microplate, arranged with one or multiple wells having reaction volumes in the microliters' order. Typical microplates used are composed of a matrix of 96, 48, 24 sample wells. Microplate readers' detection modes are based on spectroscopy techniques by measuring the absorbance, fluorescence, luminescence, and fluorescent polarization of the samples, but also a combination of most of the detection modes can be found in multi-mode microplate readers. The microplate reader instrument was used for evaluating the optical density (OD) of solutions at a specific wavelength range and compared to control samples (without the evaluated substance). The microplate reader was also used as a UV-vis spectrophotometer, scanning the samples in a specified wavelength range at a controlled step.

### **Microscopy techniques.**

#### **Fluorescence microscopy.**

Fluorescence microscopy is an optical microscopy technique that utilized fluorescence signals for studying the characteristics of samples, organic or inorganic. The fluorescence is used to generate an image of the sample. The sample is irradiated by light at a specific wavelength through the objective lens; the light excites the sample's fluorophore, causing a light emission at a longer wavelength collected by a detector with a higher numerical aperture. The sample needs to be fluorescent for the

correct visualization of these techniques; some samples can be intrinsically fluorescent or autofluorescence, while those that are not can be labeled with fluorescent stains. This microscopy technique was used to observe and photograph living and dead biological units. The images were taken after staining the entities, as described through the manuscript.

### **Spinning disk confocal microscopy.**

Spinning disk confocal microscopy operates by projecting a series of parallel excitation light beams on samples through multiple pinholes disk. A multiplex model is created, and the fluorescence emission from the sample, which passes through the same pinholes, is detected from the instrument detector. This method is widely suitable for fast imaging of cells and biological entities that express fluorescence properties, natural or dyed-stained. This instrument was used to collect the bright-field and fluorescence images of biological units.

### **Scanning Electron microscopy (SEM).**

The scanning electron microscope (SEM) technique utilizes a high-energy electron beam that scans a sample, generating various signals and high-resolution images at the sample's surface's nanometric scale. The signal formed during the interaction between electrons and atom of the sample can reveal valuable information about sample features such as topography or external morphology, chemical compositions, crystallinity, disposition, and orientations of material components; the signal received is processed to generate images of the show most of these properties. Electrons of high kinetic energy are focused and, on the sample surface generating various signals from the electron-sample interactions, including mainly secondary electrons, backscattered electrons, and diffracted backscattered electrons, which are used for imaging the sample; also X-rays photons (used for elemental analysis) and visible light can be detected. The samples can be observed in vacuum conditions (high or low vacuum), wet configurations, or environmental conditions. In this last configuration, instead of creating a vacuum, the chamber is evacuated of air and remained at a relatively high-water pressure, which allows the analysis of samples with volatiles substance or water, enabling the observation of wet biological samples such as living cells.

### **Thermal analysis and thermo-mechanical techniques.**

#### **Differential scanning calorimetry (DSC).**

Differential scanning calorimetry (DSC) is a thermo-analytical technique capable to directly detect the thermal effects associated with phasing transition or other chemical processes that can occur in a sample as a function of temperature. It determined the amount of heat necessary to increase the sample's temperature compared to a reference sample with a known heat capacity; both samples are subjected to the same temperature variation during the process. The principle behind these techniques is that the instrument provides heat to the sample when it goes to a thermal-related transformation (e.g., melting of a solid) to maintain the same temperature as the reference. The energy given to the sample is based on whether it goes to an exothermic (release of heat) or endothermic (absorption of heat) transformation. In the DSC tests, the samples' energy uptake and heat flow can be

calculated in a controlled increase or decrease of temperature. During the DSC experiments (heating or cooling), different peaks with positive or negative heat flow ( $\Delta H/dt$ ) are associated with a determined process's heat behavior. DSC techniques are particularly used for determining the thermal-related parameters on an amorphous or crystalline material, such as material melting point (endothermal), crystallization (exothermal), and degradation (endothermal). Moreover, with DSC, other thermal-related parameters, such as the material glass transition temperature ( $T_g$ ), can be calculated when a material changes from a rigid glassy material to a softened material by heating.

### **Dynamic mechanical analysis (DMA).**

Dynamic mechanical analysis (DMA) is a technique that gives valuable information on the thermal-mechanical properties of materials. During the test, the samples are subjected to an oscillating force (at a specific frequency), and the instrument measures the material's response. The oscillatory force causes sinusoidal stress on the sample, generating an analogous strain response. By measuring the deformation's amplitude at the sine wave's peak and the lag between the induced stress and strain sine waves (known as  $\delta$ ), magnitudes such as the sample's modulus and damping can be determined. Limit values of  $\delta$  are  $0^\circ$  (purely elastic behavior) and  $90^\circ$  (purely viscous behavior). In DMA performed in tensile configuration, a storage modulus ( $E'$ ) and the loss modulus ( $E''$ ) are calculated from the sine wave's material response. Modulus  $E'$  represents the energy that the material stores due to the elastic portion's deformation. Modulus  $E''$  represents the energy dissipated by the material (as heat), the viscous portion. The ratio between both moduli represented as  $\tan \delta = (E''/E')$ , represent the material damping under cyclic stress in the deformation process; if the material presents a  $\tan \delta$  higher than 1, prevail the viscous component. The DMA instruments can accurately detect structural relaxations of polymer materials such as the glass transition under dynamical stress (also called relaxation  $\alpha$ ), which appears as a maximum on the curve of  $\tan \delta$ .

By the DMA test, the crosslinking density of the polymeric network might also be calculated from the storage modulus ( $E'$ ) in the rubbery state ( $E'_r$ ). The conventional theory of rubber elasticity describes that the elastic modulus is independent of the chemical nature of the structure and depends primarily on the rigidity of the network composition.<sup>145,474</sup> Therefore, the strand density, which is the number of moles of crosslinked chains per unit of volume, can be correlated to rubbery modulus ( $E'_r$ ) through the equation:  $E'_r = \nu * R * T$ ; where  $\nu$  is the crosslinking density,  $R$  is the universal gas constant, and  $T$  is the absolute temperature. The value of  $E'_r$  must be chosen at a temperature  $T$  where the rubbery plateau ( $E'$ ) is reached.  $E'_r$  parameter is roughly proportional to the crosslinking density, as deviations from the ideal rubber elasticity model are frequent in densely crosslinked thermosetting systems.<sup>95</sup>

### **Tensile testing.**

The tensile equipment allows testing the mechanical properties of a specimen when subjected to controlled tension or force. The sample is positioned in the testing machine and slowly apply a force, extending the sample until its fracture. The most commonly used machines are composed of two cross-heads or cells: the lower one is used to place and fix the sample, and the upper one applied the tension to the specimen. Therefore, it is possible to evaluate material characteristics such as the elastic performance (associated with the recovery of the material's deformation when

the applied stress is removed, the plastic deformation (when the deformation is not recovered once the stress is removed, modifying the specimens' structure) and, the eventually fracture. In this way, some parameters can be directly determined, e.g., ultimate tensile strength (UTS), fracturing strength, maximum elongation, elastic modulus, or young's modulus, Poisson's ratio, yield strength, among other.

## Other characterization techniques

### Rheology experiments.

A rheometer is an instrument capable of detecting the changes of flow and deformation of materials (liquid, suspension, or slurry) as a response to an applied force in a determined time (rheology). Differently from a viscosimeter where only the viscosity of a fluid can be obtained, a rheometer measures a wide range of rheological properties of non-Newtonian fluids (e.g., viscosity and elasticity) by setting different parameters. In this doctoral dissertation, a rotational parallel-plate mode rheometer was employed. The shearing planes' modality is parallel-plates flow-type, where the material is placed between both plates at a specific distance or gap. The upper plate is computer-assisted to induce the defined shear strain or stress range, and the instrument record how the material responds to the plied shear; values such as viscosity, shear stress/strain rate, complex viscosity, and material viscoelastic moduli can be obtained.

The rheometer instrument can be configured for performing oscillatory forces. In this case, the two plates sandwiched the sample, and the upper plate exerts an oscillatory force (sinusoidal) while the lower one remains stationary. The material responds to this oscillatory force as a sinusoidal. The lag between the two sinusoidal curves (the applied force and the material response) that oscillate with the same frequency might give valuable information about the material's viscoelastic properties. For a completely rigid and elastically-ideal material, there will not be a lag between both sinusoidal curves. Viscoelastic materials respond differently and can be seen as a lag between both sine curves, also known as phase shift ( $\delta$ ) that range between  $0^\circ$  (for ideally elastic deformation behavior) and  $90^\circ$  (for ideally viscous flow behavior). From the elasticity law in an oscillatory range, the relationship between shear-stress amplitude ( $\tau$ , in Pascal) and strain amplitude ( $\gamma$ , dimensionless, or in %) gives the complex shear modulus  $G^*$  (Pascal), which described the entire viscoelastic behavior of a material. According to the material's response during the sinusoidal force, this  $G^*$  can be expressed as  $G'$  (the storage modulus) or  $G''$  (the loss modulus). The former represents the elastic portion of the viscoelastic behavior, which describes the samples' solid-state behavior. The latter represents the viscous portion of the viscoelastic behavior, which can be seen as the sample's liquid-state behavior. The loss and storage moduli ratio ( $G''/G'$ ) is known as damping or loss factor ( $\tan \delta$ ). This parameter determines the ratio of the two portions of the viscoelastic behavior. For ideally elastic behavior,  $\delta = 0^\circ$ , which means there is not viscous portion with  $G''=0$  and so  $\tan \delta = 0$ . For ideally viscous behavior,  $\delta = 90^\circ$ , which means there is no elastic portion with  $G'=0$  and  $\tan \delta$  that tend to infinity. With this information, some material's features such as gel point or sol/gel transition can be determined as the crossover between  $G''$  and  $G'$ , representing the material character changes during the experiment, e.g., from liquid to solid.

This rheometer mode was used to measure in real-time the material's changes upon direct light radiation. The instrument setup was changed, positioning a bottom quartz plate (instead of aluminum), and a visible lamp, equipped with an optical fiber



is placed beneath this. In this way, the rheometer can measure the material's response during photopolymerization and determine the material's gel point at a particular experimental condition.

### **Contact angle methods.**

Contact angle measurement is one of the most used methods to measure the wettability of materials. These techniques are based on the liquid behavior observation when a drop is deposited on a surface or substrate. The contact angle between the deposited liquid (drop-by-drop) over the surface, in the presence of air and considering its surface tension, is measured and determines the surface wettability. Different liquids can be used in these tests, including polar (water and formamide) and non-polar solvents (diiodomethane). Thus, the contact angle measurements can provide valuable information about the surface's hydrophobicity/hydrophilicity and surface energy. In general, wetting liquids form a contact angle with the substrate smaller than  $90^\circ$ , while non-wetting liquids form a contact angle between  $90^\circ$  and  $180^\circ$  with the substrate.